Optimalisatie van de stroomgolfvorm
en intelligente maximum-vermogenregeling voor windturbines

Optimal Current Waveform Shaping
and Intelligent Maximum Power Point Tracking for Wind Turbines

Jeroen De Kooning

Promotor: prof. dr. ir. L. Vandevelde
Proefschrift ingediend tot het behalen van de graad van
Doctor in de Ingenieurswetenschappen: Werktuigkunde-Elektrotechniek

Vakgroep Elektrische Energie, Systemen en Automatisering
Voorzitter: prof. dr. ir. J. Melkebeek
Faculteit Ingenieurswetenschappen en Architectuur
Academiejaar 2015 - 2016

UNIVERSITEIT
GENT

ISBN 978-90-8578-853-9
NUR 961, 959
Wettelijk depot: D/2015/10.500/97

Ghent University
Faculty of Engineering and Architecture
Department of Electrical Energy,
Systems and Automation (EESA)
Electrical Energy Laboratory (EELAB)

Promoter
Prof. dr. ir. Lieven Vandevelde (UGent – EESA)

Chairman
Prof. dr. ir. Hendrik Van Landeghem (UGent)

Exam commission
Prof. dr. ir. Anouar Belahcen (Aalto University – EEA)

Prof. dr. ir. Johan Driesen (KU Leuven – ESAT)

dr. ir. Bart Meersman (UGent – EESA)

Prof. dr. ir. Pieter Rombouts (UGent – ELIS)

Prof. dr. Mark Runacres (VUB – INDI)

Prof. dr. ir. Lieven Vandevelde (UGent – EESA)

DANKWOORD

Zoals u kan vermoeden werd dit boek niet op één dag geschreven. Het is het resultaat van vijf jaar onderzoek, waarbij de bijdrage van heel wat mensen niet mag onderschat worden. Hierna probeer ik zo volledig mogelijk iedereen te bedanken, wat een onmogelijke taak is. Treur dus niet wanneer uw naam niet vermeld wordt, het is niet persoonlijk!

Tijdens het schrijven van mijn masterthesis, in 2010, werd ik overtuigd door mijn begeleider Bart om te starten met een doctoraat. Zonder hem zou dit boek er nooit geweest zijn. Ook als bureaugenoot hebben we de voorbije jaren heel wat afgelachen, bedankt! Lieven, je oneindige positieve ingesteldheid en rust zullen me altijd bijblijven. Deze eigenschappen hebben een niet te onderschatten waarde als promotor. Verder wil ik ook de juryleden bedanken voor hun feedback die zeker de kwaliteit van dit werk heeft verhoogd.

Doorheen de jaren heb ik heel wat bureaugenoten gehad: Bart, Brecht, Christof, Jan, Joannes, Giustino, Lieven, Louis, Samie, Sophie en Tine. Bedankt voor het leuke gezelschap, de vaak hilarische gesprekken en professionele samenwerking. Dat laatste heeft bovendien tot heel wat gezamenlijke publicaties geleid.

De eindfase van een doctoraat geeft onvermijdelijk extra stress. Gelukkig gaf Lemuria mij steeds een uitlaatklep. Bart, Gaël, Vincent en Wesley: merci! Dat we ooit nog op Wacken mogen spelen! Wie onze muziek niet kent: breng een bezoek aan www.Lemuria.be.

Bedankt ook aan alle vrienden en vriendinnen voor het gezelschap op de vele etentjes en barbecues. Ik heb ondervonden dat wetenschappelijk onderzoek beter gaat met een volle maag. Ik wil hiermee niemand pushen, maar dat er nog veel trouwfeesten en babyborrels mogen volgen!

Mijn ouders, schoonouders, broer, schoonbroer en schoonzus wil ik bedanken voor hun gastvrijheid, opvang van de kindjes en hulp bij onze renovatiewerken.

Het laatste woord is natuurlijk voor de drie belangrijkste vrouwen in mijn leven: Jolien, Aline en Hanna. Jolien, bedankt om mij heel deze periode te steunen. Vooral tijdens de laatste maanden, die niet eenvoudig waren. Je weet als geen ander wanneer je mij gewoon eventjes moet laten werken, ook al heb je volop weeën! Aline en Hanna, jullie zijn nog te klein om te beseffen waarom ik zo veel aan mijn computer heb zitten tokkelen. Stiekem hoop ik dat jullie dit boek ooit zullen lezen, of er zelf een zullen schrijven!

Beste lezer, het is nu tijd om ook de rest van dit werk te lezen. Veel plezier!

November 2015
Jeroen De Kooning

From September 2010 - September 2011, this research has been funded by the FWO Project G.0587.07N. J. De Kooning would like to thank the FWO for the funding.

From October 2011 - August 2015, the research of Jeroen De Kooning is financially supported by the Special Research Fund (BOF) of Ghent University. J. De Kooning thanks Ghent University for the fellowship received.

SUMMARY

English summary

Wind energy is one of the most promising sources of renewable energy for the future. Although the technology of wind turbines is more mature than, e.g., wave and tidal energy converters, there is still room for improvement. Especially small and medium wind turbines often have a disappointing energy yield. The research presented in this dissertation aims at improving this energy yield. An increased economic profitability could encourage the market, which leads to more installed turbines and produced renewable energy.

The research focuses on the topology of a typical state-of-the-art turbine. This turbine design uses a Permanent Magnet Synchronous Machine (PMSM) as a generator. PMSMs are known for their high efficiency and favorable dynamic properties. They can be modeled by an equivalent scheme in a rotating reference frame. An iron loss resistance represents the eddy current and hysteresis losses. Regarding the rectifier, commercial turbines use a passive diode rectifier combined with a boost dc/dc chopper. Although simple and cheap, this topology has a limited control flexibility. For instance, the current waveform in the generator cannot be controlled, has a high harmonic content and low power factor. Therefore, the more advanced four-wire full active rectifier is used in this work. This topology allows the use of optimal current waveform shaping, which is one of the main topics here.

In theory, an ideal PMSM is either a Brushless AC (BLAC) or Brushless DC (BLDC) machine. The BLAC has a sinusoidal back-emf waveform, while the BLDC has a trapezoidal back-emf waveform. Normally, a sinusoidal current waveform is used for BLAC machines while a square-wave current waveform is used for BLDC machines. However, in practice, many machines have a so-called hybrid back-emf waveform, i.e., not purely sinusoidal or trapezoidal. For these machines, a sinusoidal or square-wave current waveform is not necessarily the ideal waveform considering the efficiency and torque ripples.

The concept of optimal current waveform shaping was developed to

cope with these non-ideal back-emf waveforms. Given the parameters and back-emf waveform of a PMSM, the optimal current waveform is determined such that a desired goal is achieved, e.g., minimum torque ripple or maximum efficiency. In the past, most research focussed on minimising the torque ripple. However, in the light of global warming, the efficiency has become more important. Therefore, in this work, a new optimal current waveform shaping technique is presented which simultaneously maximises the efficiency of the PMSM and the converter. The new technique uses the Cauchy-Schwarz inequality to prove that, for any given back-emf waveform, a proportional current waveform yields a minimum of losses. The main disadvantage of the new technique is the increased torque ripple, which is a natural compromise. Whether this is a problem depends on the application.

Although the basic principle of the new method appears simple, mathematical manipulations are needed to apply this concept on the complete equivalent scheme of a PMSM. For each subsystem in the rotating reference frame, an optimal current waveform is obtained. In each subsystem, a scale factor is introduced. Then, these scale factors are optimised by an iterative grid search algorithm to maximise the overall efficiency and to reach a desired mechanical operating point, i.e., speed or torque. The new optimal current waveform shaping technique is investigated further in a case study, a parameter sensitivity analysis and is finally implemented in a detailed Simulink model of a wind turbine system.

The main strength of the new technique is that it works in the time-domain and needs a minimum of assumptions and simplifications, resulting in a generic closed-form analytic formulation. In contrast, classical techniques in literature simplify the machine until a frequency domain approach is feasible in which a limited amount of harmonic components is calculated.

Since the waveform of the back-emf is the starting point of the research, the impact of speed ripples was investigated as well. No method exists to calculate this impact. Therefore, a mathematical model is developed to determine the additional back-emf harmonics caused by the speed ripples. Also, the magnitude of typical speed ripples in wind turbines is determined by simulating the effect of tower shadow and wind shear. Since this magnitude is low and the impact on the back-emf limited, the speed ripples can be neglected during the development of the optimal current waveform method.

During this research, the performance of Maximum Power Point Tracking (MPPT) algorithms was also investigated. The MPPT algorithm aims at controlling the turbine to the optimal rotor speed to maximise the power coefficient of the blades. Standardised IEC 61400-2 measurements were analysed to show that, currently, MPPT systems fail at properly controlling the turbine to the optimal operating point, leading to a reduced energy yield. The impact of the losses on the location of this optimal operating point was also investigated. A simulation model was developed which includes all dominant loss components, i.e., mechanical losses, copper and iron losses in the generator and switching and conduction losses in the converter. The simulations show that the real optimal operating point does not always coincide with the optimal operating point of solely the turbine. For the turbine investigated here, it is beneficial to use a slighly lower rotor speed than dictated by the classical MPP. By implementing this, the yearly energy yield can be increased by 1 - 2%.

During this work, there have been several contacts and collaborations with industry in the frame of the Small Wind Turbine Field Laboratory in Ostend or service projects for industry. These collaborations have shown a few critical points in the realisation of a commercial wind turbine. Often, vertical axis designs such as the Savonius are used. However, a classical three-bladed horizontal axis turbine has a higher power coefficient and should be the preferred design. Some designers even use extreme turbine designs which are aesthetically interesting, but energetically useless. Another problem is that the expected wind speeds are estimated too optimistically. Most turbines are designed for an average wind speed of 5m/s, while in reality, average speeds of 3 or 4 m/s are more common. This mismatch between design and reality results in an oversized generator and converter, which is costly, with a disappointing energy yield. Finally, the market of small and medium wind turbines is set back considerably by the negative attitude of the government, who seldomnly grants a build permit.

The main contributions of this research are the new optimal current waveform shaping method, the back-emf model including speed ripples and the MPPT concept considering the impact of losses. The optimal current waveform shaping method and advanced MPPT algorithm are able to increase the energy yield of a wind turbine. The optimal current waveform shaping method can also be applied in other applications, such as industrial drives, wave energy converters, electric vehicles, etc. The comments and advice presented in chapter 7 can be a guideline for entrepeneurs or designers who want to bring a wind turbine on the market.

Nederlandstalige samenvatting

Windenergie is een van de meest veelbelovende bronnen van hernieuwbare energie in de toekomst. Alhoewel de technologie van windturbines meer volwassen is dan die van, bijvoorbeeld, golf- en getijdenenergie, is er nog steeds ruimte voor verbetering. Kleine en middelgrote windturbines in het bijzonder hebben vaak een tegenvallende energieopbrengst. Het onderzoek voorgesteld in dit proefschrift heeft als doel deze energieopbrengst te verhogen. Een verbeterde economische winstgevendheid kan de markt aanmoedigen, wat leidt tot meer geïnstalleerde turbines en een hoger aandeel aan hernieuwbare energie.

Het onderzoek behandelt de topologie van de typische moderne turbine. Dit ontwerp gebruikt een Permanent Magneet bekrachtigde Synchrone Machine (PMSM) als generator. PMSMs zijn gekend voor hun hoge rendement en gunstige dynamische eigenschappen. Ze kunnen gemodeleerd worden door een equivalent schema in een synchroon referentiestelsel. Een ijzerverliesweerstand stelt de wervelstroom- en hysteresisverliezen voor. Betreffende de gelijkrichter maken commerciële turbines gebruik van een passieve diodegelijkrichter in combinatie met een spanningsverhogende hakker. Alhoewel dit eenvoudig en goedkoop is, geeft deze topologie weinig flexibiliteit in de controle. Bijvoorbeeld, de golfvorm van de stroom in de generator kan niet geregeld worden, heeft een hoge harmonische inhoud en een lage arbeidsfactor. Om die reden wordt de actieve gelijkrichter met neutrale geleider gebruikt in dit werk. Deze topologie laat het gebruik van geoptimaliseerde stroomgolfvormen toe, een van de hoofdonderwerpen in dit onderzoek.

In principe is een ideale PMSM ofwel een borstelloze ac (BLAC) of borstelloze dc (BLDC) machine. De tegen-emk van de BLAC heeft een sinusoidale golfvorm, de BLDC een trapezoidale. Normaal gesproken wordt een sinusoidale stroom gebruikt voor een BLAC machine en een trapezoidale stroom voor de BLDC machine. In de praktijk hebben veel machines echter een hybride golfvorm van de tegen-emk, dus niet zuiver sinusoidaal of trapezoidaal. Een sinusoidale of trapezoidale stroomvorm is niet noodzakelijk ideaal voor deze machines wanneer men het rendement en koppelrimpel in beschouwing neemt.

Het principe van stroomgolfvorm optimalisatie werd ontwikkeld om

met deze niet-ideale tegen-emk om te gaan. De optimale stroomvorm wordt zodanig berekend, gegeven de parameters en de golfvorm van de tegen-emk, dat een bepaald doel wordt bereikt, bijvoorbeeld een minimale koppelrimpel of een maximaal rendement. In het verleden lag de focus in het onderzoek voornamelijk op het minimaliseren van de koppelrimpel. Wegens de huidige aandacht voor de klimaatverandering wint het rendement echter aan belang. Daarom wordt in dit werk een stroomgolfvorm optimalisatie voorgesteld die zowel het rendement van de machine als van de converter maximaliseert. Deze nieuwe techniek gebruikt de ongelijkheid van Cauchy-Schwarz om te bewijzen dat, gegeven de golfvorm van de tegen-emk, een evenredige golfvorm van de stroom de verliezen minimaliseert. Het nadeel van deze nieuwe techniek is een verhoogde koppelrimpel, wat volgt als een natuurlijk compromis. Afhankelijk van de toepassing vormt dit al dan niet een probleem.

Het basisprincipe van de nieuwe techniek lijkt eenvoudig, maar wiskundige manipulaties zijn noodzakelijk om ze toe te passen op het volledige equivalente schema van een PMSM. Voor elke as in het synchroon referentiestelsel wordt een optimale stroomvorm bepaald. Eveneens wordt in elke as een schaalfactor geïntroduceerd. Vervolgens worden deze schaalfactoren geoptimaliseerd in een iteratief zoekalgoritme om het totale rendement te maximaliseren en om het gewenste mechanische werkingspunt (snelheid of koppel) te bereiken. De nieuwe stroomgolfvorm optimalisatie techniek wordt verder onderzocht in een gevallenstudie, een parameter sensitiviteitsanalyse en wordt uiteindelijk geïmplementeerd in een gedetailleerd Simulink model van een windturbine.

De grootste sterkte van de nieuwe techniek is dat deze in het tijdsdomein werkt en een minimale hoeveelheid veronderstellingen en vereenvoudigingen nodig heeft, wat resulteert in een algemene analytische formulering in een gesloten vorm. Klassieke technieken uit de literatuur vereenvoudigen de machine zodat een frequentie-domein methode haalbaar wordt, waarbij slechts een beperkt aantal harmonische componenten wordt berekend.

Aangezien de golfvorm van de tegen-emk het uitgangspunt vormt van dit onderzoek, werd ook de invloed van snelheidsrimpels onderzocht. Tot nu toe bestond geen methode om deze te berekenen. Daarom werd een wiskundig model uitgewerkt om te bepalen welke bijkomende spanningsharmonischen ontstaan ten gevolge van de snelheidsrimpels. Eveneens werd de grootte van een typische snelheidsrimpel bij windturbines berekend door het effect van torenschaduw en windschering te simuleren. Aangezien deze snelheidsrimpels klein zijn en de invloed ervan op de tegen-emk beperkt, worden de snelheidsrimpels verwaarloosd bij de verdere uitwerking van de stroomgolfvorm optimalisatie methode.

Er werd eveneens onderzoek verricht naar Maximum Power Point Tracking (MPPT) algoritmes. Het MPPT algoritme heeft tot doel om de turbine te regelen naar de optimale snelheid om de vermogenscoëfficiënt van de schoepen te maximaliseren. Gestandardiseerde IEC 61400-2 metingen werden geanalyseerd om aan te tonen dat de MPPT algoritmes in huidige turbines er niet in slagen om een turbine naar het optimale werkingspunt te regelen, wat de energieopbrengst verlaagt. De invloed van verliezen op de ligging van het optimale werkingspunt werd eveneens onderzocht. Een simulatiemodel werd uitgewerkt dat alle dominante verliescomponenten bevat, namelijk mechanische verliezen, koper- en ijzerverliezen in de generator en schakel- en geleidingsverliezen in de convertor. De simulaties tonen dat het werkelijke optimale werkingspunt niet altijd samenvalt met het optimale werkingspunt van enkel de turbine. Voor de turbine die hier onderzocht werd, is een lagere rotatiesnelheid voordelig dan diegene die overeenkomt met het punt van maximaal turbinevermogen. Wanneer dit geimplementeerd wordt in een turbine, kan de jaarlijkse energieopbrengst met 1 à 2 % verhoogd worden.

Tijdens dit werk zijn er verscheidene contacten en samenwerkingen geweest met de industrie, in het kader van het Kleine Wind Turbine veldlaboratorium in Oostende of dienstverleningsprojecten. Deze contacten hebben enkele kritieke punten aangetoond in de totstandkoming van een commerciële windturbine. Vaak gebruikt men verticale as turbines, bvb. van het Savonius-type. Een klassieke horizontale as turbine met drie schoepen heeft echter de hoogste vermogenscoëfficiënt en zou de voorkeur moeten krijgen. Sommige types hebben zelfs bijzonder extreme ontwerpen. Deze zijn esthetisch interessant, maar energetisch niet. Een ander probleem is dat men de verwachte windsnelheid te optimistisch inschat. De meeste turbines worden ontworpen voor een gemiddelde windsnelheid van 5m/s, terwijl men in de praktijk eerder 3 à 4m/s ervaart. Deze verkeerde inschatting leidt tot een overgedimensioneerde generator en convertor, wat kostelijk is en een teleurstellende energieopbrengst geeft. Tenslotte wordt de markt van kleine en middelgrote windturbines gevoelig afgeremd door een negatieve instelling bij de overheid. Slechts zelden wordt een bouwvergunning uitgereikt.

De grootste bijdragen van dit onderzoek zijn de nieuwe stroomgolfvorm optimalisatie methode, het tegen-emk model dat rekening houdt met snelheidrimpels en het MPPT concept dat rekening houdt met de invloed van verliezen. De nieuwe stroomgolfvorm optimalisatie methode en geavanceerde MPPT zijn in staat om de energieopbrengst van een windturbine te verhogen. De stroomgolfvorm optimalisatie kan eveneens gebruikt worden in andere toepassingen, zoals industriële convertoren, golfenergieconvertoren, elektrische voertuigen, enz. De opmerkingen en het advies voorgesteld in hoofdstuk 7 kunnen een richtlijn vormen voor ondernemers of ontwerpers die een windturbine op de markt willen brengen.

AUTHOR BIBLIOGRAPHY

[1] J. D. M. De Kooning, T. L. Vandoorn, J. Van de Vyver, B. Meersman and L. Vandevelde, “Displacement of the maximum power point caused by losses in wind turbine systems,” *Renewable Energy*, vol. 85, pp. 273–280, Jan. 2016.

[2] J. D. M. De Kooning, T. L. Vandoorn, J. Van de Vyver, B. Meersman and L. Vandevelde, “Shaft speed ripples in wind turbines caused by tower shadow and wind shear,” *IET Renewable Power Generation*, vol. 8, pp. 195–202, Mar. 2014.

[3] J. D. M. De Kooning, J. Van de Vyver, T. L. Vandoorn, B. Meersman and L. Vandevelde, “Impact of speed ripple on the back-emf waveform of permanent magnet synchronous machines,” *IET Electric Power Applications*, vol. 7, pp. 400–407, May 2013.

[4] J. D. M. De Kooning, L. Gevaert, J. Van de Vyver, T. L. Vandoorn and L. Vandevelde, “Online estimation of the power coefficient versus tip-speed ratio curve of wind turbines,” in *Proc. of the 2013 IECON conference*, (Vienna, Austria), November 10-13, 2013.

[5] J. D. M. De Kooning, J. Van de Vyver, T. L. Vandoorn, B. Meersman and L. Vandevelde, “Joule losses and torque ripple caused by current waveforms in small and medium wind turbines,” in *Proc. of the 2013 IEEE Eurocon conference (EUROCON 2013)*, (Zagreb, Croatia), July 1 - 4, 2013.

[6] J. D. M. De Kooning, B. Meersman, T. L. Vandoorn and L. Vandevelde, “Evaluation of the maximum power point tracking performance in small wind turbines,” in *Proc. of the 2012 IEEE Power & Energy Society General Meeting (PES GM 2012)*, (San Diego, USA), July 22 - 26, 2012.

[7] J. D. M. De Kooning, B. Meersman, T. L. Vandoorn and L. Vandevelde, “Efficiency improvement of a small wind turbine by adaptation of the rectifier circuit and control,” in *Proc. of the 6th IEEE Benelux Young Researchers Symposium in Electrical Power Engineering (YRS 2012)*, (Delft, Netherlands), April 16 - 17, 2012.

[8] J. D. M. De Kooning and L. Vandevelde, "Current waveform shaping in small wind turbines," in *12th FEA PhD Symposium*, (Gent, Belgium), Dec. 7, 2011.

[9] J. D. M. De Kooning, B. Meersman, T. L. Vandoorn, B. Renders and L. Vandevelde, "Comparison of three-phase four-wire converters for distributed generation," in *Proc. of the 45th International Universities Power Engineering Conference (UPEC 2010)*, (Cardiff, UK), Aug. 31 - Sep. 3, 2010.

[10] J. D. M. De Kooning, J. Laveyne, J. De Maeyer, G. Van Eetvelde and L. Vandevelde, "Kleine windturbines," *Het Ingenieursblad*, vol. 80, pp. 31–33, Dec. 2011.

[11] J. D. M. De Kooning, L. Vandevelde, B. Meersman and T. Vandoorn, "Verbetering van de netkwaliteit met behulp van decentrale energieproductie en split-link convertoren," *KBVE Revue E*, vol. 127, pp. 35–38, Dec. 2011.

[12] K. Van Wyngene, J. Laveyne, J. D. M. De Kooning, K. Stockman, P. Sergeant, W. Van Paepegem, D. Botteldooren, J. De Maeyer, G. Van Eetvelde and L, Vandevelde, "The small wind turbine field lab extensive field tests for small wind turbines," *WWEA Quarterly Bulletin*, pp. 56–63, 2013.

[13] J. Van de Vyver, J. D. M. De Kooning, B. Meersman, L. Vandevelde and T. L. Vandoorn, "Droop control as an alternative inertial response strategy for the synthetic inertia on wind turbines," *IEEE Transactions on Power Systems*, 2015.

[14] T. L. Vandoorn, J. D. M. De Kooning, B. Meersman and B. Zwaenepoel, "Control of storage elements in an islanded microgrid with voltage-based control of DG units and loads," *International Journal of Electrical Power & Energy*, 2014.

[15] T. L. Vandoorn, C. M. Ionescu, J. D. M. De Kooning, R. De Keyser and L. Vandevelde, "Theoretical analysis and experimental validation of single-phase direct vs. cascade voltage control in islanded microgrids," *IEEE Transactions on Industrial Electronics*, vol. 60, pp. 789–798, Feb. 2013.

[16] T. L. Vandoorn, J. D. M. De Kooning, B. Meersman and L. Vandevelde, "Voltage-based droop control of renewables to avoid

on-off oscillations caused by overvoltages," *IEEE Transactions on Power Delivery*, vol. 28, pp. 845–854, Apr. 2013.

[17] T. L. Vandoorn, J. D. M. De Kooning, B. Meersman, J. Guerrero and L. Vandevelde, "Voltage-based control of a smart transformer in a microgrid," *IEEE Transactions on Industrial Electronics*, vol. 60, pp. 1291–1305, Apr. 2013.

[18] T. L. Vandoorn, B. Meersman, J. D. M. De Kooning and L. Vandevelde, "Transition from islanded to grid-connected mode of microgrids with voltage-based droop control," *IEEE Transactions on Power Systems*, vol. 28, pp. 2545–2553, Aug. 2013.

[19] T. L. Vandoorn, J. D. M. De Kooning, B. Meersman and L. Vandevelde, "Review of primary control strategies for islanded microgrids with power-electronic interfaces," *Renewable & Sustainable Energy Reviews*, vol. 19, pp. 613–628, Aug. 2013.

[20] T. L. Vandoorn, J. Vasquez, J. D. M. De Kooning, J. Guerrero and L. Vandevelde, "Microgrids hierarchical control and an overview of the control and reserve management strategies," *IEEE Industrial Electronics Magazine*, vol. 7, no. 4, pp. 42–55, 2013.

[21] T. L. Vandoorn, J. D. M. De Kooning, J. Van de Vyver and L. Vandevelde, "Three-phase primary control for unbalance sharing between distributed generation units in a microgrid," *Energies*, vol. 6, pp. 6586–6607, Aug. 2013.

[22] T. L. Vandoorn, B. Meersman, J. D. M. De Kooning and L. Vandevelde, "Controllable harmonic current sharing in islanded microgrids: DG units with programmable resistive behavior towards harmonics," *IEEE Transactions on Power Delivery*, vol. 27, pp. 831–841, Apr. 2012.

[23] T. L. Vandoorn, B. Meersman, J. D. M. De Kooning and L. Vandevelde, "Directly-coupled synchronous generators with converter behavior in islanded microgrids," *IEEE Transactions on Power Systems*, vol. 27, pp. 1395–1406, Aug. 2012.

[24] T. L. Vandoorn, B. Meersman, J. D. M. De Kooning, J. Guerrero and L. Vandevelde, "Automatic power sharing modification of P/V droop controllers in low-voltage resistive microgrids," *IEEE*

Transactions on Power Delivery, vol. 27, pp. 2318–2325, Oct. 2012.

[25] T. L. Vandoorn, B. Meersman, J. D. M. De Kooning, J. Guerrero and L. Vandevelde, "Analogy between conventional grid control and islanded microgrid control based on a global dc-link voltage droop," *IEEE Transactions on Power Delivery*, vol. 27, pp. 1405–1414, July 2012.

[26] J. De Kooning, J. Van de Vyver, J. D. M. De Kooning and T. Vandoorn and L. Vandevelde, "Grid voltage control with wind turbine inverters by using grid impedance estimation," in *Proc. of the 3rd Renewable Power Generation Conference*, (Naples, Italy), Sep. 24-25, 2014.

[27] X. bracke, J. D. M. De Kooning, J. Van de Vyver and L. Vandevelde, "Effective capture of wind gusts in small wind turbines by using a full active rectifier," in *Proc. of the 3rd Renewable Power Generation Conference*, (Naples, Italy), Sep. 24-25, 2014.

[28] J. Van de Vyver, T. L. Vandoorn, J. D. M. De Kooning, B. Meersman and L. Vandevelde, "Provision of ancillary services with variable speed wind turbines," in *Proc. of the 2014 IEEE Benelux Chapter Young Researchers Symposium (YRS 2014)*, (Ghent, Belgium), Apr. 24-25, 2014.

[29] J. Van de Vyver, T. L. Vandoorn, J. D. M. De Kooning, B. Meersman and L. Vandevelde, "Energy yield losses due to emulated inertial response with wind turbines," in *Proc. of the 2014 IEEE Power & Energy Society General Meeting (PES GM 2014)*, (Washington, USA), Jul. 27-31, 2014.

[30] J. Van de Vyver, J. D. M. De Kooning, T. L. Vandoorn and L. Vandevelde, "Optimization of constant power control of wind turbines to provide power reserves," in *Proc. of the 48th International Universities Power Engineering Conference (UPEC 2013)*, (Dublin, Ireland), Sep. 2-5, 2013.

[31] L. F. M. Gevaert, J. D. M. De Kooning, T. L. Vandoorn, J. Van de Vyver and L. Vandevelde, "Evaluation of the mppt performance in small wind turbines by estimating the tip-speed ratio," in *Proc. of the 48th International Universities Power Engineering Conference (UPEC 2013)*, (Dublin, Ireland), Sep. 2-5, 2013.

[32] W. Willems, T. L. Vandoorn, J. D. M. De Kooning and L. Vandevelde, “Development of a smart transformer to control the power exchange of a microgrid,” in *Proc. of the 4th European Innovative Smart Grid Technologies Conference*, (Copenhagen, Denmark), Oct. 6-9, 2013.

[33] T. L. Vandoorn, W. Willems, J. D. M. De Kooning, J. Van de Vyver and L. Vandevelde, “Contribution of a smart transformer in the local primary control of a microgrid,” in *Proc. of the 4th European Innovative Smart Grid Technologies Conference*, (Copenhagen, Denmark), Oct. 6-9, 2013.

[34] T. Vandoorn, J. D. M. De Kooning, B. Meersman and L. Vandevelde, “Improvement of active power sharing ratio of P/V droop controllers in low-voltage islanded microgrids,” in *Proc. of the 2013 IEEE Power & Energy Society General Meeting (PES GM 2013)*, (Vancouver, Canada), July 21-25, 2013.

[35] T. Vandoorn, J. D. M. De Kooning, B. Meersman and L. Vandevelde, “Soft curtailment for voltage limiting in low-voltage networks through reactive or active power droops,” in *Proc. of the IEEE International energy conference & exhibition (EnergyCon)*, (Florence, Italy), Sep, 2012.

[36] T. Vandoorn, J. D. M. De Kooning, B. Meersman and L. Vandevelde, “Communication-based secondary control in microgrids with voltage-based droop control,” in *Proc. of the 2012 IEEE PES Transmission and Distribution conference and exposition (PES TD)*, (Orlando, USA), May, 2012.

[37] T. Vandoorn, B. Zwaenepoel, J. D. M. De Kooning, B. Meersman and L. Vandevelde, “Smart microgrids and virtual power plants in a hierarchical control structure,” in *Proc. of the 2nd European conference and exhibition on Innovative Smart Grid Technologies (ISGT-Europe 2011)*, (Manchester, UK), Dec. 2011.

[38] M. Jacxsens, B. Meersman, T. L. Vandoorn, J. D. M. De Kooning and L. Vandevelde, “Overview of voltage control strategies in medium voltage networks with implementation of distributed generation,” in *Proc. of the IET Renewable Power Generation Conference (RPG 2011)*, (Edinburgh, UK), Sep. 5-8, 2011.

[39] K. Martens, B. Meersman, J. D. M. De Kooning, B. Renders, T. L. Vandoorn and L. Vandevelde, “Influence of bus voltage variations on two maximum power point control loops,” in *Proc. of the 14th International Conference on Harmonics and Quality of Power (ICHQP 2010)*, (Bergamo, Italy), Sep. 26-29, 2010.

[40] B. Meersman, J. De Kooning, T.L. Vandoorn, L. Degroote, B. Renders and L. Vandevelde, “Overview of PLL methods for distributed generation units,” in *Proc. of the 45th International Universities Power Engineering Conference (UPEC 2010)*, (Cardiff, UK), Aug. 31 - Sep. 3, 2010.

[41] B. Meersman, B. Renders, L. Degroote, T.L. Vandoorn, J. D. M. De Kooning and L. Vandevelde, “Overview of three-phase inverter topologies for distributed generation purposes,” in *Proceedings of the 2nd conference on Innovation for Sustainable Production (i-SUP 2010)*, (Bruges, Belgium), Apr. 18-21, 2010.

[42] J. Laveyne, K. Van Wyngene, J. D. M. De Kooning, S. Van Ackere, G. Van Eetvelde and L. Vandevelde, “The small wind turbine field lab,” in *BERA Wind Workshop*, (Brussels, Belgium), Sep. 13, 2013.

[43] J. Van de Vyver, J. D. M. De Kooning, T. L. Vandoorn, B. Meersman and L. Vandevelde, “Grid support with wind turbines by the provision of ancillary services,” in *BERA Wind Workshop*, (Brussels, Belgium), Sep. 13, 2013.

ABBREVIATIONS

ADC	Analog to Digital Converter
BLAC	Brushless Alternating Current
BLDC	Brushless Direct Current
CFD	Computational Fluid Dynamics
DFIG	Doubly-Fed Induction Generator
DRFF	Duty-Ratio Feed Forward
DSP	Digital Signal Processor
EMF	Electromotive Force
FEM	Finite Element Method
FPGA	Field Programmable Gate Array
IGBT	Insulated Gate Bipolar Transistor
MOSFET	Metal-Oxide Semiconductor Field-Effect Transistor
MPP	Maximum Power Point
MPPT	Maximum Power Point Tracking
OFAT	One-Factor-At-a-Time
OMPP	Overall Maximum Power Point
P&O	Perturb and Observe
PI	Proportional Integral
PLL	Phase-Locked Loop
PMSM	Permanent Magnet Synchronous Machine
PWM	Pulse-Width Modulation
TMPP	Turbine Maximum Power Point
TSR	Tip-Speed Ratio
VSI	Voltage-Source Inverter

LIST OF FIGURES

List of Tables

Contents

1

INTRODUCTION

This introductory chapter explains the broader context, motivation and goal of the research presented in this dissertation. Also, an overview of the work is given.

Contents

1.1 Context of the research

Global warming, carbon emission and climate change are topics which have been discussed immensely, and with reason, as they form the biggest problems of the 21^{st} century and are a major challenge for technology and engineering.

It is expected that global warming can only be tackled by numerous measures together, instead of one single magical solution. This dissertation aims at delivering a few puzzle pieces to the greater whole. The research presented here lies in the domain of electrical power engineering, with wind turbines as the main application. It is believed that wind turbines will be an important source of renewable energy in the future, alongside photovoltaics, wave, tidal, geothermal, biomass, etc.

Wind turbines play an important role in the production of renewable energy. The global installed capacity of wind power reached 370 GW at the end of 2014 [44], growing 51 GW during the last year. The majority of these wind turbines have a rated power of several MW. However, small and medium wind turbines with a rated power below 300 kW can also have a valuable contribution in the production of renewable energy. They have less visual impact and can be installed close to the consumer in a decentralized manner, for example, in rural, urban or industrial areas.

Although small and medium wind turbines undeniably have a positive impact on the environment [45], they often have a disappointing energy yield and economical profitability. This can be caused by many aspects, such as a mismatch between the wind speed range for which the turbine was designed and the actual wind speed at the location. Also, the performance of the Maximum Power Point Tracker (MPPT) determines the efficiency of the wind turbine system to a large extent.

The two main contributions of this research are a new optimal current waveform shaping technique and an advanced MPPT algorithm taking into account the losses of the system. The optimal current waveform shaping technique simultaneously increases the efficiency of Permanent Magnet Synchronous Machines (PMSMs) and power-electronic converters by using a non-conventional current waveform. The new

MPPT algorithm takes into account that the optimal operating point of the turbine is not necessarily the overall optimal operating point, which is affected by the losses. The new MPPT algorithm increases the yearly energy yield of a wind turbine by regulating the turbine to this overall optimal operating point.

It is important to note that this research is not solely limited to wind energy. The principles presented here can also be applied in electric vehicles, robotics, industrial motor drives, battery-powered applications, etc. The application of wind energy serves as a test case for validation of the new concepts presented in this work.

1.2 Overview

This dissertation is organised as follows:

Chapter 2 gives an overview of the state-of-the-art technology in wind turbines. Mathematical models are given for the turbine, generator and converter, which will be used in later chapters.

One of the key subjects of this research is optimal current waveform shaping. This technique uses non-classical current waveforms to improve the efficiency of the generator and converter. Chapter 3 gives an overview of optimal current waveform shaping techniques in literature and presents the basic concept of the new technique developed in this work.

Chapter 4 discusses the presence of rotor speed ripples in wind turbines and their effect on the back-emf waveform of the generator. This effect was neglected in chapter 3. Therefore, the validity of this is investigated in detail here. This topic can be seen as a secondary research path, but clearly linked to the topic of optimal current waveform shaping techniques.

Chapter 5 expands the new optimal current waveform technique presented in chapter 3 by developing more advanced waveform equations for the complete generator model instead of a simplified one. The advanced technique is validated and investigated by simulations in a case study, a parameter sensitivity analysis and a detailed model of a wind turbine system.

Chapter 6 discusses a different aspect of the rectifier control in a wind turbine, i.e., MPPT. In the first part of the chapter, the steady-state performance of MPPT in state-of-the-art wind turbines is evaluated by analysing standardised IEC 61400-2 test data. This analysis shows that MPPT algorithms often do not perform well in turbines currently on the market. In the second part of the chapter, the impact of losses on the location of the overall optimal operating point of the system is determined. It is shown that the energy yield of a wind turbine can be increased by taking into account the losses.

Chapter 7 discusses common mistakes made by companies who are manufacturing or selling small and medium wind turbines. It is meant as an advice to entrepeneurs and designers who wish to bring a new turbine on the market.

Chapter 8 resumes the main findings and conclusions of this dissertation and presents possible topics for further research.

2

State-of-the-art small and medium wind turbines

This chapter describes the state-of-the-art wind turbine systems based on a Permanent Magnet Synchronous Machine (PMSM), which is currently the most commonly used generator in wind energy. Mathematical models are given for each component, which will be used further in the thesis.

Contents

2.1 Overview of the system

Fig. 2.1 gives an overview of a wind turbine system based on a PMSM. The turbine (a) drives the PMSM (b). Since the shaft speed is variable, the PMSM produces an ac voltage with a variable fundamental frequency and amplitude. This voltage is converted to dc by the rectifier (c), which can be either active or passive in combination with a boost chopper. An inverter (d) then injects an ac current with a fixed frequency into the grid (e).

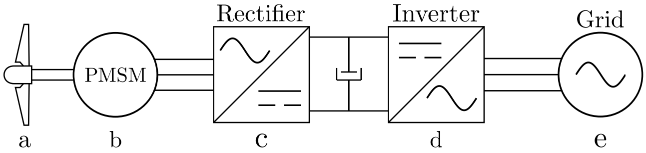

Figure 2.1: Overview of the most common wind turbine system

Other topologies can be encountered as well, such as turbines based on slip-ring induction generators. Also, turbines with a dc generator exist. For dc applications, such as battery charging, the inverter is omitted in the above topology. Small and medium wind turbines can also be used to feed microgrids, provided that a suitable control strategy is used for the inverter. Possible future wind turbines might use a switched reluctance generator or squirrel cage induction generator instead of a PMSM to reduce cost, since the price of magnets has increased significantly in recent years. However, this has an impact on the complexity of the converter topology and control. Also, the efficiency of a squirrel cage induction generator will be less than for a PMSM, since it has Joule losses in the rotor.

It is difficult to predict the wind turbine systems of the future. The topology of Fig. 2.1 is the most widely used today. Therefore, only this topology will be considered here.

2.2 Wind turbine

The turbine converts kinetic energy in the wind to mechanical energy on a rotating shaft. The general operating principle is that the air flow is diverted by a rotating blade, creating a lift force while reducing the wind speed. The combined lift forces on all blades result in the driving torque of the turbine. In some turbines, such as the Savonius, drag instead of lift is used to generate power. A large diversity of turbine designs can be found in the small and medium power range, i.e., horizontal axis turbines with 3 or 5 blades, vertical axis Savonius or Darrieus turbines and even complex 3D designs. Fig. 2.2 shows the three most common basic turbine types, i.e., the three-bladed horizontal axis turbine (a), the Savonius (b) and the Darrieus (c).

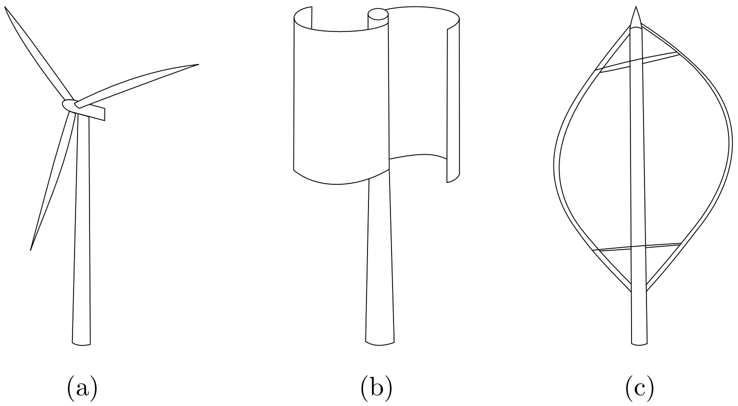

Figure 2.2: Common wind turbine types: (a) Three-bladed horizontal axis turbine, (b) Savonius, (c) Darrieus

Independent of the turbine type, the mechanical output power P_t is given by:

$$P_\mathrm{t} = \frac{1}{2}\rho A v^3 \; C_\mathrm{p}(\theta_p, \lambda) \tag{2.1}$$

where ρ is the air density, which equals 1.225 kg/m^3 at 15°C and at sea level, A is the swept area and v is the wind speed. For a horizontal axis turbine, the swept area is calculated as πR^2 where R is the turbine radius. For a vertical axis wind turbine, the swept area is the projection of the surface encountered by the wind, e.g., height multiplied by the diameter for a cylindrical rotor. The factor C_p is the power coefficient of the turbine and reflects the aerodynamic performance. It is determined by the Tip-Speed Ratio (TSR) λ and the pitch angle θ_p. The pitching system allows to rotate a blade around its longitudinal axis and is mainly used to create stall at high wind speeds to limit the output power. Most small and medium wind turbines do not contain a pitching system to reduce costs. In large wind turbines, the pitching system remains inactive as long as wind speeds are normal. Therefore, the pitch angle can be considered zero in this work.

The TSR characterizes the air flow around the blades and is defined by:

$$\lambda = \frac{R\,\Omega}{v} \tag{2.2}$$

where Ω is the rotational speed of the turbine. R is the turbine radius, which equals the blade length for classical horizontal axis turbines. The TSR is a dimensionless representation of the rotor speed. The relation between the power coefficient C_p and the TSR λ is determined by the shape of the blade. For a given blade, it can be calculated by Computational Fluid Dynamics (CFD) software, measured in a wind tunnel or on a turbine or calculated theoretically.

In [46], an analytical $C_\mathrm{p}(\lambda)$ curve was presented for the 2-bladed 2.5 MW NASA MOD-2 turbine. There, the blade manufacturer calculated the power coefficient by using blade theory. This involves calculating the elemental torque of a blade section and integrating over the blade radius. Then, [46] used a non-linear least squares fit to approximate this manufacturer data. Based on the non-linear approximation, a more general model was developed in [47]. In [48, 49], this general model was used to develop the following $C_\mathrm{p}(\lambda)$ relation:

$$C_\mathrm{p}(\lambda) = \left(\frac{116.46}{\lambda} - 10.53\right)\, e^{-18.4/\lambda} \tag{2.3}$$

This power coefficient $C_\mathrm{p}(\lambda)$ is shown graphically in Fig. 2.3. For a given wind speed, the output power of a turbine is maximized when the power coefficient C_p is at a maximum, i.e., when the blades are able to divert the air flow in the best way. Fig. 2.3 shows that the power coefficient C_p has a maximum value of 0.44 for a tip-speed ratio λ of 6.91, which is called the Maximum Power Point (MPP). In other words, for each wind speed, there is an optimal rotor speed, proportional to the wind speed. Modern blades reach maximum C_p values between 0.4 and 0.5. The Betz limit of 0.593 is the theoretical maximum power coefficient, regardless of the type of turbine, which can be calculated by applying the conservation of mass and energy laws on the wind flow through the turbine.

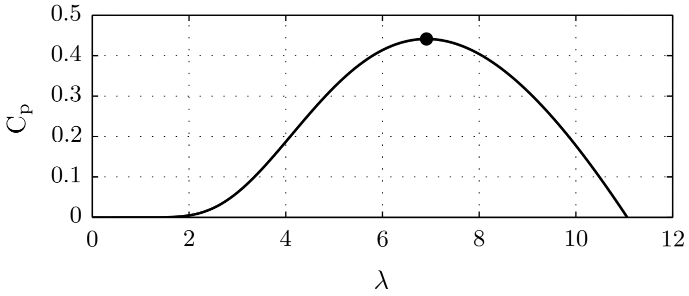

Figure 2.3: Empiric $C_{\mathrm{p}}(\lambda)$ curve [48,49]

The $C_{\mathrm{p}}(\lambda)$ curve (2.3) was developed in [48] for a large wind turbine. It will be used for small and medium turbines in this work. This is an approximation, since the $C_{\mathrm{p}}(\lambda)$ curve of a certain blade design depends on the blade size, and thus, rated power of the turbine. However, a reliable empiric $C_{\mathrm{p}}(\lambda)$ curve for a small or medium wind turbine was not found during the literature search. Also, the main parameters of the curve (2.3), i.e., maximum C_{p} and optimal λ are realistic for a three-bladed horizontal axis turbine, even at small or medium size. Therefore, this approximation does not have a negative impact on the validity of the results presented in this work.

Three-bladed horizontal axis turbines reach a maximum C_{p} at a TSR somewhere between 5 and 9. In contrast, a Savonius turbine reaches a maximum C_{p} of about 0.15 for a TSR around 1. This means that the rotor speed is low, and that for the same swept area, less power is produced. Vice versa, turbines with a low C_{p} value must be larger to reach the same power levels, which uses more material and increases costs. The design of the turbine rotor is a crucial step in the development of a wind turbine, as it determines the power output for a given wind speed and the rated rotor speed. The choice of a proper turbine rotor will be discussed in more detail in chapter 7.

Finally, to model the dynamic behavior of a turbine, the inertia J_t is needed. For a horizontal axis turbine with three blades, the inertia can be calculated from the mass of one blade M_b and the turbine radius R [50]:

$$J_t = \frac{1}{3} M_b R^2 \tag{2.4}$$

This equation is valid under the assumption that the center of mass is located at 1/3 of the radius and that a three-bladed horizontal axis turbine is considered.

2.3 Mechanical losses

Although modeling of the mechanical components is outside the scope of this work, it is useful to have a basic model of the mechanical losses. This allows to calculate realistic values for the energy yield of a turbine. Therefore, three basic mechanical losses are described here for use in later chapters.

The first mechanical loss component can be found in the bearings. According to the bearing manufacturer SKF [51], the friction losses can be approximated by:

$$P_{\mathrm{f1}} = \mu \; M \; \frac{d}{2} \; \Omega \tag{2.5}$$

The friction coefficient μ generally equals 0.001. M is the total radial force, which can be approximated by the weight of both the turbine and generator rotors, multiplied by the gravitational constant g. d is the diameter of the pitch circle of the bearings, which is slightly larger than the shaft diameter. Finally, the losses are proportional to the rotor speed Ω.

The second mechanical loss is the friction of the radial shaft seals, which are used to prevent water or dirt entering the bearings or the generator:

$$P_{\mathrm{f2}} = 0.442 \; S \; \Omega \tag{2.6}$$

This simple equation is again provided by SKF [52] and is an empiric first-order approximation, where S is the amount of shaft seals in the system.

The third loss component is caused by the aerodynamic friction of the rotating generator with the surrounding air [53]:

$$P_{\mathrm{f3}} = 0.0017\ D^3\ L\ \Omega^3 \tag{2.7}$$

The generator is assumed to be a cylinder with diameter D and length L. This model is valid for most outer-rotor generators.

The complete mechanical loss model is summarized as follows:

$$P_{\mathrm{f}} = \mu\ M\ \frac{d}{2}\ \Omega + 0.442\ S\ \Omega + 0.0017\ D^3\ L\ \Omega^3 \tag{2.8}$$

2.4 Permanent Magnet Synchronous Machine

In the past, mainly slip-ring induction generators, also called 'Doubly Fed Induction Generators' (DFIGs), were used in combination with a gearbox, especially for large turbines. However, in the 2000s, both wound-rotor and permanent magnet synchronous machines became popular since they allow direct-drive systems. These generators have a high number of pole pairs so that a gearbox can be avoided. Currently, the popularity of the PMSM continues to increase and it has a considerable market share in newly installed wind turbines. Compared to a wound-rotor machine, a PMSM has a higher efficiency since losses in the rotor winding are avoided. Also, it requires less maintenance and shutdowns since there are no slip-rings.

The advantages of a direct-drive PMSM do not remain undeniably valid in terms of rated power. As the size of the turbine increases, the rotor speed decreases. This results in a high rated torque for the PMSM, which becomes a burden on the mechanical design and increases cost. One of the largest turbines at the moment is the Vestas V164 with a rated power of 8 MW. The V164 uses a planetary gearbox and a medium-speed 400 rpm PMSM instead of a direct-drive system [54].

A PMSM consists of a stator with a three-phase winding and a rotor with permanent magnets. As the rotor is driven by a wind turbine, the stator winding observes a varying magnetic field, which induces a voltage, i.e., the back-emf voltage. From this voltage, power can be delivered by the stator winding to the power-electronic converter.

Classical PMSMs are radial flux machines, where both the rotor and stator have a cylindrical shape. In industrial drives, the rotor is placed inside the stator. However, for wind turbines, the rotor is often placed outside the stator, with the connections coming out of a hollow shaft. This allows for an easier mounting of turbine blades on the rotor. A rather recent development are axial flux PMSMs where both the rotor and stator have the shape of a disc, placed close to eachother. Fig. 2.4 shows an axial flux machine with one stator disc in the middle and two rotor discs, one on each side, to compensate axial forces.

The advantage of axial flux machines is the compact and simple design, which reduces material and manufacturing costs [55, 56]. Moreover, the efficiency is higher than for a radial flux machine. This makes them particularly interesting as a generator for small and medium wind turbines or as a motor in electric vehicles. However, the construction of an axial flux machine is more challenging, e.g., it is not straightforward to quarantee a constant air gap distance between the rotor and stator discs. Due to the lower cost and higher efficiency, axial flux machines are a promising new development for use as a generator in wind turbines.

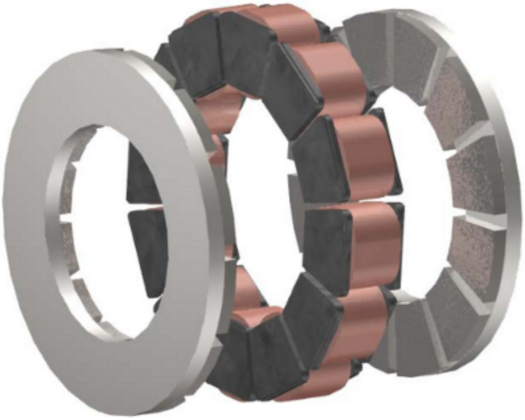

Figure 2.4: Axial Flux PMSM

The main disadvantage of PMSMs is the fact that magnet prices have increased considerably in recent years. This is caused by a combination of the Chinese quasi-monopoly on the production of magnets and the worldwide booming market of wind energy. This development may lead to alternative wind turbine designs, e.g., going back to using induction generators, although their efficiency is significantly lower than that of a PMSM. Economical aspects aside, the PMSM is the best choice as a wind turbine generator to reach high efficiencies.

In the following chapters, the analytical model of the PMSM will prove to be crucial, e.g., for the analysis of optimal current waveforms. Therefore, it is explained in high detail here. The model developed here differs from classical models found in literature in the sense that harmonics in the back-emf and the zero-sequence behavior are both included.

2.4.1 Definitions

Fig. 2.5 gives a schematic representation of the PMSM. The stator is represented by three windings a, b and c while the rotor is shown as a magnet with a rotating d and q axis.

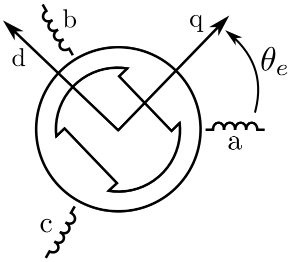

Figure 2.5: Definition of reference axis in a PMSM

The physical or mechanical angle θ_m is the angle between the stator reference axis a and rotor reference axis q. The derivative of this angle is the rotor speed Ω_m. Both rotor angle and speed can be expressed in electrical radians by introducing the number of pole pairs N_p:

$$\theta_e = N_\mathrm{p}\ \theta_m \qquad\qquad \Omega_e = N_\mathrm{p}\ \Omega_m \tag{2.9}$$

The following assumptions are made for the derivation of the PMSM model:

- The stator winding is three-phase symmetrical.

- Slotting effects are neglected, with the exception of the reluctance effect.
- Skin- and proximity effects in the conductors are neglected.
- Saturation is neglected.

No limiting assumptions are made regarding the waveform of the back-emfs and stator currents. Therefore, both can contain harmonics and unbalance.

2.4.2 Stationary reference frame model

First, the PMSM model in a stationary reference frame is derived. All voltages and currents are instantaneous values in this model. No waveforms are assumed at this moment, i.e., all voltages, currents and fluxes have arbitrary waveforms. Also, iron losses are temporarily neglected in the derivation of the model, but will be added later. All vectors in the stationary reference frame will be written with an apostrophe to clarify the difference with the rotating reference frame.

The terminal stator voltage and current vectors $\mathbf{v}'$ and $\mathbf{i}'$ are defined as:

$$\mathbf{v}' = \begin{bmatrix} v_a & v_b & v_c \end{bmatrix}^T \tag{2.10}$$

$$\mathbf{i}' = \begin{bmatrix} i_a & i_b & i_c \end{bmatrix}^T \tag{2.11}$$

The positive reference direction of the stator current is chosen according to generator-operation, i.e., consuming mechanical power and producing electrical power. This is motivated by the fact that wind energy is the main application envisioned in this research. An equivalent wye scheme is used for the model, so that all voltages are phase-voltages.

The flux vector $\boldsymbol{\Psi}'_{\mathrm{PM}}(\theta_e)$ is the flux of the permanent magnets as seen in the stator, i.e., coupled with the stator windings:

$$\boldsymbol{\Psi}'_{\mathrm{PM}}(\theta_e) = \begin{bmatrix} \Psi_{\mathrm{PM,a}}(\theta_e) & \Psi_{\mathrm{PM,b}}(\theta_e) & \Psi_{\mathrm{PM,c}}(\theta_e) \end{bmatrix}^T \tag{2.12}$$

Although no waveform is assumed for the flux at this point, it is important to note that the fundamental component of the flux in phase a is usually zero at a rotor angle θ_e of 0 and reaches a maximum at $\pi/2$. This corresponds with the reference axis of Fig. 2.5, where the flux of the magnets is aligned with the d-axis.

The stator resistance matrix $\mathbf{R}'$ is defined as:

$$\mathbf{R}' = \begin{bmatrix} R_s & 0 & 0 \\ 0 & R_s & 0 \\ 0 & 0 & R_s \end{bmatrix} \tag{2.13}$$

The stator inductance matrix $\mathbf{L}'(\theta_e)$ is defined as:

$$\begin{aligned} \mathbf{L}'(\theta_e) &= \begin{bmatrix} L_s & M_s & M_s \\ M_s & L_s & M_s \\ M_s & M_s & L_s \end{bmatrix} \\ &\quad -L_{re} \begin{bmatrix} \cos 2\theta_e & \cos 2\left(\theta_e - \frac{\pi}{3}\right) & \cos 2\left(\theta_e - \frac{2\pi}{3}\right) \\ \cos 2\left(\theta_e - \frac{\pi}{3}\right) & \cos 2\left(\theta_e - \frac{2\pi}{3}\right) & \cos 2\left(\theta_e - \frac{3\pi}{3}\right) \\ \cos 2\left(\theta_e - \frac{2\pi}{3}\right) & \cos 2\left(\theta_e - \frac{3\pi}{3}\right) & \cos 2\left(\theta_e - \frac{4\pi}{3}\right) \end{bmatrix} \end{aligned} \tag{2.14}$$

The first term contains the stator self-inductance L_s on the diagonal and the mutual inductance M_s on all other locations. The second term represents the reluctance effect, which causes the inductance to vary with the rotor position θ_e. The reluctance effect is caused by the different magnetic properties of the flux paths for different positions of the rotor.

The stationary reference frame model of the PMSM, by using the definitions above, is now given by:

$$\mathbf{v}' = \frac{d}{dt}\mathbf{\Psi}'_{\mathrm{PM}}(\theta_e) - \mathbf{R}'\,\mathbf{i}' - \frac{d}{dt}\left[\mathbf{L}'(\theta_e)\,\mathbf{i}'\right] \tag{2.15}$$

The first term is the back-emf $\mathbf{e}'_{\mathrm{PM}}$, induced by the magnet flux in the stator winding. The second term represents the resistive voltage drop. The third term contains all inductance effects.

2.4.3 Rotating reference frame model

The stationary reference frame model (2.15) can be simplified by transforming it to a rotating qd reference frame, linked to the rotor. The zero-sequence component is deliberately included in the model, since it will be needed further in this work. Naturally, the zero-sequence current is automatically zero in wye connected machines without neutral wire.

First, the Clarke transformation matrix T_C is used to obtain $\alpha\beta$ components:

$$T_C = \frac{1}{3}\begin{bmatrix} 1 & 1 & 1 \\ 2 & -1 & -1 \\ 0 & \sqrt{3} & -\sqrt{3} \end{bmatrix} \tag{2.16}$$

Then, the Park transformation matrix T_P is used to obtain qd components:

$$T_P = \begin{bmatrix} 1 & 0 & 0 \\ 0 & \cos\theta_e & \sin\theta_e \\ 0 & -\sin\theta_e & \cos\theta_e \end{bmatrix} \tag{2.17}$$

In the rotating reference frame, the terminal stator voltage and current vectors $\mathbf{v}$ and $\mathbf{i}$ are defined by:

$$\mathbf{v} = T_P \cdot T_C \cdot \mathbf{v}' = \begin{bmatrix} v_0 & v_q & v_d \end{bmatrix}^T \tag{2.18}$$

$$\mathbf{i} = T_P \cdot T_C \cdot \mathbf{i}' = \begin{bmatrix} i_0 & i_q & i_d \end{bmatrix}^T \tag{2.19}$$

The magnet back-emf $\mathbf{e}_{\mathrm{PM}}$ is defined in the rotating reference frame as:

$$\mathbf{e}_{\mathrm{PM}} = T_P \cdot T_C \cdot \frac{d}{dt}\boldsymbol{\Psi}'_{\mathrm{PM}}(\theta_e) \tag{2.20}$$

The stator resistance matrix is unaffected by the transformations:

$$\mathbf{R} = T_P \cdot T_C \cdot \mathbf{R}' \cdot T_C^{-1} \cdot T_P^{-1} = \mathbf{R}' \tag{2.21}$$

Instead of the inductance matrix $\mathbf{L}'(\theta_e)$ of the stationary reference frame model, two new matrices $\mathbf{L}$ and $\mathbf{G}$ are introduced:

$$\mathbf{L} = \begin{bmatrix} L_0 & 0 & 0 \\ 0 & L_q & 0 \\ 0 & 0 & L_d \end{bmatrix} \qquad \mathbf{G} = \begin{bmatrix} 0 & 0 & 0 \\ 0 & 0 & L_d \\ 0 & -L_q & 0 \end{bmatrix} \tag{2.22}$$

The parameters L_0, L_q and L_d are defined by:

$$\begin{aligned} L_0 &= L_s + 2M_s \\ L_q &= L_s - M_s - \frac{3}{2}L_{re} \\ L_d &= L_s - M_s + \frac{3}{2}L_{re} \end{aligned} \tag{2.23}$$

The rotating reference frame model of the PMSM, by using the definitions above, is now given by:

$$\mathbf{v} = \mathbf{e}_{\mathrm{PM}} + \dot{\theta}_e\ \mathbf{G}\ \mathbf{i} - \mathbf{R}\ \mathbf{i} - \frac{d}{dt}\left[\mathbf{L}\ \mathbf{i}\right] \tag{2.24}$$

Compared to the stationary reference frame model, the inductance matrix $\mathbf{L}$ is now a diagonal matrix, in contrast with $\mathbf{L}'$. The transformation does give rise to an extra term $\dot{\theta}_e\ \mathbf{G}\ \mathbf{i}$, which is an emf of movement. The sum of the permanent magnet back-emf $\mathbf{e}_{\mathrm{PM}}$ and this additional term is defined as the total back-emf $\mathbf{e}$:

$$\mathbf{e} = \mathbf{e}_{\mathrm{PM}} + \dot{\theta}_e\ \mathbf{G}\ \mathbf{i} \tag{2.25}$$

The first term is the voltage induced in the stator by the rotor flux, while the second term is the voltage induced in the stator by the flux of the stator currents themselves. The second term is defined as the armature reaction effect.

Equation (2.24) can be used to construct the equivalent schemes shown in Fig. 2.6. The zero-sequence scheme is simply a back-emf in series with an RL impedance. The q and d schemes contain an additional back-emf each proportional to the current of the other scheme. Therefore, the q and d schemes are coupled.

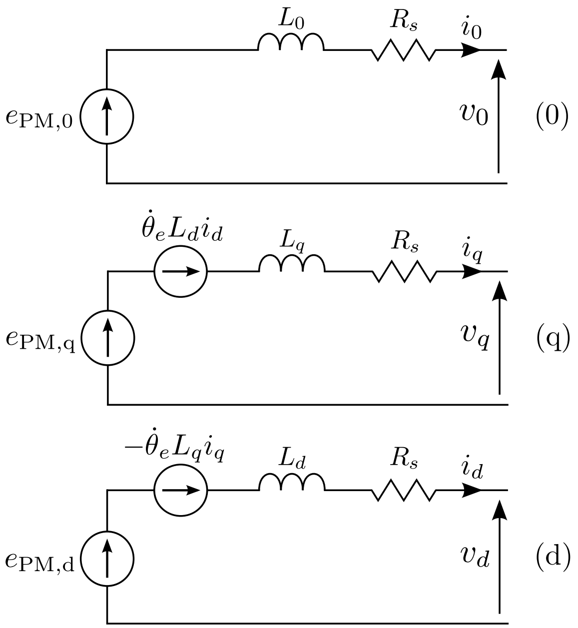

Figure 2.6: Equivalent schemes of a PMSM in a rotating reference frame

In a machine with a purely sinusoidal back-emf waveform and no zero-sequence component, only $e_{\mathrm{PM,q}}$ differs from zero and is a constant, proportional to the rotor speed. However, in this dissertation, machines with any possible waveform are investigated, so that generally all three back-emf components will differ from zero and vary with time.

2.4.4 Iron losses in the equivalent scheme

The main reason for the high efficiency of a PMSM is that there is no rotor winding where Joule losses can occur, in contrast to induction machines or wound rotor synchronous machines. The only Joule losses can be found in the stator winding resistance R_s, which is included in the equivalent scheme of Fig. 2.6. Strictly speaking, there are also Joule losses in the permanent magnets, due to eddy currents. However, these magnet losses are discussed later in §8.2.2 on p.206

and will not be included in the analysis here.

The machine also has iron losses, which consist of eddy current losses, hysteresis losses and excess or anomalous losses. Eddy current losses are Joule losses from stray currents, caused by induced voltages in the iron laminations. They are proportional to the square of the rotor speed. The hysteresis losses are proportional to the rotor speed. The excess or anomalous losses contains all other iron losses and have a more complex dependency on the rotor speed. For example, the Joule losses of localized eddy currents near moving domain walls are included in the excess losses. The copper losses and iron losses together are the dominant electrical losses in a PMSM.

Iron losses are complex and difficult to model. In literature, they are often approximated by an equivalent iron loss resistance R_c [57–60], which depends on the rotor speed Ω and is calculated by:

$$R_c = \frac{1}{K_f + K_h/\Omega} \tag{2.26}$$

K_f and K_h are constants representing eddy current losses and hysteresis losses respectively [61]. They can be determined for a given machine by parameter identification methods [57]. Fig. 2.7 shows the iron loss resistance in the equivalent schemes of the PMSM. The equivalent iron loss resistance only models the eddy current and hysteresis losses. The excess losses are not included in this model due to their complexity. Also, they have a limited contribution to the total losses. In [62], the iron losses were computed for a PMSM by using the Finite Element Method, including the excess losses. For the PMSM investigated there, the excess losses amount to only 4.5% of the total iron losses. The remaining 95.5% consists of the eddy current and hysteresis losses.

The addition of R_c to the equivalent schemes of the PMSM makes the schemes more complex, since now there is a parallel branch. For clarity, the currents on the left of R_c and the voltage over R_c are denoted with an asterisk. The currents on the left of R_c will be called the inner currents.

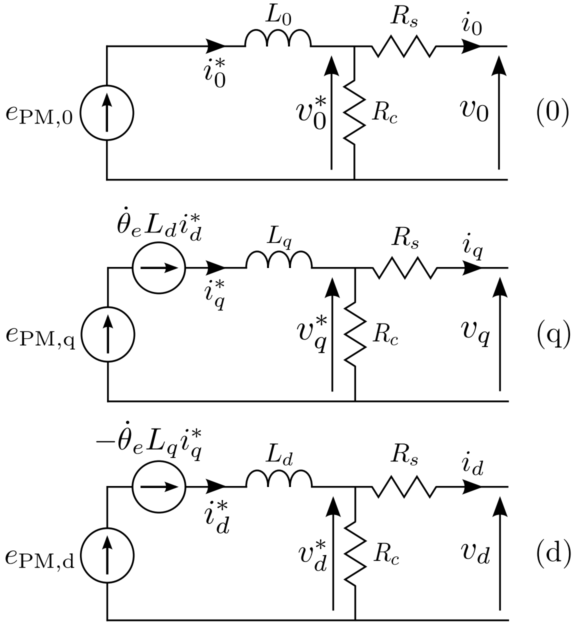

Figure 2.7: Equivalent schemes of a PMSM including iron losses

2.5 Rectifier

Modern wind turbines have a variable speed, which allows to operate the turbine with a maximum power coefficient C_{p} in a large wind speed range. Since the rotor speed is variable, the waveform of the back-emf of the PMSM has a variable fundamental frequency and amplitude. Such a signal is called 'wild ac' in the field of wind energy. This wild ac must be converted to a dc voltage before it can be converted to a correct ac again by an inverter. The purpose of this converter is not only to rectify the wild ac, but also to control the speed of the turbine to maximize the power coefficient C_{p}.

Many converter topologies can be used for this purpose. In practice, mostly the passive diode rectifier in combination with a boost dc/dc chopper is used. A full active rectifier without chopper is another possibility. In literature, other converter topologies are encountered as well, such as matrix converters or Z-source converters. In this work, the passive diode rectifier with boost chopper and the full active rectifier will be discussed. Also, a variant of the full active rectifier, i.e., the four-wire rectifier will be described. The four-wire rectifier is able to extract zero-sequence currents from the generator by connecting the neutral wire. This will prove to be advantageous for the optimal current waveform shaping techniques which are discussed later.

2.5.1 Passive diode rectifier with boost chopper

Fig. 2.8 shows the topology of the passive diode rectifier with boost dc/dc chopper. The diode rectifier is directly connected to the generator terminals. The rectified voltage is filtered by a capacitor, which serves as the input of the boost chopper. The chopper consists of a choke coil, a PWM switched IGBT or MOSFET and a diode. A capacitor is used to filter the output voltage, which is connected to the inverter.

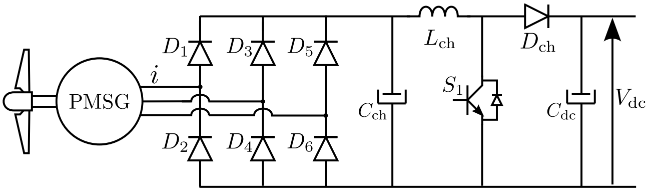

Figure 2.8: Passive diode rectifier with boost dc/dc chopper

The main advantages are the low cost of the rectifier and the circuit simplicity. Only one active switch is present, which means that only one gate driver circuit has to be used. However, it must be noted that the choke coil can be an expensive and heavy component, as it contains a substantial amount of copper and iron [63]. The amount of copper and iron mainly depends on the switching frequency and the power level.

Another disadvantage is that there is no control of the generator currents. Due to the diode rectifier, these currents contain a high amount of harmonics and the fundamental component always lags the terminal voltage, leading to a poor power factor. The result is a reduced efficiency of the generator. In the scope of this research, this topic was investigated in detail and published in [64]. Fig. 2.9 shows a simulated current waveform for a passive diode rectifier system. It is clear that this waveform causes undesired torque ripples and losses. Compared to a theoretical ideal sinusoidal waveform, the waveform of Fig. 2.9 results in 14% additional losses.

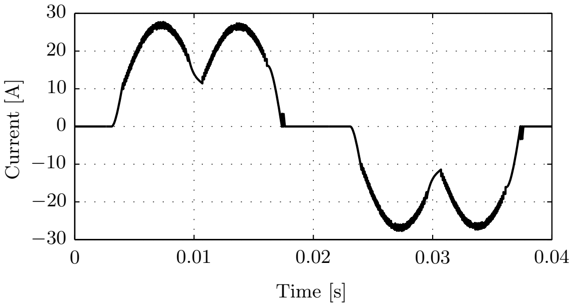

Figure 2.9: Typical generator current waveform for a passive diode rectifier system

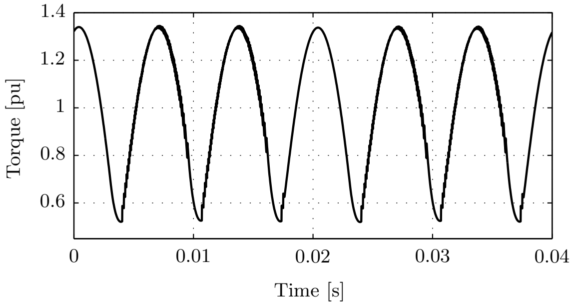

Figure 2.10: Typical torque ripple for a passive diode rectifier system

The distorted current waveform also causes strong torque ripples, as shown in Fig. 2.10. These torque ripples cause vibrations and noise, reducing the lifetime of mechanical components such as bearings. Currently, small wind turbines mostly use passive diode rectifiers, and thus, have strong torque ripples due to the current harmonics. Since turbine manufacturers claim a lifetime of at least 20 years, the mechanical effects of these torque ripples seem to be acceptable. However, some small turbines are known to be noisy, which harms the social acceptance. More attention will be given on torque ripples in wind turbines in chapters 3, 4 and 5.

As discussed in [64], there are a few possible solutions to reduce the harmonics in the current waveform. A classical approach is to use filtering, as shown in Fig. 2.11. The filter can be passive, i.e., well-tuned inductors or capacitors. The disadvantage of this method is that the filter can only be tuned at one single frequency, while the output frequency of the generator varies from 0 to the rated value. Also, the reactive components can be costly. Another possibility is to use an active filter, i.e., a three-phase inverter [65]. The inverter can then be programmed to compensate the harmonics of the rectifier, so that the generator currents are sinusoidal. Although this active filtering method is original, it is also rather complex and unpractical. It is simpler to completely replace the diode bridge and boost chopper with a full active rectifier. This way, there is full control over the current waveforms and power factor. The full active rectifier will be discussed in more detail later.

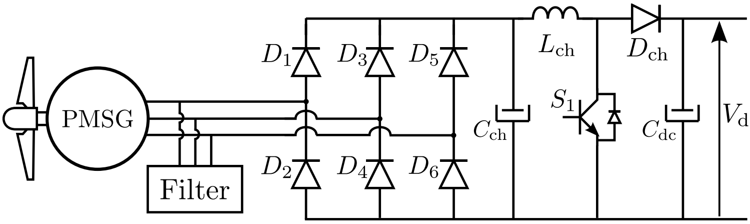

Figure 2.11: Placement of a filter on the generator terminals

Regarding the control of the boost chopper, the duty ratio of the switch determines the input dc voltage of the chopper, as the output voltage is fixed by the inverter. By varying this input dc voltage, the generator currents are changed. For example, when the dc voltage is lowered, a larger voltage difference exists over the internal impedance of the PMSM, which increases the current, and thus the torque. This causes the turbine to accelerate, which can be used to bring the turbine to the MPP. The implementation of the MPPT on this converter is simple, since the duty ratio of the switch directly affects the mechanical operating point of the turbine.

A more detailed description of MPPT algorithms will be given later on in this chapter. However, it must be noted that some MPPT algorithms require a measurement of the rotor speed. When the passive diode rectifier with boost chopper topology is used, this rotor speed measurement can be performed without speed sensor. Fig. 2.12 schematically shows the sensorless speed measurement method. First, one of the generator currents is measured. Then, a strong low pass filter is used to eliminate noise and harmonics. The zero crossings of the resulting sine wave are determined. Since a possible phase lag of the fundamental is not an issue, and only the time difference between the zero crossings is of interest, the cut-off frequency of the filter can be set significantly low. Finally, the rotor speed can be calculated from the time difference between the zero crossings.

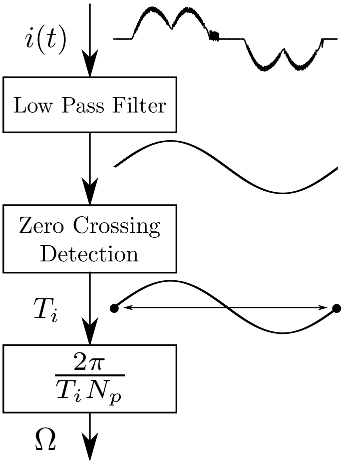

Figure 2.12: Sensorless rotor speed measurement

In conclusion, the passive rectifier with boost chopper is a commonly used topology in small and medium wind turbines due to its simplicity. The component count is low and the implementation of MPPT algorithms is straightforward. However, the reduced generator efficiency and the cost of the choke coil must be mentioned as important disadvantages.

2.5.2 Full active rectifier

As an alternative for the passive rectifier, the full active rectifier topology of Fig. 2.13 can be used. Six PWM controlled IGBT or MOSFET switches are used to convert the wild ac to the dc bus. The dc bus voltage is fixed by the grid-side inverter.

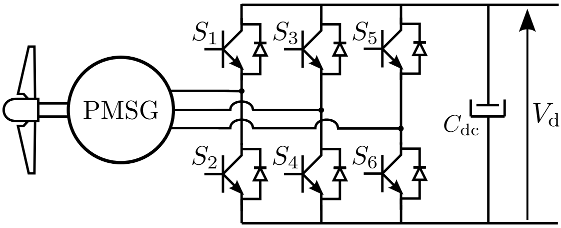

Figure 2.13: Full active rectifier

Compared to the passive rectifier topology, the active rectifier requires considerably more circuitry to drive the six switches. However, a choke coil is no longer needed as the internal inductance of the generator now serves this purpose. The control of an active rectifier is more complex than the single switch of the boost chopper in the previous topology. However, this also gives more control flexibility, a better current waveform, an improved power factor and a shorter reaction time. This can increase the efficiency of the generator and increase the speed of the MPPT, resulting in a higher energy yield. In contrast to the passive diode rectifier, the full active rectifier allows bidirectional power flow. This means that motor operation is feasible, which can be used to start a turbine that suffers from a low starting torque.

The preferred control method for this application is field orientation, as shown in Fig. 2.14. Current controllers, in this case Proportional-Integral (PI) controllers, are used to regulate the generator current in the *dq* frame. The current in the *d*-axis is set to zero, while the current in the *q*-axis is a dc value which is proportional to the torque of the generator. The *q*-axis current is regulated by a torque controller. The torque setpoint $\hat{T}$ can be used to control the turbine to a certain operating point to perform MPPT.

In order to transform the measured currents and applied PWM voltages from *abc* components to the *dq* frame and vice versa, a Clarke and Park transformation is needed. This requires a measurement of the rotor position θ_e. Therefore, the use of an active rectifier implies that a position sensor is needed. Absolute encoders could be used, but they have the reputation of being unreliable under the rough en-

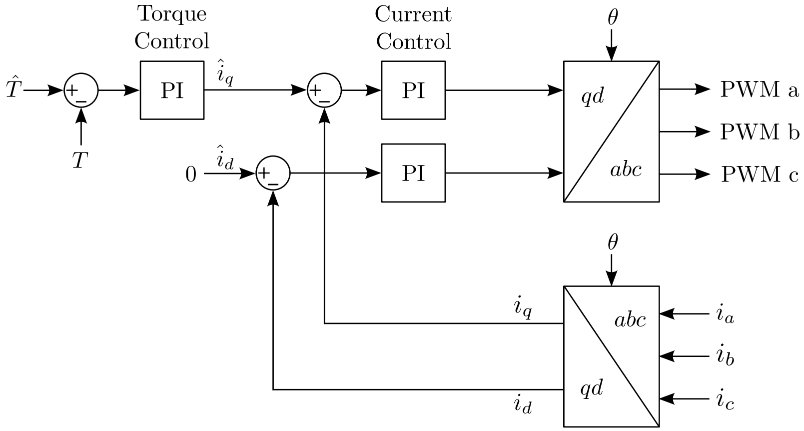

Figure 2.14: Scheme of field orientation control

vironmental conditions in a wind turbine [66]. Also, the vibrations of the turbine considerably shorten the lifetime of the encoder as they burden the small bearings and gearboxes. Another problem is the deterioration of the shaft seals due to temperature cycles, allowing moisture and dirt to enter the encoder. When an encoder fails in the nacelle of a turbine, it is unpractical and costly to replace.

The expansion of the wind turbine market in recent years has drawn attention to these reliability issues of encoders. Encoder manufacturers have improved their products to deal with the harsh conditions of a wind turbine. Two major improvements are magnetic and bearing-less encoders. A magnetic encoder uses magnetic fields instead of optics, making it less prone to moisture and dirt. Bearing-less encoders have a radically different mechanical design without bearings, making them more robust. Another solution for the reliability issues of encoders is to use hall sensors, which are inherently more robust. Also, sensorless techniques exist to estimate the rotor position based on electrical measurements and models [67], but this is outside the scope of this research.

The fact that the rotor position is needed to implement field orientation has a favorable side-effect. When the rotor position is known, also the rotor speed is known. This parameter gives important information for the MPPT algorithm, which allows to control the turbine to the MPP in a more effective way.

Regarding cost, it is difficult to say whether the active rectifier or the passive rectifier with boost chopper costs more. Although the active rectifier requires more circuitry for the switches, there is no choke coil, which is an expensive part. Also, the cost of a product is largely determined by the size of the manufacturing batch.

2.5.3 Four-wire active rectifier

Commonly, the neutral point of the generator is not connected to the converter, so that the zero-sequence current cannot be controlled. However, zero-sequence currents could be used by optimal current waveform methods to achieve a higher efficiency, as will be explained later in chapter 5. Therefore, the neutral point of the machine can be connected to the converter by using a four-wire rectifier. Four-wire inverters for grid-connected applications were investigated in [68]. Analogous principles can be used for machine-side converters and will be briefly summarized here.

The two most common topologies for four-wire converters are four-leg converters and split-link converters [69]. The four-leg converter has an additional half-bridge leg on the dc-bus, connected to the neutral wire. The split-link converter has two dc-bus capacitors in series, with the neutral wire connected to the mid-point.

The topology of the four-leg rectifier is shown in Fig. 2.15. Compared to a classical active rectifier, the circuit is more complex since it contains two additional switches with driver and protection ciruits. Moreover, this has a large impact on the complexity of the control. The switching state of the additional leg influences the current in the other phases. Therefore, the control of the currents cannot be decoupled, as was the case for a classical active rectifier. A possible control method is three-dimensional space vector modulation (3D SVPWM) [70], which is not straightforward to implement.

The split-link rectifier is shown in Fig. 2.16. In contrast to the four-leg rectifier, the circuit is a lot simpler, i.e., comparable with a classical active rectifier. This rectifier can be controlled in the same manner as a classical active rectifier. However, the main issue is the voltage

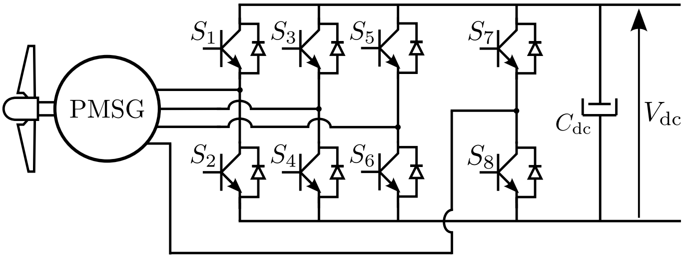

Figure 2.15: Four-leg rectifier

balance of the two dc-bus capacitors. Ideally, both capacitors share half of the total dc-bus voltage. Currents in the neutral wire destabilize this voltage balance. Normally, these currents mainly contain ac components, so that the voltage of the mid-point between both capacitors only has a small periodic fluctuation. This does not harm the operation of the converter, since the current controllers are designed to deal with small disturbances of the system.

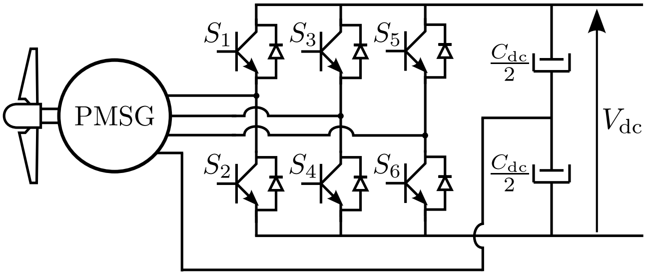

Figure 2.16: Split-link rectifier

However, even a small transient current in the neutral wire is sufficient to quickly destabilize the voltage. This proves to be unavoidable in practice, so that the split-link converter cannot be used without dedicated voltage stabilization techniques. In [68], several methods are described to stabilize the voltage. The most practical method is the injection of an additional zero-sequence current in the machine. First, the voltage of both dc-bus capacitors is measured. Then, the difference between both voltages is sent to a PI controller with zero as the setpoint value. Finally, the output of this controller is added to the input of the zero-sequence current controller if the rectifier uses a rotating reference frame control. If the rectifier uses current controllers in *abc* coordinates, i.e., stationary reference control, then the output is distributed between the controllers of each phase.

The output of the PI controller is interpreted as a current value, which is injected in the PMSM and flows into the mid-point of the dc-bus via the neutral wire. There, it corrects the voltage unbalance between the capacitors. The PI controller can be tuned to react only on an average unbalance of the voltage by setting a low bandwidth, since limited ac unbalances are normally harmless. It is important to note that this voltage stabilization technique does not cause dc currents in the PMSM. On the contrary, this method compensates any transient or dc current in the neutral wire, and thus ensures that the zero-sequence dc current in the machine is zero.

It can be concluded that it is possible to extract zero-sequence currents from a PMSM by using a four-wire rectifier. The split-link topology is more practical and less complex than a four-leg rectifier, provided that a voltage stabilization technique is used for the mid-point of the dc-bus.

2.5.4 Maximum Power Point Tracking

As explained earlier, in both the passive and active rectifier topologies, the rotor speed can or needs to be measured. This allows to construct a rotor speed control loop, which is needed for some types of MPPT algorithms. A short overview of the most important MPPT types will be given here. Rotor speed control is assumed to be available where needed, as it can be easily implemented based on the speed measurement methods described earlier.

In literature, many different MPPT algorithms can be found. Roughly speaking, there are three different basic types of algorithms, i.e., TSR control, Perturb & Observe (P&O) and tabulated power control. These basic types are often combined to achieve a better performance than each type separately. Also, more advanced techniques are used, such as neural networks, fuzzy logic or adaptive control. The three basic types will be discussed here.

Tip-Speed Ratio control

The most straightforward MPPT algorithm is TSR control. By measuring the wind speed and the rotor speed, the TSR λ can be calculated. When this value is compared with the optimal TSR λ_{opt}, the rotor speed can be adjusted by a rotor speed controller to reach the MPP. The algorithm simply consists of a PI controller comparing the actual TSR with the optimal value, and a rotor speed controller.

This algorithm is simple, effective and fast. However, the main disadvantage is that the wind speed must be measured. The use of a wind speed sensor increases the cost and is not straightforward. Currently, classical cup anemometers are placed on top of the nacelle, behind the turbine rotor. The wind speed measured there is not an accurate representation of the wind speed at the front of the blades. Therefore, a correction factor must be applied to approximate the latter. Another problem is that TSR control requires a certain accuracy and speed of the wind speed measurement. This can be a problem, especially for small and medium wind turbines where wind speed is more variable. Also, they have a disappointing reliability. Other sensor technologies are available, such as ultrasonic sensors, but they are expensive. The difficulty of measuring wind speed at low altitudes is the main reason why TSR control is rarely implemented.

Perturb & Observe

The general concept of Perturb & Observe algorithms is that a change is applied in the control variable and the response of the system is observed by measuring one or multiple key variables. In the case of a wind turbine, the most common P&O algorithm is a hill climber. The principle is that a change in rotor speed is applied by a rotor speed controller. After a certain settling time, the power is measured and compared with the value of the previous step. If the power has increased, the power point is moving towards the MPP. The next rotor speed step will be in the same direction as the previous step. If the power has decreased, the direction of the rotor speed step is changed. After sufficient steps, the system will reach the MPP and oscillate around it.

The observed power can be measured anywhere in the system. Mostly, the dc power at the output of the diode rectifier is used since it is simple to measure. Strictly, measuring the injected grid-power would be best. This way, all losses in the system are included in the optimisation, and the algorithm will search the true optimal operating point of the whole system, not only that of the turbine. This subject will be discussed in more detail in chapter 6.

The change in rotor speed is called the step size. This parameter has a large effect on the effectiveness of the algorithm. A hill climber with a large step will reach the MPP faster, but will oscillate stronger in steady-state. These oscillations cause an unnecessary reduction of the power coefficient. Therefore, more advanced hill climbers use a variable step, with a decreasing step size as the turbine comes closer to the MPP. When the MPP is reached, the step size is often set at zero to keep the turbine at the MPP. A change in power implies a change in wind speed, which reactivates the hill climber.

After each step in rotor speed, the algorithm must wait a sufficient time to allow the system to reach steady state again. This is caused by the inertia of the turbine. This aspect, together with the inherent stepwise functioning of the algorithm, causes hill climbers to be slow. This problem is not encountered in photovoltaic panels, where mechanical inertia is absent. Therefore, hill climbers work well for photovoltaic panels, but are often ineffective for wind turbines. Pure hill climbers are rarely found in wind turbines. If used, they are mostly combined with an MPPT algorithm of another type, such as tabulated power control, to increase speed.

Tabulated power control

The tabulated power control method is the most widely used MPPT method in commercial wind turbines. The implementation is simple and it has proven to be more effective than TSR control and P&O. The control variable of the algorithm can be the rotor speed, the duty ratio of the boost chopper or the rectified dc voltage. The tabulated power control method is developed as follows. First, a scale model of the turbine is placed in a wind tunnel. Then, for each wind speed, this control variable is varied to find the value where a maximum power is achieved. Finally, this value together with the corresponding power is recorded in a table. The result of this first step is an empiric curve giving the maximum power in terms of the control variable.

The empiric curve is implemented in the MPPT algorithm. The algorithm sets the control variable at a certain value. After a certain settling time, the corresponding power is measured. If this power value matches the power in the empiric curve, the turbine is in the MPP. If there is a mismatch, then the control variable is set at the value which corresponds with the measured power. This will cause the turbine to go to a new operating point, where the procedure is repeated.

The main advantage of this MPPT algorithm is the simplicity and effectiveness. This method is faster than a hill climber because larger steps are automatically taken when the turbine is farther from the MPP. The disadvantage is that wind tunnel tests are required to obtain the empiric curve. Also, the empiric curve is obtained on a single moment, while in practice the curve changes due to blade erosion or variations in air density.

More advanced algorithms based on this type use an empiric curve to quickly bring the turbine near the MPP. Then, the algorithm switches to a hill climber to correct any deviation from the real optimal operating point [71].

2.6 Grid-connected inverter

The primary purpose of the inverter is to convert the dc power, received from the rectifier, to ac power suitable for injection into the grid. Battery charging or island mode applications are not considered here. Depending on the rated power of the turbine, the inverter can be single or three phase. Here, only the three-phase topology will be considered. Fig. 2.17 shows the most common topology, which contains six PWM controlled IGBTs or MOSFETs.

On the dc side, an electrolytic dc link capacitor attenuates voltage ripples. When the converter is directly connected to the grid, i.e., without a separation transformer, the rated dc voltage is generally between 650V and 750V. On the grid side, a passive filter is used to reduce current and voltage harmonics, in this case an LC filter. The switching frequency of the switches is chosen preferably above 16 kHz to reduce noise. However, it should not be chosen too high as the

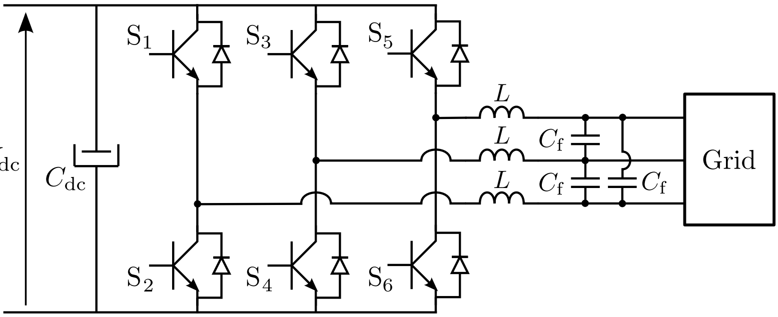

Figure 2.17: Topology of the three-phase grid-connected inverter

switching losses would become unacceptable. In modern converters, the PWM signals are created by digital chips, such as a Digital Signal Processor (DSP) or a Field Programmable Gate Array (FPGA). This chip contains the complete control strategy of the converter, uses Analog-to-Digital Converters (ADCs) to measure voltages and currents, and has built-in PWM modulators to create the switching signals.

Fig. 2.18 shows the basic control strategy of the inverter in the *abc* reference frame. A control method in the rotating reference frame is also possible, and is analogous to the field orientation control of Fig. 2.14. Since the grid voltage can contain harmonics, a Phase-Locked-Loop (PLL) is used to obtain the fundamental components. These fundamental components are scaled with an amplitude I and are then used as setpoint for the current controllers. This way, sinusoidal currents with a power factor of one are injected into the grid, regardless of the quality of the grid voltage, so that the power quality is not reduced.

Proportional-Integral (PI) controllers together with a Duty-Ratio-Feed-Forward (DRFF) can be used to follow the current setpoints. The bandwidth of the PI controller is preferably chosen around 2 kHz, since this is the 40th harmonic in a 50 Hz grid. The DRFF is an additional signal which is added to the output of the PI controllers and is derived from the measured grid voltage. When only the DRFF would be activated, the inverter would copy the grid voltage at its output. The advantage of this signal is that the current control is stabilized and the required effort of the PI controllers is reduced.

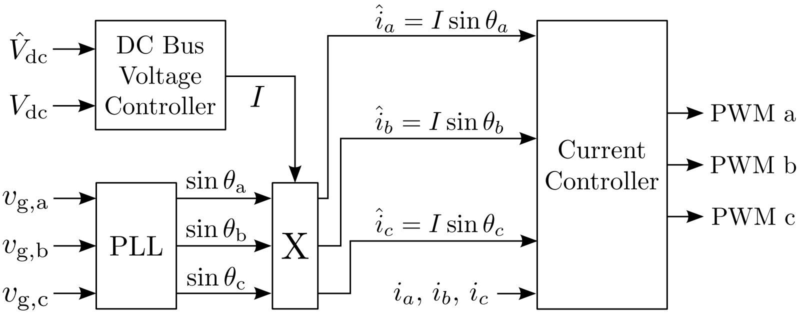

Figure 2.18: Control strategy of the three-phase grid-connected inverter

The amplitude I of the sinusoidal current waveforms can be used to set the active power injected into the grid. This is done automatically by the dc bus voltage controller. Because the source connected to the dc bus is best modeled as a current source, the dc voltage is not fixed. The PI dc bus voltage controller compares the measured dc bus voltage with its setpoint. A voltage below the setpoint means that less power is received on the dc bus than what is injected into the grid, so that I must be lowered. When the dc bus voltage is above the setpoint, I must be increased. This way, the dc bus voltage is controlled by balancing dc and ac power.

Besides the primary task of converting the dc power into ac power, the inverter can also be used to improve the power quality of the distribution grid. It can be programmed to reduce harmonics in the grid voltage by injecting well-chosen harmonic currents [72]. Also, in the case of a three-phase inverter, unbalance in the grid voltage can be reduced by injecting unbalanced currents [73]. The control strategies developed in [72] and [73] also allow the inverter to support the distribution grid during voltage dips. Another issue in distribution grids is overvoltage, e.g., during the summer when power consumption is limited while photovoltaic panels inject a significant amount of power. In this case, the inverter can be programmed to reduce the overvoltage by adapting the balance between active and reactive power. In [74], this balance is optimized by taking into account the R/X ratio of the grid impedance, which is estimated online.

2.7 Conclusions

The state-of-the-art components for small and medium wind turbines were discussed in this chapter. For the turbine rotor itself, many different designs can be used, e.g., a classical rotor with blades mounted on a horizontal axis, a Savonius rotor or a Darrieus rotor. Currently, many exotic designs are available on the market. In this work, a general model is used for the turbine, independent of the turbine design.

Regarding the generator, the focus lies on PMSMs here, as it is the most used machine at the moment. PMSMs are known for their high efficiency and dynamic properties. The main disadvantage is cost, which is caused by the high price of rare-earth materials used in the magnets. An advanced equivalent scheme for the PMSM was presented in this chapter, including armature reaction, the reluctance effect, zero-sequence components, back-emf harmonics, eddy current losses and hysteresis losses. This model will be extensively used in the following chapters.

Most turbines use a passive diode rectifier with a boost chopper to rectify the wild ac and perform MPPT. However, a full active rectifier has many advantages, such as control over the current waveform which reduces losses and torque ripples, the ability to use field orientation and even motoring of the turbine. Four-wire rectifiers, such as the split-link converter, also allow zero-sequence currents to flow in machines with a wye connection and accessible neutral. These advantages will be exploited in the following chapters.

Finally, the grid-connected inverter was described. As opposed to the generator and rectifier, the inverter is not the focus of the research in this dissertation. A simulation model of a state-of-the-art inverter will be used in chapter 6 to simulate the losses in the complete system.

3

BASIC OPTIMAL CURRENT WAVEFORM SHAPING

A key subject of this research is finding the current waveform which must be extracted from the generator to maximise the efficiency of a wind turbine system. In general, this technique is called optimal current waveform shaping. In this chapter, an overview of the existing literature is given. In this PhD research, a different and new approach to current waveform shaping is introduced. This new approach is presented at the end of this chapter.

Contents

3.1 Back-emf waveforms of PMSMs

Classicaly, there are two types of PMSMs, i.e., brushless dc and ac machines. An ideal brushless ac machine (BLAC) is designed to have a sinusoidal back-emf [75], shown in Fig. 3.1 at the top. They are used as generators where a sinusoidal voltage is desired by the loads, or as a motor in high-efficiency applications. Mostly, a BLAC motor is driven by a classical voltage-source inverter (VSI) which delivers sinusoidal currents. A sinusoidal current waveform, shown in Fig. 3.2 at the top, is the ideal waveschape for a brushless ac machine. The sinusoidal back-emf of a BLAC is normally constructed by combining a distributed winding in the stator with interior mounted permanent magnets in the rotor.

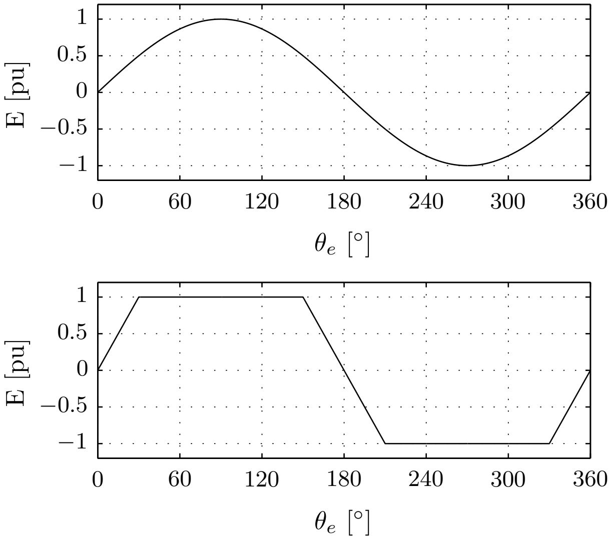

Figure 3.1: Ideal back-emf waveforms of a BLAC (top) and BLDC (bottom)

An ideal brushless dc machine (BLDC) is designed to have a trapezoidal back-emf [76–79], shown in Fig. 3.1 at the bottom. In the example of the figure, the voltage is constant for 120 electrical degrees, i.e., from 30° to 150° and again from 210° to 330°. They are used in servo applications where they are combined with an inverter, sensor and controller to become a single system with accurate position or speed control. They are the driving force of robotics and are commonly used in the manufacturing industry. The trapezoidal back-emf waveform is mostly achieved by combining concentrated windings in the stator with surface mounted permanent magnets in the rotor [80]. The converter uses a dc current which is switched to the appropriate phase where the back-emf is constant at that time. No current is injected while the back-emf of that phase varies. Hall sensors are used to dictate the switching moments. Therefore, the ideal current waveform is not trapezoidal but a square-wave, as shown in Fig. 3.2 at the bottom. The main advantage of BLDC machines is the simplicity of the converter and control, which explains their popularity in servo systems.

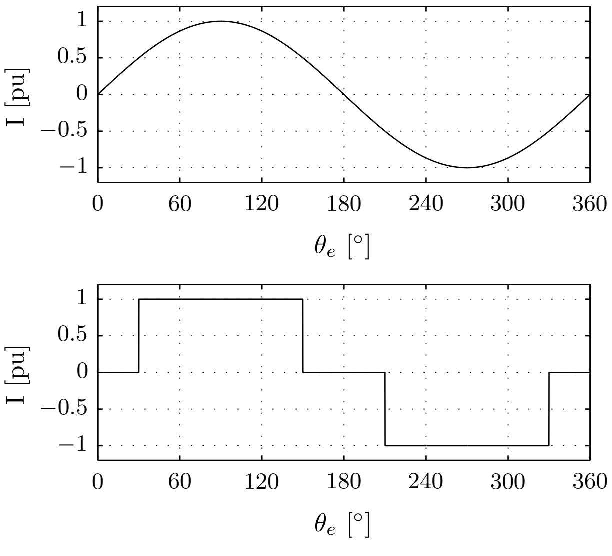

Figure 3.2: Ideal current waveforms of a BLAC (top) and BLDC (bottom)

However, in reality, ideal brushless ac and dc machines do not exist. There are always harmonics present in the back-emf of brushless ac machines. Also, brushless dc machines never have a perfect trapezoidal back-emf waveform. This has many possible causes, such as constructional limitations, design compromises or cost reduction [81]. The back-emf waveform is mainly determined by the design of the stator winding and the placement and geometry of the magnets. Sometimes, manufacturers even claim their products to be brushless dc machines, while the back-emf is close to sinusoidal. During this research, several so-called brushless dc machines were investigated which turned out to be rather brushless ac machines when measuring the back-emf waveform. After measuring the back-emf waveform of several machines, it can only be concluded that most PMSMs are hybrid machines, with a back-emf waveform between an ideal trapezoid or sinus. Only machines with a rated power below 10 kW were measured, so that this conclusion only applies for this power level.

The back-emf of several PMSMs was measured during this research. Also, an extensive literature search was performed to find back-emf waveforms [76, 78, 79, 81–88]. Fig. 3.3 gives a selection of these waveforms, both measured in the lab and found in literature, to give an overview of the different shapes in practice. The Alenco BLDC Prototype has a waveform which resembles a trapezoid, but still contains several strong harmonics. BLDC motors 1 and 2 are small unbranded motors. It is clear from the measurements that these machines are rather BLAC than BLDC, as the waveform is close to a sine wave. Still, several harmonics are present. The waveform of the Mecc Alte Eogen is close to the ideal sinusoidal shape. Again, small harmonics are present. The BLDC motors 3 and 4 are investigated in [85] and [87] respectively. The BLDC motor 3 has the most perfect BLDC waveform of the six PMSMs, since the voltage is almost flat in a wide region. BLDC motor 4 resembles a trapezoid but has several low-order harmonics, similar to the Alenco Prototype.

Although most machines are hybrid in practice, the manufacturers of converters still assume that the machine is ideal. The result is that BLAC converters use sinusoidal currents, and BLDC converters use square wave currents. When matched with an ideal brushless machine, this would lead to minimal torque ripple and losses. However, when matched with a hybrid machine, additional torque ripples, vibrations, noises and losses are introduced. Unfortunately, the latter situation is most encountered in practice. Fig. 3.4 shows a measured current waveform for a BLAC drive (left) [89] and a BLDC drive (right) [90]. The BLAC drive uses a sinusoidal current waveform, while the BLDC drive uses a square waveform with 120° conductance duration. The switching ripple is clearly visible in both waveforms.

The aforementioned problems have only increased with the recent de-

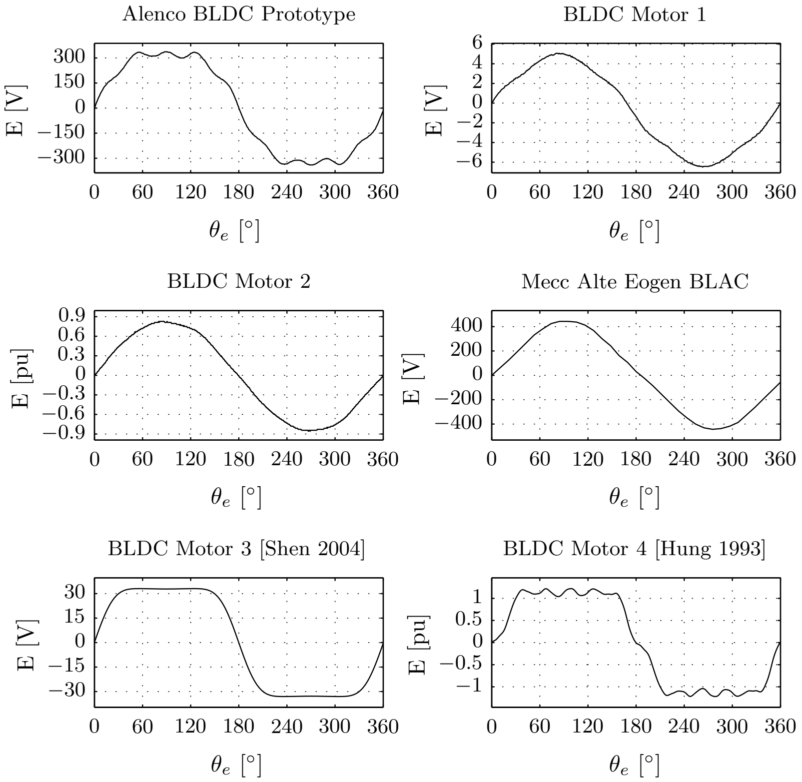

Figure 3.3: Measured back-emf waveforms

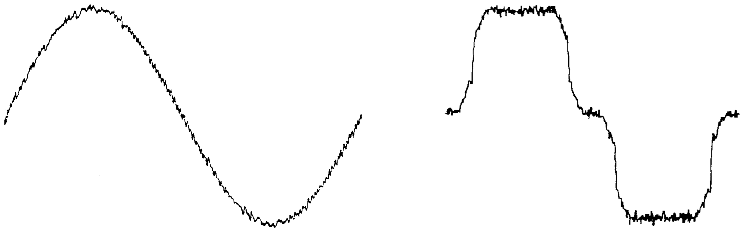

Figure 3.4: Measured BLAC (left) and BLDC (right) converter waveforms [89, 90]

velopment of axial flux machines, which were discussed in chapter 2. One of the issues with this type of machines is the back-emf waveform, which is rarely close to an ideal trapezoid or sinusoid. These machines are a typical example of hybrid PMSMs.

For a long time, in academic literature as well as in industry, there has been a consensus among machine designers that the back-emf waveform must be as ideal as possible. However, in the light of the increased environmental awareness and the focus on efficiency, minimalisation of losses, cost and material should be considered as the primary objectives during the design. A new view on this matter is that this goal can be reached at the expense of the back-emf waveform. When less attention is given to the waveform, a further decrease of losses, cost and material can be achieved during the design.

This new design philosophy would lead to more efficient and cheaper machines, but with a waveform far from the ideal shapes. Normally, when combined with classical converters, this leads to more torque ripple, noise, vibrations and losses because the converters still use ideal sinusoidal or square wave current waveforms. However, these effects can be counteracted by injecting more advanced current waveforms, which are matched with the machine. This process is called current waveform shaping and will be discussed in the next section.

From the above discussion, it can be concluded that most PMSMs must be considered to be hybrid machines, not purely BLAC or BLDC. To maximise efficiency and minimise cost and material use, there should be less focus on the back-emf waveform during the design process. The result of this would be a more efficient machine, but with a less ideal back-emf waveform. Current waveform shaping techniques can solve the negative side-effects of this waveform, which forms the main subject of this thesis.

3.2 Current waveform shaping in literature

The main idea of current waveform shaping is to achieve, for example, minimum torque ripple or maximum efficiency, by optimising the current waveform. An overview of current waveform shaping will be given here, based on the most relevant publications in the field.

3.2.1 Minimising torque ripple

Most publications solely focus on minimising torque ripple while neglecting the effect on the efficiency [86–89,91]. Minimisation of torque ripple is desired in servo applications, as it results in a more accurate speed or position control. Also, vibrations are reduced, which is crucial in robotics. Efficiency has been neglected in servo applications for a long time, but this may change in the future as fossil fuels become scarce.

The most straight-forward method for minimising torque ripple is to identify the harmonic current components which remove corresponding torque ripples in the frequency domain [87–89]. For this, the PMSM model is simplified to the equivalent scheme of Fig. 3.5 in *abc* components, neglecting iron losses, armature reaction and the reluctance effect.

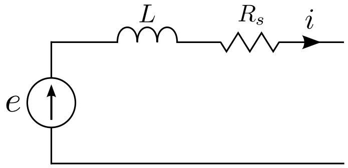

Figure 3.5: Simplified equivalent scheme of a PMSM [87–89]

For this model, the torque can be calculated by assuming that the total electric power of the back-emfs equals the mechanical power:

$$T(t) = \frac{1}{\Omega}\left[e_a(t)\ i_a(t) + e_b(t)\ i_b(t) + e_c(t)\ i_c(t)\right] \tag{3.1}$$

In an ideal situation, both the back-emfs and currents are three-phase symmetric sinusoidal components, which leads to a constant torque. However, in practice, the back-emfs do contain harmonics. In this case, a sinusoidal current would lead to torque ripples.

The concept of eliminating torque ripples by current waveform shaping is summarised here. More details can be found in [87]. The following assumptions are made:

- The rotor speed Ω is assumed to be constant.

- Iron losses, armature reaction and the reluctance effect are neglected.
- There is no neutral connection, i.e., the converter current cannot have zero-sequence components.
- The waveforms of both the back-emf and current are assumed identical for each phase.
- The back-emf waveforms have half-wave symmetry.

The back-emfs are written in the frequency domain as Fourier series:

$$e_a(\theta_e) = \sum_{k=-\infty}^{\infty} E_k \cdot e^{jk\theta_e} \tag{3.2}$$

$$e_b(\theta_e) = \sum_{k=-\infty}^{\infty} E_k \cdot e^{jk(\theta_e - 2\pi/3)} \tag{3.3}$$

$$e_c(\theta_e) = \sum_{k=-\infty}^{\infty} E_k \cdot e^{jk(\theta_e - 4\pi/3)} \tag{3.4}$$

The currents are written in an analogous manner:

$$i_a(\theta_e) = \sum_{k=-\infty}^{\infty} I_k \cdot e^{jk\theta_e} \tag{3.5}$$

$$i_b(\theta_e) = \sum_{k=-\infty}^{\infty} I_k \cdot e^{jk(\theta_e - 2\pi/3)} \tag{3.6}$$

$$i_c(\theta_e) = \sum_{k=-\infty}^{\infty} I_k \cdot e^{jk(\theta_e - 4\pi/3)} \tag{3.7}$$

The Fourier coefficients E_k and I_k are complex numbers. Also, the coefficients with a negative index are the complex conjugate of their positive index counterpart, i.e., $E_{-k} = E_k^*$ and $I_{-k} = I_k^*$. Substituting the Fourier series of the back-emfs and currents into the torque equation (3.1) yields the Fourier series of the torque:

$$T(\theta_e) = \sum_{n=-\infty}^{\infty} T_n \cdot e^{jn\theta_e} \tag{3.8}$$

The Fourier coefficients T_n are calculated by:

$$T_n = \begin{cases} T_0, & \text{if } n = 0 \\ \sum\limits_{m=-\infty}^{\infty} 2\ E_{n-m}\ I_m, & \text{if } n = \pm 6q \\ 0, & \text{if } n \neq \pm 6q \end{cases} \tag{3.9}$$

where q is a natural number. The above equation expresses that, besides the average constant torque T_0, the torque only consists of 6^{th} order harmonics and multiples. These torque ripple components are calculated by the convolution sum of the back-emf and current components. By setting the torque ripple components T_n to zero for all n except 0, and solving for I_k, all ripples are eliminated. Solving the set of equations is a complex task, and can be performed by numerical software such as Matlab. As mentioned in [87], the set of equations which have to be solved is underdetermined, i.e., there is more than one possible current waveform which eliminates the torque ripple.

For this, a finite set of Fourier components must be selected for the back-emf, current and torque. Low-order harmonics in the back-emf create the largest torque ripples, so these are the most important to eliminate. High order torque ripples are less of a problem in practice as they are more easily damped by friction and inertia.

Some papers take this concept a step further by eliminating cogging torque. In (3.1) it was assumed that torque only originates by the interaction of back-emf and current. However, in practice, the rotor magnets have a preferential position relative to the stator slots. This results in additional torque ripples which are unrelated to the current waveform. Since cogging torque does not have an average component, there is no average mechanical power due to cogging, only power ripples. In the presence of cogging torque, the total torque can be expressed by:

$$T(t) = \frac{1}{\Omega}\left[e_a(t)\ i_a(t) + e_b(t)\ i_b(t) + e_c(t)\ i_c(t)\right] + T_c(t) \tag{3.10}$$

The cogging torque T_c can be measured and then transformed to the frequency domain by:

$$T_c(\theta_e) = \sum_{n=-\infty}^{\infty} T_{c,n} \cdot e^{jn\theta_e} \tag{3.11}$$

Instead of setting the torque ripple components T_n to zero, they can now be set equal to $-T_{c,n}$. Solving the system for I_k results in a current waveform which also eliminates the cogging torque.

3.2.2 Minimising losses as a secondary goal

More advanced research adds minimisation of the losses as a secondary goal, but minimal torque ripple is maintained as the primary goal in the optimisation [81, 83, 92]. It was previously mentioned that there is more than one current waveform which eliminates torque ripple. Therefore, minimisation of the copper losses can be used as a criterium to select the most optimal current waveform [81, 87]. Only copper losses are minimised, the effect of the current waveform on iron losses is neglected.

In [92] and [83] all previous concepts are combined to find the current waveform which minimizes copper losses under the constraint of a constant torque including the elimination of cogging torque.

One recent publication has revisited the current waveform shaping techniques [82]. In this paper, the technique is investigated in more detail for back-emf waveforms close to the trapezoidal shape. The most significant added value of this paper is that iron losses are considered in the analysis, although only in post-processing. First, optimal current waveforms for maximising efficiency and minimising torque ripple are derived while neglecting iron losses. Then, the effect of these waveforms on the iron losses is calculated. The main conclusion is that for low rotor speeds, the non-sinusoidal optimised current waveform is a good choice. For high rotor speeds, it is advised to use a sinusoidal waveform, since the optimal current waveform fails to reach its goal due to the influence of the iron losses. Although the iron losses are considered in this paper, they are not included in the determination of the optimal current waveforms itself.

3.2.3 Conclusions from literature research

Since the first papers on the topic [88, 89], current waveform shaping techniques have evolved up to the point where a constant torque is achieved including cogging torque compensation, with minimalisation of copper losses as a secondary criterion. Mostly, BLDC machines were considered in servo applications, where torque ripples are to be avoided. However, in several other applications, torque ripples do not have such a clear disadvantage. For instance, in wind turbines, energy efficiency is more important. Currently, small wind turbines use passive diode rectifiers, which results in strong torque ripples. In practice, this does not seem to be a problem as wind turbines satisfy acoustic norms. In this research, the primary goal of zero torque ripple is abandoned in favor of maximum efficiency. The effect of the maximum efficiency waveform on torque ripple will be evaluated afterwards.

In literature, the current waveform is determined in the frequency domain, which seems to be an obvious choice. However, a time domain approach is also possible, resulting in a more elegant and compact formulation. This new approach will be explained in 3.3.

For a given machine, the optimal current waveform which maximises efficiency can be determined with Finite Element Method (FEM) software. When the machine is completely modeled in the software, including copper and iron losses, optimisation methods can be applied to find the amplitude and phase of each current harmonic. There are several disadvantages to this approach. The accuracy of the result is only as good as the accuracy of the model. Manufacturers rarely give access to FEM models of their machines. Also, the result is not generic and is only applicable for one machine at one operating point. As will be shown in the next section, an analytical time-domain approach gives more insight and a generic closed-form solution.

Finally, many simplifications are made in literature in order to derive the optimal current waveform. Some of them are hard to avoid, such as saturation or skin and proximity effects, as they cause nonlinearities in the models. Others are more difficult to justify, such as neglecting iron losses, reluctance effects or armature reaction. As will be shown in 3.3 and chapter 5, the time domain approach presented here can deal with more complex machine models.

3.3 New optimal waveform shaping technique

A new optimal current waveform shaping technique is presented in this section. The proof is based on the Cauchy-Schwarz inequality. First, the technique will be applied on the simplified PMSM scheme of Fig. 3.5 in order to clearly show the concept of the technique. Then, as a proof of concept, it is applied in a simulation model and compared with classical sinusoidal and square-wave current waveforms. Afterwards, in chapter 5, the technique will be refined step-by-step for application on the full equivalent scheme of Fig. 2.7.

3.3.1 Mathematical proof

The vectors x and y are elements of the inner product space V. An inner product space is a vector space with a defined inner product or scalar product $\langle \cdot, \cdot \rangle$. The Cauchy inequality is given by:

$$|\langle x, y \rangle|^2 \leq \langle x, x \rangle \cdot \langle y, y \rangle \tag{3.12}$$

Both sides in the equation are equal if x and y are linearly dependent, i.e. $x = C \cdot y$.

The norm of a vector is defined as the square root of the inner product of the vector with itself, e.g., the norm of the vector x is defined as $\|x\| = \sqrt{\langle x, x \rangle}$. Applying the square root on the Cauchy inequality results in the following:

$$|\langle x, y \rangle| \leq \|x\| \cdot \|y\| \tag{3.13}$$

The inner product space V will now be further specified as the vector space of one-dimensional real valued and integrable functions. The time dimension t will be used as the function parameter. The vectors x and y are now explicitly written as functions $x(t)$ and $y(t)$. The inner product for the vector space V is defined as:

$$\langle x(t), y(t) \rangle = \int_0^T x(t)\ y(t) dt \tag{3.14}$$

Using this definition of the inner product, a norm can be defined as follows:

$$\|x(t)\| = \sqrt{\langle x(t), x(t) \rangle} = \sqrt{\int_0^T x^2(t) dt} \tag{3.15}$$

The Cauchy inequality can now be rewritten in an integral form, resulting in the Schwarz inequality:

$$\left(\int_0^T x(t)y(t)dt\right)^2 \leq \int_0^T x^2(t)dt \cdot \int_0^T y^2(t)dt \tag{3.16}$$

The vectors $x(t)$ and $y(t)$ are now replaced by respectively the back-emf $e(t)$ and the current $i(t)$ of the PMSM. Both $e(t)$ and $i(t)$ have an arbitrary periodic waveform. The Schwarz inequality now becomes:

$$\left(\int_0^T e(t)i(t)dt\right)^2 \leq \int_0^T e^2(t)dt \cdot \int_0^T i^2(t)dt \tag{3.17}$$

First, the square root of this equation is taken. Second, the equation is divided by the time interval T. This results in:

$$\frac{1}{T}\int_0^T e(t)i(t)dt \leq \sqrt{\frac{1}{T}\int_0^T e^2(t)dt} \cdot \sqrt{\frac{1}{T}\int_0^T i^2(t)dt} \tag{3.18}$$

The left hand side of the equation can be interpreted as the average active power P_{avg} delivered by the voltage source e, which also equals the average mechanical power in this simplified model. The right hand side can be interpreted as the product of the root mean square values of the voltage e and the current i, i.e., E_{rms} and I_{rms}. The Schwarz inequality can now be written in short as:

$$P_{\text{avg}} \leq E_{\text{rms}} \cdot I_{\text{rms}} \tag{3.19}$$

If the current $i(t)$ is proportional to the voltage $e(t)$, i.e., $i(t) = g \cdot e(t)$, the equality is valid. The parameter g has the dimension of a conductance, hence the symbol g. From now on, this current waveform will be denoted as a ‘proportional current’.

For a given back-emf waveform and mechanical operating point, (3.19) shows that I_{rms} is minimal for a proportional current waveform. Since the copper losses are proportional to the square of I_{rms}, the losses are also minimized. This proves that a proportional current waveform is the most optimal considering losses. In the case of a sinusoidal back-emf waveform, this equation shows that a maximum efficiency is reached for a power factor of one, i.e., the current is in phase with the back-emf, which is straightforward. However, for an arbitrary back-emf waveform, this equation proves that a proportional current waveform achieves a maximum efficiency. This also implies a power factor of one, which is then defined as the ratio of active power P and apparent power S.

No Fourier transformation was applied in the proof, so that numerically solving a complex system of equations is avoided. The result is compact and generic. Also, a minimum amount of assumptions was made.

The insight that a proportional current waveform yields a minimum rms current for a given active power was previously observed in [93]. There, power definitions were investigated in the context of the increase in grid voltage harmonics due to nonlinear loads. In the case of a distorted grid voltage, it is beneficial for the line losses to extract a proportional instead of a sinusoidal current waveform.

3.3.2 Proof of concept

Generally, there are three possible current waveforms which have been discussed until now, i.e., a sinusoidal, square-wave and optimal waveform. The optimal waveform is the waveform proportional to the back-emf. As a proof of concept, a simulation model will now be used to calculate the losses in a machine for these waveforms.

The machine is modeled by the simplified scheme of Fig. 3.5, i.e., a back-emf in series with an inductance and a resistance. For the back-emf, the measured waveforms of the Alenco prototype are used. Fig. 3.6 shows the waveforms of all three phases.

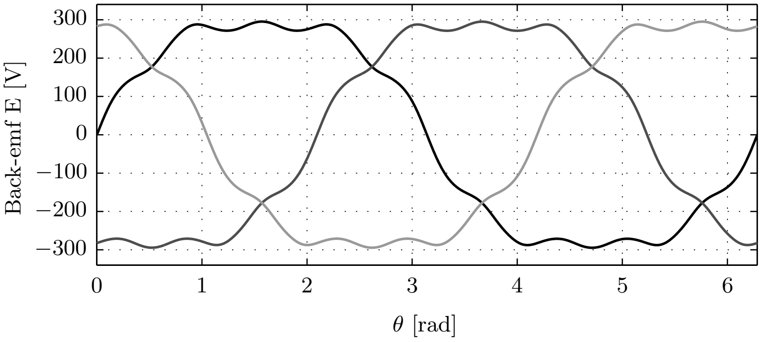

Figure 3.6: Back-emf waveforms of the Alenco prototype

The current waveforms are constructed so that their fundamental components are in phase with the corresponding fundamental components of the back-emf waveforms, i.e., the zero-crossings are aligned. The square-wave waveforms have a 120° conductance time. In order to perform a fair comparison, the amplitudes of the three sets of waveforms are calculated so that the mean mechanical power is 5 kW in each case. Fig. 3.7 shows the optimal (solid black line), sinusoidal (dashed black line) and square-wave (solid grey line) current waveforms in phase a.

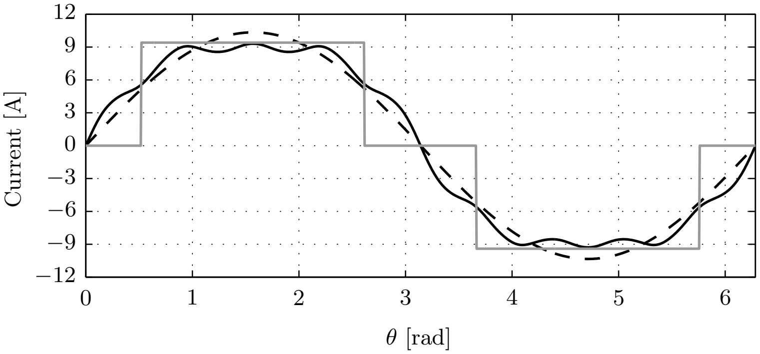

Figure 3.7: Optimal, sinusoidal and square-wave current waveforms

In the simplified model, the losses are solely determined by the rms value of the current. Table 3.1 gives a summary of the rms current, Joule losses and efficiency for the three waveforms. The losses are calculated with a resistance of 2.347 Ω, which is the average dc resistance in each phase of the Alenco prototype. This resistance value is measured at room temperature.

The simulation validates that the losses are minimal, and efficiency maximal for the optimal current waveform. The optimal waveform is slightly better than the sinusoidal waveform. The square-wave waveform leads to the most losses.

It is not straightforward to draw clear conclusions from the achieved efficiency improvement here. The decrease of 7 W in losses compared to the sinusoidal waveform may seem small, but must be seen in the right perspective. The hardware needed to achieve both waveforms

Table 3.1: Results of the proof of concept simulation

	Optimal	Sinusoidal	Square-wave
I_{rms} [A]	7.246	7.313	7.679
$3\ R\ I_{\text{rms}}^2$ [W]	370	377	415
η [%]	93.11	93.00	92.33

is identical, so there is no additional hardware cost. The difference is mere software implementation, which has a one-time development cost. Also, the reduction of losses depends greatly on the resistance of the machine, and the amount of harmonics in the back-emf. The influence of machine parameters on the achieved efficiency gain is investigated in more detail in chapter 5.

The simulated case presented here is simplified on two levels. Firstly, the simplified model of the machine is not a very accurate representation of a PMSM, certainly not when considering losses. Secondly, the optimal current waveform is based on this simplified PMSM model, which means that many effects in the machine are not taken into account. In chapter 5, the optimal current waveform technique presented in this chapter will be applied on the full PMSM model, leading to a much more realistic result. More detailed conclusions regarding the achieved improvement will be given in chapter 5.

The current waveforms not only determine the losses, but also the torque waveform. Generally, it is desired to keep torque ripples to a minimum to avoid noise and vibrations. Fig. 3.8 shows the torque waveforms for the three situations, i.e., an optimal current (solid black line), a sinusoidal current (dashed black line) and a square-wave current (solid grey line). In the case of a perfect brushless ac machine, there should be no torque ripple when the current is sinusoidal. However, since the machine has harmonics in the back-emf, even the sinusoidal waveform causes a torque ripple with an rms value of 0.40 Nm or 1.3%. The optimal current waveform causes an increase in the torque ripple to 0.89 Nm rms or 2.8%. The square-wave current has the highest rms torque ripple of 1.72 Nm of 5.4%.

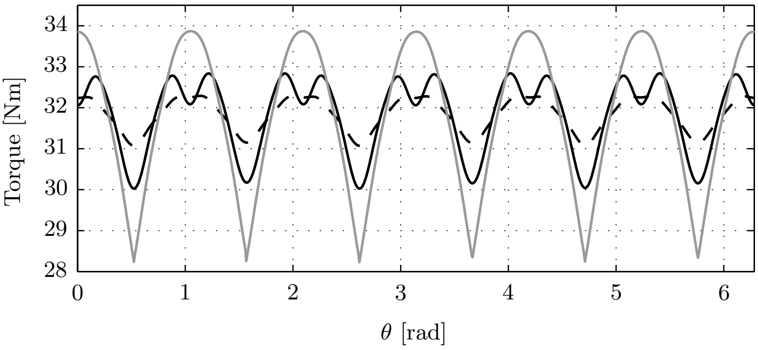

Figure 3.8: Torque waveforms for optimal, sinusoidal and square-wave current waveforms

Torque ripples are not necessarily a problem in every situation. Whether noise and vibrations are an issue depends on the application. For example, in servo applications and robotics, vibrations should be minimal. In a wind turbine, energy yield is more important, as long as the noise is within the allowed values imposed by regulations. Also, a strong torque ripple does not automatically lead to strong vibrations, as it depends on the mechanical parameters of the system, i.e., inertia, friction and damping coefficients. In applications where noise and vibrations are most important, a current waveform should be selected which minimises torque ripple, as discussed in §3.2.1. If efficiency is more important, the optimal current waveform presented in this work can be used.

The proof of §3.3.1 shows that the proportional current waveform leads to a maximum efficiency. However, it is unclear whether the proportional waveform is a necessary condition to achieve a maximum efficiency. In [92], the current waveform which results in zero torque ripple is determined in the frequency domain. Since there are multiple waveforms which yield zero torque ripple, the waveform with the highest efficiency is selected to be the most favorable. The performance of this waveform is then compared with the proportional waveform with simulations on a simplified PMSM model. The proportional waveform, which was derived in the frequency domain, yields more torque ripple than the waveform with zero torque ripple, but a higher efficiency. This suggests that the proportional waveform is indeed a necessary condition to achieve a maximum efficiency. However, the time domain analysis presented here does not provide the mathematical tools to prove this.

In the frequency domain, a waveform could be determined which results in a compromise between torque ripple and efficiency. For instance, it is possible that the torque ripple can be significantly reduced with a limited penalty on the efficiency. However, this requires a frequency domain analysis which has many drawbacks as discussed before.

Compared to small wind turbines available in the market today, the torque ripples are small in these simulations. Small wind turbines generally use passive diode rectifiers, which lead to heavily distorted current waveforms, and thus, large torque ripples. This was discussed in chapter 2 and the paper [64].

In chapter 5, the torque ripples for the different current waveforms will be calculated for the complete PMSM model with more advanced current waveforms.

3.3.3 Analogy with other engineering disciplines

It was shown that a proportional current waveform yields a maximum efficiency for any given back-emf waveform by using the Cauchy-Schwarz inequality. The same concept can be applied in other engineering disciplines as well, e.g., classical mechanics and hydraulics [94].

Linear mechanics

An analogy can be made between basic electrical and mechanical quantities, i.e., voltage and current are equivalent to force and velocity. Electrical power is expressed as the product of voltage and current, while mechanical power is the product of force and velocity. Electrical resistance is equivalent to mechanical friction. Therefore, in a mechanical system where the losses can be modeled by a friction constant, the Cauchy-Schwarz method described above can be applied directly: For a given force, as a periodic function of time, a proportional speed yields a maximum efficiency for a given amount of power.

Many applications have a periodic varying force, e.g., piston pumps, conveyor belts, wave energy converters, etc. However, it is not always possible to create a proportional velocity, since the inertia can form a considerable limitation. The electrical equivalent of inertia is inductance. In the same manner, the inductance of a PMSM limits the bandwidth of the current controller. Therefore, the practical applicability of the optimal waveform method on a mechanical or electrical system depends on the relative value of respectively the inertia or the inductance.

Rotational mechanics

The same analogy can be made for rotating systems. There, torque and rotational speed are equivalent to voltage and current. Electrical resistance is equivalent to the rotational friction. For a given torque, as a periodic function of time, a proportional rotational speed yields a maximum efficiency for a given amount of power. Rotational inertia is the limiting factor for the practical applicability of the optimal waveform method.

Hydraulics

An electric-hydraulic analogy can also be made. Voltage as delivered by a voltage source is equivalent to pressure difference, e.g., delivered by a pump or compressor. Electrical current is equivalent to volume flow rate. The hydraulic power of a pump or compressor is calculated as the product of the pressure difference and volume flow rate. Pipes form a hydraulic resistance to flow, just like a copper wire forms an electrical resistance, leading to losses.

The optimal waveform concept can be applied on hydraulics: For a given pressure, as a periodic function of time, a proportional volume flow rate yields a maximum efficiency for a given amount of power. Again, the practical applicability is limited by the hydraulic inertia, i.e., the mass of the fluid.

3.4 Impact on converter losses

The optimal current waveform which maximises the generator efficiency, automatically minimises the converter losses at the same time.

Converter losses consist mainly of conduction losses and switching losses.

Conduction losses are caused by the non-zero resistance of a power-electronic device in the on-state. As current passes through the device, Joule losses cause the component to heat up. This effect can be modeled by an equivalent series resistance. In a wind turbine converter, these resistances are connected in series with the generator stator resistance R_s so that they can be combined. Therefore, when the Joule losses of the generator are minimised, the conduction losses of the converter are minimised automatically.

Switching losses are caused by the charging and discharging of the parasitic capacitance at each switching instant. The switching losses depend on the switching frequency, the dc-bus voltage and the current. Therefore, as the Joule losses of the generator are minimised, also the switching losses of the converter are minimised.

It can be concluded that optimising the current waveform for the generator automatically minimises the converter losses. This is true both for passive diode rectifiers combined with a boost chopper and for full active rectifiers, since the loss mechanisms are analogous.

3.5 Conclusions

In this chapter, first, an overview of back-emf waveforms in PMSMs was given. Although PMSMs are marketed as brushless ac or brushless dc, most machines can be considered hybrid in practice. The back-emf waveform rarely corresponds with a perfect sinusoid or trapezoid. However, commercial converters assume the machine to be perfect, and use sinusoidal or square-wave current waveforms. When combined with a hybrid machine, this leads to more vibrations, noise and losses. The increased interest in axial flux machines has only worsened this problem.

In order to deal with hybrid machines, current waveform shaping techniques were discussed. Existing techniques in literature mainly focus on eliminating torque ripple by calculating the needed current harmonics in the frequency domain. However, in some applications, such as wind energy, efficiency is more important than torque ripple.

Therefore, in this research, the goal is to find the optimal current waveform which maximizes the efficiency of the machine, or the complete system in general.

At the end of the chapter, a new current waveform shaping technique based on the Cauchy-Schwarz inequality was presented. In contrast to classical methods in literature, the new technique uses the time domain instead of the frequency domain. Therefore, less simplifications and assumptions were needed and the result is more generic. The method was validated on a simplified PMSM model, showing the increased efficiency compared to classical sinusoidal and square-wave current waveforms. The optimal current waveform not only minimizes the generator losses, but automatically minimizes the converter losses as well, since both conduction losses and switching losses depend on the rms current.

In chapter 5, the new current waveform shaping technique will be applied on the complete PMSM scheme step-by-step, including important machine effects such as armature reaction and iron losses.

4

SPEED RIPPLES AND THEIR IMPACT ON THE BACK-EMF

In the new current waveform shaping technique presented in chapter 3, the back-emf waveform was assumed to be fixed, independent of the current waveform or variations in the rotor speed. This assumption is investigated thoroughly in this chapter. A mathematical model is developed to calculate the additional back-emf harmonics caused by speed ripples. Also, realistic speed ripples in wind turbines are calculated, caused by the tower shadow and wind shear effects. It is validated that the back-emf waveform can be assumed to be independent of speed ripples in most practical situations.

Contents

4.1 Introduction

In the proof based on the Cauchy-Schwarz inequality in §3.3, the back-emf of the magnets is assumed to be a fixed waveform, independent of, i.e., the current waveform. However, theoretically this is not the case. The harmonics in the current waveform affect the torque ripples. These torque ripples create rotor speed ripples. Since the back-emf is induced by rotating permanent magnets, variations in the rotor speed have a direct effect on this back-emf. When the back-emf depends on the current harmonics, the assumptions made in the proof are no longer valid and the Cauchy-Schwarz inequality cannot be applied. Also, torque ripples can be present in the turbine torque, e.g., caused by turbulence, tower shadow or wind shear, again resulting in speed ripples.

Here, the relation between torque ripples, speed ripples and the back-emf waveform will be investigated extensively. In the first part of this chapter, the case of torque ripples caused by tower shadow and wind shear is discussed. It will be shown that the effect of these torque ripples on the rotor speed is minimal, due to the large inertia of the turbine. Torque ripples can also originate from the generator, e.g., caused by cogging effects or by the interaction of the back-emf and current waveforms. Apart from mechanical resonances, their effect on speed ripples can also be neglected. This was thoroughly investigated in [95] and will not be treated here. The second part of this chapter discusses the effect of speed ripples on the back-emf waveform, which is shown to be nearly negligible. Both aspects combined give sufficient justification to assume that the back-emf waveform of the magnets is indeed independent of the current waveform.

However, models will be presented here which allow to calculate the speed ripples in wind turbines and the effect of speed ripples on the back-emf waveform. These models can be used in other applications where this effect is not negligible.

4.2 Speed ripples caused by the turbine

First, the effect of turbine torque ripples caused by tower shadow and wind shear on rotor speed ripples will be investigated here. This will gain insight in the magnitude of the speed ripples which can be expected in practice. As will be shown, these rotor speed ripples are small due to the inertia of the turbine. The research of this topic was published in [96], where more details can be found if needed.

The behavior of the turbine blades is determined by multiple variables, such as wind speed, air density, turbulence of the air flow and the mechanical design of the system [97]. Several of these variables can introduce vibrations, which causes ripples in the torque and rotor speed of the turbine. For example, turbulent air flow typically causes high frequent vibration of the blades [98–100]. For three-bladed horizontal-axis turbines, effects such as tower shadow and wind shear cause a torque pulsation three times per rotation [101–103], also called a 3p pulsation. Tower shadow is caused by the disturbed air flow due to the presence of the tower. Wind shear is caused by the height dependence of wind speed, i.e., wind speed decreases at low altitude due to friction with the earth's surface. As tower shadow and wind shear are dominant causes of torque oscillations, the focus lies on these torque ripple sources here.

In [101], an extensive analytical model was presented which allows to calculate the torque oscillations caused by tower shadow and wind shear. The model is applicable for classical three-bladed horizontal-axis turbines facing upwind, which is the most common and best performing turbine type at this moment. The magnitude of these oscillations depends largely on the design of the wind turbine, e.g., the radius and height of the tower, the distance between the blades and the tower and the blade length. The torque oscillations can be significant, which will be shown here by applying the model of [101] on the wind turbines of the Small Wind Turbine (SWT) Field Laboratory of Ghent University in Ostend, Belgium.

Although the model of [101] allows to accurately simulate the torque oscillations caused by tower shadow and wind shear, it remains unclear which consequences these oscillations have on the rotor speed. Therefore, the rotor speed ripples caused by tower shadow and wind shear will be calculated here.

4.2.1 Turbine model

The turbine is modeled as explained in chapter 2. Only three-bladed horizontal axis turbines will be considered here. Relevant dimensional parameters are defined by Fig. 4.1: the blade length of turbine radius R, the hub height H, the tower radius a and the distance between the blades and the center of the tower x.

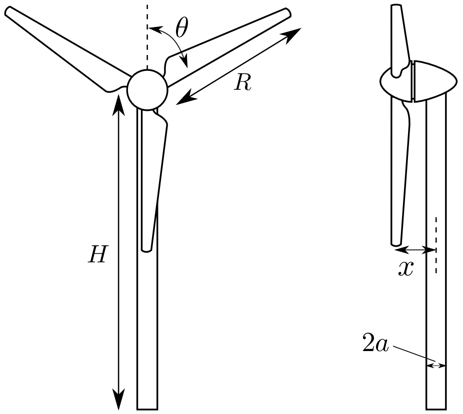

Figure 4.1: Definition of the dimensional parameters R, H, a and x

The inertia of the turbine is calculated by using (2.4). The inertia of the generator can be neglected compared to the turbine inertia. The inertia is a crucial parameter to calculate the rotor speed ripples corresponding with torque oscillations. This can be done with the following mechanical equation, written here in differential form:

$$J_t \frac{d\Omega}{dt} = T_t - T_g \tag{4.1}$$

The torque T_t is the turbine torque, which can be calculated by dividing the turbine power P_t by the rotor speed Ω. This torque will contain the oscillations caused by tower shadow and wind shear. The torque T_g is the generator torque. Although this torque can also contain oscillations due to cogging or current harmonics, it will be assumed constant here, as both effects can be investigated separately and superimposed if desired.

The MPPT of the turbine is assumed to work perfectly, so that the average rotor speed corresponds to the MPP at all time.

4.2.2 Tower shadow and wind shear model

The essence of the model of [101] is the turbine torque equation, which depends on the mechanical rotor angular position θ_m, which in turn also depends on time:

$$T_t(\theta_m) = T_0 \cdot \left[1 + 2\,\frac{1-m}{m} + \frac{2}{v_0}(v_{\mathrm{TS}} + v_{\mathrm{WS}})\right] \tag{4.2}$$

This equation contains the constants T_0, m and v_0. The parameters v_{TS} and v_{WS} are dependent on time and rotor angle and are thus responsible for the torque oscillations. The factor T_0 is the constant torque that would result from a wind speed v in the abscence of tower shadow and wind shear. As stated above, the MPPT is assumed to work perfectly so that C_p equals the maximum value $C_{\mathrm{p,max}}$ and λ equals the optimal value λ_{opt}. The factor T_0 is calculated from the classical power equation (2.1):

$$T_0 = \frac{1}{2}\,\rho\,\pi\,\frac{C_{\mathrm{p,max}}}{\lambda_{\mathrm{opt}}}\,R^3\,v^2 \tag{4.3}$$

As stated above, the wind speed v at hub height was defined and used in the power equation (2.1). In reality, the wind speed varies with height due to friction with the earth's surface. Therefore, a turbine blade encounters a higher wind speed when facing upwards compared to facing downwards, resulting in a periodic oscillation of the turbine torque which occurs three times per rotation, i.e., the wind shear effect. The wind speed can be written in function of height z with the following power law [104]:

$$v(z) = v\left(\frac{z}{H}\right)^{\alpha} \tag{4.4}$$

The parameter α is an empirical measure for the roughness of the earth's surface. It is also possible to model wind shear with a logarithmic law, which is more accurate but also more complex. To maintain the equations developed in [101], the power law model is used here. The power law offers sufficient realism for the simulations performed here.

Based on (4.4), the varying wind speed can be averaged over the rotor area, resulting in the spatial averaged wind speed v_0:

$$v_0 = \left[1 + \frac{\alpha(\alpha-1)R^2}{8H^2}\right] v = m\ v \tag{4.5}$$

Since $R < H$ and $0 < \alpha < 1$, the spatial average factor m is always smaller than 1 in practical situations, thus $v_0 < v$.

The term v_{WS} in (4.2) represents the effect of wind shear and is also dependent of the rotor position θ_m. The wind shear component v_{WS} is given by:

$$\begin{aligned} v_{\mathrm{WS}}(\theta_m) &= v\ \frac{\alpha(\alpha-1)(\alpha-2)}{60} \left(\frac{R}{H}\right)^3 \cos 3\theta_m \\ &+ v\ \frac{\alpha(\alpha-1)}{8} \left(\frac{R}{H}\right)^2 \end{aligned} \tag{4.6}$$

The wind shear effect causes a sinusoidal fluctuation and a constant offset of the torque. It is clear from the equation that the sinusoidal fluctuation indeed has a frequency of three times the rotational speed, resulting in a 3p oscillation.

The term v_{TS} in (4.2) represents the effect of tower shadow and is dependent of the rotor position θ, which in turn depends on time. The tower shadow component v_{TS} is given by:

$$\begin{aligned} v_{\mathrm{TS}}(\theta_m) &= \frac{v_0}{3R^2} \sum_{i=1}^{3} \left[\frac{a^2}{\sin^2\theta_i} \ln\left(\frac{R^2 \sin^2\theta_i}{x^2} + 1\right)\right] \\ &- \frac{v_0}{3R^2} \sum_{i=1}^{3} \left[\frac{2a^2R^2}{R^2\sin^2\theta_i + x^2}\right] \end{aligned} \tag{4.7}$$

This equation contains a summation with index i, representing the superposition of the tower shadow effect of each of the three blades. The blade angles θ_i are defined as follows:

$$\theta_i = \theta_m + (i-1)\frac{2\pi}{3} \tag{4.8}$$

When implementing (4.7), care should be taken that a torque dip is only caused when a blade is facing downwards, not upwards. The waveform of v_{TS} contains three strong dips per rotation, hence resulting in a 3p oscillation.

4.2.3 Simulation results for small turbines

The previously defined wind turbine and torque oscillation models have been implemented in Matlab. This model will be used to simulate the torque oscillations and rotor speed ripples of the wind turbines in the Small Wind Turbine Field Laboratory. The SWT Field Lab consists of 10 wind turbines, with a rated power up to 10 kW, which are continuously monitored. The dimensional parameters R, H, x and a of the three-bladed upwind turbines have been measured or estimated and will be used here. The simulation results are thus based on real measured parameters. Since the placement of accurate torque and rotor speed sensors in an existing turbine is not straightforward, directly measuring the torque oscillations and rotor speed ripples on the turbines in the SWT Field Lab is currently not possible. A detailed description of the simulation model is given in [96], but will not be discussed here.

The simulation model is used to calculate torque oscillations and rotor speed ripples for four turbines of the SWT Field Lab, i.e., the Raum 1.5, Evance R9000, Uniwind 10 and Fortis Alizé. These turbines have a horizontal axis, three blades and an upwind yaw principle so that the tower shadow and wind shear model of [101] is applicable. Table 4.1 shows the values used in the calculations.

Table 4.1: Parameters of the SWT Field Lab turbines

	P_n	Ω_n	v_n	R	H	a	x	M_b
	[kW]	[rpm]	[m/s]	[m]	[m]	[m]	[m]	[kg]
Raum 1.5	1.5	800	11	1.45	15	0.03	0.27	2.3
Evance R9000	5.0	200	12	2.75	15	0.11	0.54	14.2
Uniwind 10	10.0	120	10	4.20	15	0.14	0.54	35.0
Fortis Alizé	10.0	280	15	3.50	15	0.25	0.75	15.0

The rated values of power, rotor speed and wind speed as well as the turbine radius were obtained from the datasheets of the manufacturer. The dimensional parameters H, a and x and the blade mass M_b were measured in the SWT Field Lab before the turbines were installed.

The table contains the power P_n, the rotor speed Ω_n and the wind speed v_n at the rated power point. Furthermore, the dimensional parameters R, H, a and x and the blade mass are mentioned.

The torque oscillations and rotor speed ripples are calculated for these turbines at the rated operating point. The empirical wind shear exponent α was chosen at 0.3 [101]. The torque oscillations are presented in Fig. 4.2, in function of relative time, which is time divided by the duration of one turbine revolution. The figure thus shows one third of a revolution.

The total turbine torque oscillation is shown in Fig. 4.2 (a). This torque oscillation is a combination of the tower shadow and wind shear effects. Fig. 4.2 (b) and (c) show the torque oscillations caused by both effects separately. The torque $T_{\mathrm{WS,t}}$ is defined as calculated from (4.2) when only v_{WS} is included. In the same manner, the torque $T_{\mathrm{TS,t}}$ is defined as calculated from (4.2) when only v_{TS} is included. The oscillations caused by wind shear are clearly much smaller than the oscillations caused by tower shadow. Since all turbines are installed at a tower height H of 15 m, the wind shear oscillation is larger as the turbine radius R increases, which is expected from (4.6) and confirmed by the simulations.

The torque dip caused by tower shadow and wind shear is clearly shown in the total torque in Fig. 4.2 (a). For the smallest turbine, the Raum 1.5, the torque dip is limited to 1% of the total torque. For the larger Evance R9000 turbine, the torque dip increases to 3%. For the Uniwind 10 and Fortis Alizé turbines, the torque dip equals 5% and 8% respectively, which is a significant torque oscillation. In general, it can be concluded that the torque oscillation can be considerable.

Fig. 4.3 shows the simulated rotor speed ripple caused by the torque dip. In the region where the blade passes the tower, the torque dip causes a rapid decrease in rotor speed. Outside of this region, the rotor speed has a slow increase since the turbine torque is above the average value. For the smallest turbine, the Raum 1.5, the ripple is almost nonexistent with an amplitude of 0.00015%. The Evance R9000 turbine has a rotor speed ripple of 0.005%. The Uniwind 10 turbine has the largest ripple with an amplitude of 0.01%. Finally, the Fortis Alizé has a rotor speed ripple with an amplitude of 0.006%.

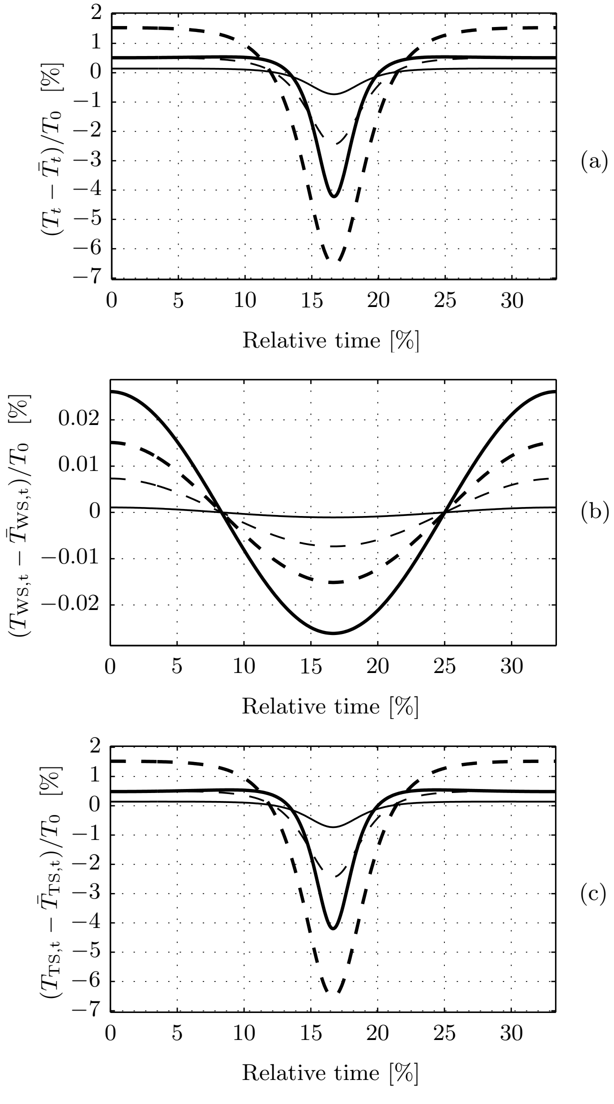

Figure 4.2: Simulated torque oscillations: Total torque (a), Wind shear component (b), Tower shadow component (c) ; — = Raum 1.5, - - = Evance R9000, —— = Uniwind 10, **– –** = Fortis Alizé

In general, the obtained speed ripples have a small amplitude.

Although the torque oscillations can be considered large, with an am-

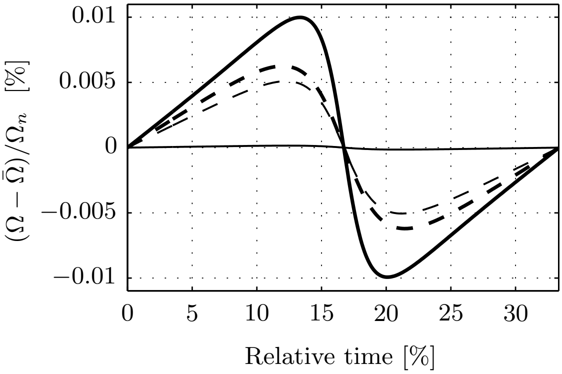

Figure 4.3: Simulated rotor speed ripples: — = Raum 1.5, - - = Evance R9000, —— = Uniwind 10, **- -** = Fortis Alizé

plitude up to 8% for the Fortis Alizé, the impact on the rotor speed is limited to a maximum amplitude of 0.01% for the Uniwind 10. This shows that the inertia of the turbine is capable of strongly reducing the impact of the torque oscillations on the rotor speed. Also, it is worth noting that the turbine with the largest torque dip, i.e., the Fortis Alizé, is not the turbine with the largest relative rotor speed ripple, which is the Uniwind 10. Although the Uniwind 10 has a larger inertia than the Fortis Alizé, the low rated rotor speed results in a larger relative rotor speed ripple. In absolute values, the Fortis Alizé would have a larger speed ripple. However, it is best to consider relative ripples, not absolute, since the relative ripples determine the impact on the rest of the system.

4.2.4 Simulation results for a large turbine

The simulation model is now also used to calculate the torque and speed ripples for the offshore 8 MW Vestas V164 turbine. The V164 is currently in the final stages of development but some technical data are already available. Table 4.2 shows the parameters used in the simulation.

The rated power P_n, rotor speed Ω_n, turbine radius R and blade mass M_b were obtained from Vestas. Since the tower dimensions will be site specific, the hub height H, tower radius a and distance between the

Table 4.2: Parameters of the Vestas V164

P_n	Ω_n	v_n	R	H	a	x	M_b
[MW]	[rpm]	[m/s]	[m]	[m]	[m]	[m]	[kg]
8.0	10.5	13	82	123	3.3	10.5	35000

blades and tower center x were estimated by rescaling common values for the smaller 3.0 MW Vestas V112 turbine. The rated wind speed v_n was also estimated based on the V112. Since the V164 is an offshore turbine, the wind shear exponent α was set at 0.1, which is realistic for open water.

Fig. 4.4 shows the simulated torque oscillations for the V164. The total torque dip (a) equals 7% of the total torque, which is comparable with the Uniwind 10 and Fortis Alizé turbines. The wind shear component is relatively larger than for the four simulated small wind turbines. The reason for this is the large R/H ratio. Although the wind shear effect is stronger, it remains considerably smaller than the tower shadow effect.

Fig. 4.5 shows the simulated rotor speed ripple for the V164. The relative speed ripple has an amplitude of 0.047%, which is more than for the four simulated small wind turbines. Although the torque ripple is comparable with the Uniwind 10, i.e., 7% for the V164 versus 5% for the Uniwind 10, the speed ripple is larger, i.e., 0.047% for the V164 versus 0.01% for the UniWind 10. This is caused by the rotational inertia which is relatively lower in the V164. This can be expected from the use of more advanced, and thus lighter, materials for large wind turbines. Still, the speed ripple is small compared to the torque ripple.

From the simulation results, it can be concluded that the torque dip created by the tower shadow and wind shear effects can become large. However, the impact of this torque dip on the rotor speed is limited by the turbine inertia, so that the rotor speed ripple is negligible in most situations. For the turbines investigated here, the inertia was sufficiently large to damp the speed ripples. However, the development of lighter blade materials in the future could reduce this inertia.

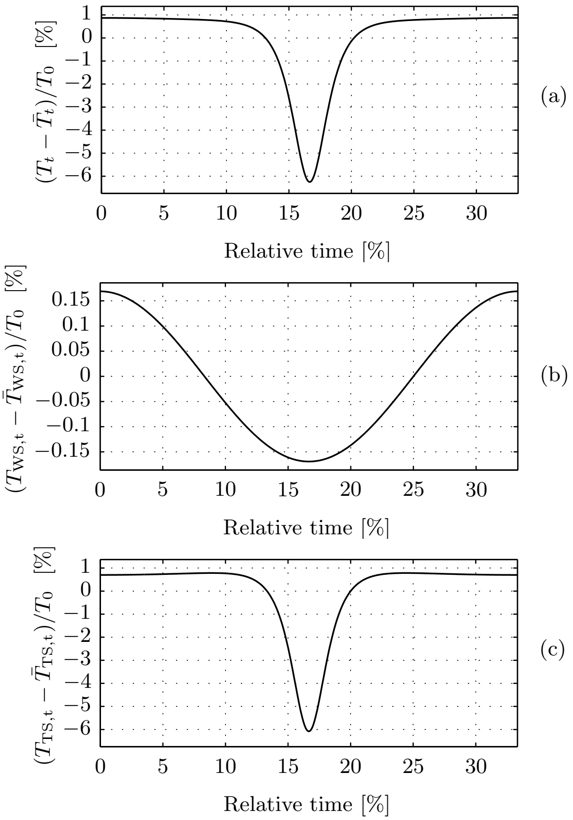

Figure 4.4: Simulated torque oscillation for the Vestas V164: Total torque (a), Wind shear component (b), Tower shadow component (c)

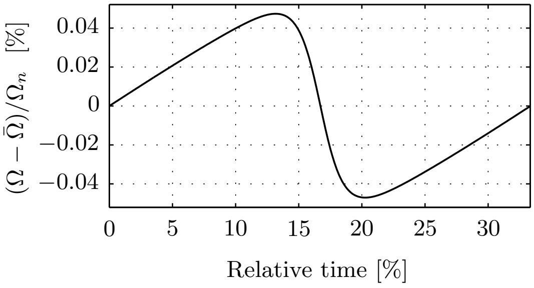

Figure 4.5: Simulated rotor speed ripple for the Vestas V164

Therefore, care should be taken when generalising the conclusions of these simulations for all wind turbines in the future.

4.2.5 Indepence of turbine size

Micro, small, medium and large turbines differ significantly in size. Therefore, the question rises whether previous conclusions can be generalised for turbines of every size. Intuitively, it is expected that a large turbine reacts differently due to the relative difference in rotational inertia, which is more than proportional to the rated power. However, the simulations have already shown that the relative torque oscillations and speed ripples have comparable amplitudes for small and large turbines. It will be shown here that the relative torque oscillations do not depend on the turbine size and the conclusions from the previous simulations can be generalised to turbines of any size.

Scalable turbine model

Assume that all necessary parameters are known for a certain reference turbine. These parameters will be written with an index "r". The dimensions of this reference turbine can be made scalable by introducing a dimensionless scaling factor S, which equals 1 for the reference turbine:

$$\begin{aligned} R &= R_r \cdot S \qquad & x &= x_r \cdot S \\ H &= H_r \cdot S \qquad & a &= a_r \cdot S \end{aligned} \tag{4.9}$$

When the dimensions of a turbine are changed with S, all other parameters such as the rated power, rated rotor speed, etc, are changed as well. Rated parameters are written with an index "n". The rated wind speed v_n changes according to (4.4):

$$v_n = v_{n,r} \cdot \left(\frac{H}{H_r}\right)^{\alpha} = v_{n,r} \cdot S^{\alpha} \tag{4.10}$$

The rated rotor speed Ω_n can be derived from the tip-speed ratio λ, under the assumption that the turbine reaches the optimal λ in the rated operating point. Since λ is a dimensionless parameter, the optimal value remains constant, hence, independent of size, as long as the same blade design is used. This results in the following scale law for Ω_n:

$$\Omega_n = \frac{v_n}{R}\,\lambda_{\text{opt}} = \frac{v_{n,r}}{R_r}\,\lambda_{\text{opt}} \cdot S^{\alpha-1} = \Omega_{n,r} \cdot S^{\alpha-1} \tag{4.11}$$

Since α is smaller than 1, Ω_n decreases with S, i.e., larger wind turbines have a lower rated rotor speed than smaller turbines. In a similar way, the rated power P_n is written in terms of the scaling factor S and the rated power $P_{n,r}$ of the reference turbine:

$$P_n = \frac{1}{2}\rho\,\pi\,R^2\,v_n^3\,C_{\text{p,max}} = P_{n,r} \cdot S^{2+3\alpha} \tag{4.12}$$

Since the volume of a blade is assumed to be proportional to the cubic power of the turbine size, the mass of a blade M_b can be written as:

$$M_b = M_{b,r} \cdot S^3 \tag{4.13}$$

From this, the inertia J_t is calculated:

$$J_t = \frac{1}{3}M_b R^2 = J_{t,r} \cdot S^5 \tag{4.14}$$

Fig. 4.6 shows the wind speed, rotor speed, rated power and inertia versus the scaling factor S and relative with respect to their reference values. Both the power and inertia increase with S, but the inertia increase is clearly stronger. With α around 0.3 [101], the rated power P_n is proportional to S with a power of around 3. The inertia on the other hand is proportional to S with a power of 5, and is thus indeed more than proportional to the rated power. In contrast to the intuition, one cannot conclude from this that smaller turbines would have larger rotor speed ripples caused by tower shadow and wind shear.

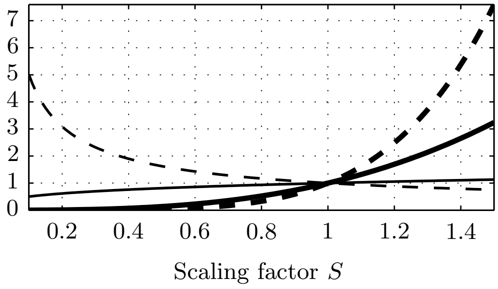

Figure 4.6: Scalable turbine model:
— $= v_n/v_{n,r}$, - - $= \Omega_n/\Omega_{n,r}$, —— $= P_n/P_{n,r}$, ▬ ▬ $= J_t/J_{t,r}$

Mathematical proof

By using the equations formulated above, it will now be proven step-by-step that the relative ripples do not depend on the turbine size S.

1. Both $v_{\mathrm{TS}}(\theta)$ and $v_{\mathrm{WS}}(\theta)$ are oscillating waveforms with a periodicity of one third of a revolution of the turbine, due to the physical nature of tower shadow and wind shear. The waveforms $v_{\mathrm{TS}}(\theta)$ and $v_{\mathrm{WS}}(\theta)$ are now divided by v_0 and the scalable dimensional parameters (4.9) are substituted in (4.6) and (4.7), which results in:

$$\begin{aligned} \frac{v_{\mathrm{WS}}(\theta)}{v_0} &= \frac{\alpha(\alpha-1)(\alpha-2)}{60\ m}\left(\frac{R_r}{H_r}\right)^3 \cos 3\theta \\ &+ \frac{\alpha(\alpha-1)}{8\ m}\left(\frac{R_r}{H_r}\right)^2 \end{aligned} \tag{4.15}$$

$$\begin{aligned} \frac{v_{\mathrm{TS}}(\theta)}{v_0} &= \sum_{i=1}^{3}\left[\frac{a_r^2}{3R_r^2\sin^2\theta_i}\ln\left(\frac{R_r^2\sin^2\theta_i}{x_r^2}+1\right)\right] \\ &- \frac{1}{3}\sum_{i=1}^{3}\left[\frac{2a_r^2}{R_r^2\sin^2\theta_i + x_r^2}\right] \end{aligned} \tag{4.16}$$

   Since m is independent of S, these equations show that the resulting waveforms $v_{\mathrm{TS}}(\theta)/v_0$ and $v_{\mathrm{WS}}(\theta)/v_0$ are both independent of S. This is caused by the fact that (4.6) and (4.7), after division by v_0, contain only ratios of dimensional parameters, i.e., R/H, a/r and R/x. These ratios remain constant when scaling the turbine.

2. Since $v_{\mathrm{TS}}(\theta)/v_0$ and $v_{\mathrm{WS}}(\theta)/v_0$ are both independent of the turbine size S, (4.3) shows that also $T_t(\theta)/T_0$ is a waveform independent of S. The factor T_0 is however dependent on S, but independent of θ. In other words, the torque $T_t(\theta)$ can be considered as a S-independent waveform $f(\theta)$, multiplied with a S-dependent factor T_0:

$$\begin{aligned} T_t &= T_0(S) \cdot \left[1 + 2 \, \frac{1-m}{m} + \frac{2}{v_0}(v_{\mathrm{TS}} + v_{\mathrm{WS}}) \right] \\ &= T_0(S) \cdot f(\theta) \qquad (4.17) \end{aligned}$$

3. As mentioned before, the generator torque T_g can be assumed equal to the average turbine torque $\bar{T}_t$ in steady-state. According to (4.1), the rotor speed ripples are determined by the difference between turbine and generator torque, which can now be written in a simplified form:

   $$T_t - T_g = T_0(S) \cdot \left[f(\theta) - \bar{f}(\theta) \right] \qquad (4.18)$$

   Substitution of this equation in (4.1) and application of the substitution rule for integration results in:

   $$\begin{aligned} \Omega(t) &= \frac{1}{J_t} \int_0^t T_0 \cdot \left[f(\theta) - \bar{f}(\theta) \right] \, dt \qquad (4.19) \\ &= \frac{T_0}{J_t \, \Omega_0} \int_0^{\theta/\Omega_0} \left[f(\theta) - \bar{f}(\theta) \right] \, d\theta \end{aligned}$$

   The substitution rule was used to transform the integral of time t to an integral of angle θ, with the approximation that $\theta \simeq \Omega_0 \, t$ which is valid since the rotor speed ripples are small. The integrand $f(\theta) - \bar{f}(\theta)$ is a periodic function of θ independent of S. The integration interval does contain Ω_0, which depends on S, so that the integral is no longer independent of S but still a periodic function of θ. The turbine size S only causes a horizontal scaling of the periodic function and does not influence the amplitude. Therefore, the amplitude of the speed ripples is entirely determined by the factor $T_0/J_t \, \Omega_0$, which is crucial in the next step.

4. The result from the previous step can now be used to show that the relative ripples, i.e., $\Omega(t)/\Omega_0$, are independent of the turbine size S. For this, the following factor must be independent of S:

   $$\frac{T_0}{J_t \, \Omega_0^2} \qquad (4.20)$$

The turbine is assumed to operate at the rated power level. The proof remains valid for every operating point, for which the proof is analogous. In the rated power point, the torque T_0 can be assumed equal to the rated torque T_n, calculated as P_n/Ω_n. The average rotor speed Ω_0 can also be assumed equal to the rated rotor speed Ω_n. Substitution of (4.11), (4.12) and (4.14) in (4.20) yields:

$$\begin{aligned}\frac{T_0}{J_t\ \Omega_0^2} &= \frac{P_n}{J_t\ \Omega_n^3} = \frac{P_{n,r}\ S^{2+3\alpha}}{J_{t,r}\ S^5 \cdot \Omega_{n,r}^3\ S^{3\alpha-3}} \\ &= \frac{P_{n,r}}{J_{t,r}\ \Omega_{n,r}^3} \qquad (4.21)\end{aligned}$$

This factor is indeed independent of S, which proves that the relative rotor speed ripples are independent of turbine size.

Discussion

The proof has shown that when the dimensions of a turbine are scaled to a larger or smaller size, the relative ripples remain unchanged. Previously, it was concluded that the effect of the torque oscillations on the rotor speed is small (below 0.01% for the turbines considered here). This conclusion can now be generalised to smaller and larger turbines.

A few approximations were made during the proof. For instance, the mass density of the blades was assumed constant, while the blades of large turbines have a lower mass density when compared to small turbines due to the use of more advanced materials. Also, the relation between the dimensional parameters R, H, a and x was assumed to be constant when scaling the turbine. However, the design of turbines of different sizes can slightly differ. Furthermore, the tower height was assumed to be proportional to the size of the turbine, while in practice the tower height is also determined by government regulations and planning permissions. For this reason, the turbines of the SWT Field Lab all have a tower height of 15 m since this is the maximum allowed by the build permit. The aformentioned approximations however do not significantly affect the overall conclusion that the relative speed ripples are independent of the size and are considerably damped by the turbine inertia.

4.2.6 Conclusions

The simulations have shown that the torque ripples caused by tower shadow and wind shear can be significant, e.g., 8% for the Fortis Alizé. However, the turbine inertia attenuates this torque ripple so that the effect on the rotor speed is strongly reduced, e.g., a maximum of 0.01% for the Uniwind. Since these rotor speed ripples have a low magnitude, it can be expected intuitively that they do not noticeably affect the waveform of the back-emf. However, this cannot be stated with certainty unless the back-emf is modeled for a non-constant rotor speed to investigate this effect quantitatively. Therefore, this model is derived in §4.3.

4.3 Impact of speed ripples on the back-emf

The magnitude of realistic speed ripples in wind turbines has been calculated for the case of tower shadow and wind shear [96] and for the case of torque ripples caused by the generator [95]. Their effect on the harmonics in the magnet back-emf will now be determined. In literature, the rotor speed is assumed to be constant in PMSM models. A model which takes into account speed ripples was not previously developed. However, it could be worthwhile to take this effect into account, not only for wind turbines. For instance, several loads in industry generate pulsating torques or consume intermittent power, which causes vibrations, e.g., conveyor belt systems [105], piston pumps and compressors [106]. Therefore, a model was developed during this research to determine the back-emf harmonics in function of the speed ripples. This work has been published in [107] and will be described here.

This section only consideres the impact of speed ripples on the magnet back-emf, not on the armature reaction. Both effects can be seen as decoupled, as becomes clear from the equivalent scheme of a PMSM in Fig. 2.7. The impact of speed ripples on the armature reaction back-emf is discussed later in this chapter.

4.3.1 Definitions

Four quantities are of interest here, i.e., the rotational speed Ω, the angular rotor position θ_m, the flux Ψ coupled with an arbitrary stator winding and the back-emf E. Each of these quantities will be represented by a Fourier series. As the Fourier transformation is only applicable on periodic signals, a steady-state situation will be assumed. A finite time interval is chosen, equal to μ times one revolution of the rotor, i.e., $\mu\ 2\pi/\Omega_0$, where Ω_0 denotes the average speed and μ is a positive integer. The factor μ can be chosen depending on the application, e.g., $\mu = 1$ if only "conventional" back-emf harmonics are studied or $\mu > 1$ if back-emf subharmonics or low-frequent speed ripples need to be included.

Speed

The starting point is the presence of speed ripples, caused by the load or by the PMSM itself. The mechanical speed $\Omega(t)$ can be written as the sum of an average speed Ω_0 and a Fourier series:

$$\Omega(t) = \Omega_0 + \sum_{n=-\infty}^{+\infty} \hat{\Omega}(n) \cdot e^{jn\Omega_0 t/\mu} \tag{4.22}$$

The complex coefficients $\hat{\Omega}(n)$ are calculated with the Fourier transformation:

$$\hat{\Omega}(n) = \frac{\Omega_0}{\mu 2\pi} \int_0^{\mu \frac{2\pi}{\Omega_0}} \Omega(t) \cdot e^{-jn\Omega_0 t/\mu} dt \tag{4.23}$$

Since the complex formulation of the Fourier transformation is used, the components with a negative index are the complex conjugate of the corresponding components with a positive index, i.e., $\hat{\Omega}_{-n} = \hat{\Omega}_n^*$.

Angular rotor position

The angular rotor position $\theta_m(t)$ can be calculated from $\Omega(t)$ by integrating (4.22):

$$\theta_m(t) = \int_0^t \Omega(t) dt = \Omega_0 t + \sum_{n=-\infty}^{+\infty} \mu \frac{\hat{\Omega}(n)}{jn\Omega_0} \cdot e^{jn\Omega_0 t/\mu} \tag{4.24}$$

The second term is a series of harmonics caused by the speed ripples. Their amplitudes are clearly attenuated due to the division of n. However, this does not mean they can be neglected, as will become clear further in the analysis.

Flux

The back-emf of a PMSM is induced by the flux coupled with the stator winding. This total flux is the superposition of two components, i.e., the flux of the permanent magnets of the rotor and the flux caused by the stator windings themselves. The first component is the main flux component while the second component is a smaller additional effect due to armature reaction. The permanent magnet flux contains several spatial harmonics in the air-gap of the machine. A large part of this flux is coupled with the stator-winding and is capable of inducing a back-emf. The winding factors of the stator winding, defined by its design, determine how strong the different harmonics are coupled with the stator. This results in a stator-coupled flux waveform containing harmonics. Here, only the dominant flux component caused by the permanent magnets is considered. The impact of speed ripples on the armature reaction flux can be seen as decoupled from the permanent magnet flux and will be discussed later in this chapter.

The waveform of the flux Ψ, can be written as the following Fourier series in terms of θ_m:

$$\Psi\left(\theta_m(t)\right) = \sum_{k=-\infty}^{+\infty} \hat{\Psi}(k) \cdot e^{jk\theta_m(t)/\mu} \tag{4.25}$$

In contrast to the Fourier series of $\Omega(t)$ and $\theta_m(t)$, this is not a Fourier series in time but in space, i.e., the rotor angle θ_m. The coefficients $\hat{\Psi}(k)$ are therefore space harmonics and not time harmonics. The coefficients $\hat{\Psi}(k)$ are calculated from the flux $\Psi(\theta_m)$ by using the Fourier transformation:

$$\hat{\Psi}(k) = \frac{1}{\mu 2\pi} \int_0^{\mu 2\pi} \Psi(\theta_m) \cdot e^{-jk\theta_m/\mu} d\theta_m \tag{4.26}$$

In agreement with the time period $\mu\ 2\pi/\Omega_0$, a period of $\mu\ 2\pi$ is used here in the transformation since it also corresponds to μ times one revolution of the rotor. The consequence of this choice is that conventional harmonics have an order k equal to a multiple of $\mu\ N_p$. The fundamental component results in two Fourier components, i.e., one with an order $\mu\ N_p$ and one with an order $-\mu\ N_p$. When μ is chosen large enough, also subharmonics can be included in the analysis. For instance, flux subharmonics are often present in PMSMs with fractional slot windings [108].

It is important to note that the Fourier series of the flux given in (4.25) depends on θ_m. This angle itself has a Fourier series given by (4.24). In other words, the Fourier series (4.25) contains a second Fourier series (4.24). This complicates the mathematical model but will be treated appropriately.

Back-emf

The back-emf E induced by the permanent magnet flux is calculated by:

$$E = -\frac{d\Psi}{dt} \tag{4.27}$$

The derivative causes higher-order flux time harmonics to be magnified in the back-emf. This shows the importance of these flux harmonics, even if their amplitude seems negligible.

4.3.2 Constant-speed situation

When no speed ripples are present, the rotor angle becomes linear, i.e., $\Omega_0 t$. The flux Ψ and back-emf E simplify to:

$$\Psi_0(t) = \sum_{k=-\infty}^{+\infty} \hat{\Psi}(k) \cdot e^{jk\Omega_0 t/\mu} \tag{4.28}$$

$$E_0(t) = -\sum_{k=-\infty}^{+\infty} \frac{jk\Omega_0}{\mu} \cdot \hat{\Psi}(k) \cdot e^{jk\Omega_0 t/\mu} \tag{4.29}$$

Equations (4.28) and (4.29) show that the flux harmonics of (4.25), which are space harmonics, are directly converted to time harmonics in the flux $\Psi_0(t)$. Therefore, the fluxes $\Psi(\theta_m)$ and $\Psi_0(t)$ have exactly the same waveform.

In [85], the back-emf waveform of a PMSM was measured and the dominant harmonics were given, i.e., a third harmonic of 22.45%, a fifth harmonic of 5.43% and a seventh harmonic of 0.87%. This waveform has been used here to construct Fig. 4.7, which shows the flux and back-emf as calculated by (4.28) and (4.29). The speed Ω equals 750 rpm, i.e., the synchronous speed for a 50 Hz machine with a pole pair number N_p of four. The back-emf waveform is typical for a brushless dc machine.

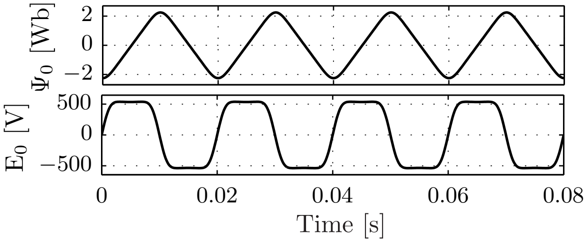

Figure 4.7: Constant speed flux Ψ_0 and back-emf E_0

4.3.3 Harmonic model including speed ripples

Here, the definitions of Ω, θ_m, Ψ and E are applied to a more general situation where speed ripples are present. This leads to a harmonic model of the flux and back-emf, including an analytical expression for the harmonics caused by the speed ripples.

The combination of (4.24) and (4.25) gives the flux $\Psi(t)$ in the presence of speed ripples:

$$\Psi(t) = \sum_{k=-\infty}^{+\infty} \hat{\Psi}(k) \cdot e^{jk\Omega_0 t/\mu} \cdot \\ \exp\left(-jk \sum_{n=-\infty}^{+\infty} \frac{\hat{\Omega}(n)}{jn\Omega_0} \cdot e^{jn\Omega_0 t/\mu}\right) \tag{4.30}$$

This equation is not straightforward, since it contains a complex exponential function, which in turn contains a complex exponential function of time. However, as long as the ripples $\hat{\Omega}(n)$ are limited, the argument of the second exponential function in this equation is small enough to apply a first-order Taylor approximation, i.e., $\exp(x) \simeq 1 + x$. This considerably simplifies the equation. The accuracy of this approximation will be verified later. The flux can now be written as follows:

$$\Psi(t) = \sum_{k=-\infty}^{+\infty} \hat{\Psi}(k) \cdot e^{jk\Omega_0 t/\mu} \quad - \quad \left(\sum_{k=-\infty}^{+\infty} k\hat{\Psi}(k) \cdot e^{jk\Omega_0 t/\mu}\right) \cdot \left(\sum_{n=-\infty}^{+\infty} \frac{\hat{\Omega}(n)}{n\Omega_0} \cdot e^{jn\Omega_0 t/\mu}\right) \tag{4.31}$$

The first term is equal to the constant speed flux Ψ_0. The second term is the product of two Fourier series with the same periodicity $2\pi\mu/\Omega_0$. This second term can therefore be rewritten as a single Fourier series and will be called the ripple-induced flux Ψ_v, which results in:

$$\begin{aligned}\Psi(t) &= \sum_{k=-\infty}^{+\infty} \hat{\Psi}(k) \cdot e^{jk\Omega_0 t/\mu} + \sum_{v=-\infty}^{+\infty} \hat{\Psi}_v(v) \cdot e^{jv\Omega_0 t/\mu} \\ &= \quad \Psi_0(t) \quad + \quad \Psi_v(t) \end{aligned} \tag{4.32}$$

The Fourier coefficients $\hat{\Psi}_v(v)$ of the ripple-induced flux are calculated with a discrete convolution or Cauchy product:

$$\begin{aligned}\hat{\Psi}_v(v) &= -\left(k\hat{\Psi}(k)\right) * \left(\frac{\hat{\Omega}(n)}{n\Omega_0}\right) \\ &= -\sum_{s=-\infty}^{+\infty} \frac{s}{v-s} \cdot \hat{\Psi}(s) \cdot \frac{\hat{\Omega}(v-s)}{\Omega_0} \end{aligned} \tag{4.33}$$

The superposition of the flux as the sum of the classical constant-speed flux and an additional ripple-induced flux is an elegant and convenient result. More specifically, the combination of a constant speed flux harmonic with order k and a speed ripple with order n causes one flux harmonic with order $k+n$ and one with order $k-n$.

The back-emf E can also be split up into two parts, i.e., the classical constant-speed term E_0 and a ripple-induced term E_v:

$$\begin{aligned}E(t) &= \sum_{k=-\infty}^{+\infty} \frac{jk\Omega_0}{\mu}\, \hat{\Psi}(k)\, e^{j\frac{k\Omega_0}{\mu}t} + \sum_{v=-\infty}^{+\infty} \frac{jv\Omega_0}{\mu}\, \hat{\Psi}_v(v)\, e^{j\frac{v\Omega_0}{\mu}t} \\ &= \quad E_0(t) \quad + \quad E_v(t) \end{aligned} \tag{4.34}$$

The previously drawn conclusions for the flux induced by speed ripples are equally valid for the back-emf induced by speed ripples. The only approximation made in the derivation of the model is the first order Taylor series expansion.

4.3.4 Application of the model

The model of the previous section has been programmed in Matlab and two situations are simulated. In the first situation, a speed ripple is imposed on a PMSM. In the second situation, a PMSM with a torque ripple is simulated. For both situations, the parameter μ is set at 1 so that subharmonics are not included.

Imposed speed ripple

The following speed is now imposed on the PMSM:

$$\begin{aligned} \Omega(t) &= \Omega_0 + \frac{\hat{\Omega}(N_h)}{2} \cdot e^{jN_h\Omega_0 t} + \frac{\hat{\Omega}(N_h)^*}{2} \cdot e^{-jN_h\Omega_0 t} \\ &= \Omega_0 + \hat{\Omega}(N_h) \cdot \cos(N_h\ \Omega_0\ t) \qquad (4.35) \end{aligned}$$

As in the constant-speed simulation, the speed Ω_0 is set at 750 rpm and the pole pair number N_p is set at 4. The frequency of the ripple is expressed by the order N_h, which has a value of 8. Four different simulations are performed, each with a different real-valued ripple amplitude $\hat{\Omega}(8)$, i.e., 10%, 30%, 60% and 90% of Ω_0 respectively. Although these values are unrealistic for practical situations, they allow to validate the accuracy of the model in extreme situations.

Fig. 4.8 shows the resulting flux waveforms. For each simulation, three flux waveforms are shown. The dotted line represents the constant speed flux Ψ_0, calculated by (4.28) and shown in Fig. 4.7 as well. The full line shows the real flux Ψ given by (4.30). The dashed line shows the flux $\Psi_0 + \Psi_v$, which is the flux approximated by the model, given by (4.32) and (4.33). Fig. 4.9 shows the back-emf waveforms. Again, the dotted line shows the constant speed back-emf E_0 given by (4.29), the full line shows the real back-emf E given by (4.27) and the dashed line shows the approximated back-emf $E_0 + E_v$ given by (4.34).

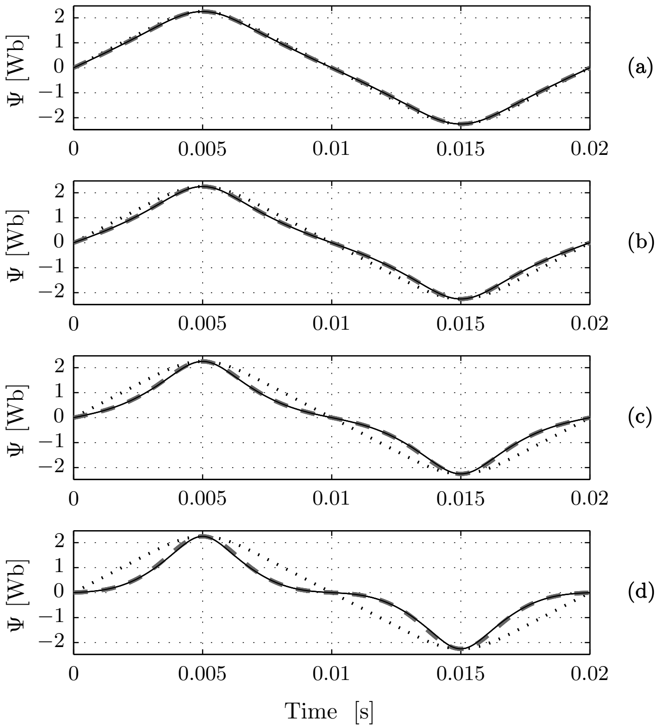

Figure 4.8: Flux waveforms for an imposed speed ripple: (a) $\hat{\Omega}(8)=0.10\ \Omega_0$, (b) $\hat{\Omega}(8)=0.30\ \Omega_0$, (c) $\hat{\Omega}(8)=0.60\ \Omega_0$, (d) $\hat{\Omega}(8)=0.90\ \Omega_0$, . . . = constant-speed waveform, – = real waveform, - - = simplified model

In situation (a), where the speed ripple is only 10%, the three flux waveforms are similar since the flux components caused by the speed ripple are small. However, in the back-emf waveforms, the effect of the ripple is visible, since E and $E_0 + E_v$ differ from E_0. The real back-emf E and the approximated back-emf $E_0 + E_v$ have a perfect match, so the model is valid in this case. In situation (b), where the ripple is 30%, a small difference between the real flux Ψ and the constant speed flux Ψ_0 can be observed. However, the difference between E and E_0 has become significant. Still, the approximated waveforms match the real waveforms accurately enough so that the model remains valid. In situation (c), where a large ripple of 60% is present, there is a considerable difference between Ψ and Ψ_0. In the back-emf

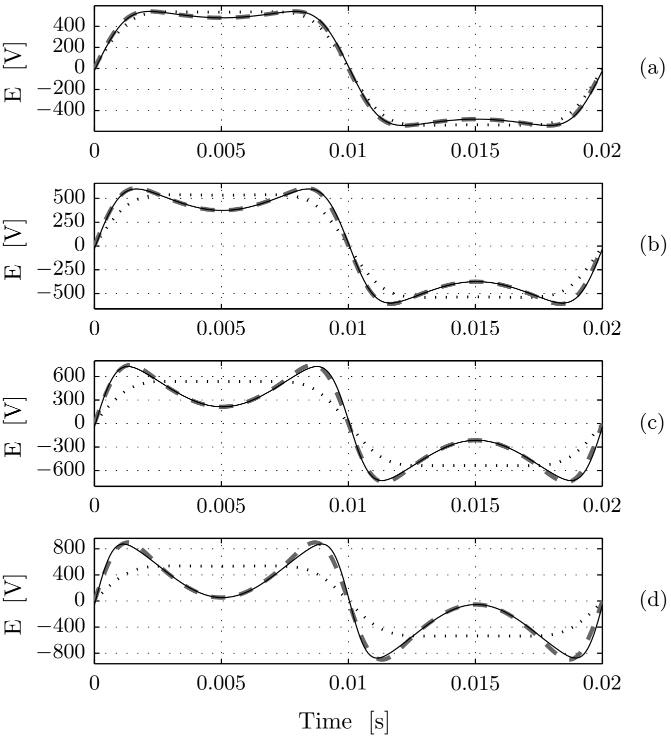

Figure 4.9: Back-emf waveforms for an imposed speed ripple: (a) $\hat{\Omega}(8)$=0.10 Ω_0, (b) $\hat{\Omega}(8)$=0.30 Ω_0, (c) $\hat{\Omega}(8)$=0.60 Ω_0, (d) $\hat{\Omega}(8)$=0.90 Ω_0, . . . = constant-speed waveform, – = real waveform, - - = simplified model

waveforms, the real waveform E and the constant speed waveform E_0 have a large deviation since the ripple-induced back-emf E_v has an important influence. Despite the large speed ripple, the approximated waveforms are still close to the real waveforms. In situation (d), an extreme speed ripple of 90% causes a large ripple-induced flux Ψ_v and back-emf E_v. Although a speed ripple of 90% has no practical relevance, it remains interesting to simulate this case in order to validate the mathematical accuracy of the model. In the back-emf, a small difference is noticeable between the model and the real waveform, which could be expected since the Taylor approximation is only valid for small ripples. However, the model still corresponds very well with the real waveform. Thus, the approximation made for the model remains valid even for extreme speed ripples.

The ripple in the speed Ω has an order k of 8. The constant-speed flux Ψ_0 includes components with an order n of 4, 12, 20 and 28. The ripple flux Ψ_v includes components with an order v of 4, 12, 20, 28 and 36. This confirms that the orders v result from combining the orders k and n as $k \pm n$.

The previous simulation has shown how a speed ripple can influence the waveforms of the flux and the back-emf. It has also shown the validity of the model. Only for extreme ripples, the model is no longer valid. The simulation however has only shown the particular case of an order N_h equal to 8. Therefore, these simulations will now be repeated for other orders and amplitudes, which allows to make a more general conclusion concerning the accuracy. The accuracy will be quantified by calculating the root mean square of the difference between the actual waveform and the constant speed waveform:

$$\delta_\Psi = \frac{1}{\Psi_{0,\mathrm{rms}}} \cdot \sqrt{\frac{1}{T} \int_0^T (\Psi - \Psi_0)^2 \, dt} \tag{4.36}$$

$$\delta_E = \frac{1}{E_{0,\mathrm{rms}}} \cdot \sqrt{\frac{1}{T} \int_0^T (E - E_0)^2 \, dt} \tag{4.37}$$

Due to (4.32) and (4.34), these quantities equal the rms value of the flux and back-emf components caused by the speed ripples. They are divided by the rms values $\Psi_{0,\mathrm{rms}}$ and $E_{0,\mathrm{rms}}$, so that δ_Ψ and δ_E are relative quantities. A high value of δ means that the ripple causes a large deviation between the real waveform and the constant-speed waveform.

Fig. 4.10 shows both δ_Ψ and δ_E in function of the ripple amplitude $\hat{\Omega}_h$ for different orders N_h as defined in (4.35). This calculation shows that the accuracy of the model decreases for large ripple amplitudes $\hat{\Omega}_h$, which is expected since the argument of the exponential function in (4.30) becomes large so that the Taylor approximation loses accuracy. Nevertheless, the calculation shows that the model has a high overall accuracy.

Fig. 4.11 shows both δ_Ψ and δ_E in function of discrete values of the order N_h for different ripple amplitudes $\hat{\Omega}_h$. The values calculated

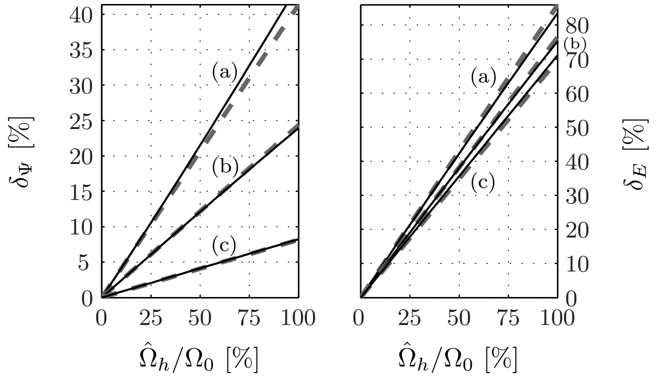

Figure 4.10: δ_Ψ and δ_E in function of the ripple amplitude $\hat{\Omega}_h$: (a) N_h=7, (b) N_h=12, (c) N_h=35, – = Calculated from real Ψ and E, - - = Calculated from approximated Ψ and E

from the model have a perfect agreement with the real values if the order N_h is sufficiently large. For small values of N_h, the accuracy is reduced, which can be explained by the limited validity of the Taylor approximation.

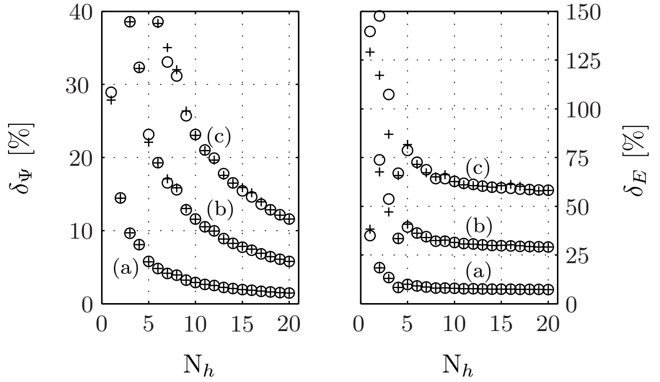

Figure 4.11: δ_Ψ and δ_E in function of the order N_h: (a) $\hat{\Omega}_h$=10%, (b) $\hat{\Omega}_h$=40%, (c) $\hat{\Omega}_h$=80%, + = Calculated from real Ψ and E, ○ = Calculated from approximated Ψ and E

It is concluded that the simplified model has a high accuracy when compared to the real waveforms. Also, it offers a significant improvement when compared to the constant-speed model and is thus capable of accurately predicting the back-emf of a PMSM in the presence of speed ripples.

Torque ripple

The concept of the ripple-induced flux and ripple-induced back-emf will now be applied on a PMSM connected to a constant-torque load. This load ensures that the speed ripples are only caused by the PMSM itself. Torque ripples are often present in PMSMs and have been widely discussed in literature, since they can have a negative effect on certain loads [109–111]. Torque ripples arise for example when sinusoidal currents are injected into a brushless motor with harmonics in the back-emf. The back-emf harmonics cause ripples in the mechanical power and, thus, also in the torque. The torque of the PMSM will be calculated from the speed, the back-emf and current waveforms of the three phases by using:

$$T = \frac{E_a\ I_a + E_b\ I_b + E_c\ I_c}{\Omega} \tag{4.38}$$

A sinusoidal current with an amplitude of 10 A, in phase with the fundamental component of the back-emf, will be imposed on the machine. This can be achieved in practice with a current-controlled converter and an encoder as a position sensor, resulting in a field-oriented situation [112]. The current waveform used here is representative for a practical vector-controlled drive, as it also contains the switching ripple. This current waveform was obtained by simulating the vector-controlled drive with a switching frequency of 5 kHz connected to the PMSM with the machine parameters of [85]. The effect of this current ripple on the torque, speed and subsequently back-emf waveform will also be discussed here.

The mean speed Ω_0 is set at 750 rpm and N_p equals 4. It is assumed that the torque of the constant-torque load equals the average torque $\bar{T}$ of the PMSM, which is the case in steady-state. The speed ripples can be calculated from the mechanical equation:

$$\Omega = \Omega_0 + \frac{1}{J}\int (T - \bar{T})dt \tag{4.39}$$

The goal of the simulation is to show that the torque ripple is influenced by including the impact of ripples on the back-emf. Therefore, the torque ripple with and without the ripple-induced back-emf will be calculated and compared. For this, the inertia J is set at a low value of 0.001 kgm^2 to make the effect clearly visible.

Fig. 4.12 shows the resulting speed, current waveforms, back-emf and torque. The current waveforms are sinusoidal with a current ripple. The combination of these current waveforms with the back-emf harmonics, clearly causes torque ripples.

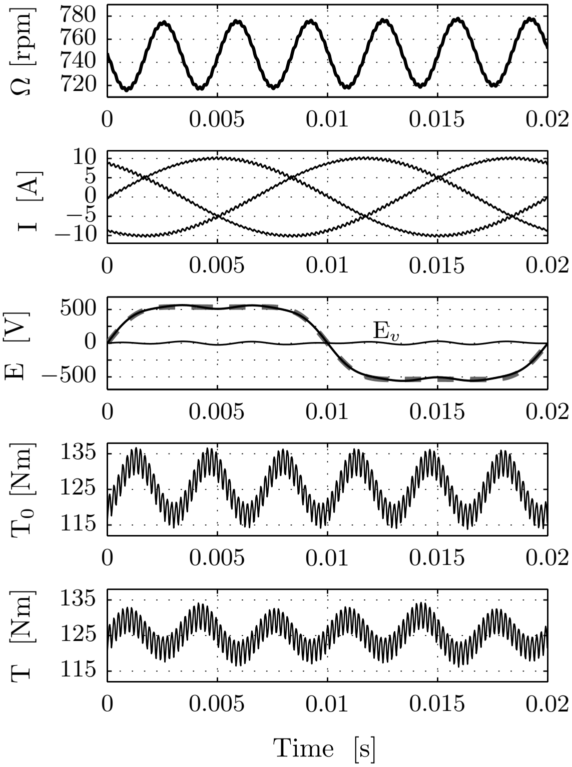

Figure 4.12: PMSM with torque ripple: speed Ω, currents I, back-emf E, torques T_0 and T; - - = neglecting speed ripples, – = including speed ripples

The torque waveforms contain a nearly sinusoidal low-frequent ripple component, caused by the dominant third harmonic in the flux and back-emf, and a high-frequent ripple caused by the switching ripple. The low-frequent torque ripple causes a speed ripple which is also nearly sinusoidal. On the other hand, the high-frequent torque ripple has a limited impact on the speed as it is more effectively filtered by the inertia.

The constant-speed back-emf E_0 is shown as a grey dashed line while the real back-emf E is shown as a black full line. E diverts from E_0 due to the speed ripples. To further clarify this, the waveform E_v (calculated as $E - E_0$) is also shown. For the first torque waveform T_0, the constant-speed back-emf E_0 and the real speed Ω were used in (4.38). The torque T_0 can therefore be interpreted as the result of the classical approach, where the impact of speed ripples on the back-emf is neglected. For the second torque waveform T, the real back-emf E and the real speed Ω were used. The torque T can therefore be interpreted as the real torque which would occur in practice. T clearly diverts from T_0 due to the speed ripples.

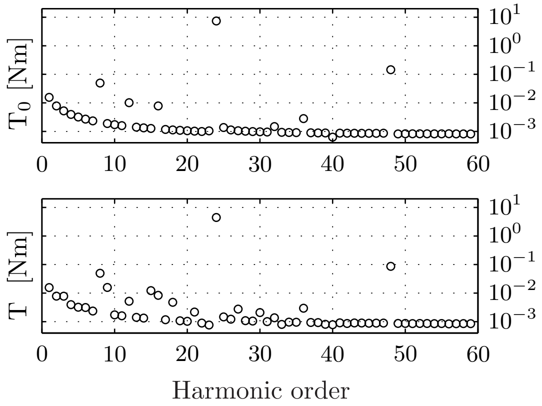

Figure 4.13: Fourier amplitude spectrum of T_0 and T on a logarithmic scale

Both T_0 and T have the same fundamental frequency. However, the amplitude and phase are changed by taking into account the effect of the speed ripples. The fundamental torque ripples of T_0 and T have an amplitude of 7.38 Nm and 4.46 Nm respectively. Fig. 4.13 shows a Fourier amplitude spectrum of T and T_0 on a logarithmic scale. These data were calculated with a Fast Fourier Transform algorithm applied on the waveforms of T_0 and T with a high sampling frequency of 50 MHz. Both T_0 and T have two dominant components, i.e., 24 and 48, which is expected for a three-phase machine with 4 pole pairs and a third harmonic in the back-emf since the order of the torque ripples can be calculated as $3(k \pm 1)N_p$. Both dominant components are affected by the speed ripples. The other components have a smaller amplitude, i.e., mostly below 10^{-2} Nm. Nevertheless, these components are also slightly affected by the speed ripples.

4.4 Impact of speed ripples on armature reaction

The armature reaction voltages are induced by the flux caused by the stator currents and the stator self-inductance. As shown in Fig. 2.7, these voltages are of the form:

$$v = \Omega\ L\ i \tag{4.40}$$

It is clear that a rotor speed ripple directly causes additional harmonics in the voltage. Since practical rotor speed ripples are small, these harmonics are expected to be small as well. Also, the magnet back-emfs are much larger than the armature reaction, which reduces the effect on the total voltage.

To validate this presumption, a simplified case will be simulated here. A realistic rotor speed ripple will be imposed on a PMSM with a sinusoidal magnet back-emf and sinusoidal field-oriented currents. The back-emf has a phase rms value of 230 V. The current amplitude is chosen so that the mechanical power is 5 kW, i.e., a constant current of 10.248 A in the q-axis and 0A in the d-axis. The rotor speed has an average of 1500 rpm with a sinusoidal ripple of 0.047%, which is the largest ripple found in the simulation of the Vestas V164 in §4.2.4. The inductances L_q and L_d are both set at 50 mH, which is a fairly high value.

Fig. 4.14 shows the total back-emf in a stationary reference frame with and without the rotor speed ripple. It is clear that there is no difference visible between both waveforms. Therefore, Fig. 4.15 shows the difference between both waves for each phase. Here, the effect is more clear. The additional voltage waveform caused by the speed ripple reaches a maximum value of 38mV, which is 0.12% of the amplitude of the fundamental component.

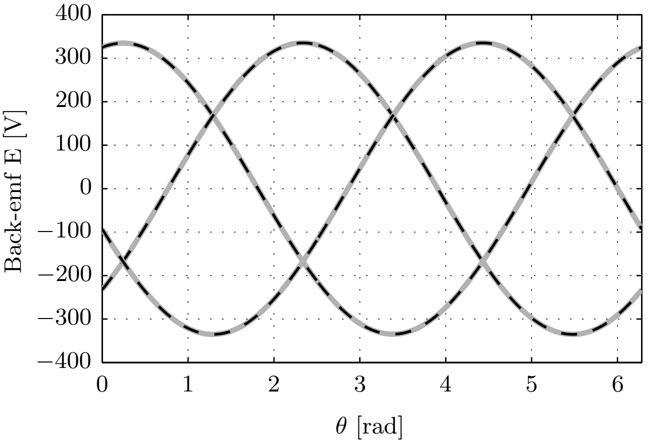

Figure 4.14: Total back-emf: Grey full line = without speed ripple, Black dashed line = with speed ripple

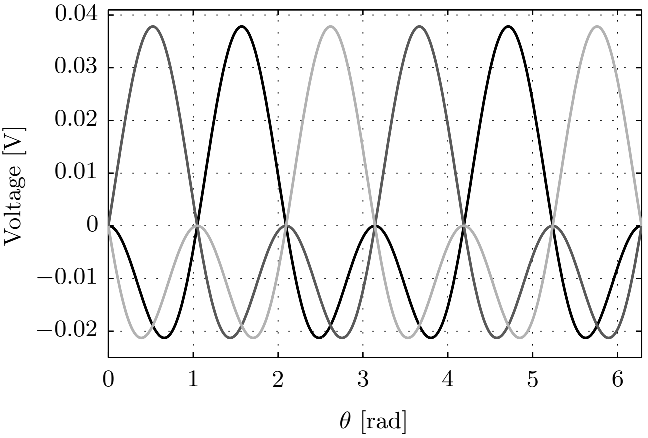

Figure 4.15: Additional back-emf due to the speed ripple

The simulation validates that the impact of a speed ripple on the back-emf is small, but it is not entirely negligible. A harmonic of 0.12% can be in the same order of magnitude as certain higher order harmonics of the magnet back-emf. This influences the optimal current waveforms as determined by the new waveform shaping method presented in §3.3. Theoretically, it would be possible to include this effect in the determination of the optimal current waveforms. However, it is not considered to be worthwhile to take this into account in the scope of this work. It is expected that the impact on the losses is negligible and therefore will not be discussed further. Nevertheless, it must be noted that it is feasable, but complex, to take this effect into account in the analysis presented in chapter 5.

4.5 Conclusions

In this chapter, the impact of rotor speed ripples on the harmonics of the back-emf waveform was investigated. First, the torque dips caused by tower shadow and wind shear in a wind turbine were simulated to obtain the speed ripples. Although the torque dips can be significant, the inertia of the turbine succesfully attenuates the speed ripples, which have an amplitude between 0.0001% and 0.05%.

Then, the relation between speed ripples and harmonics in the magnet back-emf was investigated. A mathematical model was developed to calculate these harmonics. Simulations have shown that the model is accurate, even for strong ripples. The model also shows that a speed ripple must have a high amplitude to cause any effect on the waveform of the magnet back-emf.

Speed ripples also affect the armature reaction, which is part of the total back-emf voltage. The Vestas V164 had the strongest speed ripple of all simulations in this chapter, with an amplitude of 0.047%. A sinusoidal ripple with the same amplitude was imposed on a PMSM with a sinusoidal magnet back-emf. In simulation, the speed ripple caused a change of 0.12% in the total back-emf. Although this impact is small, it is not entirely negligible. However, it was discussed that the effect is not worthwhile to take into account as the effect on the optimal current waveform and the losses would be minimal, while the mathematical complexity would be considerable.

It can be concluded that, theoretically, speed ripples can affect the back-emf waveform. However, the magnitude of realistic speed ripples in a wind turbine is so small that this effect is negligible. Therefore, it was justified in chapter 3 to assume that the back-emf waveform is fixed and independent of the current waveform.

The developed model for the ripple-induced harmonics in the magnet back-emf will no longer be used in this work, as the effect can be neglected in the application of wind turbines. However, the model could prove to be useful in other applications such as conveyor belts or piston pumps. These applications are outside the scope of this work and will not be discussed.

5

ADVANCED OPTIMAL CURRENT WAVEFORM SHAPING

The new current waveform shaping technique was presented in chapter 3, where it was applied on a simplified machine model. Here, the technique is applied on the more advanced complete machine model step by step, going much further than the state of the art techniques found in literature. A case study and parameter sensitivity analysis are performed. Also, the developed technique is applied on a wind turbine system.

Contents

5.1 Introduction

The basic optimal current waveform shaping technique based on the Cauchy-Schwarz inequality was presented in chapter 3. The main conclusion was that the optimal current waveform is proportional to the given back-emf waveform. This so-called ‘proportional current waveform’ maximises the efficiency.

The proof given in chapter 3 is only valid for a fixed back-emf waveform, while in reality this back-emf waveform depends on speed ripples and on the current waveform due to the armature reaction effect. The impact of speed ripples on the back-emf was discussed in chapter 4. It was shown that speed ripples are small in practice, just as their impact on the back-emf. Therefore, the back-emf waveform will be assumed to be solely dependent on the average rotor speed, not on the speed ripples. However, the dependence of the back-emf on the current waveform due to the armature reaction effect cannot be neglected and will be dealt with in this chapter.

Besides being complex and cumbersome, the state-of-the-art waveform shaping techniques in literature often neglect important effects in the PMSM, such as the armature reaction, the reluctance effect and the iron losses. In literature, these effects were neglected to keep the technique mathematically feasable. In this chapter, the Cauchy-Schwarz method will be applied on a PMSM while including these effects. Certain mathematical manipulations will be needed to maintain the applicability of the Cauchy-Schwarz method. By including these effects, higher efficiencies will be reached with the optimal waveform, since the model is a more realistic representation of a PMSM.

The determination of the optimal waveforms will consist of two steps. In step one, analytical optimal current waveform equations are obtained with the Cauchy-Schwarz method. These equations will contain three scale factors, one for each axis in the machine. In step two, the optimal relation between these three factors is obtained numerically. The main advantage of this method is that, in the first step, the problem is transformed from optimising time-domain waveforms to simple constants. This greatly simplifies the numerical part in step two, where these constants are optimised. The numerical optimisation is deliberately discussed in a separate section to maintain focus on the waveform optimisation in the first part of the chapter.

Also, the zero-sequence component will be taken into account here. In literature, it was always assumed that no neutral connection is available, so that zero-sequence currents cannot flow in the machine. Since most optimal current waveform techniques use the frequency domain, this implies that the 3rd order harmonic and all its multiples are set zero. This reduces the amount of parameters which must be calculated. Here, using a time domain approach, this assumption is not needed. Therefore, the zero-sequence component is included in the analysis, which leads to a current waveform that can further reduce the losses. When the optimal current waveform method is applied in practice, the zero-sequence components can be set to zero if a neutral connection is not available, although the waveform will be suboptimal in that case.

The goal of this chapter is to develop a new optimal current waveform technique which needs less assumptions and simplifications than existing techniques in literature. Also, it should be generally applicable, i.e., written in a closed analytic form.

5.2 Optimal current waveform equations

5.2.1 Application on a basic PMSM model

The PMSM model in a rotating reference frame was derived in chapter 2. First, the optimal current waveform equations will be determined for a simplified model, including the reluctance effect, unbalance and the zero-sequence component but neglecting armature reaction and iron losses. This simplified model is shown in Fig. 5.1. The reluctance effect is embedded in the fact that a *qd* system is used, where L_d is not necessarily equal to L_q.

Since the 0, q and d schemes are decoupled in this model, the application of the Cauchy-Schwarz technique is straightforward. In this case, the optimal current waveform equations are:

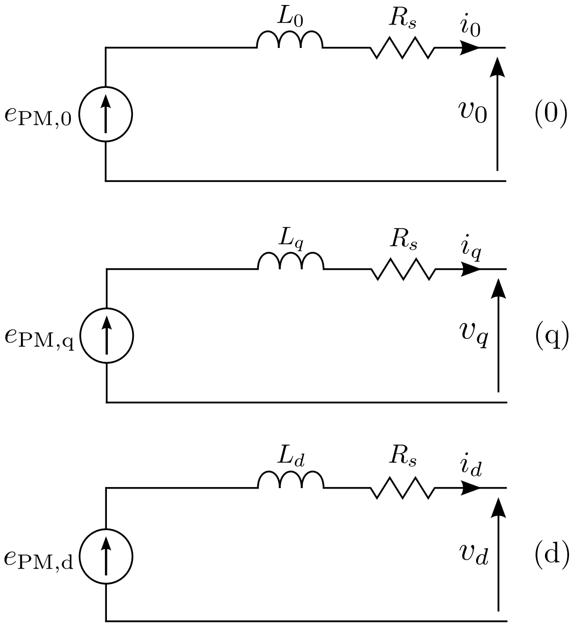

Figure 5.1: Simplified PMSM model in a rotating reference frame

$$i_0 = G_0 \cdot e_{\mathrm{PM},0} \tag{5.1}$$

$$i_\mathrm{q} = G_\mathrm{q} \cdot e_{\mathrm{PM},\mathrm{q}} \tag{5.2}$$

$$i_\mathrm{d} = G_\mathrm{d} \cdot e_{\mathrm{PM},\mathrm{d}} \tag{5.3}$$

Two substitions are now performed which will prove to be advantageous later. The back-emf functions are proportional to the rotor speed Ω. The first substitution replaces these back-emfs by the product of the rotor speed and flux functions:

$$e_{\mathrm{PM},0} = \Omega\ \varphi_0 \qquad e_{\mathrm{PM},\mathrm{q}} = \Omega\ \varphi_\mathrm{q} \qquad e_{\mathrm{PM},\mathrm{d}} = \Omega\ \varphi_\mathrm{d} \tag{5.4}$$

The second substitution replaces the scale factors G_0, G_q and G_d:

$$G_0' = G_0\ \Omega \qquad G_\mathrm{q}' = G_\mathrm{q}\ \Omega \qquad G_\mathrm{d}' = G_\mathrm{d}\ \Omega \tag{5.5}$$

This substitution is justified since the scale factor in the Cauchy-Schwarz method is arbitrary, as long as it is a constant.

These substitutions result in the following optimal current waveform equations:

$$i_0 = G'_0 \cdot \varphi_0 \tag{5.6}$$

$$i_\mathrm{q} = G'_\mathrm{q} \cdot \varphi_\mathrm{q} \tag{5.7}$$

$$i_\mathrm{d} = G'_\mathrm{d} \cdot \varphi_\mathrm{d} \tag{5.8}$$

The theorem has been applied on each scheme separately, resulting in a proportional current waveform for each. However, each scheme has its own scale factor. The relation between these factors must be determined by optimising the three schemes together, under the constraint that a certain power or torque must be obtained. In contrast with waveform shaping methods in literature, here, the optimisation process regards optimising three constants instead of a large array of amplitudes and phases of the different harmonic components, which offers a considerable simplification. The optimisation process will be explained in §5.4.

Although a simplified PMSM model was used here to determine the optimal current waveforms, the model did take into account more effects than most papers on the topic. In literature, the PMSM is simply modeled by a back-emf waveform in series with an inductance and a resistance [81, 83, 89, 92], which was also done in the proof of concept in chapter 3, paragraph §3.3.2. In contrast, the simplified model used here includes the zero-sequence component and the reluctance effect. Also, there is no limitation on the amount of harmonic components in the waveforms.

The realism of the used machine model has a direct impact on the accuracy of the optimal current waveforms, leading to a higher efficiency when a more advanced model is used. This is the most notable difference between classical current waveform shaping techniques in literature and the research done here. This will become more clear later in this chapter, when the optimal current waveforms are determined for the complete PMSM model, including armature reaction and iron losses.

5.2.2 Including the iron losses

Now, the iron losses are included in the analysis, while the armature reaction is still neglected. Including the iron losses results in a considerable increased realism of the total losses. The iron losses together with the copper losses form the lion's share of the total losses in a PMSM [113], i.e., about 90% - 98%. In [113], about 50% - 70% of the total losses are copper losses. However, the ratio of copper versus iron losses differs greatly between machines and is often a compromise made during the design process. The remaining losses in a PMSM are magnet losses, i.e., caused by eddy currents in the magnets. These eddy currents are induced since a permanent magnet never has an ideal infinite magnetic permeability. Due to their limited share in the total losses, the magnet losses are not included in the analysis here. They are mentioned in chapter 8 as a future research topic.

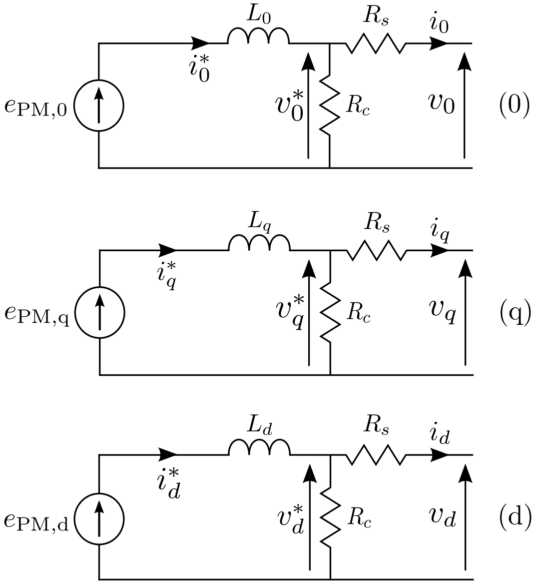

Figure 5.2: PMSM model including iron losses

Fig. 5.2 shows the equivalent scheme of the PMSM including the equivalent iron loss resistance R_c. The iron loss resistance forms a parallel branch in the schemes, so that the Cauchy-Schwarz theorem cannot be applied directly. However, Thévenin-equivalents can be determined for each axis. Then, the optimal current waveform is proportional to the Thévenin-voltage. The Thévenin-impedances are not determined here since they are irrelevant for the determination of the current waveforms. The Thévenin-voltages are given by:

$$e_{\mathrm{Th,0}} = \frac{R_c}{R_c + sL_0}\, e_{\mathrm{PM,0}} \tag{5.9}$$

$$e_{\mathrm{Th,q}} = \frac{R_c}{R_c + sL_q}\, e_{\mathrm{PM,q}} \tag{5.10}$$

$$e_{\mathrm{Th,d}} = \frac{R_c}{R_c + sL_d}\, e_{\mathrm{PM,d}} \tag{5.11}$$

The voltage divider forms the transfer function of a low-pass filter with ‘s’ as the Laplace operator. In other words, the iron loss resistance acts as a low-pass filter on the back-emf. The transfer functions can be rewritten by introducing the following time-constants, which depend on the rotor speed:

$$\tau_0 = \frac{L_0}{R_c} = \frac{K_h + K_f\Omega}{\Omega}\, L_0 \tag{5.12}$$

$$\tau_q = \frac{L_q}{R_c} = \frac{K_h + K_f\Omega}{\Omega}\, L_q \tag{5.13}$$

$$\tau_d = \frac{L_d}{R_c} = \frac{K_h + K_f\Omega}{\Omega}\, L_d \tag{5.14}$$

The two previously introduced substitutions (5.4) and (5.5) are performed as well, resulting in the following optimal current waveform equations:

$$i_0 = G_0'\, \frac{1}{1 + s\tau_0}\, \varphi_0 \tag{5.15}$$

$$i_q = G_q'\, \frac{1}{1 + s\tau_q}\, \varphi_{\mathrm{q}} \tag{5.16}$$

$$i_d = G_d'\, \frac{1}{1 + s\tau_d}\, \varphi_{\mathrm{d}} \tag{5.17}$$

The equations show that the optimal current waveforms are now a filtered version of the flux waveforms due to the iron losses. The transfer function is a simple first-order low-pass filter, which is easy to implement in a controller as a difference equation in discrete time.

By including the iron losses in the analysis, the resulting optimal current waveforms have a reduced harmonic content.

The cut-off frequency of the filters is of the form:

$$f_{\mathrm{co}} = \frac{1}{2\pi\tau} = \frac{R_c}{2\pi L} \tag{5.18}$$

Typically, this frequency has a high value, as will be shown in the case study later in this chapter. The consequence is that the filter merely attenuates high order harmonics. Therefore, the waveform is not significantly changed by the filter in most situations.

It can be concluded that the optimal current waveform including iron losses can be determined by using Thévenin equivalents. The effect of the iron losses is a low-pass filter in the optimal current waveforms, attenuating higher order harmonics.

5.2.3 Including the armature reaction back-emf

The optimal current waveform equations are now derived including the armature reaction back-emf, but neglecting the iron losses. Later, both iron losses and armature reaction will be included. Fig. 5.3 shows the equivalent scheme of the PMSM with the armature reaction back-emf.

The zero sequence scheme is again decoupled from the q and d schemes. Therefore, the optimal current waveform for the zero-sequence component is:

$$i_0 = G_0 \; e_{\mathrm{PM},0} \tag{5.19}$$

The q and d schemes are now coupled by the armature reaction, which causes an additional back-emf component. In the q scheme, the i_{d} current can be assumed to be given and fixed, i.e., independent of i_{q}. Then, the armature reaction back-emf can be seen as an additional fixed and given voltage. This allows to apply the Cauchy-Schwarz method in the q scheme. The same assumption can be made for the d scheme. This results in the following optimal current waveforms equations for the q and d axis:

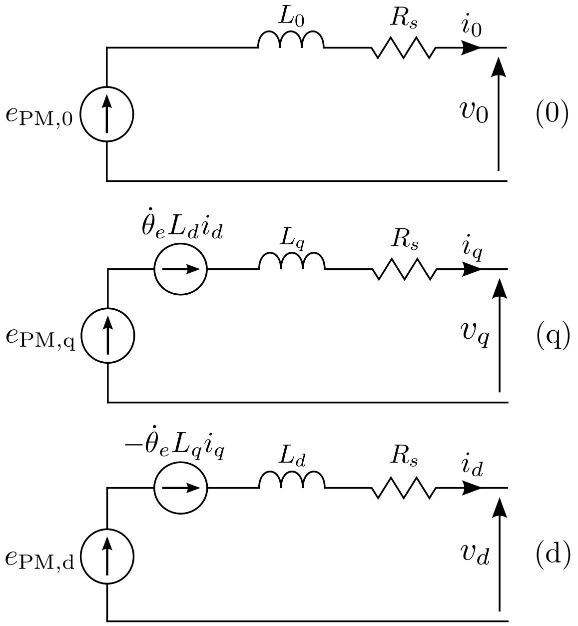

Figure 5.3: PMSM model including the armature reaction back-emf

$$i_{\mathrm{q}} = G_{\mathrm{q}}\ (e_{\mathrm{PM,q}} + \Omega L_d i_{\mathrm{d}}) \tag{5.20}$$

$$i_{\mathrm{d}} = G_{\mathrm{d}}\ (e_{\mathrm{PM,d}} - \Omega L_q i_{\mathrm{q}}) \tag{5.21}$$

Both equations can be separated, which gives independent solutions for i_{q} and i_{d}. Together with the zero-sequence component, this results in the following set of optimal current waveform equations:

$$i_0 = G_0\ e_{\mathrm{PM,0}} \tag{5.22}$$

$$i_{\mathrm{q}} = \frac{G_{\mathrm{q}}}{1 + G_{\mathrm{d}} G_{\mathrm{q}} \Omega^2 L_q L_d}\ (e_{\mathrm{PM,q}} + G_{\mathrm{d}} \Omega L_d\ e_{\mathrm{PM,d}}) \tag{5.23}$$

$$i_{\mathrm{d}} = \frac{G_{\mathrm{d}}}{1 + G_{\mathrm{d}} G_{\mathrm{q}} \Omega^2 L_q L_d}\ (e_{\mathrm{PM,d}} - G_{\mathrm{q}} \Omega L_q\ e_{\mathrm{PM,q}}) \tag{5.24}$$

By performing the two substitutions (5.4) and (5.5), the equations simplify to:

$$\begin{aligned} i_0 &= G'_0 \ \varphi_0 && (5.25)\\ i_\mathrm{q} &= \frac{G'_\mathrm{q}}{1+G'_\mathrm{d}G'_\mathrm{q}L_dL_q}\ (\varphi_\mathrm{q} + G'_\mathrm{d}\ L_d\ \varphi_\mathrm{d}) && (5.26)\\ i_\mathrm{d} &= \frac{G'_\mathrm{d}}{1+G'_\mathrm{d}G'_\mathrm{q}L_dL_q}\ (\varphi_\mathrm{d} - G'_\mathrm{q}\ L_q\ \varphi_\mathrm{q}) && (5.27) \end{aligned}$$

Due to the substitutions, the rotor speed has disappeared from the equations. The effect of including the armature reaction back-emf is that the q and d currents are now determined as a weighted sum of the flux functions in the q and d axis.

5.2.4 Application on the complete PMSM model

In this chapter, the Cauchy-Schwarz method was first applied on a basic PMSM model, neglecting the armature reaction back-emf and the iron losses. Then, both effects were investigated separately in order to include them in the analysis. Now, the optimal current waveform equations are derived for the complete PMSM model including both effects. The complete model is shown in Fig. 5.4.

The Cauchy-Schwarz method is applied on the Thévenin equivalents to cope with the parallel branch of the iron losses. The optimal current equations in the q and d axis are coupled by the armature reaction, but can be rewritten as shown previously. Finally, the substitutions (5.4) and (5.5) are performed to simplify the equations. The optimal current waveform equations for the complete PMSM model are:

$$i_0 = G'_0 \ \frac{1}{1+s\tau_0}\ \varphi_0 \tag{5.28}$$

$$i_\mathrm{q} = \frac{G'_\mathrm{q}(1+s\tau_d)}{(1+s\tau_q)(1+s\tau_d)+G'_\mathrm{d}G'_\mathrm{q}L_dL_q}\left(\varphi_\mathrm{q} + \frac{G'_\mathrm{d}\ L_d}{1+s\tau_d}\ \varphi_\mathrm{d}\right) \tag{5.29}$$

$$i_\mathrm{d} = \frac{G'_\mathrm{d}(1+s\tau_q)}{(1+s\tau_q)(1+s\tau_d)+G'_\mathrm{d}G'_\mathrm{q}L_dL_q}\left(\varphi_\mathrm{d} - \frac{G'_\mathrm{q}\ L_q}{1+s\tau_q}\ \varphi_\mathrm{q}\right) \tag{5.30}$$

Compared to the previous cases, the equations are more complex. As they contain a second order transfer function, the implementation in a digital controller becomes more complex. Still, the implementation

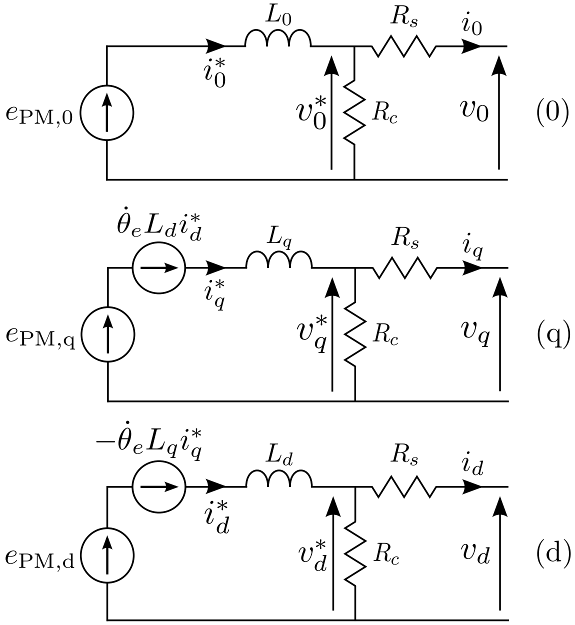

Figure 5.4: Complete PMSM model

is feasible with limited programming effort.

Compared to waveform shaping techniques in literature, a far more advanced PMSM model was used here, including zero-sequence components, the reluctance effect, armature reaction and iron losses. These effects can be included in the optimal waveforms since the method presented here is based on the time domain instead of the frequency domain. By using a more advanced and realistic PMSM model, higher efficiency levels can be achieved compared with classical methods.

5.3 Analytical optimisation of scale factors

The optimal current waveform equations have been developed for several cases. However, since the machine has three subsystems in the rotating reference frame, three scale factors G_0', G_d' and G_q' are introduced in the equations. These factors still need to be mutually optimised to maximise the efficiency of the complete system for each operating point. The optimisation process can be performed analytically or numerically. The analytical optimalisation method will be shown here for the simplified PMSM model. The numerical method is shown later for the complete model.

The optimal current waveforms for the simplified PMSM model are given by:

$$i_0 = G'_0 \cdot \varphi_0 \tag{5.31}$$

$$i_\mathrm{q} = G'_\mathrm{q} \cdot \varphi_\mathrm{q} \tag{5.32}$$

$$i_\mathrm{d} = G'_\mathrm{d} \cdot \varphi_\mathrm{d} \tag{5.33}$$

The optimal relation between G'_0, G'_q and G'_d must now be determined, so that the efficiency is maximised. Also, there should be only one degree of freedom left, i.e., to determine the mechanical operating point. The optimum is found by application of the Lagrange multiplier method. The following function λ represents the copper losses:

$$\lambda(G'_0, G'_\mathrm{q}, G'_\mathrm{d}) = 3\ R_s\ i_0^2 + \frac{3}{2}\ R_s\ i_\mathrm{q}^2 + \frac{3}{2}\ R_s\ i_\mathrm{d}^2 \tag{5.34}$$

The average of the fuction λ must be minimised:

$$\frac{1}{T}\int_0^T \lambda(G'_0, G'_\mathrm{q}, G'_\mathrm{d})\ dt = 3\ G'^2_0\ A + \frac{3}{2}\ G'^2_\mathrm{q}\ B + \frac{3}{2}\ G'^2_\mathrm{d}\ C \tag{5.35}$$

The parameters A, B and C are defined as:

$$A = \frac{1}{T}\int_0^T \phi_0^2\ dt \tag{5.36}$$

$$B = \frac{1}{T}\int_0^T \phi_\mathrm{q}^2\ dt \tag{5.37}$$

$$C = \frac{1}{T}\int_0^T \phi_\mathrm{d}^2\ dt \tag{5.38}$$

The losses must be minimised under the constraint that a certain torque setpoint must be met. The torque is determined by:

$$\sigma(G'_0, G'_\mathrm{q}, G'_\mathrm{d}) = 3\ \phi_0\ i_0 + \frac{3}{2}(\phi_\mathrm{q}\ i_\mathrm{q} + \phi_\mathrm{d}\ i_\mathrm{d}) \tag{5.39}$$

The average of the function σ must be constrained, i.e., equal to the torque setpoint T_s:

$$\frac{1}{T}\int_0^T \sigma(G'_0, G'_\mathrm{q}, G'_\mathrm{d})\ dt = 3\ G'_0\ A + \frac{3}{2}(G'_\mathrm{q}\ B + G'_\mathrm{d}\ C) = T_s \quad (5.40)$$

Now that both the function to be minimised and the constraint function are defined, the Lagrange function is given by:

$$\begin{aligned}\Lambda(G'_0, G'_\mathrm{q}, G'_\mathrm{d}) = &\quad \frac{1}{T}\int_0^T \lambda\ dt + \xi\ \left[\frac{1}{T}\int_0^T \sigma\ dt - T_s\right] \quad (5.41)\\ = &\quad 3\ G'^2_0\ A + \frac{3}{2}\ G'^2_\mathrm{q}\ B + \frac{3}{2}\ G'^2_\mathrm{d}\ C\\ &\quad + \xi \cdot \left[3\ G'_0\ A + \frac{3}{2}(G'_\mathrm{q}\ B + G'_\mathrm{d}\ C) - T_s\right]\end{aligned}$$

The solutions are found by solving the following system:

$$\begin{aligned}\frac{\partial \Lambda}{\partial G'_0} &= 6\ A\ G'_0 + 3\ \xi\ A = 0\\ \frac{\partial \Lambda}{\partial G'_\mathrm{q}} &= 3\ B\ G'_\mathrm{q} + \frac{3}{2}\ \xi\ B = 0\\ \frac{\partial \Lambda}{\partial G'_\mathrm{d}} &= 3\ C\ G'_\mathrm{d} + \frac{3}{2}\ \xi\ C = 0\\ \frac{\partial \Lambda}{\partial \xi} &= 3\ A\ G'_0 + \frac{3}{2}(G'_\mathrm{q}\ B + G'_\mathrm{d}\ C) - T_s = 0 \quad (5.42)\end{aligned}$$

The first three equations show that G'_0, G'_q and G'_d must be equal:

$$G'_0 = G'_\mathrm{q} = G'_\mathrm{d} = -\frac{\xi}{2} \quad (5.43)$$

Since all scale factors are equal, they can simply be denoted by G. Then, the scale factor is proportional to the torque setpoint:

$$G = \frac{T_s}{3\ A + \frac{3}{2}\ B + \frac{3}{2}\ C} \quad (5.44)$$

When torque feedback is unavailable, this equation can be used by an open-loop torque controller to determine the needed current given a torque setpoint. In a closed loop system, it can be used as a feedforward to stabilise the controller.

The equality of the scale factors simplifies the practical implementation of the optimal current waveform technique. However, it is only valid for the simplified PMSM model, where the armature reaction effect and iron losses are neglected. As will be explained later, a numerical approach is used to optimise the scale factors for the complete PMSM model. In theory, an analytical approach is feasible on the complete PMSM model. However, including the armature reaction and iron losses considerably increases the complexity of the equations.

5.4 Numerical optimisation of scale factors

In theory, it is possible to determine an analytical solution for the optimal relation between the scale factors for more advanced PMSM models, e.g., including armature reaction and iron losses. However, the analytical expressions for the scale factors become increasingly complex as more effects are added to the model. Therefore, a numerical approach is recommended in this situation. This optimisation can be performed offline and does not have to be included in the controller.

At first sight, it may seem contradictory that numerical optimisation is needed here, while one of the key advantages of the Cauchy-Schwarz method was that numerical optimisation in the frequency domain could be avoided. However, the difference is that here, three constants are optimised, while in classical current waveform shaping methods, the amplitudes and phases of all relevant harmonic components must be determined. The amount of parameters greatly increases the required computational effort of the optimisation.

Also, classical methods require a large amount of tabulated data in the controller, i.e., the amplitudes and phases of all harmonic components. In variable speed systems, such as a wind turbine, this data must be calculated and tabulated for several operating points after which interpolation can be used. In the optimal current waveform shaping method presented in this work, only three values must be saved for each operating point, i.e., G'_0, G'_d and G'_q. The current waveforms are then constructed by the analytical equations calculated earlier, imposing no limit on the amount of harmonic components. Moreover, as will be shown later, these parameters can be accurately approximated by a polynome in function of the rotor speed. Since the constant terms in these polynomes are zero, a total of only nine values is needed, i.e., three for each subsystem. When implemented in a digital controller, this leads to more accurate results compared to interpolation, while less memory space is required.

The optimisation of the scale factors can be formulated as a constrained minimization, where the total losses are to be minimized under the constraint of a certain power or torque value. First, the optimisation algorithm itself will be explained. Then, it will be shown how the losses and torque are determined.

5.4.1 Optimisation algorithm

For a given set of scale factors G'_0, G'_q and G'_d, the current waveforms i_0, i_q and i_d can be calculated by using the optimal current waveform equations presented earlier. Which set of equations is used depends on the desired accuracy and realism. To include all effects of the complete PMSM model, equations (5.28) - (5.30) must be used.

When the current waveforms are known, the losses and torque can be calculated by using the equivalent PMSM model of Fig. 5.4. The needed equations for this calculation will be given later. For now, it is assumed that both losses and torque can be calculated for a given set of current waveforms, and thus, scale factors. The losses for one revolution of the machine are denoted by λ, which is the function whose average must be minimised. Analogously, the torque is denoted by σ, whose average must be constrained to a certain torque setpoint.

Many possible numerical algorithms exist to solve the optimisation problem, e.g., Newton, Quasi-Newton, Gradient Descent or Simplex. During this research, the Iterative Grid Search method was used. This algorithm is robust and relatively simple, leading to satisfactory computation times and accuracy. More advanced algorithms could lead to shorter computation times or an even higher accuracy, but these are not further investigated as it is outside the scope of this research.

The Iterative Grid Search algorithm can be summarised by the following three steps:

Step 1
The first step comprises the creation of a two-dimensional grid. Two arrays are defined for the scale factors G'_0 and G'_d, each with 5 elements. In the first iteration, the central value of both arrays is zero and a large step size ε is used:

$$\begin{aligned} \mathbf{G}'_0 &= \begin{bmatrix} -\varepsilon & -\frac{\varepsilon}{2} & 0 & \frac{\varepsilon}{2} & \varepsilon \end{bmatrix} \\ \mathbf{G}'_d &= \begin{bmatrix} -\varepsilon & -\frac{\varepsilon}{2} & 0 & \frac{\varepsilon}{2} & \varepsilon \end{bmatrix} \end{aligned} \qquad (5.45)$$

The step size ε must be chosen large enough so that the optimum is certainly included in the initial arrays. In the following iterations, the central value is the optimum found at the end of the previous iteration and the step size is halved:

$$\mathbf{G}'_0 = \begin{bmatrix} G'_0 - \frac{\varepsilon}{2^i} \\ G'_0 - \frac{\varepsilon}{2^{i+1}} \\ G'_0 \\ G'_0 + \frac{\varepsilon}{2^{i+1}} \\ G'_0 + \frac{\varepsilon}{2^i} \end{bmatrix}^T \qquad \mathbf{G}'_\mathrm{d} = \begin{bmatrix} G'_\mathrm{d} - \frac{\varepsilon}{2^i} \\ G'_\mathrm{d} - \frac{\varepsilon}{2^{i+1}} \\ G'_\mathrm{d} \\ G'_\mathrm{d} + \frac{\varepsilon}{2^{i+1}} \\ G'_\mathrm{d} + \frac{\varepsilon}{2^i} \end{bmatrix}^T \qquad (5.46)$$

where i is the iteration counter and G'_0 and G'_d are the optimum scale factors found in the previous iteration.

Step 2
For each of the 25 combinations of G'_0 and G'_d, an internal optimisation algorithm finds G'_q such that the torque constraint is satisfied. Starting at zero, G'_q is updated in a loop by:

$$G'_{\mathrm{q}}(n) = G'_{\mathrm{q}}(n-1) + \alpha \, \frac{T_s - \bar{\sigma}}{|T_s|} \tag{5.47}$$

The step taken in each iteration is proportional to the difference between the actual torque $\bar{\sigma}$ and the desired torque T_s. The parameter α controls the size of the steps, and thus the speed of the algorithm. However, when α is chosen too high, instability can occur and no solution is found.

The internal while loop is executed until the average of the torque function $\bar{\sigma}$ differs less than e of the torque setpoint T_s:

$$|\bar{\sigma} - T_s| < e \tag{5.48}$$

The parameter e is a small error value which determines the accuracy of the internal optimisation loop.

At the end of this step, 25 combinations of the scale factors are known which all result in the same torque. In this manner, the torque constraint is satisfied.

Step 3
For all 25 combinations of the scale factors, the average $\bar{\lambda}$ of the loss function is calculated. The combination for which $\bar{\lambda}$ is minimum, is the optimum set of scale factors. This optimum is used to construct the two arrays in step 1 of the following iteration.

The general concept of the algorithm is that a grid is constructed in which the optimum is determined. In each iteration, a new refined grid is constructed near this optimum and a new optimum is determined. This process continuous until the gradient of the losses $\bar{\lambda}$ is smaller than a certain threshold., i.e., the optimum combination of scale factors has been found.

Fig. 5.5 shows an example of the search grids for 3 iteration steps. The grid of the first step is shown in light grey and ranges from -10 to 10 centered around zero. The losses are minimal in the point (0,5). In the next step, a refined grid is constructed around (0,5) with half the size of the previous grid, shown in grey. In this grid, the losses are minimal in (2.5,5). The grid constructed after this step is shown in black. After several iterations, the optimum is determined to be the cross at (2.19,4.38).

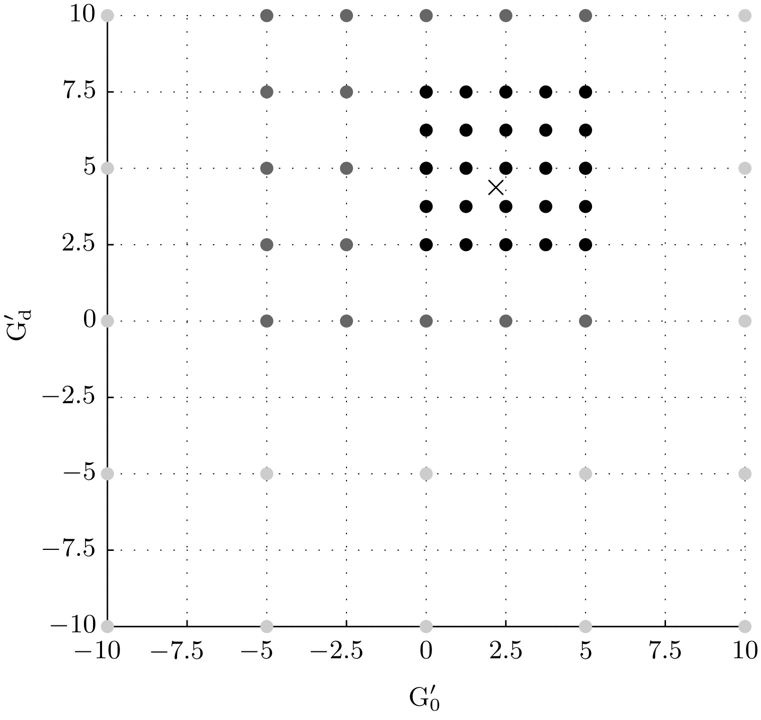

Figure 5.5: Illustration of the grid search algorithm (× = optimum)

The grid can be refined for a fixed number of iterations, or until a certain condition is satisfied. Here, the grid is refined until the decrease in losses $\bar{\lambda}$ becomes lower than a certain treshold. By setting the treshold, a compromise is made between computation time and accuracy. In the example shown above, the treshold was set at a very low value of 10 μW. The computation time was 74 s and 6 iterations were needed to find the optimum.

5.4.2 Calculation of inner currents

In the optimisation algorithm, the losses λ and the torque σ were used. In order to calculate both, the inner currents i_0^*, i_q^* and i_d^* must be written in terms of the stator currents i_0, i_q and i_d. The calculation of the losses and the torque will be explained later. First, the relation between the stator currents and the inner currents is defined.

To determine the inner currents, the Kirchhoff voltage law is written for the left loop of each subsystem in Fig. 5.4:

$$\begin{aligned}
\Omega\varphi_0 &= sL_0 i_0^* + R_c(i_0^* - i_0) \\
\Omega\varphi_\mathrm{q} &= -\Omega L_d i_d^* + sL_q i_q^* + R_c(i_q^* - i_q) \\
\Omega\varphi_\mathrm{d} &= \Omega L_q i_q^* + sL_d i_d^* + R_c(i_d^* - i_d)
\end{aligned} \tag{5.49}$$

From the first equation, the zero-sequence component can be directly calculated:

$$i_0^* = \frac{1}{1+s\tau_0}\left(i_0 + \frac{\Omega}{R_c}\varphi_0\right) \tag{5.50}$$

The equations for the q and d axis are coupled due to the armature reaction effect. They are written in matrix-form as:

$$\begin{bmatrix} 1+s\tau_q & -\Omega\tau_d \\ \Omega\tau_q & 1+s\tau_d \end{bmatrix} \cdot \begin{bmatrix} i_q^* \\ i_d^* \end{bmatrix} = \begin{bmatrix} i_q + \frac{\Omega}{R_c}\varphi_\mathrm{q} \\ i_d + \frac{\Omega}{R_c}\varphi_\mathrm{d} \end{bmatrix} \tag{5.51}$$

By inverting the 2 by 2 matrix on the left-hand side, the inner currents i_q^* and i_d^* can be calculated:

$$\begin{bmatrix} i_q^* \\ i_d^* \end{bmatrix} = \frac{1}{D} \cdot \begin{bmatrix} 1+s\tau_d & \Omega\tau_d \\ -\Omega\tau_q & 1+s\tau_q \end{bmatrix} \cdot \begin{bmatrix} i_q + \frac{\Omega}{R_c}\varphi_\mathrm{q} \\ i_d + \frac{\Omega}{R_c}\varphi_\mathrm{d} \end{bmatrix} \tag{5.52}$$

The determinant D is a second order polynome of the Laplace operator:

$$D = \tau_q\tau_d s^2 + (\tau_q + \tau_d)s + 1 + \Omega^2\tau_q\tau_d \tag{5.53}$$

These equations are implemented in Matlab by defining transfer functions in the continuous time domain. Then, they are transformed to the discrete time domain and applied on the stator current and flux waveforms, which are discrete time series.

5.4.3 Loss function λ

In the optimisation algorithm explained earlier, the average of the losses $\bar{\lambda}$ was minimized by optimising the scale factors G'_0, G'_d and G'_q. Now, it is explained how the losses can be calculated for a given set of scale factors. These losses vary with time and are periodic. It is the average of this periodic function which is minimized in the optimisation algorithm.

For a given set of scale factors, the stator current waveforms can be calculated by using the optimal current waveform equations developed in §5.2. These waveforms can then be used to calculate the inner current waveforms. The losses λ are calculated by:

$$\begin{aligned}\lambda(i_0, i_q, i_d) &= 3R_s i_0^2 + 3R_c\left(i_0^* - i_0\right)^2 \\ &+ \frac{3}{2}R_s i_q^2 + \frac{3}{2}R_c\left(i_q^* - i_q\right)^2 \\ &+ \frac{3}{2}R_s i_d^2 + \frac{3}{2}R_c\left(i_d^* - i_d\right)^2 \qquad (5.54)\end{aligned}$$

The equation clearly shows three terms corresponding to the copper losses and three terms corresponding to the iron losses. Alternatively, the losses can also be calculated by:

$$\lambda(i_0, i_q, i_d) = 3R_s i_0^2 + 3\frac{{v_0^*}^2}{R_c} + \frac{3}{2}R_s(i_q^2 + i_d^2) + \frac{3}{2}\frac{{v_q^*}^2 + {v_d^*}^2}{R_c} \qquad (5.55)$$

The voltages v_0^*, v_q^* and v_d^* are given by:

$$\begin{aligned}v_0^* &= \Omega\varphi_0 - sL_0 i_0^* \\ v_q^* &= \Omega\varphi_\mathrm{q} + \Omega L_d i_d^* - sL_q i_q^* \\ v_d^* &= \Omega\varphi_\mathrm{d} - \Omega L_q i_q^* - sL_d i_d^* \qquad (5.56)\end{aligned}$$

5.4.4 Torque function σ

The torque σ can be calculated by dividing the total power of the voltage sources by the rotor speed. This results in the following well-known equation:

$$\sigma(i_0, i_q, i_d) = 3\varphi_0 i_0^* + \frac{3}{2}\varphi_{\mathrm{q}} i_q^* + \frac{3}{2}\varphi_{\mathrm{d}} i_d^* + \frac{3}{2}(L_d - L_q) i_d^* i_q^* \qquad (5.57)$$

The first three terms are caused by the rotor flux. The last term is the reluctance torque, caused by the reluctance effect and armature reaction. The torque calculated by this equation is a function of time. It is the average value which needs to be equal to a desired torque.

5.5 Case study

The theory developed earlier is now validated step-by-step in a Matlab model of a BLDC generator. The model calculates the waveforms with a sample frequency of 10 kHz. As it is not straightforward to find all needed parameters of a machine, the machine simulated here is hypothetical. However, the parameters are all based on real machines. The back-emf waveform is taken from [87], where the first 49 Fourier components of the back-emf waveform were given for a BLDC. All other parameters, i.e., rated values and equivalent scheme parameters, are based on the machine investigated in [57].

Fig. 5.6 shows the back-emf waveform of the simulated machine. The dominant harmonics are a third order component of 21.46%, a fifth order component of 2.25%, a seventh order component of 4.35% and a ninth order component of 4.65%. The complete list of harmonic components is given in Appendix A. This waveform is typical for a BLDC machine.

The machine has a rated mechanical power of 2.5 kW, a rated speed of 2000 rpm, a rated line-to-line voltage of 220 V and rated current of 7 A. Since the machine has six poles, the rated frequency is 100 Hz. Table 5.1 shows the relevant machine parameters. The zero-sequence inductance was not available in [57] and is therefore set at the average of L_q and L_d.

In chapter 3, it was explained that optimal current waveform shaping techniques not only maximise the machine efficiency, but also the converter efficiency. The conduction losses in the converter can be modeled by an equivalent series resistance, since they are proportional to the square of the rms current. The switching losses are also minimised

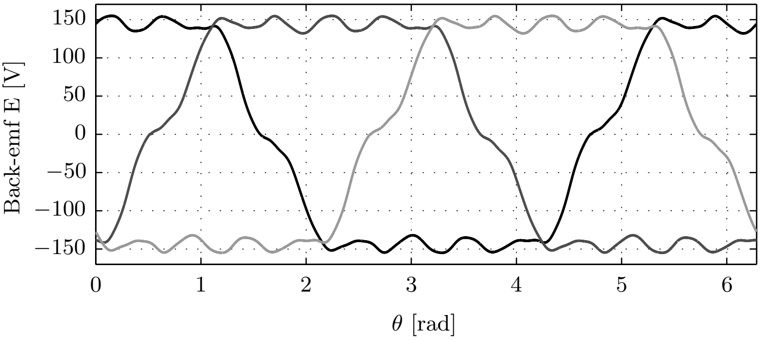

Figure 5.6: Back-emf waveforms simulated machine

Table 5.1: Machine parameters for the case study

$R_{s,0}$	N_p	L_0	L_q	L_d	K_f	K_h
[Ω]	[/]	[mH]	[mH]	[mH]	[μS]	[mS/s]
2	3	14	17.32	10.68	380.2	139.5

by the optimal current waveform, but are more complex to model since they depend on the PWM switching. Therefore, the switching losses are not included in the calculations here. To include the effect of the current waveform on the conduction losses of the converter, an equivalent series resistance of 0.75 Ω is added to the stator resistance of the PMSM. This value is based on the 9.2A Vishay IRFSL9N60APBF Mosfet. In this manner, the converter losses are taken into account in the optimisation of the scale factors, so that the machine and converter are optimised simultaneously.

The influence of temperature on the stator resistance is included in the model by implementing a classical linear approximation. The equivalent converter resistance is assumed to be independent of temperature. The total resistance is calculated by:

$$R_s = R_{s,0}\left[1 + \alpha(T - T_0)\right] + 0.75\Omega \tag{5.58}$$

The temperature T_0 is the reference temperature at which $R_{s,0}$ was measured, i.e., 25°C [57]. The parameter α is the temperature coefficient of resistance, which equals 0.0039 /°C for copper. The temperature T is the stator winding temperature for continuous operation in steady-state and nominal load. The stator winding forms a hot-spot in the machine and can easily reach temperatures above 100°C, depending on the cooling mechanism and environment temperature [114,115]. In the simulations, a value of 100°C is used. At this temperature, the total equivalent stator resistance R_s equals 3.335 Ω.

5.5.1 Case 1: Simplified PMSM model

The machine is modeled by the simplified PMSM model shown in Fig. 5.1. The model neglects the armature reaction effect and the iron losses but includes zero-sequence components in the back-emf. Three different current waveforms are applied on the machine: sinusoidal, square-wave and optimal. The sinusoidal waveform is typical for a BLAC converter, the square-wave waveform for a BLDC converter. The optimal waveform is calculated by (5.6) - (5.8). The current waveforms are regulated such that the machine operates as a generator at a speed of 2000 rpm with a mechanical power of 2.5 kW. This is done by adapting the amplitude of the sinusoidal and square waveforms and the scale factors of the optimal waveforms.

Fig. 5.7 shows the sinusoidal waveform (dashed line), the square-wave waveform (full grey line) and the optimal waveform (full black line). The optimal waveform is proportional to the back-emf waveform, as was expected.

Regarding the scale factors, no numerical optimisation is needed, since it was analytically proven that they must be equal. For confirmation, the iterative grid search algorithm was executed, which results in three identical scale factors of 10.8181. Fig. 5.8 shows a mesh plot of the total efficiency η_{tot}, calculated for the different combinations of G'_0 and G'_{d} by the optimisation algorithm. The figure clearly shows how the search grid is refined near the optimum in each step. This iterative approach significantly reduces the computational effort compared to a non-iterative grid search.

The numerical results of the simulation are summarised in Table 5.2. P_{Cu} and P_{Cond} denote the copper losses in the PMSM and the con-

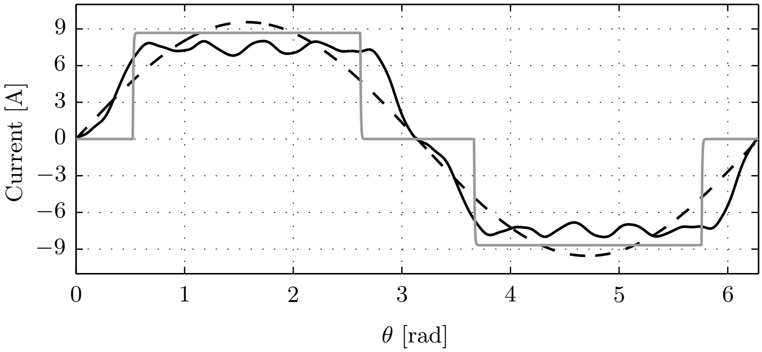

Figure 5.7: Sinusoidal, square-wave and optimal current waveforms for case 1

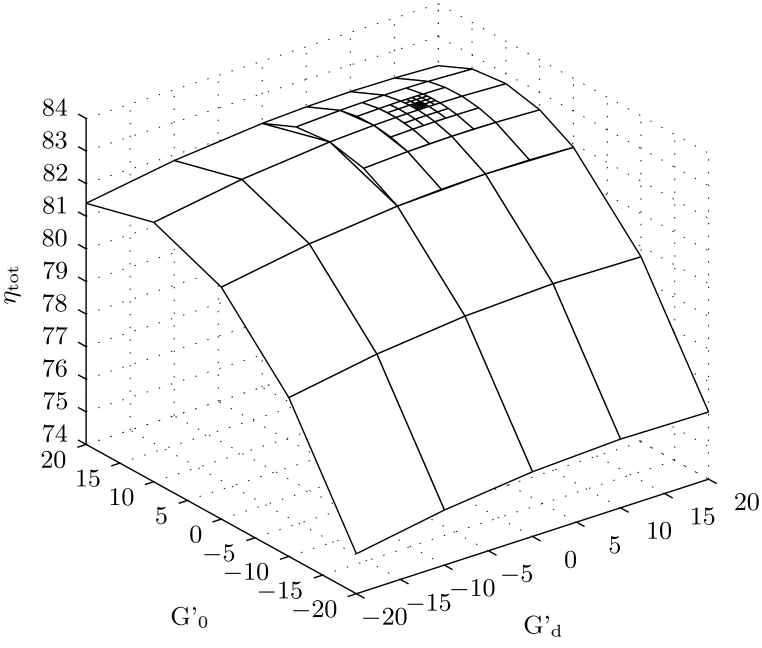

Figure 5.8: Total efficiency η_{tot} for all calculated combinations of G_0' and G_d'

duction losses in the converter, respectively. Since the iron losses are neglected in this case, the rms current directly determines the copper losses in the machine and the conduction losses in the converter.

As expected, the optimal current waveform results in the lowest rms current, lowest losses and highest efficiency. The machine efficiency is denoted by η_M, the converter efficiency by η_C. The total efficiency η_{tot} is simply the product of the machine and converter efficiencies. Although the model represents a BLDC machine, the square-wave current waveform has the worst performance, yielding a total efficiency which is 2.79 percentage points below the optimal waveform. The results for the sinusoidal waveform lie between the square-wave and optimal waveforms.

Table 5.2: Numerical results of the case 1 simulation

	$I_{\text{a,rms}}$	P_{Cu}	P_{Cond}	η_M	η_C	η_{tot}
Waveform	[A]	[W]	[W]	[%]	[%]	[%]
Square-wave	7.0734	388.00	112.57	84.48	94.67	79.98
Sinusoidal	6.7523	353.58	102.58	85.86	95.22	81.76
Optimal	6.5608	333.81	96.85	86.65	95.53	82.77

The simulations confirm that the optimal current waveform results in the highest efficiency. An important difference between the current waveform shaping technique presented in this dissertation and classical methods in literature is that the main focus is maximising the efficiency, instead of minimising torque ripples. The reasoning behind this is that energy efficiency is more important than torque ripple in certain applications, especially in the current context of global warming. Nevertheless, it is interesting to investigate the torque ripples for the simulated current waveforms.

Fig. 5.9 shows the torque ripple for a sinusoidal current waveform (dashed line), a square-wave waveform (full grey line) and the optimal waveform (full black line). Clearly, the optimal waveform results in the highest torque ripple. The magnitude of the torque ripple is best described by the rms value of the deviation from the mean torque. The square-wave waveform results in the smallest rms torque ripple, i.e., 0.5106 Nm. For the sinusoidal waveform, the torque ripple is slightly higher, i.e., 0.8325 Nm. The optimal waveform yields a larger torque ripple of 2.0837 Nm. The negative consequences of this torque ripple depend largely on the application, i.e., the sensitivity to vibrations or noise and the absorbing capacity of the inertia and friction.

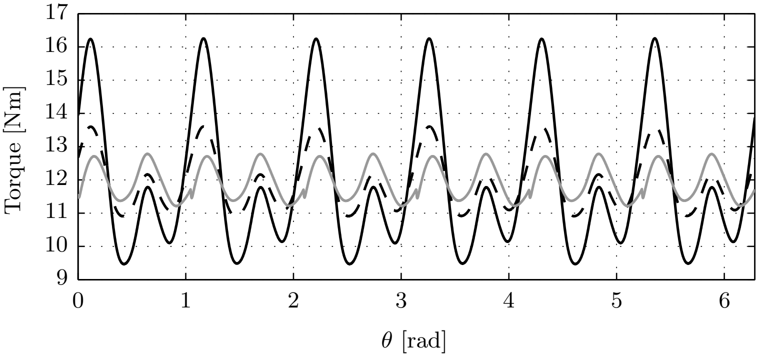

Figure 5.9: Torque ripples for case 1

It can be concluded that the square-wave current waveform results in the lowest torque ripple, which is beneficial in servo and robotics applications. However, in applications where energy efficiency is important, such as renewable energy systems or mobile battery-powered systems, the square-wave waveform has the worst performance. A considerable improvement is achieved by the optimal current waveform, which results in an increase of 3 percentage points for the total efficiency. The sinusoidal current waveform has a torque ripple and efficiency between the square-wave and optimal waveforms. In general, the simulations show that there is a trade-off between torque ripple and efficiency.

5.5.2 Case 2: Including armature reaction

The PMSM model is now extended by including the armature reaction effect, as shown in Fig. 5.3. The iron losses are not included yet. Again, a sinusoidal, square-wave and optimal waveform are imposed on the machine and regulated to the rated operating point of 2.5 kW and 2000 rpm. The optimal current waveforms are calculated by (5.25) - (5.27). The iterative grid search algorithm is used to determine the following optimal scale factors:

$$G'_0 = 10.5818 \qquad G'_\mathrm{q} = 10.8540 \qquad G'_\mathrm{d} = 5.8934 \tag{5.59}$$

Fig. 5.10 shows the mesh plot of the total efficiency, for all combinations of G'_0 and G'_d calculated by the optimisation algorithm.

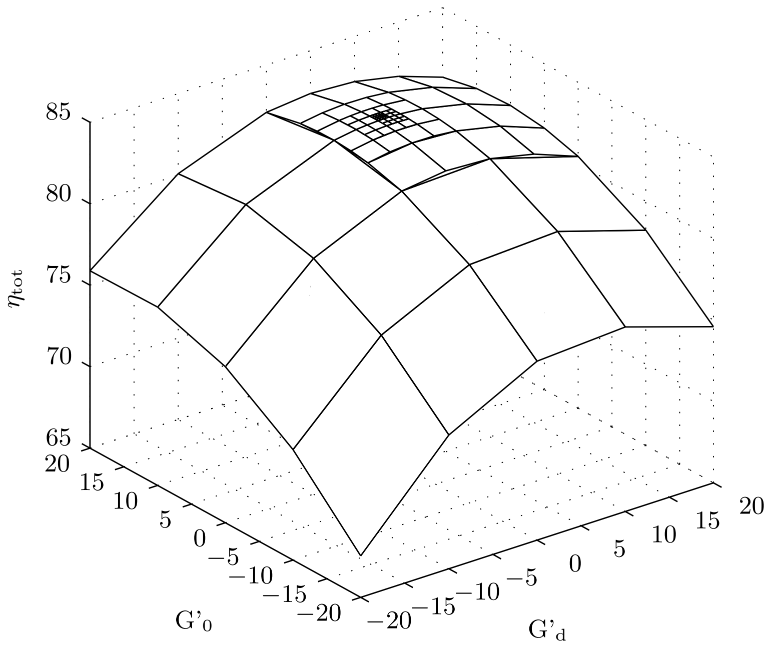

Figure 5.10: Total efficiency η_tot for all calculated combinations of G'_0 and G'_d

Fig. 5.11 shows the sinusoidal waveform (dashed line), the square-wave waveform (full grey line) and the optimal waveform (full black line).

The numerical results of the simulation are summarised in Table 5.3. Again, the rms current directly determines the copper losses in the machine and the conduction losses in the converter. As expected, the optimal current waveform has the highest efficiency while the square-wave waveform has the lowest. Here, the difference between the efficiency of the square-wave and optimal waveform equals 3.01 percentage points, which is slightly larger than in case 1.

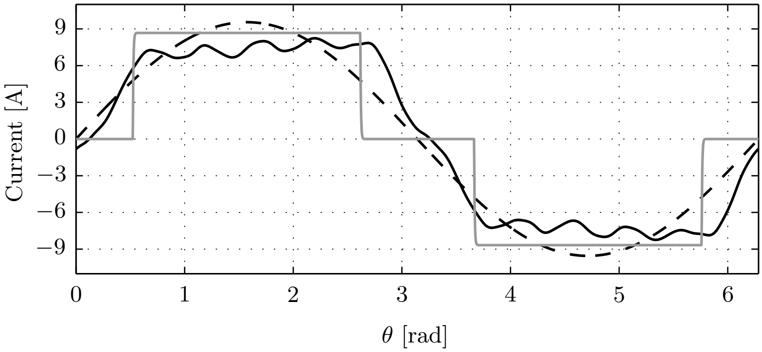

Figure 5.11: Sinusoidal, square-wave and optimal current waveforms for case 2

Table 5.3: Numerical results of the case 2 simulation

	$I_{\mathrm{a,rms}}$	P_{Cu}	P_{Cond}	η_M	η_C	η_{tot}
Waveform	[A]	[W]	[W]	[%]	[%]	[%]
Square-wave	7.0711	387.75	112.50	84.49	94.67	79.99
Sinusoidal	6.7523	353.58	102.58	85.86	95.22	81.76
Optimal	6.5180	329.47	95.59	86.82	95.60	83.00

Fig. 5.12 shows the torque ripple for a sinusoidal current waveform (dashed line), a square-wave waveform (full grey line) and the optimal waveform (full black line). Again, the optimal waveform results in the highest torque ripple. The square-wave waveform results in the smallest rms torque ripple, i.e., 0.4800 Nm. For the sinusoidal waveform, the torque ripple is slightly higher, i.e., 0.8325 Nm. The optimal waveform yields a larger torque ripple of 2.0815 Nm.

Compared to case 1, a higher efficiency is achieved with the optimal current waveform. This can be explained by the reluctance effect, which results in an additional torque term, i.e., the reluctance torque. The consequence is that this torque can be used to achieve the rated operating point with less current, and thus, a higher efficiency. This advantage of the reluctance torque is not exploited by the sinusoidal

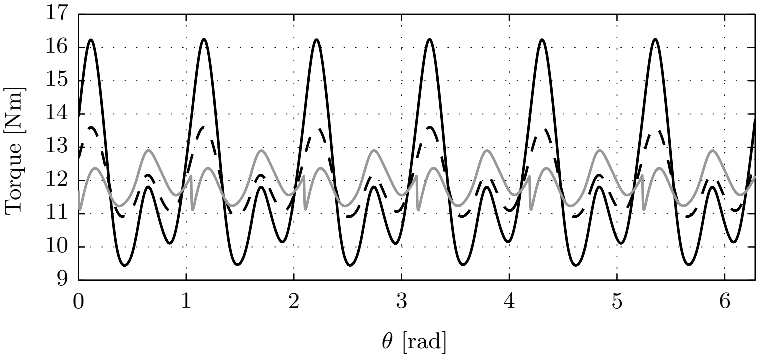

Figure 5.12: Torque ripples for case 2

current waveform, where the reluctance torque has no average component. The magnitudes of the torque ripples are comparable with case 1.

5.5.3 Case 3: Including iron losses

The current waveforms are now simulated for the PMSM model of Fig. 5.2, including the iron losses but neglecting the armature reaction effect. The optimal current waveforms are calculated by (5.15) - (5.17). For the rated speed, the equivalent iron loss resistance R_c equals 956 Ω. The iterative grid search algorithm is used to determine the optimal scale factors. Fig. 5.13 shows the used search mesh. The resulting scale factors are:

$$G'_0 = 10.5859 \qquad G'_{\mathrm{q}} = 10.6038 \qquad G'_{\mathrm{d}} = 10.5664 \tag{5.60}$$

Fig. 5.14 shows the sinusoidal waveform (dashed line), the square-wave waveform (full grey line) and the optimal waveform (full black line). The low-pass filters in the optimal current waveform equations have reduced the harmonic content, but this effect is not visible for this machine. The reason is that the cut-off frequencies of the filters are too high to have any effect. The cut-off frequencies for the different subsystems are given by:

$$f_{\mathrm{co,0}} = 10868\mathrm{Hz} \qquad \mathrm{f_{co,q}} = 8785\mathrm{Hz} \qquad \mathrm{f_{co,d}} = 14246\mathrm{Hz} \tag{5.61}$$

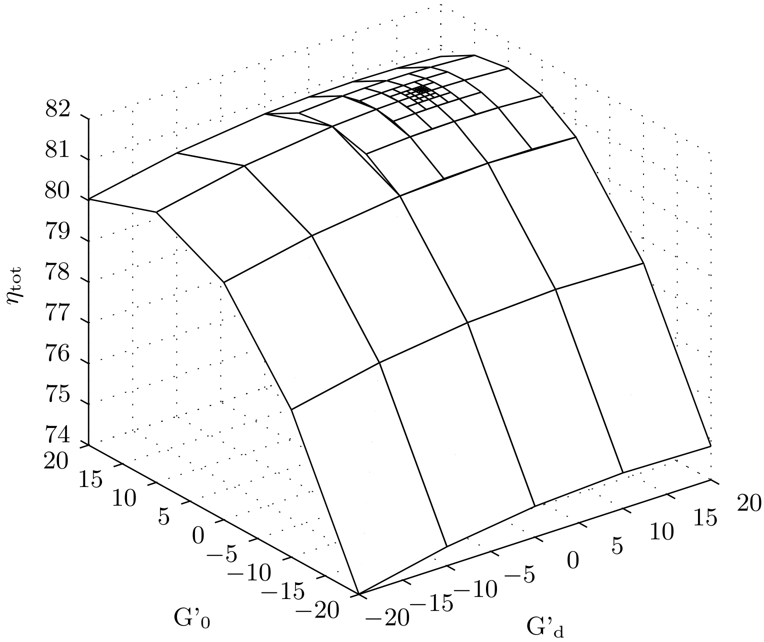

Figure 5.13: Total efficiency η_{tot} for all calculated combinations of G'_0 and G'_{d}

Clearly, these frequencies will not noticeably affect the waveform. The high value of the cut-off frequency can be expected intuitively, since the iron loss resistance has a high value, i.e., 956Ω and the inductances are low.

The numerical results of the simulation are summarised in Table 5.4. An additional column P_{Fe} is added to the table, denoting the iron losses of the PMSM. Compared to cases 1 and 2, lower efficiency values are achieved for all three waveforms, since the iron losses are now taken into account. Nevertheless, the general conclusion that the optimal waveform achieves the highest efficiency remains valid. The square-wave waveform has the lowest efficiency.

Fig. 5.15 shows the torque ripples, which are similar to the previous cases. The rms torque ripples equal 0.5040 Nm, 0.8574 Nm and 2.0636 Nm for the square-wave, sinusoidal and optimal waveforms respectively.

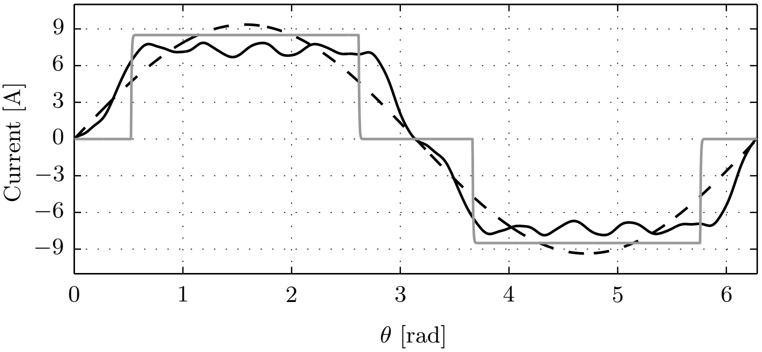

Figure 5.14: Sinusoidal, square-wave and optimal current waveforms for case 3

Table 5.4: Numerical results of the case 3 simulation

	$I_{\mathrm{a,rms}}$	P_{Cu}	P_{Fe}	P_{Cond}	η_M	η_C	η_{tot}
Waveform	[A]	[W]	[W]	[W]	[%]	[%]	[%]
Square-wave	6.9321	372.69	50.64	108.13	83.07	94.79	78.74
Sinusoidal	6.6155	339.36	50.64	98.46	84.40	95.33	80.46
Optimal	6.4298	320.61	50.64	93.02	85.15	95.63	81.43

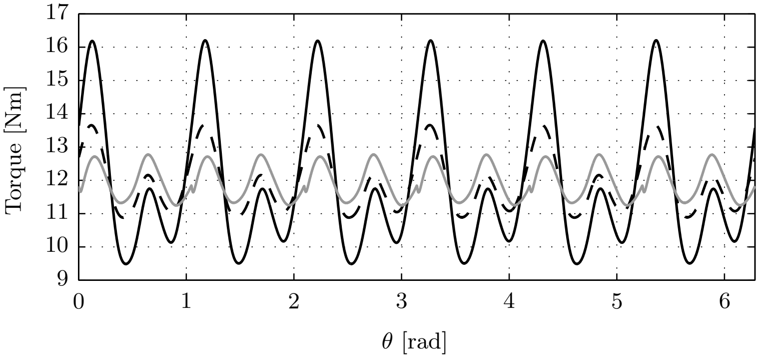

Figure 5.15: Torque ripples for case 3

It can be concluded that the iron losses have no significant effect on the shape of the optimal waveform for this machine, since the cut-off frequencies of the low-pass filters are too high to have any effect. The iron losses do affect the calculated efficiency values and rms current, as can be expected.

5.5.4 Case 4: Complete PMSM model

The current waveforms are now simulated for the complete PMSM model of Fig. 5.4, including both the armature reaction effect and iron losses. The optimal current waveforms are calculated by (5.28) - (5.30). The iterative grid search algorithm is used to determine the optimal scale factors. Fig. 5.16 shows the search mesh of the iterative grid search algorithm. The resulting scale factors are:

$$G'_0 = 10.3711 \qquad G'_\mathrm{q} = 10.6277 \qquad G'_\mathrm{d} = 6.4648 \tag{5.62}$$

Fig. 5.17 shows the sinusoidal waveform (dashed line), the square-wave waveform (full grey line) and the optimal waveform (full black line).

The numerical results of the simulation are summarised in Table 5.5. Again, the optimal waveform yields the highest efficiency, the square-wave waveform the lowest. The optimal waveform yields a considerable improvement of 3.04 percentage points when compared to the square-wave case.

Table 5.5: Numerical results of the case 4 simulation

	$I_\mathrm{a,rms}$	P_Cu	P_Fe	P_Cond	η_M	η_C	η_tot
Waveform	[A]	[W]	[W]	[W]	[%]	[%]	[%]
Square-wave	6.9410	373.65	53.94	108.41	82.90	94.77	78.56
Sinusoidal	6.6149	339.30	53.74	98.44	84.28	95.33	80.34
Optimal	6.3873	316.35	51.81	91.78	85.27	95.70	81.60

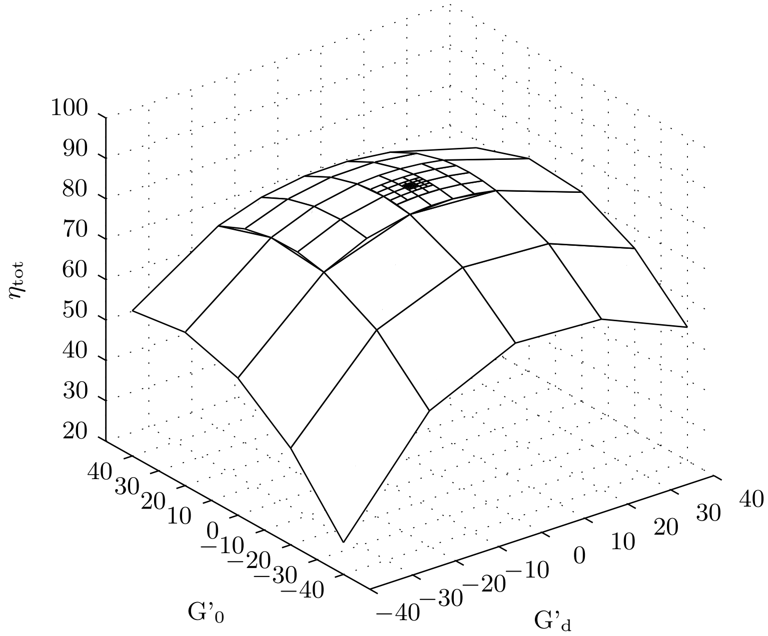

Figure 5.16: Total efficiency η_{tot} for all calculated combinations of G'_0 and G'_{d}

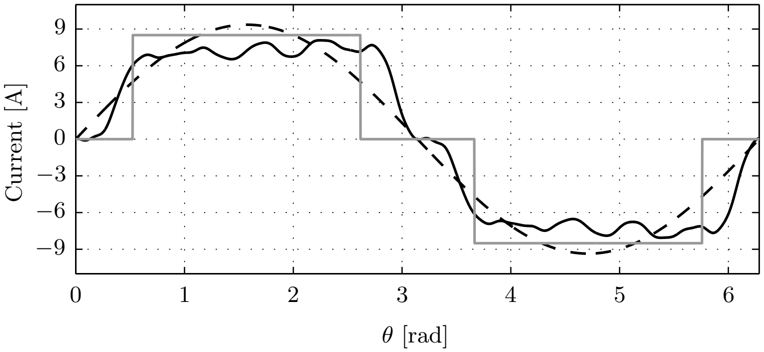

Figure 5.17: Sinusoidal, square-wave and optimal current waveforms for case 4

Fig. 5.18 shows the torque ripples. The rms torque ripples equal 0.4827 Nm, 0.8573 Nm and 2.1017 Nm for the square-wave, sinusoidal and optimal waveforms respectively. These values are similar to the previous cases.

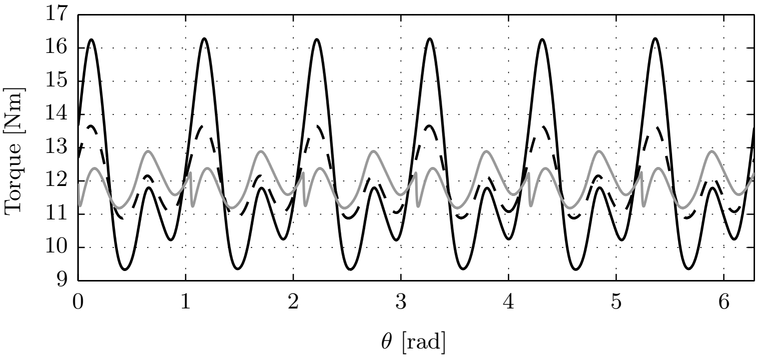

Figure 5.18: Torque ripples for case 4

Compared to the previous cases, the PMSM model used in this case is the most realistic representation of an actual machine. The used optimal current waveform equations (5.28) - (5.30) are the most complex presented in this chapter. However, it is interesting to investigate whether this complexity has an added value in the efficiency. Therefore, the effect of the simplified optimal current waveforms (5.6) - (5.8), i.e., neglecting armature reaction and iron losses, is simulated on the complete PMSM model of Fig. 5.4.

The iterative grid search algorithm determines the following scale factors:

$$G'_0 = 10.4102 \qquad G'_\mathrm{q} = 10.4575 \qquad G'_\mathrm{d} = 20.0391 \qquad (5.63)$$

Table 5.6 compares the numerical results of the previously simulated optimal waveform with the simplified optimal waveform. As expected, the efficiency is lower for the simplified waveform, but the difference is negligible.

It can be concluded that, although the complex optimal current waveforms result in the maximum efficiency, it is not worthwhile to take into account the armature reaction and iron losses. The simplified equations require a minimal implementation effort while yielding a similar efficiency. It is important to note that this conclusion is only valid for the machine investigated in this case study. This machine

Table 5.6: Comparison of the optimal and simplified optimal waveforms in case 4

	$I_{\mathrm{a,rms}}$	P_{Cu}	P_{Fe}	P_{Cond}	η_M	η_C	η_{tot}
Waveform	[A]	[W]	[W]	[W]	[%]	[%]	[%]
Optimal	6.3873	316.35	51.81	91.78	85.27	95.70	81.60
Optimal simple	6.3884	316.58	52.10	91.85	85.25	95.69	81.58

has a small inductance, leading to a small reluctance torque, and limited iron losses. Therefore, the results obtained here can be expected. In the following section, a parameter sensitivity analysis is performed to investigate how the machine parameters influence the achieved efficiency gain. This allows to make more general conclusions.

5.6 Parameter sensitivity analysis

In the case study, the effect of the optimal current waveform was investigated for one particular machine. However, the achieved efficiency depends on a large amount of parameters, e.g., resistance and inductance values, temperature, the back-emf waveform, etc. Therefore, a parameter sensitivity analysis is performed to gain a better understanding of how these parameters affect the efficiency gain. This allows to quantify the achievable gain and determine which machines are most suitable for application of the optimal current waveform shaping technique.

The classical OFAT (One-Factor-At-a-Time) method is used to identify the effect of each parameter on the efficiency. According to this method, one factor is varied while the others are kept at a fixed value. A disadvantage of this method is that it does not explore simultaneous variation of the variables. This would require a large amount of calculations. However, intuitively, the effect of the variations of the factors can be predicted beforehand.

5.6.1 Waveform of the back-emf

Although the optimal waveform technique ensures a maximum efficiency for any given machine, the efficiency improvement when compared to a sinusoidal or square-wave waveform strongly depends on the harmonic content of the back-emf. For instance, compared to a sinusoidal current waveform, no improvement is possible in an ideal BLAC, since the optimal waveform is itself sinusoidal. In general, it can be expected that the more the back-emf deviates from an ideal sinusoidal or trapezoidal waveform, the more the efficiency improvement will be for an optimal current waveform, as it takes into account this deviation.

Clearly, it is not possible to calculate the efficiency improvement for all possible waveforms, as this requires to vary the amplitude and phase of each harmonic component. Therefore, a different approach is taken here, as proposed in [82]. The magnet back-emf of phase a is represented by the following Fourier series:

$$E_a = \frac{4}{\pi}\ \Omega\ \Psi \sum_{k=0}^{\infty} a_n \sin n\theta_e \tag{5.64}$$

where $n = 2k + 1$ and a_n is defined as:

$$a_n = \frac{\sin nF}{n^2 F} \tag{5.65}$$

In this manner, the back-emf can be varied from a trapezoidal shape for a low F, to a waveform that resembles a sinusoidal shape for a large F. The waveforms of phases b and c are simply shifted 120° and 240° respectively. Fig. 5.19 shows the back-emf waveforms for F equal to 10°, 35°, 55° and 80° from darker to lighter. In the simulations here, F is varied from 10° to 80° in steps of 5°. For each value, the three possible current waveforms, i.e., sinusoidal, square-wave and optimal, are calculated to determine the losses and efficiency. For every value of F, the factor Ψ is recalculated such that the rms value of the back-emf remains the same, i.e., equal to the rated value. This results in an objective comparison of the different simulations.

Besides the back-emf waveform, all machine parameters remain the same as in the case study. For the optimal current waveforms, the complete equations (5.28) - (5.30) are used. Also, to better match

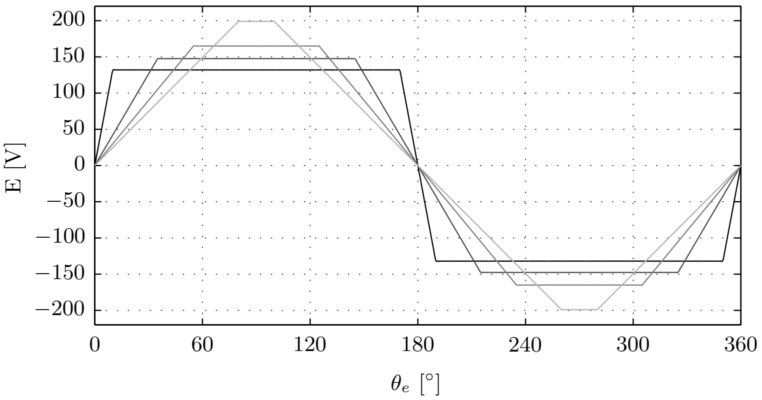

Figure 5.19: Back-emf waveforms for F equal to 10°, 35°, 55° and 80° from darker to lighter

the back-emf waveform, the square-wave current waveforms simulated here have a 180° conductance duration, instead of 120° in the case study simulations.

Fig. 5.20 shows the simulated efficiency values for the square-wave (dark grey), sinusoidal (light grey) and optimal (black) current waveforms in function of F. For a low value of F, the back-emf waveform is predominantly trapezoidal. Clearly, the square-wave current waveform achieves a higher efficiency than the sinusoidal waveform. On the other side of the spectrum, i.e., high values of F, the back-emf waveform is more sinusoidal. There, the sinusoidal current waveform achieves higher efficiencies than the square-wave waveform. These results are as expected, i.e., a sinusoidal current waveform is best suited for a BLAC machine, a square-wave current waveform for a BLDC machine.

However, the optimal current waveform achieves a maximum efficiency for the full range of F values. Only in the region of 55° to 65° the sinusoidal waveform can match the efficiency of the optimal waveform. For other values of F, it is worthwhile to implement the optimal current waveform technique to increase the energy yield. It can be noticed that the efficiency of the optimal waveform is nearly constant for the whole range. The reason for this is that the rms value of the magnet back-emf is identical for all simulations while the armature reaction effect is small. Therefore, the rms value of the current waveform will be nearly identical for all simulations as well, since the mechanical power is regulated equal to the rated value, leading to practically the same losses and efficiency values.

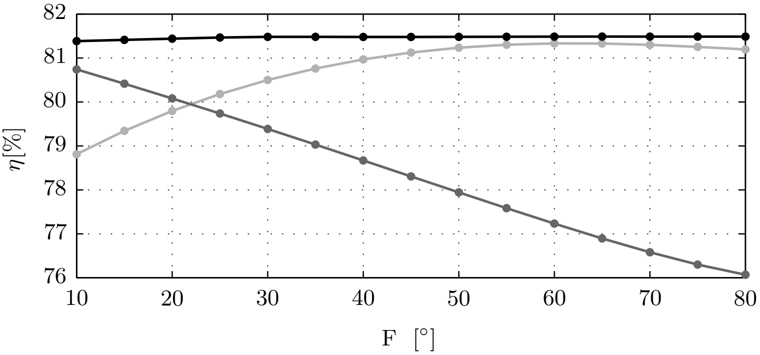

Figure 5.20: Efficiency in function of F for the square-wave (dark grey), sinusoidal (light grey) and optimal (black) current waveforms

This simulation confirms that the optimal current waveform technique has a higher efficiency gain compared to classical waveforms if the back-emf deviates more from the ideal shape. For BLAC machines with a predominantly sinusoidal back-emf waveform, a simple sinusoidal current waveform will already result in a maximum efficiency. The effectiveness of the optimal current waveform shaping technique compared to a sinusoidal waveform can be condensed in one single parameter E_h, defined by:

$$E_h = \sqrt{\frac{1}{T}\int_0^T \left[e_a - e_{a,1}\right] dt} \tag{5.66}$$

This parameter is the rms value of the total harmonic content of the back-emf in phase a. Fig. 5.21 shows this parameter together with the added efficiency of the optimal waveform relative to the efficiency of the sinusoidal waveform, i.e., $\eta_{\text{opt}} - \eta_{\text{sin}}$. Clearly, there is a strong correlation between both parameters. Therefore, E_h can be used as a qualitative measure for the added efficiency of an optimal waveform compared a sinusoidal waveform. In other words, it shows the room for improvement.

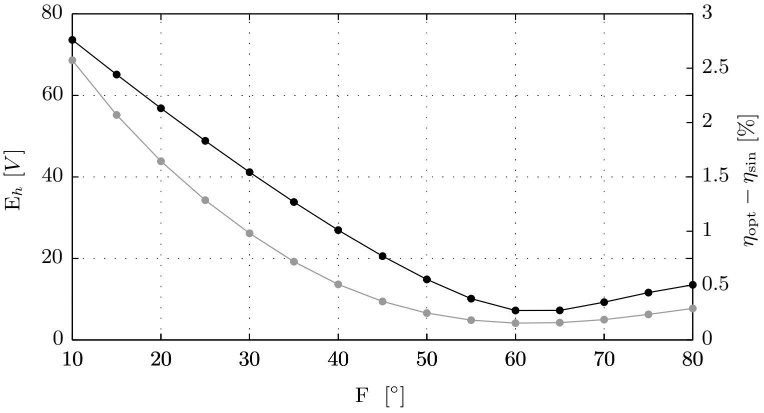

Figure 5.21: Rms value of the harmonic content E_h (black) and added efficiency $\eta_{\text{opt}} - \eta_{\text{sin}}$ (grey) in function of F

5.6.2 Stator resistance

The stator resistance R_s has a straightforward effect on the efficiency. A lower resistance results in less copper losses, an increased efficiency and a smaller impact of the current waveform. It is expected that the efficiencies achieved by the three different current waveforms become identical as the resistance decreases. This hypothesis is tested by varying the stator resistance in the simulation model from 20% to 180% of the rated value. All other parameters remain at their normal value. The used back-emf waveform is the same as in the case study, i.e., the waveform of [87].

Fig. 5.22 shows the efficiency in function of R_s for the square-wave (dark grey), sinusoidal (light grey) and optimal (black) current waveforms. As expected, the waveform has a small impact on the efficiency for low resistance values, since the copper losses are small. As the resistance increases, the efficiency drops and the difference between the performance of the current waveforms becomes more obvious. In general, it can be concluded that the effect of the current waveform on the efficiency is stronger for machines with high copper losses.

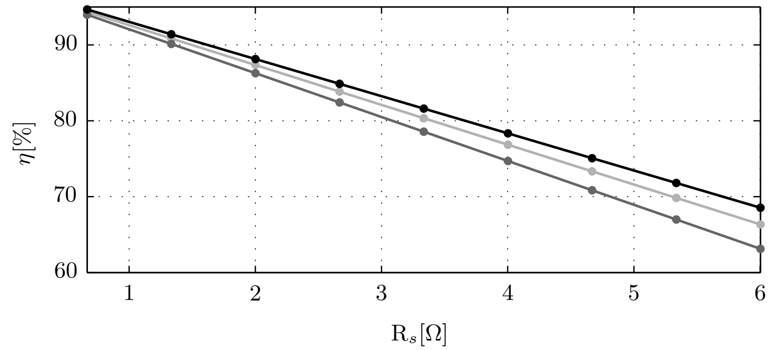

Figure 5.22: Efficiency in function of R_s for the square-wave (dark grey), sinusoidal (light grey) and optimal (black) current waveforms

5.6.3 Ratio of copper and iron losses

The main principle of the optimal current waveform shaping technique is that the rms current is reduced by extracting power from the harmonic components in the back-emf, by including harmonic currents. This reduces the copper losses, increasing the efficiency. The machine investigated in the case study roughly has 9 times more copper losses than iron losses, which is a realistic proportion. However, in practice, the ratio of copper and iron losses can vary significantly. It is expected that this ratio has an influence on the efficiency gain of the optimal current waveform technique, i.e., the efficiency gain will be lower for machines with high iron losses.

This hypothesis is investigated by varying the ratio of copper and iron losses. To achieve an objective comparison, the stator resistance R_s and iron loss resistance R_c are varied in such a way that the total losses, and thus efficiency, remain the same for a sinusoidal current waveform. Table 5.7 shows the simulated combinations of R_s and R_c. The first simulation uses the rated values and corresponds with case 4 of the case study.

Fig. 5.23 shows the efficiency in function of R_c for the square-wave (dark grey), sinusoidal (light grey) and optimal (black) current waveforms. For low values of R_c, the iron losses are high and the efficiency of the optimal current waveform reduces. For the lowest value of R_c,

Table 5.7: Simulated combinations of R_s and R_c

R_s	3.335	3.260	3.078	2.460	1.445
R_c	955.782	750	500	250	150

the ratio of copper and iron losses is only 0.44. Still, the optimal current waveform achieves a higher gain than the sinusoidal current waveform. It can be concluded that the efficiency gain of the optimal current waveform is indeed smaller for machines with high iron losses. However, the optimal current waveform still clearly yields a higher efficiency. In general, the efficiency gain does not vary much in function of the ratio between iron and copper losses.

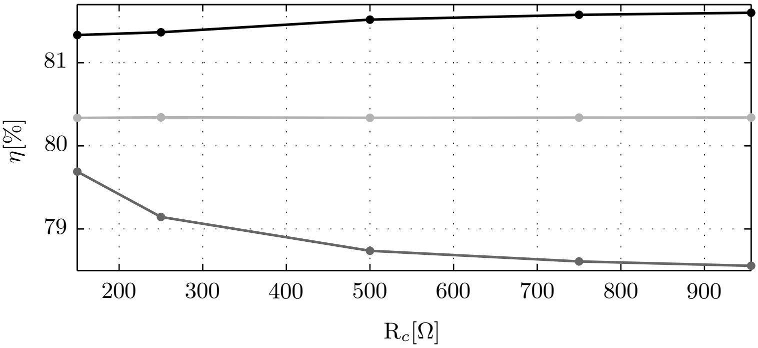

Figure 5.23: Efficiency in function of R_c for the square-wave (dark grey), sinusoidal (light grey) and optimal (black) current waveforms

For the previous simulations, the complete optimal current waveform equations (5.28) - (5.30) were used. These equations take into account the armature reaction effect and the iron losses. However, in case 4 of the case study, it was shown that the added efficiency for using these complete equations was negligible, compared to the simplified equations (5.6) - (5.8). Therefore, the simulations for a variable R_c are now repeated with the simplified optimal current equations.

Fig. 5.24 shows the efficiency for the complete optimal current equations in black, and the simplified optimal current equations in light grey. For high values of R_c, i.e., low iron losses, the efficiency of the simplified equations is close to the complete equations. At the far right, the difference is only 0.02 percentage points. However, at the far left, i.e., high iron losses, the difference increases to 0.07 percentage points. Clearly, including the iron losses in the optimal current waveform becomes more important if the machine has more iron losses, which was to be expected.

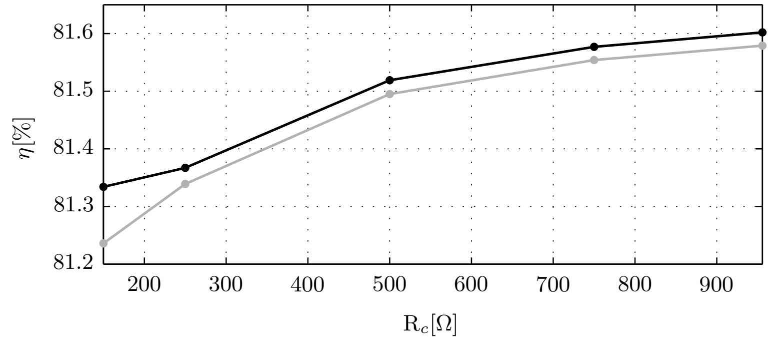

Figure 5.24: Efficiency in function of R_c for the complete optimal (black) and simplified optimal (light grey) current waveform

However, it is important to point out that the contribution of including the iron losses in the waveform rather depends on the ratio of inductance on the iron loss resistance, than on the iron loss resistance alone. This can be expected since the cut-off frequencies of the low-pass filters in (5.15) - (5.17) are determined by the ratio R_c/L.

5.6.4 Inductance

The machine simulated in the case study has inductance values around 10 mH. For this value, the armature reaction back-emfs are small, leading to a small gain in case 2. Also, as shown previously, the low inductance results in high cut-off frequencies, even when the iron loss resistance was increased. Therefore, the effect of an increased inductance is now investigated. It is expected that including both the armature reaction effect and iron losses in the optimal current waveform becomes more important as the inductance increases.

Here, the parameter sensitivity is investigated by varying all the inductances by the same factor γ:

$$L_0 = \gamma L_{0,\mathrm{n}} \qquad L_q = \gamma L_{\mathrm{q,n}} \qquad L_d = \gamma L_{\mathrm{d,n}} \tag{5.67}$$

The subscript n denotes the nominal values. The factor γ is varied from 1 to 5 in steps of 0.5. In this way, both the size of the inductances and the magnitude of the reluctance effect, i.e., $L_d - L_q$, is increased.

Fig. 5.25 shows the efficiency in function of γ for the square-wave (dark grey), sinusoidal (light grey), complete optimal (black) and simplified optimal (black dashed) current waveforms. The simplified optimal waveform performs better than the classical sinusoidal and square-wave waveform, for the whole range of γ. As the inductance increases, the efficiency achieved by these waveforms decreases.

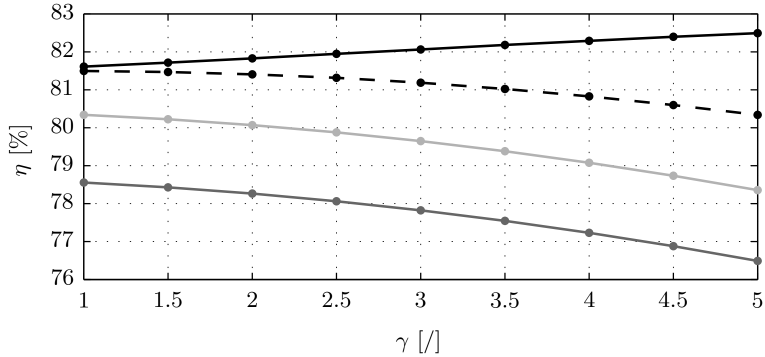

Figure 5.25: Efficiency in function of γ for the complete optimal (black), simplified optimal (black dashed), sinusoidal (light grey) and square-wave (dark grey) current waveforms

However, the complete optimal waveform takes into account the effect of the increasing inductance and is able to achieve a higher efficiency. As the inductance increases, both the armature reaction effect and the influence of the iron losses become more important. This also increases the difference between the simplified optimal and the complete optimal current waveform. Clearly, for machines with a higher inductance, it is advantageous to implement the more advanced complete optimal current waveform instead of the simplified one.

5.6.5 Conclusions

In the parameter sensitivity analysis, four important parameters were investigated by using the classical OFAT method, i.e., the waveform of the back-emf, the stator resistance, the ratio of copper and iron losses, and the inductance. In the first series of simulations, it was shown that a sinusoidal or square-wave current waveform perform better as the back-emf respectively becomes more sinusoidal or trapezoidal. However, the optimal current waveform achieves a high efficiency for the whole range of waveforms, and performs better than the classical sinusoidal and square-wave waveforms.

The effect of the stator resistance is straightforward. A higher resistance increases the copper losses, increasing the efficiency difference between the optimal and classical waveforms.

The impact of the iron losses was investigated by varying the ratio of iron and copper losses, while keeping the efficiency of the sinusoidal current waveform constant. As the iron loss resistance decreased, the iron losses became larger. This slightly reduced the efficiency of the optimal waveform. It was also shown that, as the iron losses increase, it becomes more important to include the iron losses in the optimal current waveform.

When the value of the inductance is increased, the efficiency of the classical waveforms reduces. The simplified optimal current waveforms still achieves a higher efficiency, but also reduces as the inductance increases. However, the complete optimal current waveforms, which take into account the effect of the inductance and the iron losses, achieves higher efficiency values. This clearly shows the important of using the complete optimal current waveforms instead of the simplified ones for certain machines.

5.7 Application on a wind turbine

In this chapter, the optimal current waveform shaping technique was presented theoretically and validated with simulations in a case study. Also, a parameter sensitivity analysis was performed to investigate the influence of selected machine parameters on the performance of the technique. Now, the practical implementation of the method on a wind turbine will be discussed, as it would be applied in practice. The results will be validated on a simulation model of a wind turbine system in Simulink, including the generator and the split-link rectifier. This model will be referred to as the wind turbine model, uses the SimPowerSystems toolbox and includes the high-frequent PWM switching of the rectifier. The model used previously in the case study and parameter sensitivity analysis is implemented purely as Matlab code and will be referred to as the theoretical model.

In order to apply the optimal current waveform shaping technique on a practical wind turbine, the following steps should be taken:

1. Judging the applicability
2. Parameter identification
3. Calculation of the scale factor curve fits
4. Implementation in the controller

In what follows, these steps will be discussed in detail.

5.7.1 Judging the applicability

First, it must be decided whether the optimal current waveform shaping technique can or should be applied on the wind turbine system. The technique can only be applied if there is sufficient control over the current waveform, i.e., it is preferred that a split-link rectifier is used and a neutral wire connection is available on the machine. If a neutral connection is unavailable, the zero-sequence subsystem must be neglected in the analysis.

The technique should only be applied if the back-emf waveform contains sufficient harmonics. If the back-emf waveform is nearly sinusoidal, the efficiency gain from an optimal current waveform will be negligible. Also, there should be enough stator resistance to make a difference in the copper losses.

It would be helpful to have a simple quantitative approximation of the efficiency gain which can be expected, preferably with a minimum of parameters. A simple method is proposed here. The efficiency is calculated for a sinusoidal and optimal current waveform in the rotating reference frame, while neglecting the armature reaction and the equivalent iron loss resistance.

For a sinusoidal current waveform and ideal field orientation, the mechanical power P_m is expressed as:

$$P_m = \frac{3}{2}\frac{1}{T}\int_0^T e_q i_q dt = \frac{3}{2}\bar{E}_q I_{\mathrm{q}} \tag{5.68}$$

where $\bar{E}_q$ is the mean value of the q-axis back-emf and I_{q} is the constant current in the q axis. The d axis current is zero due to the field orientation. This equation gives the required current for a given desired mechanical power. The Joule losses for a sinusoidal current can be calculated as:

$$P_j = \frac{3}{2}RI_{\mathrm{q}}^2 = \frac{2}{3}R\frac{P_m^2}{\bar{E}_q^2} \tag{5.69}$$

Since the armature reaction and the iron losses are neglected, the three scale factors of the optimal current waveform can be chosen equal. In this case, the optimal current waveform equations are:

$$i_0 = G\ e_0 \qquad i_q = G\ e_q \qquad i_d = G\ e_d \tag{5.70}$$

The mechanical power P_m is expressed as:

$$\begin{aligned} P_m &= 3\frac{1}{T}\int_0^T e_0 i_0 dt + \frac{3}{2}\frac{1}{T}\int_0^T e_q i_q dt + \frac{3}{2}\frac{1}{T}\int_0^T e_d i_d dt \\ &= 3GE_0^2 + \frac{3}{2}GE_q^2 + \frac{3}{2}GE_d^2 \end{aligned} \tag{5.71}$$

where E_0, E_q and E_d are the rms values of the back-emf in the three subsystems. The Joule losses for the optimal current waveform are calculated as:

$$P_j = 3RG^2E_0^2 + \frac{3}{2}RG^2E_q^2 + \frac{3}{2}RG^2E_d^2 \tag{5.72}$$

$$= R\frac{P_m^2}{3E_0^2 + \frac{3}{2}E_q^2 + \frac{3}{2}E_d^2} \tag{5.73}$$

The Joule losses are now written in terms of the back-emf, the mechanical power and the total resistance. These parameters are available or can be measured. The benefit of using the optimal current waveform compared to a sinusoidal current waveform can now be quantitatively estimated by the ratio of the Joule losses:

$$\frac{\bar{E}_q^2}{2E_0^2 + E_q^2 + E_d^2} \tag{5.74}$$

As can be expected intuitively, this ratio also shows how strong the back-emf waveform deviates from an ideal sinusoidal shape. For a purely sinusoidal back-emf waveform, this ratio equals 1, since $E_0 = E_d = 0$ and $\bar{E}_q = E_q$.

For the back-emf waveform used in this chapter, the ratio equals 0.9442. In other words, the optimal current waveform reduces the Joule losses by 5.59% compared to a sinusoidal waveform. In case 1 of the case study, the simulations show a Joule loss reduction of 5.59%, which indeed equals the expected value. In the cases 2, 3 and 4, the optimal waveform reduces the Joule losses by 6.82%, 5.53% and 6.76% respectively. Naturally, as the armature reaction effect and the iron losses become more important, the predicted ratio (5.74) becomes less accurate. However, the predicted Joule loss reduction lies close to the obtained values in all four cases of the case study. It can be concluded that this ratio is a good measure for the expected reduction of the losses. The efficiency can be estimated beforehand as well by using the equations for P_m and P_j stated above.

5.7.2 Parameter identification

In order to determine the optimal current waveforms, a parameter identification must be performed on the generator. All parameters of the complete equivalent scheme must be measured, i.e., the back-emf waveform, inductances, stator resistance and hysteresis and eddy current loss constants. Naturally, the accuracy of these parameters must be sufficiently high to achieve a good performance of the optimal current waveform.

The stator resistance and inductances can be easily measured with an LCR meter at standstill. A correction factor can be applied to take into account the impact of temperature on the stator resistance. Measurement of the equivalent iron loss resistance, i.e., the K_f and K_h

constants is more difficult. In [57], a method is presented to identify these constants by using a full active rectifier, without the need for a torque sensor.

In general, many advanced parameter identification methods are described in literature. The parameters can be identified by using multi-sinusoidal test signals injected by a voltage-source inverter [116]. Another method uses a current decay test combined with particle swarm optimization [117]. Also, extended Kalman filters can be used [118]. Parameter identification of synchronous machines is an entire research topic on its own, and will not be further discussed in this work. It is assumed that the needed parameters of the machine are known.

The wind turbine simulated here has a rated power of 2.5 kW at a wind speed of 11 m/s. The rated rotor speed is 487 rpm and the blade length is 1.49 m. The blades are modeled by the $C_{\mathrm{p}}(\lambda)$ curve (2.3), with a maximum of 0.44 at a TSR of 6.91. If the turbine operates in the Maximum Power Point at all times, the following relation between torque and rotor speed can be assumed:

$$T = \frac{P_{\mathrm{t}}}{\Omega} = \frac{1}{2\Omega}\ \rho\ \pi\ R^2\ 0.44\ \left(\frac{R\ \Omega}{6.91}\right)^3 = K\ \Omega^2 \tag{5.75}$$

The K-factor of the turbine equals 0.0188 Nm s^2. The generator is identical to the one from the case study, with the exception of the pole pair number and fundamental frequency, which equal 6 and 48.7 Hz respectively. The parameters of the equivalent scheme can be found in Table 5.1.

The rectifier is a split-link converter with MOSFETs and an ideal dc-bus. The grid-connected inverter is not included in the analysis as the system can be considered decoupled at the dc bus, i.e., the control system and behavior of the machine-side rectifier does not influence the behavior of the grid-side inverter.

5.7.3 Scale factor curve fits

Since all necessary parameters of the generator are known, the complete optimal current waveform equations (5.28) - (5.30) can be implemented. First, the scale factors need to be calculated by the iterative grid search algorithm beforehand. Then, they can be programmed in the controller of the rectifier.

In contrast to previous simulations, the scale factors must now be calculated for the full operating range of the turbine, i.e., from the cut-in speed to the rated speed. This will be done by executing the iterative grid search algorithm for a discrete set of rotor speed values. The desired torque is chosen according to (5.75). The result is a set of optimal scale factors for each rotor speed value. By using a simple polynomial curve fit, the scale factors can be written as a function of the rotor speed and implemented in the controller with limited memory usage.

Fig. 5.26 shows the simulated optimal scale factors for each subsystem for several rotor speed values. The data can be approximated by the following second order polynomial curve fits:

$$\begin{aligned} G'_0 &= 0.0010\ \Omega^2 + 0.0001\ \Omega - 0.1423 \\ G'_\mathrm{q} &= 0.0010\ \Omega^2 - 0.0004\ \Omega - 0.1407 \\ G'_\mathrm{d} &= 0.0005\ \Omega^2 + 0.0175\ \Omega - 0.0289 \end{aligned} \tag{5.76}$$

These curves are also shown on the figure and show a good match with the simulated points. The second order polynomial curve fit implies that only 9 parameters must be stored in the memory of the controller.

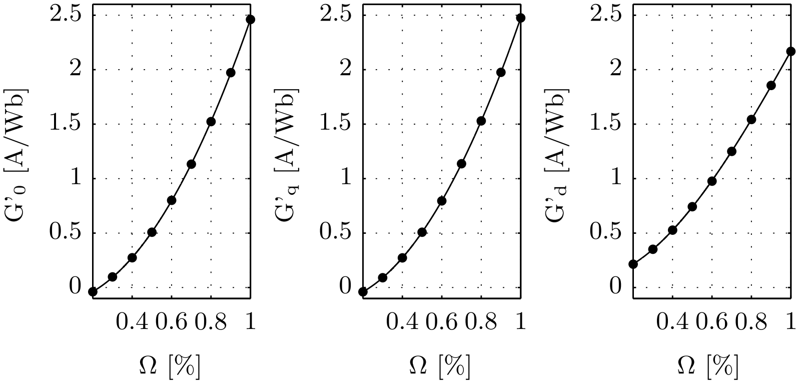

Figure 5.26: Scale factors and polynomial curve fits

As will be shown in the simulations later, the second order curve fits are sufficiently accurate to approximate the optimal scale factors. A simple polynomial approximation is applicable in most practical applications, such as fan drives, pumps, compressors, etc. This implies that there are alternative ways of determining these curves, without the need of running the iterative grid search algorithm for multiple operating points.

For instance, it is possible to determine the parameters of the curves by using adaptive control [119]. The curves can be initialised as linear curves, only knowing the optimal scale factor at the rated operating point. The values at the rated operating point can be determined by the iterative grid search algorithm or can even be set at an equal estimated value. By systematically perturbing the system, i.e., deviating from the curve and measuring the effect on the efficiency, the curve can be fine-tuned. After sufficient iterations, the curve fits (5.76) can be approximated. This process can be performed on a test bench with speed and torque sensors. In the case of a wind turbine, it can even be performed in a wind tunnel.

5.7.4 Implementation in the controller

The simulated active rectifier consists of six MOSFET switches, each with an equivalent resistance of 0.75Ω consistent with the simulations of the case study. The switches are controlled by a uniformly sampled PWM with a triangular carrier wave. The switching frequency is set at 20 kHz. The neutral wire of the generator is connected to the midpoint of the split dc-bus, which has a constant total voltage of 400 V.

The optimal current waveform equations are implemented in Simulink by transfer functions in the Laplace domain. The optimal current waveform equations are transformed to abc coordinates, where they are sampled by three PI current controllers which determine the duty ratios of each inverter leg.

5.7.5 Simulation results

First, a simulation is performed without the rectifier, i.e., the current waveforms calculated by Simulink are injected directly into the generator of the wind turbine model. In this manner, the calculated scale factor curve fits and implemented transfer functions can be validated. Fig. 5.27 shows the optimal current waveforms extracted from the machine. The time period of the figure is $1/6^{\text{th}}$ of one rotation, i.e., showing one period of the waveforms. The simulated waveforms, i.e., calculated by Simulink with the scale factor curve fits, are shown as a full black line, a full dark grey line and a black dashed line. The waveforms calculated by the theoretical model, i.e., using the exact scale factors, are shown in light grey, and show a good correspondence with the waveforms from the wind turbine model.

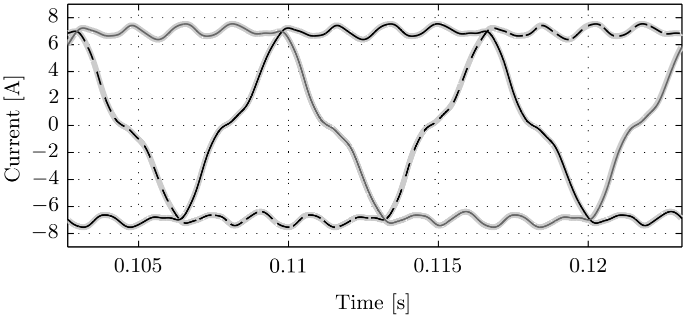

Figure 5.27: Simulated optimal current waveforms: theoretical waveforms in light grey, simulated waveforms in full black, full dark grey and dashed lines

Fig. 5.28 shows the torque waveform. The simulated waveform from the wind turbine model is shown as a dashed black line. The waveform from the theoretical model is shown in light grey. Again, there is a good correspondence between both models.

The mean value of the simulated torque waveform is 48.9603 Nm, resulting in a mechanical power of 2498 W. This is close to the desired torque value of 48.9562 Nm, with a mechanical power of 2.5 kW. The small difference between both models is caused by the second order scale factor curve fits, which have a small deviation from the ideal curve. However, the difference is small, showing that the second order polynomials are sufficiently accurate in this case.

In the next simulation, the active rectifier is connected to the machine. Now, the current waveform will be more realistic as it will include a high-frequent current ripple. Also, the current controllers

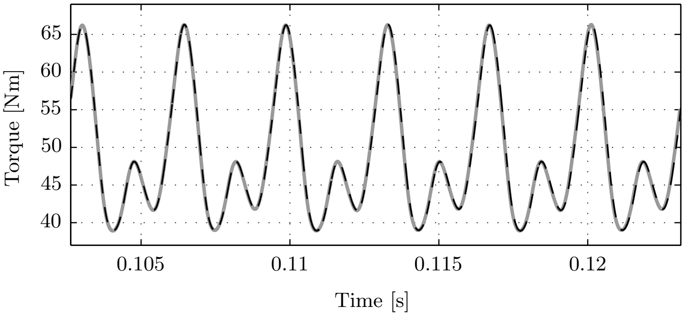

Figure 5.28: Simulated torque: dashed black line is the wind turbine model, light grey is the theoretical model

cannot track their setpoints perfectly, which will cause a deviation from the optimal waveforms. The high-frequent current ripple will also be visible in the dynamic torque as a high-frequent torque ripple.

Fig. 5.29 shows the current waveform in phase a. The waveform from the theoretical model is shown in black, the simulated waveform from the wind turbine model in grey. As expected, the waveform from the wind turbine model contains a high-frequent current ripple. The figure shows that the current controllers work properly as the real and desired waveforms correspond well. As always, the parameters of the current controllers are chosen as a compromise between robustness and control performance. A robust controller inevitably has an imperfect tracking performance.

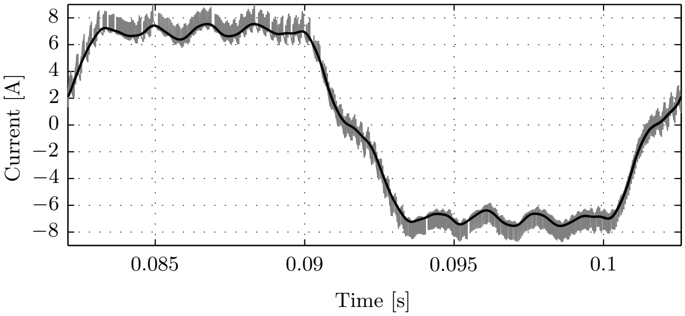

Figure 5.29: Simulated current waveform in phase a

Fig. 5.30 shows the theoretical torque in grey and the torque from the wind turbine model in black. Again, both torque waveforms correspond well. The simulated torque from the wind turbine model contains a small high-frequent ripple, caused by the switching ripple in the current waveform. However, the torque ripple is far less pronounced than the current ripple. This can be explained by the fact that the torque is determined by the inner currents, not the stator currents, as shown by the torque function σ in (5.57) on p. 116. According to (5.50) and (5.52), the inner currents will always contain less current ripple than the stator currents.

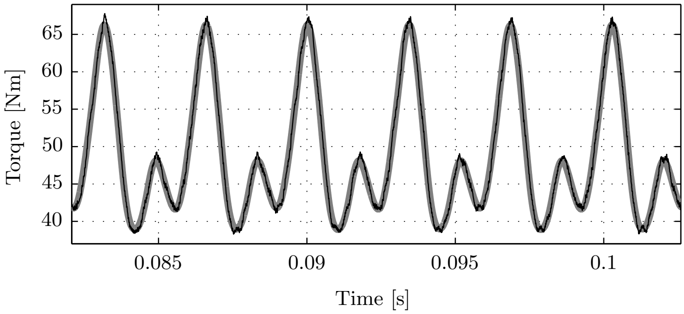

Figure 5.30: Simulated torque: black line is the wind turbine model, light grey is the theoretical model

For comparison, a sinusoidal current waveform is simulated as well. Fig. 5.31 shows the sinusoidal setpoint waveform as a black full line and the real waveform in grey. Again, the current ripple is clearly visible.

Fig. 5.32 shows the simulated torque. A small ripple is present due to the high-frequent switching ripple in the current waveform. Also, the low-frequent torque variation, caused by the harmonics in the flux waveform, is smaller than for the optimal current waveform. Here, the rms value of the torque ripple equals 7.67% of the mean torque. For the optimal current waveform, the rms value of the torque ripple equals 17.66%. It was already discussed earlier that the increased torque ripple is a disadvantage of the optimal current waveform shaping technique. The gravity of this depends on the application, i.e., noise and vibration restrictions, wear of mechanical components, the

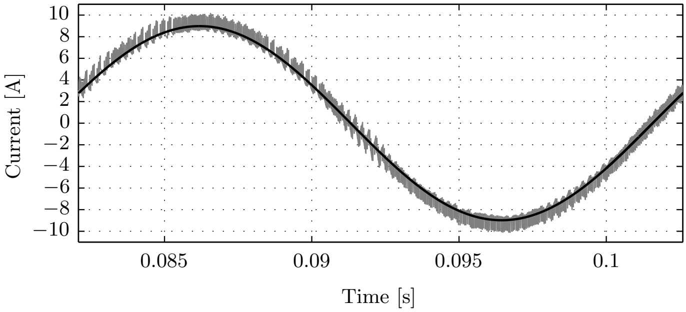

Figure 5.31: Sinusoidal current waveform in phase a

value of the inertia, etc.

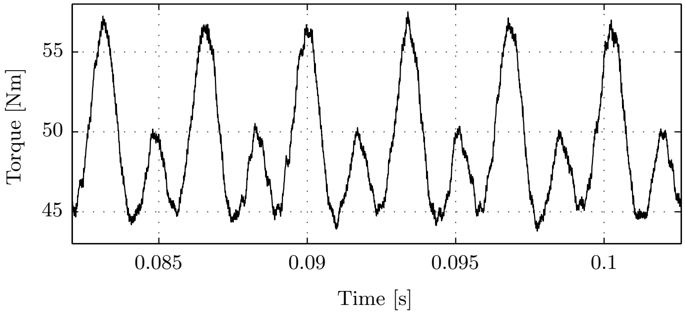

Figure 5.32: Torque for a sinusoidal current

Table 5.8 summarizes the simulation results of the theoretical model, comparing the sinusoidal and optimal current waveforms. The optimal waveform reduces the copper losses with 6%. The iron losses are only slightly reduced. The efficiency gain of the optimal waveform is 0.93 percentage points.

Table 5.9 summarizes the simulation results of the wind turbine model. Compared to the theoretical model, the copper losses have increased slightly. This is caused by the switching ripple in the current, which increases the Joule losses in the stator resistance of the machine and in the equivalent resistance of the converter. Since the current ripple is independent of the chosen waveform, this additional loss component is identical for both the sinusoidal and optimal current waveforms, i.e.,

Table 5.8: Application on a wind turbine: Theoretical results

	T [Nm]	P_{m} [W]	P_{Cu} [W]	P_{Fe} [W]	P_{dc} [W]	η [%]
Sinusoidal current	48.956	2500	402	152	1946	77.84
Optimal current	48.956	2500	379	151	1970	78.77

9 W. The optimal current waveform reduces the total copper losses with 23 W, just as predicted by the theoretical model.

The difference between the iron losses is negligible, i.e., the optimal current waveform has almost no impact. Also, the iron losses have increased considerably when compared to the theoretical model. This is caused by the PWM voltage which is imposed on the stator by the rectifier. This PWM voltage is largely transferred from the stator terminals to the equivalent iron loss resistance, causing high losses there. These iron losses mainly depend on the PWM switching, less on the chosen current waveform. It is well known that a machine connected to a PWM converter has more iron losses than a machine connected to a classical grid voltage due to its high harmonic content [120,121].

Table 5.9: Application on a wind turbine: Results from the wind turbine model

	T [Nm]	P_{m} [W]	P_{Cu} [W]	P_{Fe} [W]	P_{dc} [W]	η [%]
Sinusoidal current	49.006	2500	411	413	1677	67.04
Optimal current	48.997	2500	388	413	1700	67.98

Due to the additional losses, the efficiency is about 10 percentage points lower than in the theoretical model. Still, the efficiency gain equals 0.94 percentage points, which is practically identical to the predicted efficiency gain of the theoretical model. This validates that the optimal current waveform shaping technique has a positive impact on the efficiency of both the machine and the converter.

5.7.6 Conclusions

The optimal current waveform shaping technique was applied on a Simulink simulation model of a wind turbine. The model includes the high-frequent PWM switching of the rectifier, and thus, represents a more realistic situation compared to the theoretical calculations. Although the control system can be seen as an open-loop control, the desired mechanical operating point is reached, as calculated by the theoretical model. Therefore, no closed loop control system is required here.

As expected, the simulation results show a high-frequent switching ripple in the current waveform and torque. This switching ripple increases the copper losses in both the generator and rectifier. Nevertheless, the reduction in copper losses achieved by the optimal current waveform remains the same as predicted by the theoretical model. The high voltage distortion at the machine terminals, caused by the PWM switching of the rectifier, increases the iron losses. Overall, the efficiency gain of the optimal current waveform technique equals 0.94 percentage points, which matches the efficiency gain predicted by the theoretical calculations.

5.8 Imperfections of the optimal current waveform shaping method

Naturally, there is no perfect PMSM model. All models have imperfections and drawbacks. Analytical models and equivalent schemes have the advantage of being useful for theoretical analysis and dynamic simulations. Finite Element Methods allow to model advanced effects in detail, such as hysteresis effects, slotting or cogging. Certain effects which were not included in the analysis before will be discussed here. Others are outside the scope of this work and are left for further research. They are discussed in chapter 8.

5.8.1 Positive temperature feedback

In the parameter sensitivity analysis, the resistance of the stator winding was varied to simulate the impact on the efficiency gain. The effect of the temperature of the stator winding is similar, since the resistance increases as the temperature increases. However, a comparison between the different waveforms in function of temperature is more complex than it seems. All simulations in the case study were performed for the same temperature of 100°C. However, since the optimal current waveform results in fewer losses, the steady state temperature will be lower, reducing the stator resistance, and thus, the copper losses.

This shows that the temperature causes a positive feedback effect. Therefore, it is expected that the efficiency gain of the optimal current waveform will be higher when this effect is taken into account. However, a thermal model is required to determine the expected stator winding temperature in function of the losses. Also, the calculations must be performed iteratively until the model converges to the correct steady state temperature. The modeling of this temperature feedback is not investigated further here, as it is outside the scope of this research.

5.8.2 Skin and proximity effects

Due to the skin and proximity effects, the stator resistance will increase with frequency, while the inductances will decrease. Therefore, the parameters of the equivalent scheme differ for each harmonic component. This frequency-dependence was not taken into account previously, due to several reasons. Firstly, this causes a non-linearity in the model, considerably increasing the complexity of the calculations. Secondly, the proof presented in 3.3 based on the Cauchy-Schwarz inequality is no longer valid if the resistance depends on frequency.

The reason why a proportional current yields a maximum efficiency is that by introducing harmonic currents, the fundamental current can be reduced while the desired mechanical power or torque is still reached, thus reducing the Joule losses. However, when the skin and proximity effects would be included, the harmonic current components will have a larger relative contribution in the total Joule losses than the fundamental current. Therefore, the proof would no longer be valid. In this case, a frequency domain calculation is required to determine the optimal current waveform.

Intuitively, the impact of the skin and proximity effects on optimal current waveform shaping can be explained. Since the harmonic currents have a larger relative contribution in the Joule losses, it is less beneficial to increase the harmonics. Therefore, including these effects will bring the optimal current waveform closer to a sinusoidal waveform.

Obviously, whether the optimal current waveform is infuenced by the skin and proximity effects depends on the gravity of these effects. In some machines, the parameters have a strong frequency-dependence while in others this is not the case. The gravity of the skin and proximity effect depends on several parameters such as the nominal frequency, resistivity of the conductor material, conductor diameter, etc.

Normally, the dominant back-emf harmonics have a low harmonic order, so that the skin- and proximity effects are still limited for these components. Therefore, it is expected that the skin- and proximity effects do not have a significant impact on the validity of the optimal current waveform shaping method for most machines.

5.8.3 Iron loss model

The iron loss model used in this work has proven its usefulness in literature multiple times, e.g., it was used for dynamic simulations of synchronous machines in [57–60]. However, it must be mentioned that iron losses are a complex phenomenon and the equivalent resistance is not incontestably a perfect representation. For instance, it does not model minor hysteresis loops in the iron core.

As the iron losses are not perfectly modeled by the equivalent resistance, the optimal waveform shaping method taking into account the iron losses is not perfect as well. A limited deviation from the theoretical results can be expected in practice. Still, the optimal current waveform shaping method presented in this work is the first to actively take into account the iron losses in the optimisation. This can be considered as a significant improvement compared to classical methods in literature.

Finite element calculations can be used to model the iron losses more accurately, as presented in [120–122]. However, it is a complex or even unfeasible task to combine this with the optimal current waveform shaping method presented here, as it needs a linear equivalent model of the machine. It is due to the linear equivalent machine model that the optimal current waveforms can be expressed by generic closed-form analytic expressions, which is the main strength of the method.

5.9 Conclusions and discussion

In this chapter, the basic optimal current waveform technique of chapter 3, which was based on the Cauchy-Schwarz inequality, was extended to a more advanced machine model. The goal of the research presented in this chapter was to develop a new optimal current waveform shaping technique which needs less assumptions and simplifications than existing techniques in literature. This increases the performance, i.e., the efficiency gain compared to classical sinusoidal and square-wave current waveforms. The following aspects were successfully included in the technique presented here:

- Zero-sequence components
- Unlimited harmonic components in the back-emf
- Iron losses
- Armature reaction
- The reluctance effect

The basic concept of the technique is to translate the optimisation of waveforms in the time-domain to the optimisation of three constants, i.e., the scale factors. A numerical optimisation is still required to determine the scale factors, for which a simple but performant algorithm was presented, i.e., the iterative grid search algorithm.

The developed technique was further investigated and validated in a case study, a parameter sensitivity analysis and an application on a wind turbine. The case study was used to demonstrate the iterative grid search algorithm and the different optimal current waveform equations developed in 5.2, i.e., step-by-step including the different machine effects.

The parameter sensitivity analysis was used to demonstrate the effect of several relevant machine parameters on the performance of the optimal current waveform shaping technique. Investigated parameters are the back-emf waveform, the stator resistance, the ratio of copper and iron losses and the inductance values. It was shown that the optimal current waveform behaves as expected, i.e.:

- The efficiency gain of the optimal waveform increases as the back-emf waveform deviates more from an ideal sinusoidal or trapezoidal waveform.
- A higher stator or converter resistance increases the efficiency gain of the optimal waveform.
- A machine with a higher ratio of iron to copper losses has less efficiency gain. However, it becomes more important to use the complete current waveform equations (5.28) - (5.30) which take into account the iron losses, instead of the simplified equations (5.6) - (5.8).
- In general, the efficiency reduces as the inductance increases for the classical waveforms. However, the optimal current waveform technique maintains a maximum efficiency.

Finally, a practical application, i.e., a small wind turbine system, was simulated in Simulink. The model includes the high-frequent PWM switching of the rectifier. It is explained how the optimal current waveform technique can be applied in practice. There is a good accordance between the desired and actual torque value, even for the proposed open-loop control system. The simulations show the impact of the switching ripples of the current on the efficiency and torque. The optimal waveform still achieves a higher efficiency than a sinusoidal waveform.

Naturally, the presented technique has disadvantages as well. As mentioned before, the torque ripple increases. Depending on the application, this can be an undesired side-effect. For instance, in robotics and servo-applications, torque ripples are to be avoided. In applications where energy efficiency is more critical, such as renewable energy systems, certain industrial drives or battery powered applications, the increased efficiency prevails. The impact of the increased torque ripple also depends on the inertia, damping, speed and overall mechanical design of the application. In electric vehicles, a good compromise between efficiency and torque ripple is required, so that it is less clear which current waveform is best.

Another disadvantage is that there is still a limited amount of numerical optimisation needed, i.e., the determination of the optimal scale factors. However, the optimisation is less time-consuming than in the techniques presented in literature. The numerical optimisations peformed in literature are frequency-domain optimisations or Finite-Element calculations. They often yield an optimal current waveform for one specific machine in a single mechanical operating point. In contrast, the method presented here gives the waveforms in analytical closed-form expressions, for any machine in any operating point. Only the scale factors must be optimised for each machine and operating point. In 5.7.3, it was discussed that the practical implementation can be simplified by using simple second order polynomial curve fits for the scale factors. This can even be simplified further by training these curves on a test bench by an adaptive controller, e.g., starting from linear curves.

At the end of the chapter, a few imperfections of the optimal current waveform shaping method were discussed. These imperfections were not included in the model due to their complexity or even impossibility. The stator resistance causes a positive temperature feedback effect which would increase the efficiency gain of the optimal current waveform if taken into account. The skin and proximity effects cause a frequency dependence of the stator resistance and the inductances. They cannot be taken into account as they cause a non-linearity in the model and the Cauchy-Schwarz proof would no longer be valid. Finally, it is discussed that the equivalent iron loss resistance is not a perfect representation of the iron losses, which are complex. Currently, Finite Element calculations can model the iron losses in more detail, but these cannot be combined with the optimal current waveform shaping method, as this requires a linear equivalent model of the machine.

6

EFFECTIVENESS OF MAXIMUM POWER POINT TRACKING AND THE IMPACT OF LOSSES

The performance of Maximum Power Point Tracking in small and medium wind turbines is investigated. First, the effectiveness of MPPT in steady state is evaluated by analysing measurement data. Then, the influence of losses on the location of the overall MPP is determined. It is shown that it is beneficial to operate the turbine in the overall MPP instead of, classicaly, the MPP of the turbine.

Contents

6.1 Introduction

In the previous chapters, control of the generator currents on the level of the waveform was discussed. In this chapter, the current control is investigated on a higher level, i.e., Maximum Power Point Tracking. First, the steady-state effectiveness of MPPT in commercial small wind turbines is investigated by analysing measurements which conform to the IEC 61400-2 standard, published by the National Renewable Energy Laboratory (NREL). It is shown that small wind turbines often fail at regulating the turbine to the MPP properly. This means that there is room for improvement to increase the energy yield by properly setting up the MPPT algorithm. This research was published in [123].

In the second part of this chapter, the impact of losses on the MPP is investigated by simulating the complete system, including the most important losses. Classicaly, it is assumed that the MPPT must regulate the turbine to the optimal operating point of the turbine. However, this operating point is not necessarily optimal for the complete system. For instance, it could be worthwhile to operate at a slightly lower rotor speed to reduce mechanical losses and iron losses in the generator, leading to an overall increase in power. In this chapter, it is shown that 1% to 2% more energy yield can be achieved by taking this effect into account. This research was published in [124].

At the end of the chapter, a few research opportunities are given to improve the MPPT in the future. During this research, no research was performed on MPPT algorithms itself as it was not an objective of the research. Also, much work has already been done on this topic in literature.

6.2 Evaluation of the MPPT performance in existing turbines

Manufacturers of wind turbine systems and converters claim a good operation of the MPPT, and thus a maximal power coefficient. Since the MPPT is of high importance for the cost-effectiveness of small wind turbines, it is worthwhile to verify whether the MPPT in commercial turbines actually performs well. Therefore, the performance of the MPPT in commercial wind turbines is evaluated by using measurements based on the IEC 61400-2 standard [125]. Manufacturers perform these measurements to calculate the power curve, since this is vital information to calculate the yearly energy yield for a customer. These test data will now be used to calculate the operating point of the turbine for each wind speed such that it can be compared with the optimal operating point. The goal is to make a sound evaluation of the performance of MPPTs in commercial turbines. This also leads to an estimation of the room for improvement.

6.2.1 Ideal TSR versus wind speed curve

All MPPT algorithms should result in a TSR equal to the optimal value for each wind speed, independent of the actual implementation. In other words, the TSR should be constant for a well functioning MPPT. Exceptions can however be found at very low and very high wind speeds. For a very low wind speed, i.e., below the cut-in speed v_{ci}, the turbine will not be able to start, since the turbine cannot overcome the cogging torque of the generator. For a very high wind speed, i.e., above the nominal wind speed v_{nom}, the rotor speed should be limited to the nominal value Ω_{nom} to prevent mechanical damage. This leads to an ideal λ versus wind speed curve, e.g., as shown in Fig. 6.1.

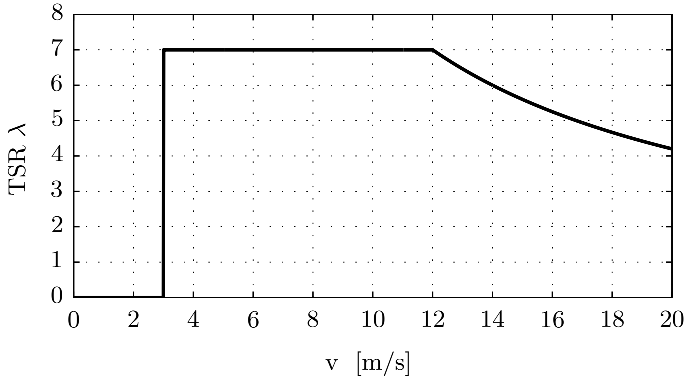

Figure 6.1: Ideal λ versus wind speed curve

This curve can be divided in three zones:

1. **Low wind zone:** $v < v_{\text{ci}}$
   The wind speed is too low for the turbine to start. The rotor

speed Ω, and thus λ, is zero:

$$\lambda = 0 \tag{6.1}$$

2. **Normal wind zone:** $v_{\text{ci}} < v < v_{\text{nom}}$
This is the normal operation zone, where the MPPT should control λ equal to the optimal value λ_{opt}:

$$\lambda = \lambda_{\text{opt}} \tag{6.2}$$

3. **High wind zone:** $v_{\text{nom}} < v$
In high wind conditions, the rotor speed Ω must be kept constant to prevent mechanical damage. The TSR λ will decrease for increasing wind speeds, according to:

$$\lambda = \frac{R\Omega_{\text{nom}}}{v} \tag{6.3}$$

For a small wind turbine with a well functioning MPPT, the $\lambda(v)$ curve should match the ideal curve of Fig. 6.1. The turbine then produces the maximum achievable power for each wind speed. This will now be analysed for measurements of three commercial wind turbines.

6.2.2 Evaluation of commercial turbines

The estimated yearly energy output of a small wind turbine is of high importance for potential customers. Together with the investment and maintenance costs, this allows to calculate the financial profit and payback time. The yearly energy output can be calculated from the wind speed distribution of the specific location and the power curve of the turbine. Therefore, accurate knowledge of the power curve is very important.

In order to guide a correct measurement of the power curve, the IEC 61400-2 [125] standard has been introduced. The compulsory use of this standard ensures that every manufacturer gives reliable power curve data to the customers. According to the standard, the power injected into the grid must be measured together with the wind speed. The data are then grouped and averaged in intervals of 0.5 m/s, resulting in the power curve.

Sometimes, not only power and wind speed are measured, but also the rotor speed Ω. When an encoder is present in the generator, this measurement is easily done. In this paper, the results of these IEC 61400-2 measurements including rotor speed will be used to calculate the real $\lambda(v)$ curve and compare it with the ideal curve of Fig. 6.1. The data have been collected for the Fortis Alizé [126], the Xzeres 442 [127] and the Mariah Windspire [128].

The Fortis Alizé and Xzeres 442 are both turbines with a horizontal axis and three blades. The Mariah Windspire is a vertical axis turbine. These three turbines are selected here since they are the only turbines of which IEC 61400-2 measurement data were found where the rotor speed was included in the measurements. Table 6.1 shows the relevant parameters of these turbines, i.e., the nominal power P_{nom}, the cut-in wind speed v_{ci}, the nominal wind speed v_{nom}, the cut-out wind speed v_{co}, the turbine radius R, the nominal rotor speed Ω_{nom}. The nominal values must be interpreted in the sense that, in theory, the nominal power is delivered if the wind and rotor speeds equal their nominal values. In practice, this is not necessarily the case due to, e.g., MPPT deviations or wind variability.

Table 6.1: Wind turbine parameters

	P_{nom}	v_{ci}	v_{nom}	v_{co}	R	A	Ω_{nom}
	[kW]	[m/s]	[m/s]	[m/s]	[m]	[m^2]	[rpm]
Fortis Alizé	10	3	12	25	3.5	38.5	300
Xzeres 442	10	2.2	11	?	3.6	40.7	145
Mariah Windspire	1	4	11	12	1.5	18.6	370

These data can be found in the datasheets of the turbines and the IEC test reports. A remark must be made concerning the diameter of the Xzeres 442. According to the manufacturer, the rotor diameter of the Xzeres 442 is 7.2 m. However, a diameter of 7.4 m was measured by the NREL. In the research presented here, a diameter of 7.2 m is used. The cut-out wind speed of the Xzeres is unknown, although the measurements indicate that there is power until at least 18 m/s.

The table in appendix B shows the relevant data from [126–128], i.e., the power P injected in the grid, the power P_w available in the wind, the wind speed v and the rotor speed Ω. The power P_w was calculated with:

$$P_w = \frac{1}{2}\rho A v^3 \tag{6.4}$$

To calculate this power, a value for the air density ρ is needed. For the Fortis Alizé, a value of 1.225 kg/m^3 at a temperature of 15°C is assumed. For the Xzeres 442, an average value of 1.035 kg/m^3 was measured [127]. For the Mariah Windspire, an average value of 0.970 kg/m^3 was measured [128]. The air density differs for the three turbines due to differences in temperature and altitude.

The optimal TSR λ_{opt} cannot be simply found in the datasheet as it is often proprietary information. There are several possibilities to estimate this value. As a first possibility, the optimal TSR can be calculated from the nominal operating point:

$$\lambda_{\text{opt}} = \frac{R\Omega_{\text{nom}}}{v_{\text{nom}}} \tag{6.5}$$

However, it is not certain that the nominal parameters were chosen to match the optimal TSR during the design of the turbine. Several other aspects such as noise or cost reduction can influence the design.

Therefore, the optimal TSR λ_{opt} can also be estimated by identifying the operating point where the ratio of grid power versus wind power is at a maximum. There, the product of the turbine's power coefficient and the efficiency of the generator and converter is at a maximum. This condition is reached for a wind speed of 6 m/s for the Fortis Alizé, 7 m/s for the Xzeres 442 and 10 m/s for the Mariah Windspire. Then, the optimal TSR is calculated from the measured rotor speed. The validity of this estimation method is limited by the spread on the measured operating points. It cannot be stated with certainty that no other more optimal TSR value exists which was not encountered in the measurements.

A third possible way to estimate the optimal TSR is to take the average of all measured TSR values in the normal wind speed zone. Under the hypothesis that the deviation of the MPPT has a normal distribution, the measured TSR is as often above as below the optimal value.

In that case, the average TSR corresponds with the optimal value.

Table 6.2 shows the optimal TSR values for the three possible estimation methods mentioned above. The TSR λ_{nom} is based on the nominal operating point. The TSR λ_{max} is based on the operating point where the ratio of grid power and wind power is at a maximum. The TSR λ_{mean} is the average of the measured values in the normal wind speed zone.

Table 6.2: Estimations of the optimal TSR

	λ_{nom}	λ_{max}	λ_{mean}
Fortis Alizé	9.16	9.29	8.95
Xzeres 442	4.97	5.65	4.86
Mariah Windspire	5.28	5.76	5.50

The estimated optimal values are comparable for the three methods. All three methods have their strengths and imperfections so that there is no perfect choice. It is preferential to obtain the optimal value from the manufacturer, but this rarely possible in practice. For the calculations which follow, the values of the first column λ_{nom} were used.

The Mariah Windspire is a giromill-type turbine, which is a variant of the Darrieus and is lift-based. The obtained TSR value around 5.5 is a normal value for a giromill. However, the values for the Xzeres and Fortis turbines are notably low and high respectively. For three-bladed horizontal axis turbines, an optimal TSR between 6 and 8 can be expected. This deviation can be partly explained by the blade design. Other possible reasons are that the manufacturer of the Xzeres turbine deliberately set a low TSR to reduce noise, mechanical losses or iron losses in the generator. The manufacturer of the Fortis turbine may have set a high TSR to reduce the converter losses and the copper losses in the generator, since a high speed means more voltage and less current for the same power.

Fig. 6.2 shows the measured power curves $P(v)$ of the turbines. The power curves clearly show that there is no produced power for wind speeds below the cut-in speed v_{ci}. For higher wind speeds, the power

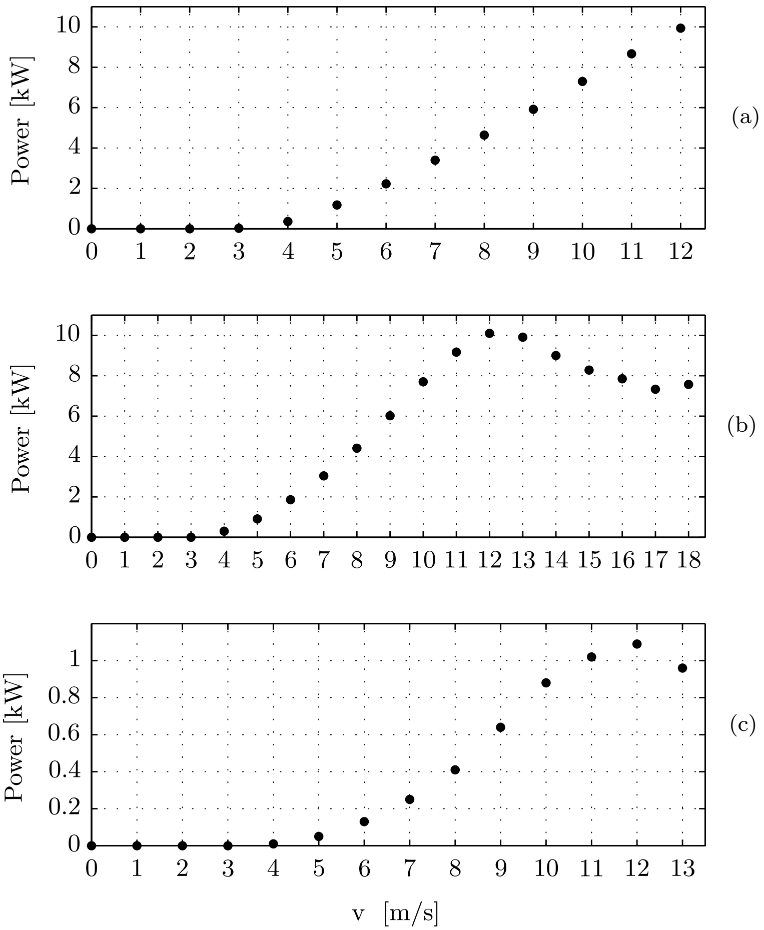

Figure 6.2: Power curves: (a) Fortis Alizé, (b) Xzeres 442 and (c) Mariah Windspire

curve resembles a third order function according to (2.1). For the Fortis Alizé, there are only data available up to a wind speed of 12 m/s, which is the nominal wind speed. For the Xzeres 442 and Mariah Windspire however, measurements have been made for wind speeds higher than the nominal value of 11 m/s. In this high-speed region, the power of the turbine is clearly limited, which can be caused by an overvoltage protection in the rectifier, a rotor speed limiting mechanism or stall.

From the rotor speed and wind speed data, the $\lambda(v)$ curves can now be plotted together with the ideal $\lambda(v)$ curve of Fig. 6.1. Fig. 6.3 shows these curves for the Fortis Alizé, the Xzeres 442 and the Mariah Windspire respectively. The solid line represents the ideal $\lambda(v)$ curve, while the dots represent the real λ values.

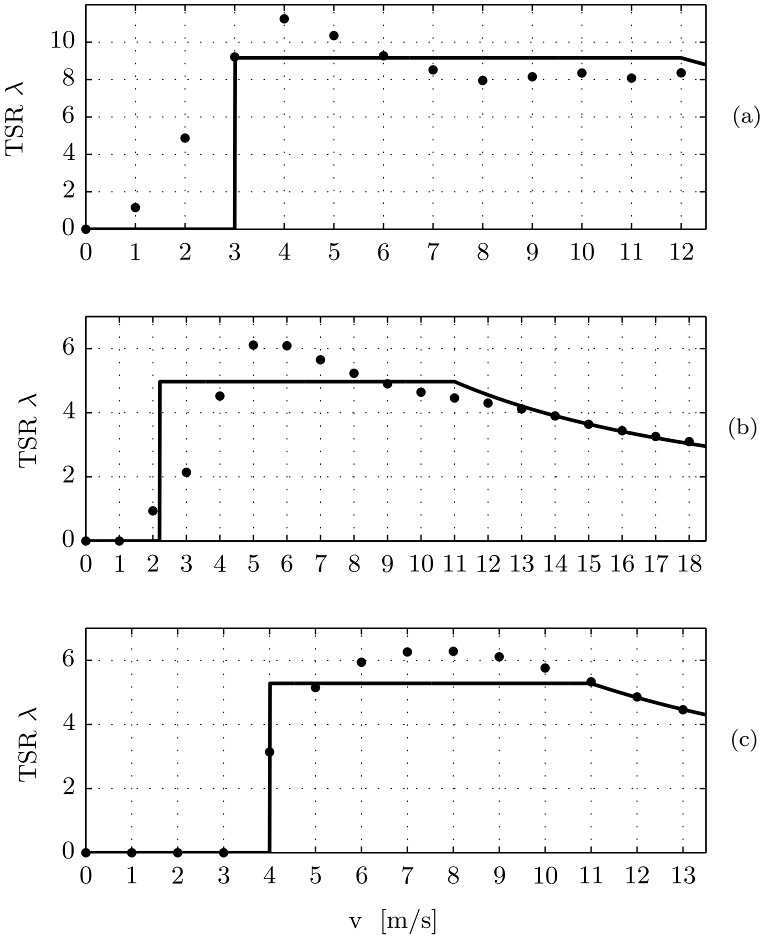

Figure 6.3: $\lambda(v)$ curves: (a) Fortis Alizé, (b) Xzeres 442 and (c) Mariah Windspire

These figures give a clear overview of the MPPT performance for the complete range of wind speeds. This figure can be plotted for other wind turbines as well. A rotor speed and wind speed measurement is sufficient to plot these curves. The figures will now be discussed in more detail.

Low wind speed zone: $v < v_{\mathrm{ci}}$

In the low wind speed zone, no power is injected into the grid as can be seen in the power curves. The $\lambda(v)$ curves however show that the Fortis Alizé and Xzeres 442 turbines have a non-zero TSR and thus are rotating. The power produced by the rotating turbine is converted into losses since no power is injected into the grid. Therefore, this only leads to mechanical wear and no power production.

Normal wind speed zone: $v_{\mathrm{ci}} < v < v_{\mathrm{nom}}$

The small wind turbine system should have the largest part of its energy production in the normal wind speed zone, since it is the most frequently encountered zone of operation. Therefore, the MPPT performance is of high importance in this zone. The $\lambda(v)$ curves of the figures show that there is a deviation from the optimal $\lambda(v)$ for all three wind turbine systems. This shows the ineffective operation of the MPPT in this zone. On the other hand, an improvement of the MPPT in this zone could create a considerable increase in the yearly energy output, as will be calculated later in this chapter.

High wind speed zone: $v_{\mathrm{nom}} < v$

In the high wind speed zone, the rotor speed must be limited to prevent mechanical damage. There are no data available in this zone for the Fortis Alizé. The Xzeres 442 and Mariah Windspire however show that there is a very good agreement between the real $\lambda(v)$ and the optimal value. This shows that the turbine systems perform well in the high wind zone. Therefore, little improvement in the energy output can be found there.

The overall conclusion from the $\lambda(v)$ curves is that the low wind zone can be improved by stopping the turbine rotation to avoid unnecessary wear, the normal wind zone can be improved by a more accurate MPPT and the high wind zone is already performant enough as it is. Especially an improved MPPT performance in the normal wind zone can result in a significant increase in energy production. This increase will be estimated in the following section.

6.2.3 Increased energy production for an ideal MPPT

From the previously calculated real and ideal $\lambda(v)$ curves, an estimation can be made of the increase in yearly energy production if the MPPT would have an ideal operation. For this estimation, the following steps will be taken:

1. A realistic $C_\mathrm{p}(\lambda)$ curve will be chosen from literature, which was fitted on measured turbine data.
2. Based on this $C_\mathrm{p}(\lambda)$, the power curve that corresponds with an ideal MPPT will be calculated from the original power curve.
3. A realistic wind speed distribution will be chosen to calculate the yearly energy output for both the new and original power curves.

Selection of the $C_\mathrm{p}(\lambda)$ curve

Several empiric $C_\mathrm{p}(\lambda)$ curves can be found in literature [46,48,49,129–135]. These curves differ slightly in shape but correspond well with eachother around the maximum power point. The previously shown $C_\mathrm{p}(\lambda)$ curve (2.3) of Fig. 2.3 will be used here.

Although this $C_\mathrm{p}(\lambda)$ curve has a maximum C_p of 0.44 and an optimal λ of 6.91, this is not necessarily the case for the three commercial turbines discussed in this paper. The maximum C_p of these turbines is not known. The optimal λ however was discussed and estimated before. The uncertainty of the maximal C_p is not a problem for the following calculations, since the $C_\mathrm{p}(\lambda)$ curve of (2.3) can be divided by the maximum value of 0.44. The curve can then be shifted such that the maximum is reached for the correct optimal λ. This results in a relative $C_\mathrm{p}(\lambda)$ curve, which will be denoted $c_\mathrm{pr}(\lambda)$ here:

$$c_\mathrm{pr}(\lambda) = \left(\frac{249.9}{\lambda + 6.91 - \lambda_\mathrm{opt}} - 22.59\right) \cdot e^{\left(\frac{-18.4}{\lambda+6.91-\lambda_\mathrm{opt}}+0.055\right)} \tag{6.6}$$

Power curve with ideal MPPT

The original power curve $P(v)$ can be converted to the power curve that corresponds to an ideal MPPT in the normal wind speed zone. The low and high wind speed zones remain unchanged. This new power curve will be denoted $P_n(v)$ and can be calculated as follows:

$$P_n(v) = \begin{cases} P(v), & \text{for } v < v_{\text{ci}} \\ \frac{1}{c_{\text{pr}}(\lambda)} P(v), & \text{for } v_{\text{ci}} < v < v_{\text{nom}} \\ P(v), & \text{for } v_{\text{nom}} < v \end{cases} \tag{6.7}$$

For each wind speed, the measured power value is corrected to the value corresponding to the MPP by rescaling with the relative power coefficient.

The $C_{\text{p}}(\lambda)$ curve used here does not necessarily correspond to the true $C_{\text{p}}(\lambda)$ curve of the considered turbine. Therefore, the calculated power values and energy yields which are calculated hereafter are approximations. However, by scaling and shifting the $C_{\text{p}}(\lambda)$ curve, only the shape is relevant in the calculations. The accuracy of the calculations is mainly determined by the wideness of the true $C_{\text{p}}(\lambda)$ curve around the maximum. Preferably, the shape of the true $C_{\text{p}}(\lambda)$ curve is as close as possible to the shape of (6.6) around the maximum.

Realistic wind speed distribution

Wind speed is modeled here by a Rayleigh probability distribution $r(v)$, which is given by:

$$r(v) = \frac{\pi}{2}\,\frac{v}{\bar{v}^2}\,\exp\left(-\frac{\pi}{4}\frac{v^2}{\bar{v}^2}\right) \tag{6.8}$$

The parameter $\bar{v}$ is the average wind speed and is the only parameter in this probability distribution function. This Rayleigh distribution is shown in Fig. 6.4 for an average wind speed $\bar{v}$ of 5 m/s.

Other distributions can be used to model wind speed as well, such as a Weibull distribution, Generalized Gamma, Lognormal, etc [136]. Also, a histogram of measured data can be used to model the wind of a specific location. Due to the strong variability and unpredictability and the influence of the environment, the distribution of wind speed

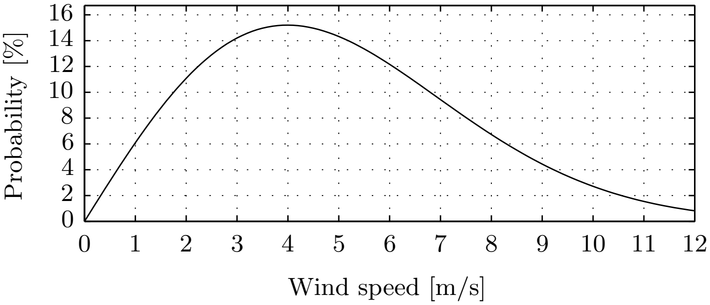

Figure 6.4: Rayleigh wind speed distribution for $\bar{v}$ =5 m/s

differs for each location. Therefore, there is no general correct distribution.

Since the power curve is available in a discrete form, the probability distribution should be discretized. The probability that the wind speed is in an interval of 1 m/s around the discrete value u is calculated by:

$$\begin{aligned} R(u) &= \int_{u-0.5}^{u+0.5} \frac{\pi}{2} \frac{v}{\bar{v}^2} \exp\left(-\frac{\pi}{4}\frac{v^2}{\bar{v}^2}\right) \, dv \\ &= \exp\left(-\frac{\pi}{4}\frac{(u-0.5)^2}{\bar{v}^2}\right) - \exp\left(-\frac{\pi}{4}\frac{(u+0.5)^2}{\bar{v}^2}\right) \end{aligned} \tag{6.9}$$

Yearly energy yield

Based on the original power curve $P(v)$, the new power curve $P_n(v)$ and the discrete wind speed distribution $R(u)$, the yearly energy output E of the turbine can be calculated. The yearly energy output E for the original power curve is calculated as follows:

$$E = 8760 \cdot \sum_{u=0}^{v_{\max}} R(u) \cdot P(u) \tag{6.10}$$

The factor 8760 is the number of hours in a year. The parameter $v_{\max}$ is the wind speed up to which data is available in appendix B. In an analogous way, the yearly energy output E_n of the new power curve is calculated as follows:

$$E_n = 8760 \cdot \sum_{u=0}^{v_{\max}} R(u) \cdot P_n(u) \tag{6.11}$$

Results

The results of the energy yield calculation are presented in Fig. 6.5. The energy yields E and E_n are calculated for different values of the mean wind speed $\bar{v}$, which is determined by the location of the turbine. Fig. 6.6 shows the procentual improvement of E_n versus E.

These figures show that the improvement of the energy yield strongly depends on the average wind speed of the location. Most locations suitable for small wind turbines have an average wind speed between 4 m/s and 6 m/s. Locations with an average wind speed below 3 m/s are not suitable for these small wind turbines while locations with an average wind speed above 6 m/s are rare, i.e., only encountered in coastal areas or the desert. Therefore, a more interesting value is 5 m/s. Here, the Fortis Alizé has an energy yield improvement of 7.7%, 2.9% for the Xzeres 442 and 4.5% for the Mariah Windspire. This corresponds to a yearly increase of the energy output of 1220 kWh for the Fortis Alizé, 452 kWh for the Xzeres 442 and 61.5 kWh for the Mariah Windspire. Averaged for the three turbines, the improvement is 5.0% at 5 m/s. On a location with a lower average wind speed of 4 m/s, this improvement is even 6.2%.

For high average wind speeds, data above the nominal wind speed starts to have an impact on the energy yield. However, at these high wind speeds, the behavior of the considered wind turbines is not entirely certain. According to the test reports, the Fortis Alizé maintains its nominal power up to 16 m/s, although the nominal wind speed is 12 m/s. Above 16 m/s, the power drops to about 4 kW. At the cut-out wind speed of 25 m/s, the turbine is shut down for safety reasons. The manufacturer of the Xzeres turbine provides no information on the produced power above the nominal wind speed. The measurements in the NREL test report show how the power gradually decreases to about 7.5 kW at 18 m/s. No measurements are available above 18 m/s. Also, the cut-out wind speed is unknown. The only turbine for which the behavior above nominal wind speed is clear, is the Mariah Windspire. This turbine shuts down at the cut-out wind

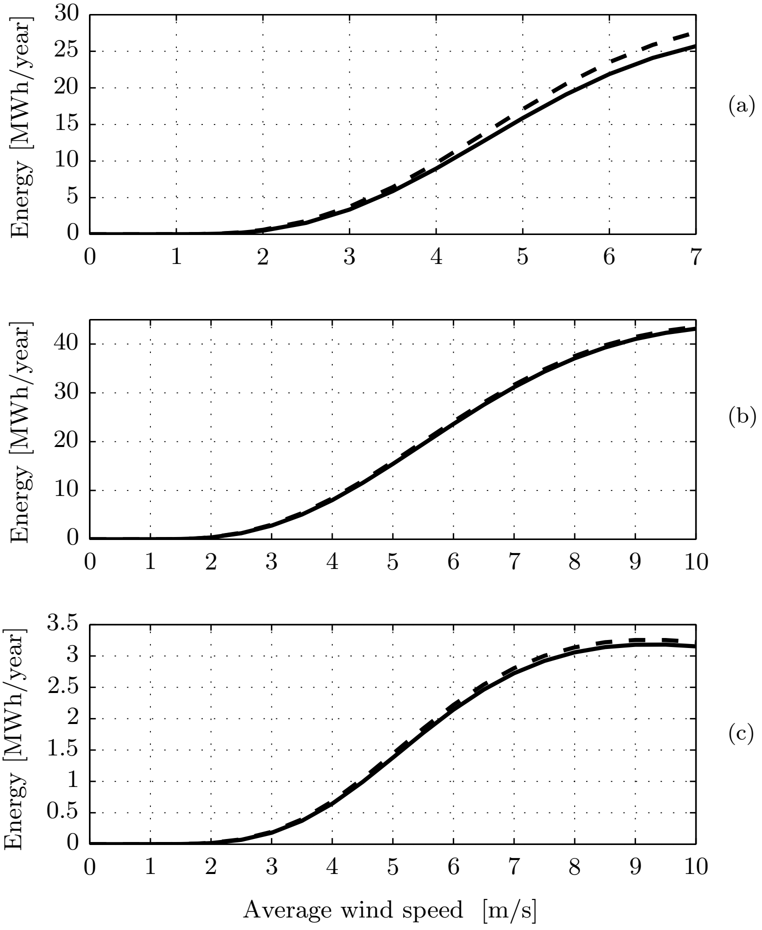

Figure 6.5: Energy yields E (full line) and E_n (dashed line): (a) Fortis Alizé, (b) Xzeres 442 and (c) Mariah Windspire

speed of 12 m/s, which is just slightly above the nominal value.

For the reasons stated above, the energy yields for the Fortis Alizé are simulated up to 7 m/s. Above this value, the behavior of the turbine above nominal wind speeds starts to have an impact. This behavior is not sufficiently certain. For the Xzeres and Mariah Windspire turbines, there is sufficient data to calculate the energy yield for average wind speeds up to 10 m/s.

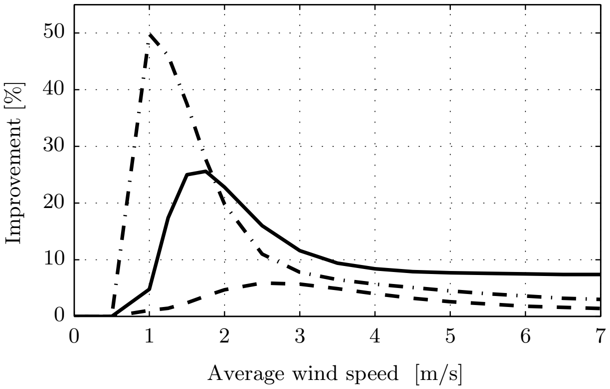

Figure 6.6: Improvement of E_n versus E: full line = Fortis Alizé, dashed line = Xzeres 442 and dot dash line = Mariah Windspire

6.2.4 Conclusions

Publicly available measurement data from IEC 61400-2 measurements was used to verify whether the MPPT works effectively. For the considered turbines, the Fortis Alizé, the Xzeres 442 and the Mariah Windspire, a deviation from the MPP was noted in the normal wind zone, caused by the ineffective operation of the MPPT.

The cause of this deviation cannot be easily found, since manufacturers are mostly not willing to give proprietary details about their products. An improved MPPT accuracy would result in an increased yearly energy yield. This improvement was estimated by calculating the power curve that corresponds to an ideal MPPT in the normal wind speed zone. The result is an average 5.0% increase in yearly energy production in a 5 m/s average wind speed location. The overall conclusion is that there is a room for improvement in financial profit of small wind turbines by increasing the MPPT performance. This improvement reaches even higher values in locations with a lower average wind speed.

It must be noted that the calculated improvement can only be reached if the MPPT is perfect and the MPP is exactly reached for all wind speeds in the normal wind zone. In practice, it cannot be expected that an MPPT performs perfectly. Therefore, it must be seen as a theoretical room for improvement.

It is also important to see that the analysis performed here only concerns steady-state situations. Wind at low altitudes is known to be rather chaotic. Due to the mechanical inertia and limited reaction time of the system, it is impossible for a turbine to follow all variations in wind speed. Theoretically, this would lead to a considerable increase in energy output. At the end of this chapter, in §6.4, the possibility of following these dynamic variations of wind speed with a turbine will be discussed.

6.3 Impact of losses on the location of the MPP

In the design of MPPT algorithms, it is often assumed that the controller must maximize the power coefficient of the turbine. Although this is the optimal operating point of the turbine, this is not necessarily the optimal operating point of the complete system, i.e., including the generator and power electronics. In [71], it was already mentioned that the generator and converter losses can cause a difference between the turbine MPP and the overall MPP, which will be called TMPP and OMPP here. For example, since mechanical losses increase with rotational speed, it is beneficial to operate at a speed slightly below the value corresponding with the TMPP. Moreover, the iron and copper losses of the generator differ for each mechanical operating point, again resulting in a difference between the OMPP and the TMPP. Finally, the switching and conduction losses of the converter have a similar effect.

It is crucial to know the location of the OMPP of the turbine system, such that the controller can be programmed to regulate the turbine to this OMPP instead of the TMPP. This will reduce losses and, thus, increase the total energy yield of the turbine system. In [137], it was shown how the generator losses can affect the optimal rectified dc voltage, and thus the MPP. Here, also the converter losses are included in the analysis and the mechanical loss model is extended, including friction in the radial shaft seals and windage losses. This allows to calculate the OMPP by taking into account the complete system, up to the grid connection. The research of this topic was published in [124], where more details can be found if needed.

A simulation model was developed for a complete 1kW turbine system in Matlab/Simulink using the SimPowerSystems toolbox. Details of the models can be found in chapter 2. The parameters used in the model are based on realistic components as much as possible. They are summarised in the following tables. The weight of the turbine m_T is based on the Raum 1.5, which has a similar blade length R. The simulated PMSG has the same parameters as the PMSG in the Wind Turbine Emulator 1 (WTE1) setup of EELAB, i.e., a Mecc Alte Eogen 60/16. The equivalent resistance R_D and forward voltage V_F of the diodes in the rectifier are based on the NXP BYC5B-600 diode. The resistance $R_{M,bc}$ of the switch in the boost chopper is based on the 12 A Ixys IXFH12N100F Mosfet. The resistance $R_{M,i}$ of the switches in the inverter is based on the 1.5 A Vishay IRF710PBF Mosfet. $f_{\mathrm{SW,bc}}$ and $f_{\mathrm{SW,i}}$ are the switching frequencies of the boost chopper and the inverter respectively. The dc voltage at the inverter input is regulated at 750 V.

Table 6.3: Turbine parameters

P_r	ρ	R	F	v_r	Ω_r	m_T
[kW]	[kg/m^3]	[m]	[Nm s]	[m/s]	[rpm]	[kg]
1	1.225	1.27	0.06	9	470	7

Table 6.4: PMSG parameters

P_r	N_p	Ψ_PM	R_s	L_d	L_q	K_f
[kW]	[/]	[Wb]	[Ω]	[mH]	[mH]	[μS]
1	8	1.188	13.47	257	103	283
K_h	m_G	d	D	L	S	μ
[mS/s]	[kg]	[mm]	[mm]	[mm]	[/]	[/]
26.6	26.6	95	193	215	2	0.0015

Table 6.5: Converter parameters

C_{ch}	L_{ch}	C_{dc}	L_f	R_D	V_F	$R_{\mathrm{M,bc}}$	$R_{\mathrm{M,i}}$	$f_{\mathrm{SW,bc}}$	$f_{\mathrm{SW,i}}$
[μF]	[mH]	[mF]	[mH]	[mΩ]	[V]	[Ω]	[Ω]	[kHz]	[kHz]
100	5	2	40	90	1.3	1.05	3.6	2	20

6.3.1 Simulated losses and efficiencies

First, the model is used to simulate the losses for a whole range of operating points. From this, the efficiencies of the turbine, generator, diode rectifier, boost chopper and inverter can be calculated, which offers more insight in how the losses affect the position of the MPP. Here, the efficiency is represented as a 3D surface in function of torque and rotational speed. Temperature influences are not considered.

Mechanical efficiency

Fig. 6.7 shows the contour plot of the mechanical efficiency η_{M}, defined as $P_{\mathrm{m}}/P_{\mathrm{t}}$. The efficiency ranges from 70% for low torque up to 96% for high torque values. Since the friction losses in the bearings and radial shaft seals dominate the windage losses, the total mechanical losses are approximately linear with speed, according to (2.8). From this, it becomes clear that the mechanical efficiency η_{M} mainly depends on torque, as is confirmed by Fig. 6.7.

Generator efficiency

The generator efficiency η_{G} is calculated as $P_{\mathrm{e}}/P_{\mathrm{m}}$. Fig. 6.8 shows the contour plot of η_{G}. Implicitly, the impact of current harmonics on the losses is included in these calculations, since the complete converter was connected to the PMSG during the simulations. Consequently, also torque ripples are present in the model.

The efficiency reaches peak values of 80% around the rated operating point of 1 kW at a speed of 470 rpm and a torque of 20 Nm. Roughly speaking, more torque means more copper losses since torque is determined by current. Higher rotational speed means more iron losses. There is a small area with a reduced efficiency of 50% - 60% for high torque and low rotational speed, which is caused by the fact that copper losses will be high due to the high torque, but total power is low due to the low rotational speed. The efficiency is significantly reduced (below 50%) for low torque in the whole speed range. This is caused by the iron losses which remain relatively high while total power is low.

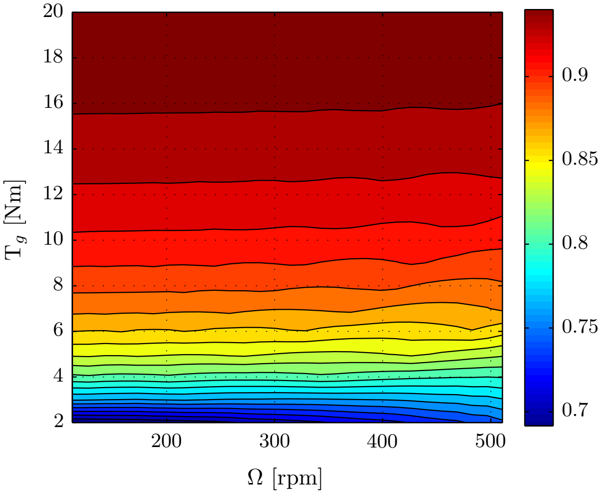

Figure 6.7: Mechanical efficiency η_{M}

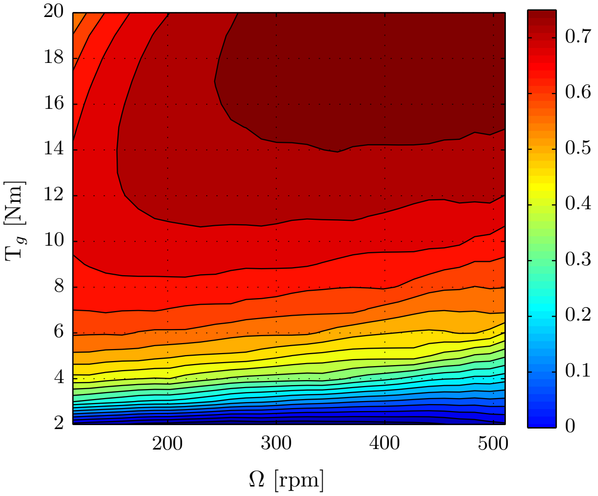

Figure 6.8: Generator efficiency η_{G}

The impact of the generator losses on the MPP can be qualitatively predicted based on Fig. 6.8. For high wind speeds, where speed, torque and power are high, the generator efficiency is rather constant and lies between 70% and 80%. Since the efficiency does not vary much in this region, the generator will only cause a small shift of the MPP. In contrast, for low wind speed and thus low rotational speed, torque and power, the efficiency surface has a stronger gradient. From this, it can be expected that the generator has a significant impact on the MPP for low wind speeds.

Converter efficiency

The efficiency η_C of the converter is calculated as P_e/P_g and shown in Fig. 6.9. The efficiency surface is similar in shape as the generator efficiency. Again, high efficiency values of 86% are reached for high power levels, around the rated operating point of 1 kW.

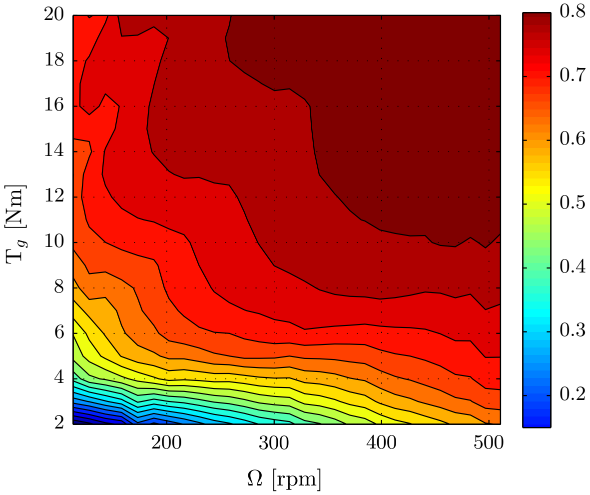

Figure 6.9: Converter efficiency η_C

For high torque and low rotational speed, the efficiency reduces a little to values between 70% and 80%. Here, conduction losses in the diodes and the switch are high since current is high, but the power is low due to the low speed, leading to a reduced efficiency. For low torque and low speed, the efficiency is below 60%. Although conduction losses decrease when torque is reduced, the switching losses remain constant, leading to these low efficiency values.

Since the shape of the efficiency surfaces in Fig. 6.8 and Fig. 6.9 are similar, the effect on the MPP will also be similar to that of the generator. For high wind speeds, where torque and speed are high, η_{C} does not vary much such that the shifting of the MPP will be limited. For low wind speed however, the η_{C} surface has a strong gradient, leading to a larger shift of the MPP.

6.3.2 Simulation results

The simulation model is now used to calculate the effect of the losses on the location of the MPP. A constant wind speed is imposed on the turbine while the duty ratio of the PWM modulator for the boost chopper is varied from 0, i.e., an open switch, to 1, i.e., a closed switch. There is no MPPT algorithm present in the control of the chopper. In this manner, a whole range of operating points is calculated in which the power first increases, then reaches a maximum and finally decreases. From this, it can be visualized how the MPP shifts by including the several losses in the system. At the turbine output, the MPP equals the TMPP. At the grid side, the MPP has shifted to the OMPP which is the true optimal operating point of the turbine system. The simulations are performed for several wind speed values, showing the impact of the losses for low, medium and high power.

Low wind speed

Most small wind turbines have a cut-in wind speed around 3 m/s. Below this wind speed, the starting torque of the turbine is not sufficient to overcome the cogging torque and the static friction in the drivetrain. The first simulations will be performed at a value slightly above this cut-in speed, i.e., 5 m/s.

Fig. 6.10 shows the simulated power and efficiency curves in function of λ. The maxima are shown with a circle. The maximum of the turbine power P_{t} is the TMPP with a value of 171 W at a TSR of 6.91. Going further in the system, the power reduces due to losses, and the maximum shifts to the left. The maximum of the grid power

P_g is the OMPP which has a value of 47 W at a TSR of 6.33.

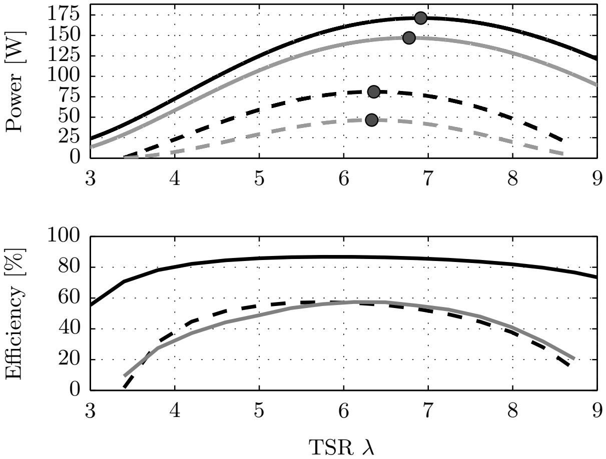

Figure 6.10: Power and efficiency versus λ: Low wind speed of 5 m/s
Power: — P_t, — P_m, ‒ ‒ P_e, ‒ ‒ P_g,
Efficiency: — η_M, ‒ ‒ η_G, — η_C

This simulation shows that, for a low wind speed, the λ value of the OMPP differs considerably from the TMPP. Classical MPPT methods operate the turbine in the TMPP, which would lead to a grid power of 43 W. The OMPP results in 9% more power, i.e., 47 W. The generator has the largest impact on the MPP. This can be explained by the gradient of the efficiency η_G around the MPP.

Medium wind speed

For the medium wind speed, a value of 7 m/s is set. Fig. 6.11 shows the simulated power and efficiency curves in function of λ. The turbine power equals 471 W at a TSR of 6.91. For the grid power, the OMPP has a value of 254 W at a λ of 6.60. Again, the losses in the system cause the MPP to shift to the left. However, the effect is less dramatic, which can be explained by the fact that the efficiency curves are more flat around the MPP. In the TMPP, the grid power equals 253 W, which is only 1 W below the real optimum of 254 W.

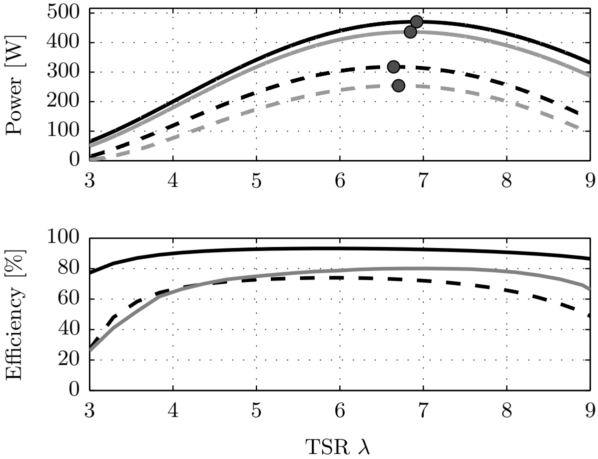

Figure 6.11: Power and efficiency versus λ: Medium wind speed of 7 m/s
Power: — P_{t}, — P_{m}, - - P_{e}, - - P_{g},
Efficiency: — η_{M}, - - η_{G}, — η_{C}

High wind speed

The wind speed is now set at the rated value of 9 m/s. Fig. 6.12 shows the simulated power and efficiency curves in function of λ. The TMPP has a turbine power value of 1000 W at a TSR of 6.91. The difference between the TSR value of the OMPP and the TMPP has become negligible, as both have a grid power of 644 W. The mechanical losses cause a displacement to the left, but this is compensated by the generator and converter losses which cause a shift to the right.

Discussion

As the previous simulations have shown, the TSR value of the OMPP can differ considerably from the TMPP for low wind speeds. The procentual gain is high for low wind speeds, e.g., reaching 30% for 4 m/s. For high wind speeds, the gain drops and the effect becomes negligible.

On the one hand, power values are low in the region where the procentual gain is high. On the other hand, these low wind speeds have a higher probability of occurence. The parameter of interest is the yearly energy production, as it determines the return on investment time and economical profit. To calculate this, a Rayleigh wind speed

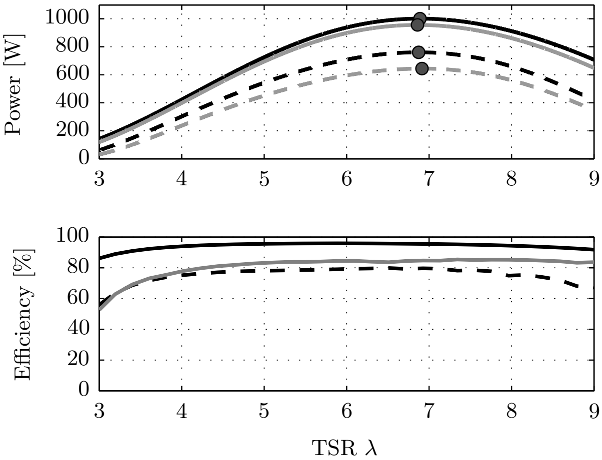

Figure 6.12: Power and efficiency versus λ: High wind speed of 9 m/s
Power: — P_{t}, — P_{m}, - - P_{e}, - - P_{g},
Efficiency: — η_{M}, - - η_{G}, — η_{C}

distribution is used. It is assumed that the power is kept constant at the rated value for wind speeds above the rated wind speed of 9 m/s. At 20 m/s the turbine is shut down to prevent damage. The most important parameter in the Rayleigh distribution is the average wind speed, which depends on the location. Windy open spaces reach average speeds of 6 m/s and more. A more realistic value for a location with buildings and trees, i.e., rural or urban areas, is 4 or 5 m/s. At a location where the average wind speed is 4 m/s, the resulting yearly energy yield is 601 kWh if the turbine operates in the TMPP. For the OMPP, the energy yield increases with 1.9% to 612 kWh. At a location where the average wind speed is 5 m/s, the resulting yearly energy yield is 1234 kWh for operation in the TMPP. For the OMPP, the energy yield increases with 1% to 1246 kWh.

It can be concluded that for the simulated wind turbine system, the energy yield can be increased with 1 - 2% for realistic rural or urban areas. To achieve this, only the tabulated data in the MPPT controller must be changed such that the turbine operates in the OMPP instead of the TMPP. Since this is merely a software adaptation, the cost of the system does not increase.

It is important to note that, in the simulations above, the optimal operating point moves to the left for low wind speeds. This is explained by the fact that a reduced rotor speed decreases the iron losses of the generator, compensating the decrease in captured wind power. However, for some turbine systems, the optimal operating point might as well move to the right. Whether the optimal operating point moves to the left or the right depends on the system parameters, e.g., the ratio of iron versus copper losses in the generator. For a generator with high copper losses, it could be beneficial to have a higher rotor speed, since this causes a higher back-emf and reduces current, decreasing the copper losses. In general, the simulations show that the optimal operating point moves away from the classical optimum due to losses. However, the exact location of the overall maximum power point for a particular wind turbine system must be determined by simulating or measuring the complete system.

6.3.3 Experimental validation

The impact of losses on the location of the MPP was validated with measurements on a wind turbine emulator setup. Fig. 6.13 gives a schematic overview of the setup. A Danfoss AutomationDrive FC302 inverter (a) controls the torque of a 2.2 kW KEB induction motor (b) such that the induction motor behaves as a wind turbine. A digital signal processor sends the desired torque to the inverter, which is calculated from the programmed $C_\mathrm{p}(\lambda)$ curve (2.3). The processor measures the rotational speed with an encoder. A gearbox is used to reduce the output speed of the induction motor. The generator (c) is a 1 kW Mecc Alte Eogen 60/16 PMSG with a pole pair number of 8. The output of the generator is connected to a diode rectifier (d). The dc bus (e) of the rectifier has a capacitance C_ch of 2 mF and a variable load resistance R_L. This load resistance replaces the boost dc/dc chopper and inverter, which are not included during the tests. The rectified power is measured by multiplying the dc current and voltage.

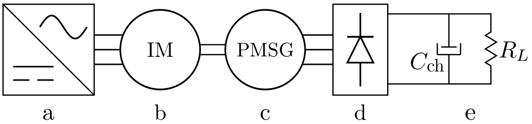

Figure 6.13: Wind turbine emulator test setup

For the measurements, the wind speed is set at 5 m/s, 6.5 m/s and 9 m/s respectively. By changing the load resistance R_L, the operating point is varied. Fig. 6.14 shows the measured power versus λ curves for each wind speed. In all three cases, the turbine power reaches a maximum for a λ-value of 6.91. However, the rectified output power has its maximum at 6.14 for 5 m/s, 6.36 for 6.5 m/s and 6.84 for 9 m/s. The MPP is shifted to the left due to the losses of the generator and the diode rectifier. The effect is strong for the low and medium wind speed, but less pronounced for the high wind speed. These measurements confirm the conclusions of the simulations, i.e., the losses affect the location of the MPP and the effect is strongest for low wind speed values.

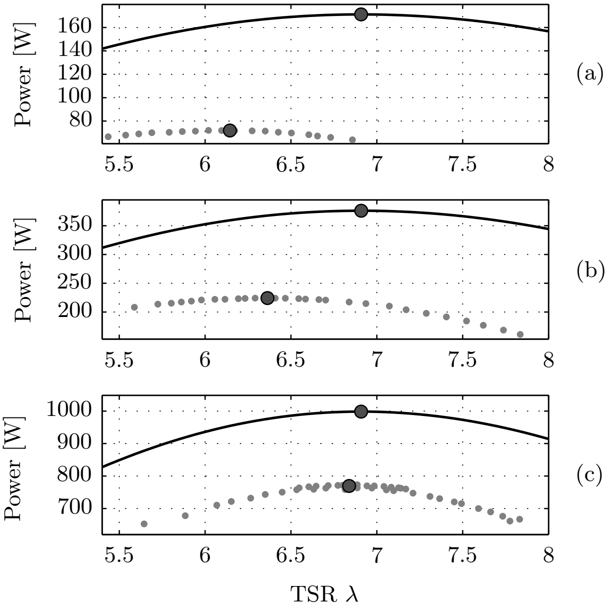

Figure 6.14: Measured power versus λ: (a) 5 m/s, (b) 6.5 m/s, (c) 9 m/s — Turbine power, — Rectified power

6.3.4 Implementation in MPPT algorithms

The previous simulations and experiments have shown that when the losses are included in the analysis, the optimal operating point of the complete system differs from the maximum power point of the turbine. This information is now used to simulate the performance of two different MPPT algorithms, i.e., a Perturb & Observe (P&O) and Power Signal Feedback (PSF) algorithm.

Overview of the model and MPPT

The simulation model which will be used in the following simulations contains the complete mechanical dynamics. Since the turbine inertia dominates the dynamical behavior, averaged models are used for the other components to reduce the simulation time. The losses are simulated by linear interpolation of the efficiency maps, shown previously in Fig. 6.7 - 6.9. The control system contains a PI rotor speed controller. The setpoint value of this controller is determined by the MPPT algorithm. In practice, the rotor speed can be measured by an encoder, hall sensors or by detecting the zero crossings of the generator current waveform.

The P&O algorithm perturbs the system by changing the rotor speed setpoint, after which the change of power is measured. The step imposed on the rotor speed is given by:

$$\Delta\Omega_{i+1} = \beta \cdot \mathrm{sign}(\Delta \mathrm{P_i}) \cdot \mathrm{sign}(\Delta\Omega_\mathrm{i}) \tag{6.12}$$

The parameter β determines the aggressiveness of the MPPT. The algorithm will search for the maximum power value step by step. When the maximum power is reached, the algorithm will oscillate around the maximum, leading to a suboptimal average power. These oscillations can be reduced by decreasing β, but this reduces the speed of the algorithm. The advantage of P&O algorithms is that no tabulated or predetermined data is needed. However, the stepwise search results in a slow performance, often incapable of tracking fast wind speed variations. In most papers, the P&O algorithm tracks the electric output power of the generator P_e. However, as shown in this paper, tracking the grid power P_g takes all losses into account and will result in more power and an increased energy yield. Therefore, the P&O algorithm will track the grid power here.

The PSF controller is the most widely used in wind turbines today, due to its simplicity and effectiveness. The algorithm uses a tabulated relation between maximum power and rotor speed, which can be simulated or measured in a wind tunnel beforehand. The controller measures power, reads the corresponding optimal rotor speed from the table and sends this value to the rotor speed controller as setpoint. Depending on the tabulated data, a PSF controller can regulate a turbine to the TMPP or the OMPP. Classicaly, the controller aims at the TMPP, while measuring the generator output power P_e, since the turbine power is difficult to measure. To calculate the tabulated data, a fixed value is used for the efficiency of the generator [71], neglecting the effect of the losses on the overall MPP.

In the simulations, three MPPT trackers will be compared:

- P&O controller tracking P_g
- PSF controller tracking the TMPP
- PSF controller tracking the OMPP

The tabulated data for the PSF controllers is extracted from the simulations of section 6.3.2. All MPPT algorithms have a sample period of 8s. For the P&O tracker, β is set at 0.25. To have an objective assessment, all parameters have been optimizd to maximize the performance of the tracker.

Simulation results and discussion

A dynamic simulation is performed with a wind speed containing step changes. Fig. 6.15 shows the wind speed profile and the grid power for each of the MPPT algorithms. For the P&O controller, the perturbations are visible in the grid power. Also, at the sudden decrease in wind speed at 250 s, the P&O controller clearly has a slower response when compared to the PSF controllers.

Table 6.6 shows the steady state average grid power P_g for the three MPPT algorithms, before the wind speed changes. As expected, the PSF algorithm achieves more power when tracking the OMPP instead of the TMPP, which confirms the results found earlier. The effect is more visible for a low wind speed. In theory, the P&O controller takes into account the effect of the losses. However, in practice, it suffers from a slow dynamic response and a reduced average power due to the oscillations.

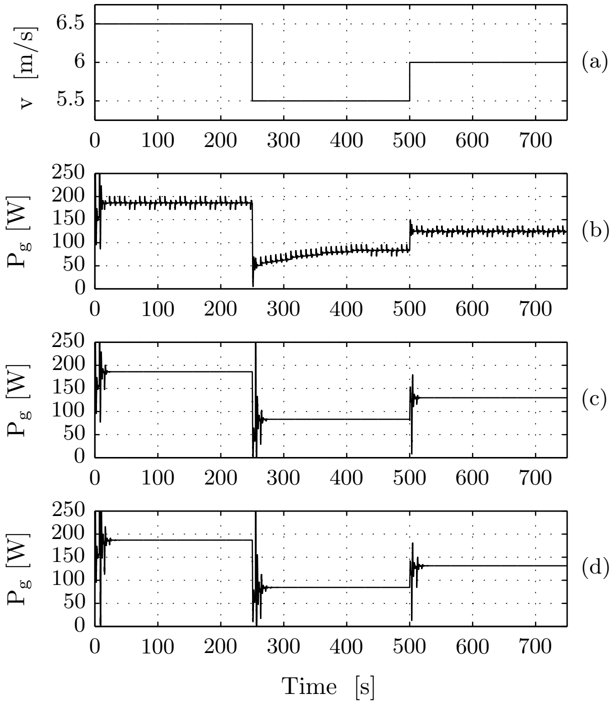

Figure 6.15: MPPT performance for varying wind speed: (a) Wind speed profile, (b) P&O controller, (c) PSF controller tracking the TMPP and (d) PSF controller tracking the OMPP

The performance of the P&O controller can be improved by decreasing β as the algorithm approaches the maximum, reducing the oscillations [138]. This will result in a steady state performance comparable with the PSF controller tracking the OMPP. However, an adaptive P&O still suffers from a slow response, which significantly reduces the energy yield in variable wind conditions.

The parameter of interest is the total energy injected into the grid, which can be calculated by integrating the simulated grid power. For the P&O controller, the energy equals 1251 Ws. The PSF controller tracking the TMPP achieves a higher energy yield of 1299 Ws. The PSF controller tracking the OMPP achieves the highest energy yield of 1317 Ws, as was expected.

Table 6.6: Steady state grid power P_g

	250 s	500 s	750 s
P&O	186.1 W	83.6 W	125.4 W
PSF TMPP	186.1 W	83.2 W	129.8 W
PSF OMPP	187.0 W	84.5 W	131.4 W

Conclusions

The impact of losses on the MPP was implemented in a PSF MPPT algorithm. The performance of this PSF controller tracking the OMPP was compared with a PSF controller tracking the TMPP and a P&O controller tracking the grid power. In theory, the P&O controller takes into account the losses and should regulate the turbine to the OMPP. However, in practice, the slow response and oscillations diminish this advantage, resulting in poor performance. The PSF controller tracking the OMPP clearly performs better than both the PSF controller tracking the TMPP and the P&O controller. This validates the results from section 6.3.2.

6.3.5 Influence of MPP shifting on the ideal TSR curve

The displacement of the MPP due to losses affects the ideal TSR versus wind speed curve of Fig. 6.1. Fig. 6.16 schematically shows the ideal curve when the losses are taken into account as a dashed black line. The original curve of Fig. 6.1 is shown in grey.

The curve remains the same in the low and high wind speed zones. In the normal wind speed zone, the ideal λ is no longer constant, but increases with wind speed. The new curve equals the old curve in the rated operating point, since the effect of the losses on the ideal TSR is negligible there. Note that the ideal curve shown in the figure is only an example. It could also be the case that the ideal TSR starts at a value above the rated TSR and decreases with wind speed. This depends on the parameters of the system and the behavior of the losses, i.e., whether the MPP shifts to the right or to the left.

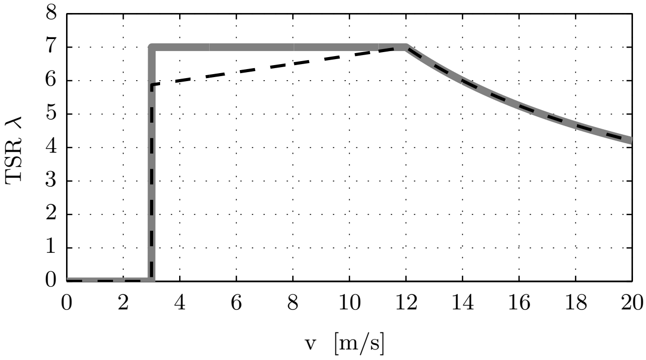

Figure 6.16: Influence of losses on the ideal λ versus wind speed curve

6.3.6 Conclusions

The displacement of the maximum power point due to losses was investigated. Classical MPPT methods operate the turbine in the Turbine Maximum Power Point (TMPP) instead of the Overall Maximum Power Point (OMPP). The OMPP differs from the TMPP due to losses. A simulation model was built representing a 1 kW wind turbine including the dominant losses in the mechanical drivetrain, the generator and the power-electronics. The simulation results have shown that the displacement of the MPP is significant for low wind speeds but negligible for high wind speeds. The effect of this displacement on the produced power is less pronounced since the power curves have a low gradient around the MPP. Nevertheless, low wind speeds have a higher probability of occurence, which leads to an estimated improvement of the yearly energy yield of 1 - 2%. Furthermore, this improvement is reached at no cost since it only requires a change in the tabulated setpoint of the MPPT controller.

It must be noted that the displacement of the MPP is automatically and implicitly taken into account by Perturb & Observe MPPT algorithms, under the condition that the grid power is observed, not the generator output or the dc power. However, P&O algorithms are rarely used in practice since they are often too slow to track realistic wind speed variations.

In practice, the improvement of the energy yield depends on a lot of parameters, i.e., the ratio between copper and iron losses in the generator, the amount of conduction and switching losses in the converter, mechanical friction, etc. In general, strong gradients in the efficiency surfaces create stronger displacements of the MPP. Also, the average wind speed, with respect to the rated wind speed, affects the gain in energy yield as well. At windy locations, the effect is small. However, in rural, urban or industrial locations, where the average wind speed is lower, the gain quickly rises to levels where it is worthwhile to take the effect into account.

6.4 Research opportunities to improve MPPT

In the first part of this chapter, the steady-state behavior of MPPT was considered. However, wind is a quickly varying energy source, especially at low altitudes. In literature, research on dynamic performance of MPPT is rare. Mostly, only the step response is investigated, to minimize the settling time. Here, two research opportunities are given regarding dynamic behavior of MPPT. They have not been thoroughly investigated in the scope of this work, but are open for further research in the future.

6.4.1 Predictive MPPT

Classical MPPT algorithms are made to chase the changing wind speed. A change in wind speed is detected by an anemometer of a sensorless detection algorithm. Then, the MPPT is triggered to search the new optimal operating point. In practice, this method is rather slow. For large wind turbines, where wind speed is stable, the performance is satisfactory. However, at low altitudes, wind speed changes occur too fast and chasing the optimum becomes ineffective.

A possible solution is to place an anemometer at a certain distance from the wind turbine to detect upcoming wind speed changes. In this manner, the MPPT can decide to speed up or slow down the turbine before an actual wind speed change has arrived at the wind turbine. The result is a predictive MPPT algorithm.

One problem with this concept is that a fixed anemometer only provides useful information for one wind direction. However, wind has a dominant direction, e.g., the south-west in Belgium. It can be sufficient to place the anemometer such that wind speed is measured in the most profitable wind direction. Another solution is to place several anemometers in a circular pattern. It is expected that cheap anemometers can be used since only changes in wind speed need to be detected.

Many parameters need to be thoroughly investigated before this concept of a predictive MPPT can be realized. The amount, placement and desired accuracy of the sensors must be optimized and related to the possible increase of energy yield in the MPPT. An economical optimization is also needed to balance the cost of the sensors with the gain in energy yield. Finally, the MPPT algorithm must be adapted to take into account the sensor information and control the turbine.

6.4.2 Dynamic MPPT

As mentioned before, classical MPPT algorithms consider the wind speed to be a constant. The dynamic behavior is then tuned as good as possible by minimizing the settling time for a step response. However, the dynamic behavior could be improved much more by designing the MPPT to react on true dynamic wind speed regimes.

In cooperation with Xavier Bracke as a master thesis student, a method was developed to harvest more energy from wind gusts at low average wind speeds [139]. The investigated case was a wind gust arriving at a turbine at standstill. Due to the low starting torque, a turbine generally does not start and no energy is harvested. However, when a full active rectifier is available, it is possible to operate the PMSM in motor mode. By motoring the turbine for a short period of time, the operating point can be brought near the MPP. Then, the turbine can capture the energy in the gust which can be delivered to the grid in generator mode.

The wind gust is modeled as the positive part of a sine wave. The duration and amplitude determine the available energy in the gust. Obviously, short and small gusts are not worthwhile to capture. A detection algorithm based on a wind speed measurement was developed to decide whether the gust is energetically interesting. The duration of motoring and the motoring torque were both optimized to maximize the harvested energy. Since the motoring period is short, it is allowed to overload the PMSM with three times the rated current, provided that enough time is taken to cool off. It was concluded that 40% of the energy available in a gust can be captured when motoring, while no energy could be captured without motoring.

The response of a turbine on other dynamic events in the wind speed could be investigated as well. The end result would be a dynamic MPPT which detects the varying wind speed regime and imposes the corresponding optimal control strategy on the turbine. A dynamic MPPT is more suited for the varying wind speed conditions at low altitudes and is thus mainly applicable on small wind turbines.

6.5 Conclusions

This chapter investigated the control of the generator currents on a high level, i.e., MPPT. It was shown that there is a considerable room for improvement in the effectiveness of existing MPPT algorithms. Commercial turbines fail to regulate the turbine to the optimal λ in the normal wind speed zone, which reduces the captured renewable energy.

The location of the true optimal operating point of the complete turbine system was also investigated. It is shown with simulation and experiments how the losses cause a displacement of the MPP. The end-result is that the true optimal λ differs from the theoretical optimal value and depends on the wind speed. By taking this effect into account, 1 - 2% additional energy can be produced. These findings were also validated in a dynamic simulation of a P&O and a PSF MPPT algorithm.

Two possible research opportunities were given to improve MPPT. A predictive MPPT can be developed which uses sensor information at a certain distance of the turbine to anticipate wind speed changes. Another concept is a dynamic MPPT which reacts on variations in the wind speed. A method was developed to extract 40% of the energy available in a wind gust at standstill by motoring the turbine for a well chosen amount of time with a certain torque. In contrast, classical turbines extract no energy from these gusts.

7

COMMENTS AND ADVICE FOR THE WIND TURBINE INDUSTRY

During this research, there have been numerous contacts and collaborations with manufacturers and distributors of small and medium wind turbines. Some of these contacts were in the frame of the Small Wind Turbine Field Laboratory in Ostend, others were part of a service, i.e., performing calculations or measurements. These contacts have uncovered certain critical points and pitfalls in the design and marketing of a turbine. In this chapter, the findings and experience gathered during this time are summarised. The goal of this is to offer valuable advice to designers and manufacturers of small and medium wind turbines.

Contents

7.1 Turbine rotor

In chapter 2, an overview was given of the most common rotor types, i.e., a three-bladed HAWT, a Savonius and a Darrieus rotor. Fig. 7.1 gives an overview of the power coefficient curves for different types of turbines. Clearly, a classical three-bladed HAWT reaches the highest power coefficient, with the Darrieus rotor as a close second. However, the maximum power coefficient of a Savonius rotor is significantly lower. This can be expected as the driving part of the rotor is counteracted partially by the other half of the rotor. This effect is also present to a lesser degree in Darrieus turbines. Also, the Savonius rotor operates on the drag concept instead of lift, leading to a completely different power coefficient curve.

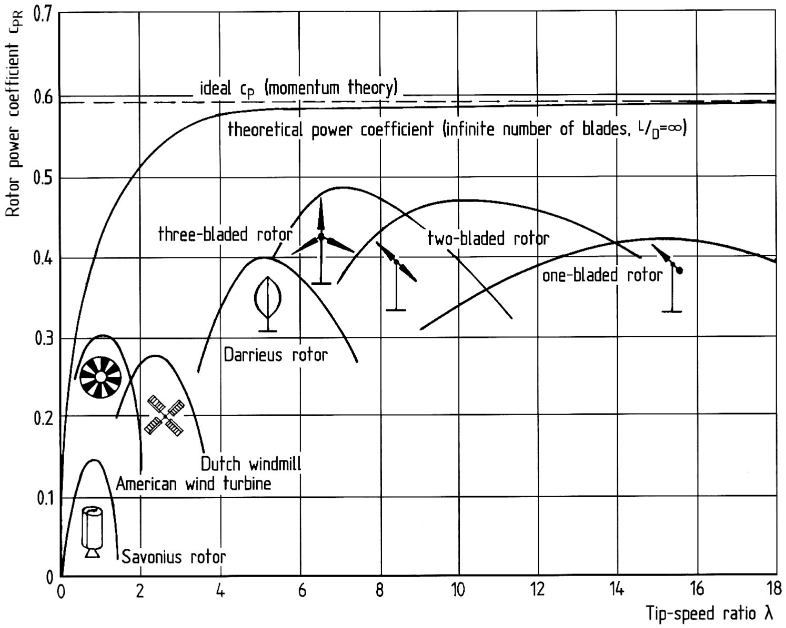

Figure 7.1: Power coefficients for different turbine rotor types [140]

Despite the clear evidence that a three-bladed HAWT reaches the highest power coefficient, many starting manufacturers, and so-called inventors, design the most extreme turbine rotors. However, these rotors often have a low power coefficient, leading to disappointing energy yields. Since the economic profitability of a turbine is crucial for its succes, these extreme designs should be avoided. The three-bladed HAWT should be the prefered rotor type.

However, a low maximum power coefficient does not necessarily result in a turbine with a low energy yield or a low economic profitability. It the rated power of the generator and converter are well matched with the maximum power delivered by the rotor, the complete system can still be profitable. The only consequence is that a larger rotor is required to reach a certain power level, increasing the material cost and weight. If the cost of the rotor is small compared to the total cost of the system, the choice of, e.g., a Savonius rotor, can be justified economically.

An important remark concerning Savonius rotors is that their optimal tip-speed ratio is low, leading to a low rated rotor speed. Permanent magnet synchronous generators with a low rotor speed are expensive and heavy. Normally, small and medium wind turbines use PMSGs with a high pole pair number to reach low rotor speeds. However, the rated rotor speed of a Savonius rotor is often too low for a regular direct-drive PMSG. Therefore, a gearbox is required, but this also represents a cost, requires maintenance and increases the mechanical losses. In the design of a Savonius turbine, a techno-economic trade-off must be made to select an appropriate generator speed, and thus, a suitable combination of a PMSG and a gearbox. The trade-off must include both the investment costs and the annual costs of maintenance. Also, the expected yearly energy yield will differ, since the losses vary. This trade-off is rarely made in practice, as it is time-consuming and requires detailed price information and technical data. However, it is advised to perform this study, at the least in a simplified form.

Regarding vertical axis turbines, the Darrieus design clearly has more economic potential than a Savonius turbine. A Darrieus has a higher power coefficient and rotor speed. Due to the higher rotor speed, a gearbox can be avoided. The same holds for a giromill, which is a variant of the Darrieus design, but with straight blades in an H-form. In order to develop an economically profitable vertical axis turbine, it is advised to focus on Darrieus and giromill turbines instead of Savonius turbines.

7.2 Overestimation of expected wind speeds

When analysing the data sheets of commercial wind turbines, it can be observed that most manufacturers design their turbine for an average wind speed of 5 m/s. These turbines reach their rated power for a wind speed between 10 and 13 m/s. However, these wind speeds are an overestimation of the actual situation, especially in urban or residential areas. The average wind speed of the SWT Field Lab in Ostend is 4.570 m/s at a height of 15 m, averaged since the start of the measurements. However, the SWT Field Lab has favorable conditions, i.e., close to the coast and a limited amount of obstructions in the dominant south-west wind direction. In urban environments, average wind speeds of 3 m/s are more common. Since the power available in the wind is proportional to the cubic power of the wind speed, this has a large impact on the available power.

It is no surprise that a wind turbine designed for an average of 5 m/s has a disappointing performance when installed on a location where an average of only 3 or 4 m/s is reached. These turbines have an oversized generator and converter, representing an unnecessary cost. Also, when operated at partial load, their efficiency is significantly reduced, which was observed in the simulations of chapter 6 in Figs. 6.7, 6.8 and 6.9. In practice, the reduced energy yield destroys the economic profitability of the turbine. In the end, small and medium wind turbines have received a negative image mainly for this reason.

However, it is incorrect to conclude that small and medium wind turbines cannot be profitable in average wind speeds of 3 or 4 m/s. It is a matter of designing the wind turbine in such a way that it matches this more realistic average wind speed value. This means that the rated power of the generator and converter must be chosen lower, such that the turbine reaches this power value faster, thus operating at high efficiency levels. The disadvantage of this design is that the turbine cannot capture significant amounts of energy when the wind speed is high, since the generator and converter can only be overloaded for a limited time. However, the Rayleigh distribution shows that high wind speeds occur rarely, so that the impact on the yearly energy yield is small.

The value of the rated power and the rated wind speed have a large impact on both the investment cost and the yearly energy yield, and should be chosen wisely. An optimal value of the rated power can be calculated by taking into account a realistic wind speed distribution and determining the optimal trade-off between energy yield and cost. The losses of the generator and converter in function of power should be taken into account.

It can be concluded that a correct estimation of the wind speed is critical for the design of a turbine. This estimation must then be used in a techno-economic study to select a proper rated power of the system. The study is techno-economic in the sense that both economical aspects, i.e., the price of the different components and the return on investment of the complete system, and technological aspects, i.e., rated power, wind speed distribution and efficiency data must be included in the analysis.

7.3 Marketing

In the past, there were no international standards regarding wind turbines. Manufacturers of wind turbines could claim any estimated yearly energy yield, often being unrealistic. Since 2001, the IEC 61400 standards have imposed guidelines for the design, safety, construction, exploitation, maintenance and testing of wind turbines. The IEC 61400-2 standard particularly handles small and medium wind turbines. This standard imposes a strict methodology for measuring the power curve of a wind turbines. Summarized, the turbine must be tested by an independent and certified company. The power injected into the grid must be logged together with wind speed. Then, the data is averaged in intervals of 0.5 m/s. The end result is an objective power curve, which allows to calculate the yearly energy yield when combined with a wind speed distribution.

The wind speed distribution differs for every location. Therefore, the turbine manufacturer chooses an unrealistic wind speed distribution, with an average value of 5 m/s, in order to have an impressive yearly energy yield. Often, the financial profit linked to this energy yield draws the attention of the consumer. The consumer is often unaware of the unrealistic wind speed distribution. Due to the rivalry between turbine manufacturers, no company dares to deviate from this unrealistic wind speed distribution, as it would make their turbine appear less performant.

It is advised to extend the IEC standard by including a few realistic values of the average wind speed, e.g., 3 m/s for urban environments, 4 m/s for rural environments with an open landscape and 5 m/s for favorable coastal areas. In this manner, the turbine manufacturer can present estimated yearly energy yields and financial profits for all three cases. This would be more transparent for the consumer and would create a more healthy competition on the market.

However, specific obstructions in the environment can have a significant impact on the wind speed, especially at low altitudes. Therefore, the most objective method for estimating the yearly energy yield is to perform a wind speed measurement on site for a sufficient period. This allows to estimate the wind speed distribution. Care must be taken in wooded areas, as the presence of leaves on the trees greatly affects the wind speed measured in summer versus winter.

7.4 Politics

Another obstacle in the evolution of wind energy is politics. It is required for a consumer to have a build permit from the municipality to install a small wind turbine. Only in rare occasions is this permit is granted. The negative build permit atmosphere considerably limits the growth of wind turbine distributors in Belgium. Currently, Belgian politicians have a rather negative opinion on small and medium wind turbines. Also, currently, the topic seems not critical enough to open a debate. This might change in the future if oil prices go up or the problem of global warming becomes more urgent.

7.5 Conclusions

Several issues considering the wind turbine industry have been discussed in this chapter. First, the importance of a well considered turbine rotor design was emphasized. A classical three-bladed horizontal axis turbine gives the highest certainty to obtain a performant turbine, as it has a high power coefficient and high relative rotor speed. Other rotor types, such as the Savonius, require that the design of the system is done with great care in order to yield a cost-effective turbine. Regarding vertical axis turbines, the Darrieus or giromill designs have more economic potential than Savonius turbines.

Another issue is the overestimation of the average wind speed. Most small and medium turbines are designed for wind speeds which are unrealistic, leading to disappointing energy yields in practice. The rated power of the generator and converter must be better matched with the expected wind speed.

The marketing of turbines should be more transparent to consumers, since the yearly financial profits claimed by turbine manufacturers are based on unrealistic average wind speeds. It is advised to nuance this by presenting the estimated financial profit for several fixed average wind speeds, e.g., for urban, rural and coastal environments.

Finally, politics plays an important factor in the wind energy market as well. In Belgium, build permits are rarely given by the municipality, limiting the growth of the small and medium wind industry.

8

CONCLUSIONS AND FURTHER RESEARCH OPPORTUNITIES

This chapter discusses the findings of the previous chapters and summarizes the most important conclusions. Also, opportunities for further research are presented.

Contents

8.1 Conclusions

The goal of this research was to investigate technological improvements to increase the energy yield of wind turbines. Wind energy was envisioned as the direct application of the research, but certain findings have other applications as well.

In chapter 2, the state-of-the-art wind turbine system was presented, including the models used in this work. The turbine is modeled by a $C_\mathrm{p}(\lambda)$ curve. The PMSM is represented by an equivalent model in a rotating reference frame, including armature reaction and an iron loss resistance which models eddy current losses and hysteresis losses. Several converter topologies are discussed and used in this work, i.e., the classical passive diode rectifier combined with a boost dc/dc chopper, the full active rectifier and the four-wire rectifier. Also, the control and topology of a classical three-phase grid-connected inverter is presented.

The first main topic of this work is optimal current waveform shaping, in which the waveform of the current is optimised to maximise the efficiency for a given machine. Current waveform shaping is particularly applicable on machines with a hybrid back-emf waveform, i.e., with a high harmonic content. Chapter 3 presents the existing research gathered in a literature study. Classical methods simplify the machine by neglecting armature reaction, iron losses and zero-sequence currents. The optimisation is mostly performed in the frequency domain, which requires that a finite set of harmonic components is selected. Also, the waveform is optimised to minimise torque ripple, not the losses.

At the end of chapter 3, a new optimal current waveform shaping method based on the Cauchy-Schwarz inequality is presented. This new method operates in the time domain, so that there is no restriction on the amount of harmonic components included in the analysis. Also, the primary goal here is to maximise the efficiency instead of minimising the torque ripple.

One of the key assumptions in the new optimal current waveform shaping method is that the back-emf waveform is fixed and independent of the current waveform. This is only true if the torque ripples, which are linked with the current waveform, do not cause speed ripples which alter the back-emf waveform. In chapter 4, realistic speed ripples are simulated in small, medium and large wind turbines, caused by tower shadow and wind shear. It is shown that these speed ripples are small in magnitude, although the torque ripples can be large. A mathematical model was developed to determine the additional back-emf harmonics caused by these speed ripples. Again, it is shown that this effect is small. Therefore, it is justified to neglect the influence of speed ripples and the back-emf waveform can be assumed fixed and independent of the current waveform.

The optimal current waveform shaping method was applied on a simplified model of a PMSM in chapter 3. In chapter 5, the same method is applied on the complete PMSM model step-by-step, including armature reaction, iron losses and zero-sequence currents. A case study is performed to simulate the optimal, sinusoidal and square-wave current waveforms and compare their efficiency. It is shown that the optimal current waveform reaches a higher efficiency than the classical waveforms. A parameter sensitivity analysis is performed to calculate the influence of selected key parameters on the efficiency gain, i.e., the back-emf waveform, the stator resistance, the ratio of copper and iron losses and the inductance value. The efficiency behaves as expected, i.e., the complete optimal current waveform reaches a higher efficiency than the simplified optimal waveform as the armature reaction or iron losses become more dominant.

Finally, the new optimal current waveform method is validated in a simulation model of a wind turbine, including the PWM switching of the split-link rectifier. The simulations show that the switching ripple in the current increases the copper losses while the PWM voltage on the stator terminals increases the iron losses. Therefore, the efficiency is lower than predicted by the theoretical model. Still, the optimal current waveform reaches a higher efficiency than the sinusoidal reference waveform.

The second main topic of this work is MPPT. First, standardised IEC 61400-2 measurements on small wind turbines were investigated to calculate the performance of the MPPT algorithm in current state-of-the-art wind turbines. It was shown that the MPPT algorithm had a considerable steady-state error, leading to a reduced energy yield. It is concluded that the MPPT algorithm can be improved. Classically, MPPT algorithms are designed to control the turbine to the maximum power point, which is the optimal operating point for the turbine blades. However, this is not necessarily the optimal operating point of the complete system. The losses of the different components can result in a displacement of the overall maximum power point. A simulation model was developed in Simulink which includes all dominant loss components, i.e., the mechanical losses, the copper and iron losses in the generator and the conduction and switching losses in the converter. The simulations have shown that, especially for low wind speeds, a higher energy yield is achieved if the rotor speed is set slightly lower than the value corresponding to the MPP of the turbine. Taking into account the losses can increase the yearly energy yield by 1-2%.

The final chapter of this dissertation gives comments and advice for entrepeneurs and designers in the wind turbine market. The importance of selecting a proper turbine rotor is emphasized. Another crucial step in the design process is the choice of a rated and average wind speed. Most manufacturers overestimate the expected wind speed. Most turbines are designed for an average wind speed of 5 m/s, while in practice values between 3 and 4 m/s are more realistic. This overestimation leads to a wind turbine with an oversized generator and converter, increasing the investment costs. Then, the generator and converter mostly operate below the rated power, where their efficiency is low. A last remark is made concerning the negative attitude of Belgian politics, who rarely grant a build permit for a small or medium wind turbine.

8.2 Further research opportunities

During this work, certain topics and ideas have shown to be promising and interesting for further research. However, they were not explored since they were outside of the scope of this PhD. The most interesting topics are discussed here.

8.2.1 Field orientation combined with optimal current waveform shaping

Field orientation is a widely used control method for synchronous machines to achieve a fast dynamic performance with torque control. By regulating the current in the d axis to zero, the armature reaction effect in the q axis disappears and the torque becomes directly proportional to the q axis current. In the PMSM model used here, this is only valid if the zero-sequence current is also set to zero and the iron losses are neglected.

The classical field orientation method is not directly compatible with the optimal current waveform shaping method presented here. However, a compromise can be made, combining the favorable dynamic properties of field orientation with the increased efficiency of an optimal current waveform. If the iron losses are neglected, which is also done in classical field orientation, the PMSM can be represented by the scheme of Fig. 8.1.

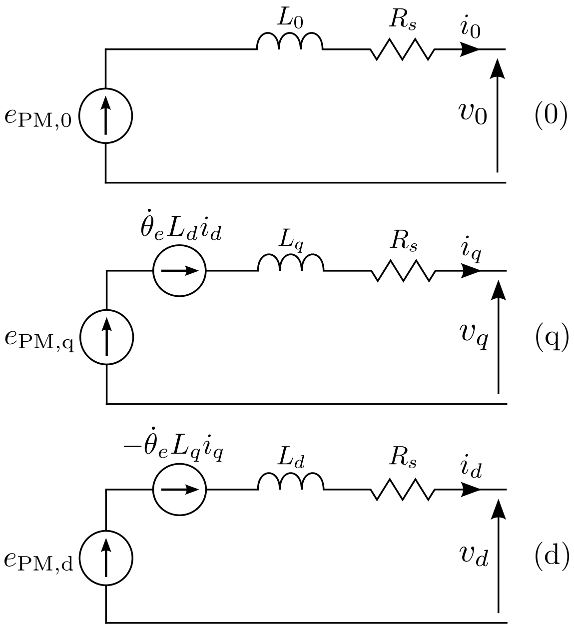

Figure 8.1: PMSM model including the armature reaction back-emf

By setting the d-axis current to zero, the armature reaction back-emf in the q-axis disappears. The Cauchy-Schwarz method can then be applied in the q-axis, leading to the following current equations:

$$i_0 = 0 \tag{8.1}$$

$$i_{\mathrm{q}} = G'_{\mathrm{q}} \cdot \varphi_{\mathrm{q}} \tag{8.2}$$

$$i_{\mathrm{d}} = 0 \tag{8.3}$$

Since the 0 and d axes currents are not according to the Cauchy-Schwarz theorem, these current equations are not optimal and do not lead to a maximum efficiency. However, the fundamental components are in a field oriented situation, i.e., the torque is directly proportional to the scale factor:

$$T = \frac{3}{2} G'_{\mathrm{q}} \varphi_{\mathrm{q}}^2 \tag{8.4}$$

Further research is needed to investigate how this combination of field orientation and optimal current waveform shaping performs energetically and dynamically.

8.2.2 Extending the PMSM model

In chapter 5, it was explained that a more advanced PMSM model results in a better optimal current waveform, achieving higher efficiencies. The model presented in this work includes zero-sequence components, armature reaction, the reluctance effect and iron losses. The simulations have shown how a considerable increase in the efficiency can be achieved by taking into account these effects in the optimal current waveform.

However, more advanced effects can be added to the model to further increase the efficiency. This involves developing an adequate model of the effect, applying the Cauchy-Schwarz method on the complete PMSM model and finally deriving the optimal current waveform equations. Depending on the effect and the machine parameters, some effects may be worthwhile to include in the analysis while others are not. This can only be judged in hindsight.

Possible effects to include in the PMSM model are listed here and briefly discussed.

Speed ripples
In chapter 4, the effect of speed ripples on the back-emf waveform

was investigated. The back-emf was modeled as a superposition of the classical back-emf induced by the permanent magnets and a new back-emf induced by the speed ripples. This new back-emf term can be included in the equivalent PMSM model. If the speed ripples are independent of the current waveform, the optimal current waveform equations can be determined easily. However, if the speed ripples are caused by the current waveform, i.e., through torque ripples, the model has a feedback loop. This considerably increases the complexity of the optimal current waveform shaping method.

Magnet losses

Besides the classical copper and iron losses, a PMSM also has magnet losses. These losses can be explained by the non-infinite magnetic permeability of the permanent magnets. Therefore, eddy currents are induced in the magnets, resulting in Joule losses. The magnet material also encounters hysteresis losses [120]. In theory, this loss component could be added to the model. However, compared to the copper and iron losses, the magnet losses are generally negligible so that their effect on the total efficiency is small.

In [122], it is shown that the magnet losses are considerably higher when taking into account the switching ripple in the current waveform due to PWM. Therefore, it can be expected that the harmonics in the optimal current waveform will increase the magnet losses as well, although having a much lower frequency than a PWM voltage. It is unlikely that this will have a noticeable effect on the efficiency, but it can have an impact on the steady state temperature of the magnets. Overheating of the magnets must be avoided as this can lead to demagnetisation. As proposed in [122], the magnet losses should be taken into account in the design stage of the machine to avoid overheating.

Positive temperature feedback

As discussed earlier in chapter 5, there is a positive temperature feedback due to the stator resistance. Since the optimal current waveform reduces the copper losses, a lower steady-state temperature will be achieved in the machine, leading to a lower resistance. Currently, this effect is not included in the model. In contrast with the effects discussed earlier, the positive temperature feedback does not have to be included in the machine model or in the optimal current waveform equations. It needs to be included in the iterative grid search algorithm. There, a thermal model of the PMSM should be added to determine the regime temperature for each set of current waveforms. This temperature must be used to run the algorithm iteratively until steady-state is achieved.

8.2.3 Alternative rectifier topologies

In order to have full control over the current waveform, a split-link topology was used in this work. The classical passive diode rectifier, currently used in state-of-the-art small and medium wind turbines, does not offer flexible control over the current waveform. However, several alternative converter topologies or techniques exist which can be suitable for application of the optimal current waveform technique.

A possible alternative topology is the matrix converter, which avoids the use of a classical dc bus. Matrix converters are a popular topic in literature, especially in the application of wind energy [141, 142]. Another possibility is the use of a multi-level converter. Although these converters require a large amount of electronics, such as protection circuits and gate drivers, they offer a significantly reduced harmonic content of the converter output. This leads to less voltage and current distortion.

In principle, it is possible to have control over the current waveform when using the classical passive diode rectifier combined with a boost chopper. Previous work in the EESA department of Ghent University has shown that the harmonic content of the current waveform can be controlled in boost Power-Factor-Correcting converters connected to the grid [143]. This requires advanced control methods and a high switching frequency. Analogous principles could be applied on a wind turbine as well.

Investigating the possibility of using different converter topologies or techniques is outside the scope of this work, but can be an interesting topic for continued research.

[44] Global Wind Energy Council, "Global wind report - annual market update 2014," March 2015.

[45] B. Fleck and M. Huot, "Comparative life-cycle assessment of a small wind turbine for residential off-grid use," *Renewable Energy*, vol. 34, pp. 2688–2696, December 2009.

[46] O. Wasynczuk, D. T. Man and J. P. Sullivan, "Dynamic behavior of a class of wind turbine generators during random wind fluctuations," *IEEE Transactions on Power Apparatus and Systems*, pp. 2837–2845, June 1981.

[47] J. R. Welty, C. E. Wicks, R. E. Wilson and G. Rorrer, *Grid Integration of Wind Energy: Onshore and Offshore Conversion Systems.* Wiley, 2006.

[48] J. G. Slootweg, S. W. H. de Haan, H. Polinder and W. L. Kling, "General model for representing variable speed wind turbines in power system dynamics simulations," *IEEE Transactions on Power Systems*, vol. 18, pp. 144–151, February 2003.

[49] V. Agarwal, R. K. Aggarwal, P. Patidar and C. Patki, "A novel scheme for rapid tracking of maximum power point in wind energy generation systems," *IEEE Transactions on Energy Conversion*, vol. 25, pp. 228–236, March 2010.

[50] J. Morren, J. Pierik and S. W. H. de Haan, "Inertial response of variable speed wind turbines," *Electric Power Systems Research*, vol. 76, pp. 980–987, 2006.

[51] SKF Group, *Rolling Bearings Catalogue*, August 2013.

[52] SKF Group, *Industrial Shaft Seals Catalogue*, June 2013.

[53] P. Andrada, M. Torrent, J. I. Perat and B. Blanqué, "Power losses in outside-spin brushless dc motors," in *Proc. of the 2004 International Conference on Renewable Energy and Power Quality (ICREPQ 2004)*, (Barcelona, Spain), 31 March - 2 April 2004.

[54] Wind Power Monthly, "Close up - the vestas v164 7mw offshore turbine," *http://www.windpowermonthly.com/article/1065676/close---vestas-v164-7mw-offshore-turbine.*

[55] H. Vansompel, P. Sergeant and L. Dupré, "Optimized design considering the mass influence of an axial flux permanent-magnet synchronous generator with concentrated pole windings," *IEEE Transactions on Magnetics*, vol. 46, pp. 4101–4107, December 2010.

[56] G. De Donato, F. G. Capponi, G. A. Rivellini and F. Caricchi, "Integral-slot versus fractional-slot concentrated-winding axial-flux permanent-magnet machines: Comparative design, fea and experimental tests," *IEEE Transactions on Industry Applications*, vol. 48, pp. 1487–1495, September/October 2012.

[57] F. Fernández-Bernal, A. García-Cerrada and R. Faure, "Determination of parameters in interior permanent-magnet synchronous motors with iron losses without torque measurement," *IEEE Transactions on Industry Applications*, vol. 37, pp. 1265–1272, September 2001.

[58] C. Cavallaro, A. O. Di Tommaso, R. Miceli, A. Raciti, G. R. Galluzzo and M. Trapanese, "Efficiency enhancement of permanent-magnet synchronous motor drives by online loss minimzation approaches," *IEEE Transactions on Industrial Electronics*, vol. 52, pp. 1153–1160, August 2005.

[59] N. Urasaki, T. Senjyu and K. Uezato, "A novel calculation method for iron loss resistance suitable in modeling permanent-magnet synchronous motors," *IEEE Transactions on Energy Conversion*, vol. 18, pp. 41–47, March 2003.

[60] S. Morimoto, Y. Tong, Y. Takeda and T. Hirasa, "Loss minimzation control of permanent magnet synchronous motor drives," *IEEE Transactions on Industrial Electronics*, vol. 41, pp. 511–517, October 1994.

[61] Collin Debruyne, "Impact of voltage distortion on energy efficiency of induction machines and line start permanent magnet machines," PhD thesis, Ghent University, 2014.

[62] A. Mansouri and H. Trabelsi, "On the performances investigation and iron losses computation of an inset surface mounted permanent magnet motor," in *Proc. of the 9th International Multi-Conference on Systems, Signals and Devices*, (Chemnitz), 20-23 March 2012.

[63] A. Van den Bossche and V. C. Valchev , "Inductors and transformers for power electronics," Taylor & Francis, 2005.

[64] J. D. M. De Kooning, J. Van de Vyver, T. L. Vandoorn, B. Meersman and L. Vandevelde, "Joule losses and torque ripple caused by current waveforms in small and medium wind turbines," in *Proc. of the 2013 IEEE Eurocon conference (EUROCON 2013)*, (Zagreb, Croatia), 1 - 4 July 2013.

[65] M. Abdel-Salam, A. Ahmed and M. Abdel-Sater, "Harmonic mitigation, maximum power point tracking, and dynamic performance of variable-speed grid-connected wind turbine," *Electric Power Components and Systems*, vol. 39, pp. 176–190, 2011.

[66] P. Dvorak, "How can you prevent encoder failures in wind turbines?." http://www.windpowerengineering.com/ featured/ business-news-projects/can-prevent-encoder-failure-wind-turbines/, 2014. Accessed 6 January 2015.

[67] F. M. L. De Belie, P. Sergeant and J. A. Melkebeek, "A sensorless drive by applying test pulses without affecting the average-current samples," *IEEE Transactions on Power Electronics*, vol. 25, pp. 875–888, April 2010.

[68] Jeroen De Kooning, "Balancing the mid-point of split-link three-phase grid-connected inverters with a neutral wire," Master thesis, Ghent University, 2010.

[69] J. D. M. De Kooning, B. Meersman, T. L. Vandoorn, B. Renders and L. Vandevelde, "Comparison of three-phase four-wire converters for distributed generation," in *Proc. of the 45th International Universities Power Engineering Conference (UPEC 2010)*, (Cardiff, UK), Aug. 31 - Sep. 3, 2010.

[70] R. Zhang, V. H. Prasad, D. Boroyevich and F. C. Lee, "Three-dimensional space vector modulation for four-leg voltage-source converters," *IEEE Transactions on Power Electronics*, vol. 17, pp. 314–326, May 2002.

[71] S. M. R. Kazmi, H. Goto, H.-J. Guo and O. Ichinokura, "A novel algorithm for fast and efficient speed-sensorless maximum power point tracking in wind energy conversion systems," *IEEE Transactions on Industrial Electronics*, vol. 58, pp. 29–36, January 2011.

[72] Bert Renders, “Convertor-gekoppelde decentrale generatoren en netkwaliteit in laagspanningsnetten,” PhD thesis, Ghent University, 2009.

[73] Bart Meersman, “Regeling van driefasige invertorgekoppelde decentrale generatoren met betrekking tot de verbetering van de netkwaliteit,” PhD thesis, Ghent University, 2012.

[74] Jonas De Kooning, “Grid voltage control with wind turbine inverters by using grid impedance estimation,” Master thesis, Ghent University, 2014.

[75] H.-S. Chen, D. G. DOrrell and M.-C. Tsai, “Design and operation of interior permanent-magnet motors with two axial segments and high rotor saliency,” *IEEE Transactions on Magnetics*, vol. 46, no. 9, pp. 3664–3675, 2010.

[76] D. Ishak, Z. Q. Zhu and D. Howe, “Comparison of pm brushless motors, having either all teeth or alternate teeth wound,” *IEEE Transactions on Energy Conversion*, vol. 21, no. 1, pp. 95–103, 2006.

[77] T. J. E. Miller and R. Rabinovici, “Back-emf waveforms and core losses in brushless dc motors,” *IEE Proceedings on ELectric Power Applications*, vol. 141, no. 1, pp. 144–154, 1994.

[78] B. Stumberger, G. Stumberger, M. Hadziselimovic, I. Zagradisnik, A. Hamler and M. Trlep, “Permanent magnet synchronous motor with exterior-rotor, distributed or concentrated windings - motor performance comparison,” *COMPEL*, vol. 25, no. 3, pp. 721–726, 2006.

[79] A. M. El-Refaie, T. M. Jahns and D. W. Novotny, “Analysis of surface permanent magnet machines with fractional-slot concentrated windings,” *IEEE Transactions on Energy Conversion*, vol. 21, no. 1, pp. 34–43, 2006.

[80] A. M. El-Refaie, “Fractional-slot concentrated-windings synchronous permanent magnet machines: Opportunities and challenges,” *IEEE Transactions on Industrial Electronics*, vol. 57, no. 1, pp. 107–121, 2010.

[81] D. C. Hanselman, “Minimum torque ripple, maximum efficiency excitation of brushless permanent magnet motors,” *IEEE*

Transactions on Industrial Electronics, vol. 41, pp. 292–300, June 1994.

[82] P. Kshirsagar and R. Krishnan, "High-efficiency current excitation strategy of variable-speed nonsinusoial back-emf pmsm machines," *IEEE Transactions on Industry Applications*, vol. 48, pp. 1875–1889, November/December 2012.

[83] A.P. Wu and P.L. Chapman, "Simple expressions for optimal current waveforms for permanent-magnet synchronous machine drives," *IEEE Transactions on Energy Conversion*, vol. 20, pp. 151–157, March 2005.

[84] C. De Angelo, G. Bossio, J. Solsona, G. O. Garcia and M. Ines Valla, "A rotor position and speed observer for permanent-magnet motors with nonsinusoidal emf waveform," *IEEE Transactions on Industrial Electronics*, vol. 52, pp. 807–813, June 2005.

[85] J. X. Shen, Z. Q. Zhu and D. Howe, "Sensorless flux-weakening control of permanent magnet brushless machines using third harmonic back EMF," *IEEE Transactions on Industry Applications*, vol. 40, pp. 1629–1636, November 2004.

[86] C.W. Lu, B.J. Chalmers, A.C. Renfrew and S. Huang, "Novel approach to current profiling for ac permanent magnet motors," *IEEE Transactions on Energy Conversion*, vol. 14, pp. 1294–1299, December 1999.

[87] J. Y. Hung and Z. Ding, "Design of currents to reduce torque ripple in brushless permanent magnet motors," *IEE Proceedings-B*, vol. 140, pp. 260–266, July 1993.

[88] H. Le-Huy, R. Perret and R. Feuillet, "Minimzation of torque ripple in brushless dc motor drives," *IEEE Transactions on Industry Applications*, pp. 748–755, July/August 1986.

[89] F. Piriou, A. Razek, R. Perret and H. Le-Huy, "Torque characteristics of brushless dc motors with imposed current waveform," *in Proceedings of the Industry Applications Society Annual Meeting 1986*, pp. 176–181, 1986.

[90] C. French and P. Acarnley, “Direct torque control of permanent magnet drives,” *IEEE Transactions on Industry Applications*, vol. 32, pp. 1080–1088, September/October 1996.

[91] E. Favre, L. Cardoletti and M. Jufer, “Permanent magnets synchronous motors: a general approach for cogging torque suppression,” *IEEE Transactions on Industry Applications*, vol. 29, no. 6, pp. 1141–1149, 1993.

[92] P.L. Chapman, S.D. Sudhoff and C.A. Whitcomb, “Optimal current control strategies for surface-mounted permanent-magnet synchronous machine drives,” *IEEE Transactions on Energy Conversion*, vol. 14, pp. 1043–1050, December 1999.

[93] J. L. Willems, “Reflections on apparent power and power factor in nonsinusoidal and polyphase situations,” *IEEE Transactions on Power Delivery*, vol. 19, pp. 835–840, April 2004.

[94] J. R. Welty, C. E. Wicks, R. E. Wilson and G. Rorrer, *Fundamentals of Momentum, Heat and Mass Transfer, 4th edition.* Wiley, 2001.

[95] J. Sopanen, V. Ruuskanen, J. Nerg and J. Pyrhönen, “Dynamic torque analysis of a wind turbine drive train including a direct-driven permanent-magnet generator,” *IEEE Transactions on Industrial Electronics*, vol. 58, pp. 3859–3867, September 2011.

[96] J. D. M. De Kooning, T. L. Vandoorn, J. Van de Vyver, B. Meersman and L. Vandevelde, “Shaft speed ripples in wind turbines caused by tower shadow and wind shear,” *IET Renewable Power Generation*, vol. 8, pp. 195–202, March 2014.

[97] Z. Zhang, A. Verma and A. Kusiak, “Fault analysis and condition monitoring of the wind turbine gearbox,” *IEEE Transactions on Energy Conversion*, vol. 27, pp. 526–535, June 2012.

[98] S. Roy, “Impact of short duration wind variations on output of a pitch angle controlled turbine,” *IEEE Transactions on Sustainable Energy*, vol. 3, pp. 566–575, July 2012.

[99] W. E. Leithead, “Dependence of performance of variable speed wind turbines on the turbulence, dynamics and control,” *IEE Proceedings C - Generation, Transmission and Distribution*, vol. 137, pp. 403–413, November 1990.

[100] E. B. Muhando, T. Senjyu, A. Yona, H. Kinjo and T. Funabashi, "Disturbance rejection by dual pitch control and self-tuning regulator for wind turbine generator parametric uncertainty compensation," *IET Control Theory & Applications*, vol. 1, pp. 1431–1440, September 2007.

[101] D. S. L. Dolan and P. W. Lehn, "Simulation model of wind turbine 3p torque oscillations due to wind shear and tower shadow," *IEEE Transactions on Energy Conversion*, vol. 21, pp. 717–724, September 2006.

[102] R. Fadaeinedjad, G. Moschopoulos and M. Moallem, "The impact of tower shadow, yaw error, and wind shears on power quality in a wind-diesel system," *IEEE Transactions on Energy Conversion*, vol. 24, pp. 102–111, March 2009.

[103] F. M. Hughes, O. Anaya-Lara, G. Ramtharan, N. Jenkins and G. Strbac, "Influence of tower shadow and wind turbulence on the performance of power system stabilizers for DFIG-based wind farms," *IEEE Transactions on Energy Conversion*, vol. 23, pp. 519–528, June 2008.

[104] T. Thiringer and J.-A. Dahlberg, "Periodic pulsations from a three-bladed wind turbine," *IEEE Transactions on Energy Conversion*, vol. 16, pp. 128–133, June 2001.

[105] L. B. Ristic and B. I. Jeftenic, "Implementation of fuzzy control to improve energy efficiency of variable speed bulk material transportation," *IEEE Transactions on Industrial Electronics*, vol. 59, pp. 2959–2969, July 2012.

[106] T.-L. Chern, L.-H. Liu, P.-L. Pan, T.-M. Huang, D.-M. Tsay, J.-H. Kuang and L.-J. Chen, "Digital signal processing-based sensor-less permanent magnet synchronous motor driver with quasi-sine pulse-width modulation for air-conditioner rotary compressor," *IET Electric Power Applications*, vol. 6, pp. 302–309, July 2012.

[107] J. D. M. De Kooning, J. Van de Vyver, T. L. Vandoorn, B. Meersman and L. Vandevelde, "Impact of speed ripple on the back-emf waveform of permanent magnet synchronous machines," *IET Electric Power Applications*, vol. 7, pp. 400–407, May 2013.

[108] F. Marignetti, V. Delli Colli, R. Di Stefano and A; Cavagnino, "Design issues of a fractional-slot windings axial flux pm machine with soft magnetic compound stator," in *Proceedings of the 33rd Annual Conference of the IEEE Industrial Electronics Society (IECON2007)*, November 5 - 8, 2007.

[109] M. Njeh, S. Cauet, P. Coirault and P. Martin, "H_∞ control strategy of motor torque ripple in hybrid electric vehicles: an experimental study," *IET Control Theory & Applications*, vol. 5, pp. 131–144, January 2011.

[110] D.-H. Lee and J.-W. Ahn, "A current ripple reduction of a high-speed miniature brushless direct current motor using instantaneous voltage control," *IET Electric Power Applications*, vol. 3, pp. 85–92, March 2009.

[111] H. Zhu, X. Xiao and Y. Li, "Torque ripple reduction of the torque predictive control scheme for permanent-magnet synchronous motors," *IEEE Transactions on Industrial Electronics*, vol. 59, pp. 871–877, February 2012.

[112] M. C. Paicu, I. Boldea, G. D. Adreescu and F. Blaabjerg, "Very low speed performance of active flux based sensorless control: interior permanent magnet synchronous motor vector control versus direct torque and flux control," *IET Electric Power Applications*, vol. 3, pp. 551–561, November 2009.

[113] T.-C. Jeong, W.-H. Kim, M.-J. Kim, K.-D. Lee, J.-J. Lee, J.-H. Jan, T.-H. Sung, H.-J. Kim and J. Lee, "Current harmonics loss analysis of 150-kw traction interior permanent magnet synchronous motor through co-analysis of d-q axis current control and finite element method," *IEEE Transactions on Magnetics*, vol. 49, pp. 2343–2346, May 2013.

[114] C. Kral, A. Haumer and S. Bin Lee, "A practical thermal model for the estimation of permanent magnet and stator winding temperatures," *IEEE Transactions on Power Electronics*, vol. 29, pp. 455–464, January 2014.

[115] R. Yabiku, R. Fialho, L. Teran, M. E. Ramos and N. Kawasaki, "Use of thermal network on determining the temperature distribution inside electric motors in steady-sate and dynamic con-

ditions," *IEEE Transactions on Industry Applications*, vol. 46, pp. 1787–1795, September/October 2010.

[116] T. L. Vandoorn, F. M. De Belie, T. J. Vyncke, J. A. Melkebeek and P. Lataire, "Generation of multisinusoidal test signals for the identification of synchronous-machine parameters by using a voltage-source inverter," *IEEE Transactions on Industrial Electronics*, vol. 57, pp. 430–439, January 2010.

[117] J. N. H. Pérez, O. S. Hernandez, R. M. Caporal, J. de Magdaleno and H. P. Barreto, "Parameter identification of a permanent magnet synchronous machine based on current decay test and particle swarm optimization," *IEEE Latin America Transactions*, vol. 11, pp. 1176–1181, September 2013.

[118] S. Yuchao, S. Kai, H. Lipei and L. Yongdong, "Online identification of permanent magnet flux based on extended kalman filter for ipmsm drive with position sensorless control," *IEEE Transactions on Industrial Electronics*, vol. 59, pp. 4169–4178, November 2012.

[119] Y. Chen, T.-H. Liu, C.-F. Hsiao and C.-K. Lin, "Implementation of adaptive inverse controller for an interior permanent magnet synchronous motor adjustable speed drive system based on predictive current control," *IET Electric Power Applications*, vol. 9, pp. 60–70, January 2015.

[120] P. Sergeant, H. Vansompel, A. Hemeida, A. Van den Bossche and L. Dupré, "A computationally efficient method to determine iron and magnet losses in vsi-pwm fed axial flux permanent magnet synchronous machines," *IEEE Transactions on Magnetics*, vol. 50, August 2014.

[121] A. Krings, J. Soulard and O. Wallmark, "Pwm influence on the iron losses and characteristics of a slotless permanent-magnet motor with sife and nife stator cores," *IEEE Transactions on Industry Applications*, vol. 51, pp. 1475–1484, March/April 2015.

[122] D. Kowal, P. Sergeant, L. Dupré and H. Karmaker, "Comparison of frequency and time-domain iron and magnet los modeling including pwm harmonics in a pmsg for a wind energy application," *IEEE Transactions on Energy Conversion*, vol. 30, pp. 476–486, June 2015.

[123] J. D. M. De Kooning, B. Meersman, T. L. Vandoorn and L. Vandevelde, "Evaluation of the maximum power point tracking performance in small wind turbines," in *Proc. of the 2012 IEEE Power & Energy Society General Meeting (PES GM 2012)*, (San Diego, USA), 22 - 26 July 2012.

[124] J. D. M. De Kooning, T. L. Vandoorn, J. Van de Vyver, B. Meersman and L. Vandevelde, "Displacement of the maximum power point caused by losses in wind turbine systems," *Renewable Energy*, vol. 85, pp. 273–280, January 2016.

[125] International Electrotechnical Commission, *IEC 61400-12-1 ed1.0: Wind turbines - Part 12-1: Power performance measurements of electricity producing wind turbines*, 2005.

[126] J. Kuikman, "Summary of test results of Fortis Alizé (10 kw) wind turbine, IEC 61400-2," *Fortis Wind Energy, http://www.fortiswindenergy.com.*

[127] J. van Dam and D. Jager, "Wind turbine generator system power performance test report for the ARE442 wind turbine," *National Renewable Energy Laboratory*, 2010.

[128] A. Huskey, A. Bowen and D. Jager, "Wind turbine generator system power performance test report for the Mariah Windspire 1 kW wind turbine," *National Renewable Energy Laboratory*, 2009.

[129] P. M. Anderson and A. Bose, "Stability simulation of wind turbine systems," *IEEE Transactions on Power Apparatus and Systems*, pp. 3791–3795, December 1983.

[130] S. Morimoto, H. Nakayama, M. Sanada and Y. Takeda, "Sensorless output maximization control for variable-speed wind generation system using IPMSG," *IEEE Transactions on Industry Applications*, vol. 41, no. 1, pp. 60–67, 2005.

[131] R. J. Wai, C. Y. Lin and Y. R. Chang, "Novel maximum-power-extraction algorithm for PMSG wind generation system," *IET Electric Power Applications*, vol. 1, no. 2, pp. 275–283, 2007.

[132] W. Qiao, L. Qu and R. G. Harley, "Control of IPM synchronous generator for maximum wind power generation considering mag-

netic saturation," *IEEE Transactions on Industry Applications*, vol. 45, pp. 1095–1105, May/June 2009.

[133] E. S. Abdin and W. Xu, "Control design and dynamic performance analysis of a wind turbine-induction generator unit," *IEEE Transactions on Energy Conversion*, vol. 15, pp. 91–96, March 2000.

[134] S. M. Barakati, M. Kazerani and J. D. Aplevich, "Maximum power tracking control for a wind turbine system including a matrix converter," *IEEE Transactions on Energy Conversion*, vol. 24, pp. 705–713, September 2009.

[135] A. Murdoch, J. R. Winkelman, S. H. Javid and R. S. Barton, "Control design and performance analysis of a 6 MW wind turbine-generator," *IEEE Transactions on Power Apparatus and Systems*, pp. 1340–1347, May 1983.

[136] E. C. Morgan, M. Lackner, R. M. Vogel and L. G. Baise, "Probability distributions for offshore wind speeds," *Energy Conversion and Management*, vol. 52, pp. 15–26, July 2011.

[137] K. Tan and S. Islam, "Effect of loss modeling on optimum operation of wind turbine energy conversion systems," in *Proc. of the 2005 International Power Engineering Conference (IPEC 2005)*, (Singapore), 29 November - 2 December 2005.

[138] M. Jinbo, G. Cardoso Junior, F. A. Farret, D. Lellis Hoss and M. Ceretta Moreira, "Fixed and adaptive step HCC algorithms for MPPT of the cylinders of magnus wind turbines," in *Proc. of the 3rd Renewable Power Generation Conference (RPG 2014)*, (Naples), 24-25 September, 2014.

[139] X. Bracke, J. D. M. De Kooning, J. Van de Vyver and L. Vandevelde, "Effective capture of wind gusts in small wind turbines by using a full active rectifier," in *Proc. of the 2014 IET Renewable Power Generation conference (IET RPG 2014)*, (Napels, Italy), 24-25 Sept. 2014.

[140] Energypedia, "Wind turbine technology," *https://energypedia.info/wiki/Wind_Turbine_Technology*.

[141] H. Hojabri, H. Mokhtari and L. Chang, “Reactive power control of permanent-magnet synchronous wind generator with matrix converter,” *IEEE Transactions on Power Delivery*, vol. 28, pp. 575–584, April 2013.

[142] S. Khwan-on, L. de Lillo, L. Empringham, P. Wheeler and C. Gerada, “Fault-tolerant, matrix converter, permanent magnet synchronous motor drive for open-circuit failures,” *IET Electric Power Applications*, vol. 5, pp. 654–667, September 2011.

[143] K. De Gussemé, W. R. Ryckaert, D. M. Van de Sype, J. A. Ghijselen, J. A. Melkebeek and L. Vandevelde, “A boost pfc converter with programmable harmonic resistance,” *IEEE Transactions on Industry Applications*, vol. 43, pp. 742–750, May/June 2007.

APPENDICES

A

MACHINE DATA

The following table lists the complex Fourier components of the BLDC motor investigated in [87]. The components are normalised to the fundamental component. Only odd components are included as the waveform has half-wave symmetry.

Table A.1: Complex Fourier components [87]

Order	Complex component	Order	Complex component
1	-0.0678 - j 0.9977	27	0.0009 + j 0.0030
3	-0.0405 - j 0.2107	29	0.0000 - j 0.0004
5	-0.0063 - j 0.0216	31	0.0005 + j 0.0013
7	0.0300 + j 0.0315	33	0.0000 - j 0.0030
9	0.0365 + j 0.0288	35	0.0014 - j 0.0006
11	0.0602 + j 0.0173	37	0.0020 + j 0.0007
13	-0.0137 - j 0.0104	39	0.0016 - j 0.0006
15	0.0073 + j 0.0027	41	0.0000 + j 0.0019
17	-0.0019 + j 0.0017	43	0.0009 + j 0.0024
19	-0.0039 + j 0.0019	45	0.0014 - j 0.0019
21	-0.0005 - j 0.0011	47	-0.0025 - j 0.0009
23	-0.0017 - j 0.0009	49	-0.0027 + j 0.0000
25	-0.0010 + j 0.0031		

B

IEC 61400-2 Data

The following table contains the relevant data from [126–128].

Wind speed v [m/s]	1	2	3	4	5	6	7	8	9	10	11	12	13	14	15	16	17	18
Fortis Alizé																		
P_w [kW]	0.02	0.19	0.64	1.51	2.95	5.09	8.09	12.07	17.18	23.57	31.37	40.73						
P [kW]	0.00	0.00	0.02	0.36	1.18	2.22	3.40	4.64	5.91	7.30	8.67	9.94						
Ω [rpm]	3	27	75	123	141	152	163	173	200	228	243	274						
Xzeres 442																		
P_w [kW]		0.00	0.57	1.35	2.63	4.55	7.23	10.79	15.36	21.07	28.04	36.41	46.29	57.82	71.11	86.30	103.52	122.88
P [kW]		0.00	0.00	0.30	0.91	1.86	3.04	4.41	6.02	7.70	9.17	10.10	9.91	9.00	8.28	7.85	7.33	7.57
Ω [rpm]		5	17	48	81	97	105	111	117	123	130	137	142	145	145	146	147	148
Mariah Windspire																		
P_w [kW]				0.58	1.13	1.95	3.10	4.62	6.58	9.02	12.01	15.59	19.82					
P [kW]				0.01	0.05	0.13	0.25	0.41	0.64	0.88	1.02	1.09	0.96					
Ω [rpm]				80	164	227	279	320	350	367	373	371	369					